Nonlinear Rate-Dependent Material Model with Damage and Plasticity from Granular Micromechanics Approach

By

Author Viraj Singh

Submitted to the graduate degree program in Department of Mechanical Engineering and the Graduate Faculty of the University of Kansas in partial fulfillment of the requirements for the degree of Doctor of Philosophy.

_____
Chairperson Dr. Anil Misra

_____
Dr. Paulette Spencer

_____
Dr. Sarah L Kieweg

_____
Dr. Jennifer S Laurence

_____
Dr. Jie Han

_____
Dr. Qiang Ye

Date Defended: May 01st, 2014

The Dissertation Committee for Viraj Singh

certifies that this is the approved version of the following dissertation:

NONLINEAR RATE-DEPENDENT MATERIAL MODEL WITH DAMAGE AND PLASTICITY FROM GRANULAR MICROMECHANICS APPROACH

_____

Chairperson Dr. Anil Misra

Date approved: May 1st, 2014

ABSTRACT

Cross-linked polymers and soft materials exhibit nonlinear rate and time dependent behavior, predominantly at high stress/strain amplitudes or at elevated temperatures. The existing constitutive relationships in the literature are phenomenological based and ignores the effect of microstructural changes on the overall mechanical behavior. Therefore, to overcome the limitation of phenomenological based models, we utilize granular micromechanics approach in conjunction with thermo-mechanics to develop a physics based constitutive model with included damage and plasticity at micro-scale. To obtain the stress-strain behavior, appropriate micro-scale force displacement relationship is used along with the kinematic assumption and theory of stress means. The advantage of this approach is that, the resultant continuum model retains the discrete nature of underlying material by incorporating the effect of nearest neighbor grain interactions. In addition to this, damage and plastic potential are defined using simple 1d functions at micro-scale.

To demonstrate the capability of the developed model, it is implemented into a finite element and Euler beam framework to predict, (a) the nonlinear bending of dentin adhesive and collagen-adhesive composite beams, (b) the creep, creep-recovery and monotonic behavior of hot mix asphalt (HMA), (c) the durability of adhesive-dentin interface subjected to monotonically increasing load and (d) the permanent deformation of HMA pavement under cyclic load. Numerical results indicate that the model is able to predict accurately (i) the nonlinear bending of dentin adhesive beams under chemically active media, (ii) tertiary creep and creep-time to failure of HMA. In addition to this, FE simulations show that, the strength of a-d interface is affected by both the loading rate and the geometry of a-d interface and the rutting depth of HMA pavement depends nonlinearly upon the applied load.

ACKNOWLEDGEMENT

First, I would like to thank, Dr. Anil Misra and Dr. Paulette Spencer for their constant support, invaluable guidance and giving me the opportunity to work on this project. This project could have never been possible without the suggestions and help provided by them.

I also wish to express my gratitude towards Dr. Sarah L. Kieweg, Dr. Jennifer Laurence, Dr. Jie Han and Dr. Qiang Ye for serving on my graduate committee and providing me their valuable insights and useful suggestions.

I would also like to thank research grants, R01DE14392, R01DE02202514392-08S1, R01 DE022054 and CMMI 1068528 from the National Institute of Dental and Craniofacial Research, National Institutes of Health and National Science Foundation, for supporting this work.

I also thank my fellow lab mates for their time and help throughout this project. Lastly, and most importantly, I express my forever gratitude to my parents, Mr. Vijai Singh and Mrs. Rajesh Kumari, and my wife, Meenakshi Mishra. I thank them for their love, emotional support and for all they have done for me. This thesis is dedicated to them.

TABLE OF CONTENTS

LIST OF FIGURES

LIST OF TABLES

Chapter 1

Introduction

1.1 Background

Wide variety of materials like cross-linked polymers, bituminous and soft materials have inherent rate and time dependent mechanical behavior. These materials are not only used in traditional engineering applications; for example, hot mix asphalt (HMA) used in the construction of pavement [1-3], but also, in other areas such as tissue engineering and tooth restoration in dentistry. In tissue engineering biodegradable synthetic polymers are used to construct scaffolds in different shapes and sizes to provide framework and mechanical stability for the artificial tissue development [4]. Whereas in dentistry, rate dependent methacrylate based polymers are used to join the subjectant tooth structure to the composite in the composite tooth restoration [5, 6]. Mechanical response of rate dependent material is assumed to linear viscoelastic when tested at low stress/strain amplitudes or at temperatures. But the mechanical behavior quickly deviates from linear viscoelastic to nonlinear rate dependent under following conditions: (a) when tested at large stress/strain amplitudes, (b) when polymers are tested close to their glass transition temperature, and (c) when these polymers are tested under the influence of physically and chemically active media like water. Here we present two specific examples for

illustration. First, the creep response of dentin adhesive changes to nonlinear when tested under changing moisture conditions [6] as shown in Figure 1-1a, and second, creep behavior of hot mix asphalt at high load or elevated temperatures [7] is also nonlinear rate dependent as shown in Figure 1-1b. It is important to understand the behavior of rate dependent materials to better design the structural components made up of these materials over the broad range of applications.

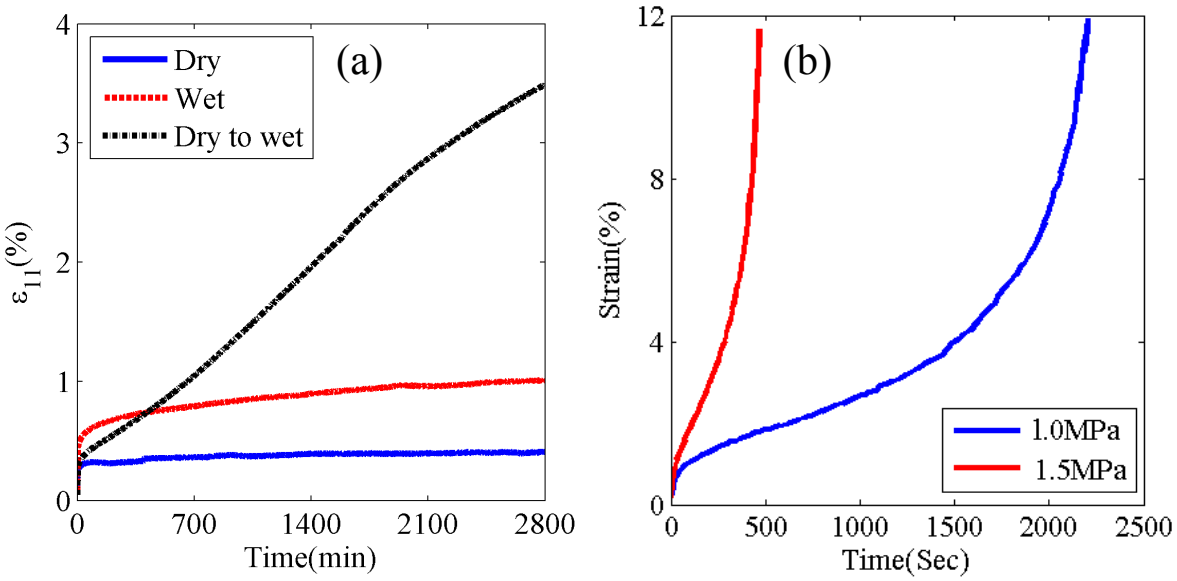

Figure 1-1: (a) Creep behavior of (a) dentin adhesive under different moisture condition and (b) hot mix asphalt at two stress amplitudes

1.2 Motivation

The observed nonlinear behavior of dentin adhesive and hot mix asphalt cannot be captured using the existing linear viscoelastic models like Kelvin Voigt, Maxwell and Burgers Model and requires nonlinear rate dependent constitutive model. Therefore, numerous constitutive models have been proposed in the literature to model nonlinear viscoelastic solids [7-14]. Comprehensive reviews about the developments in modeling such materials are provided by Wineman [9] and Schapery [12].

Schapery [11] proposed a 1d single integral constitutive theory for nonlinear viscoelastic materials. His model involves reduced time integration, which makes retardation time function of applied stress history. Several authors [10, 15, 16] have extended the work of Schapery to three dimensional frameworks, but 3d models developed are either thermodynamically inconsistent or not general. Constitutive model proposed by Pipkin-Rogers [17] involves the dependence of relaxation functions upon the step strain histories, whereas, Green-Rivlin [13] proposed multiple integral constitutive equations, where relaxation functions can be expressed as multiple integral series using Fourier series and Stone Weierstrass theorem. Other model by Drozdov [14] involves multiplicative representation of stress relaxation function. In the recent works, Abu Al Rub [18] have derived constitutive equations for materials having coupled visco-damage-plastic-healing behavior using the approach proposed by Zeigler [19]. Further, the authors used the developed model to predict the creep-recovery behavior of asphalt concrete.

But all of the constitutive models discussed above are based upon the phenomenological approach which fails to capture the effect of microstructural changes occurring due to deformation on the overall mechanical response. For example, tertiary creep or strain induced damage in amorphous cross-linked polymers, which is the consequence of polymer chains or cross-links degrading because of physical or chemical aging. Also, most of the proposed constitutive models fails to address the key research point outlined by Schapery in a review paper [12]; (a) to better understand the influence of molecular/microscale effects on the nonlinear properties of viscous solids and (b) the interaction of damage and its effects on the strength and durability on the material under investigation. Therefore, the constitutive model that captures the underlying mechanisms, and explicitly models the underlying microstructure is expected to provide better insight into the material stress-strain response.

1.3 Objective

To address the limitations of phenomenological based constitutive models and to shed light on the research areas listed by Schapery [12], we proposed a thermodynamically consistent framework for developing 3d constitutive models for nonlinear rate dependent materials with included damage and plasticity from the granular micromechanics approach. In this approach, we assume that the materials at the macro or representative volume element (RVE) scale have nonlinear time and rate-dependent characteristics due to the interactions between pseudo-molecules or grains at the sub-RVE or micro-scale. The schematic of the current approach is shown in Figure 1-2. For example, in cross-linked polymers, these interactions comprise of the non-covalent bonds, H-bonds, van der Waals forces and other physical interactions between the polymer chains. The advantage of this micromechanical approach is that it has the ability to predict a number of material phenomena, such as dilation, pressure sensitivity and tertiary creep, which manifest due to material granularity. The other advantage of the model is that, the damage, plastic potential and flow rule are defined using simple 1d function at micro-scale, whereas in phenomenological approach one has to formulate complicated 3d plastic potentials, damage functions and flow rules for their evolution. In addition to this, utilization of thermo-mechanics ensures that the deforming granular medium is in thermodynamic equilibrium at each grain or interaction scale.

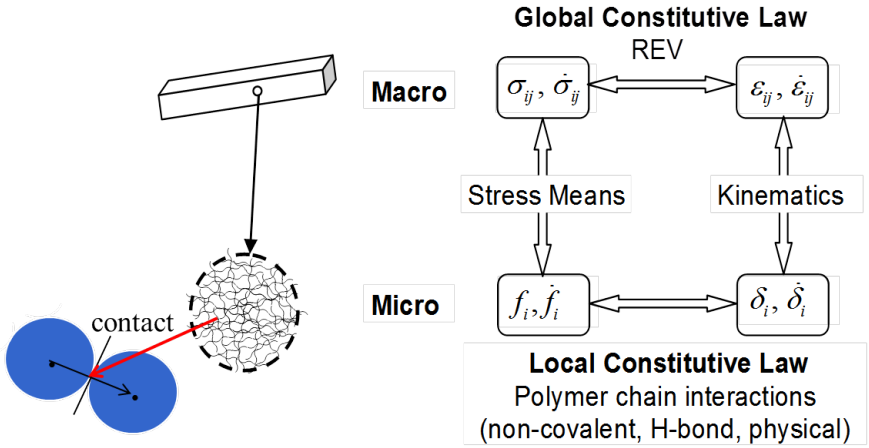

Figure 1-2: Schematic of the proposed micromechanical approach

In the current work, the developed nonlinear rate dependent micromechanical model is numerically implemented to investigate the mechanical response of hot mix asphalt at 20^{o}C, under three loading conditions, (a) monotonic tests at 3 strain rates, (b) creep at 2 stress amplitudes and (c) creep recovery at different loading under uniaxial compressive and tensile loading. Further, the constitutive model is also implemented into an Euler beam bending and finite element framework to predict the response of initial boundary value problems subjected to complicated boundary and loading conditions. In particular material model is implemented to (i) simulate the 3 point bending of dentin-adhesive and collagen adhesive composite beams under different moisture and loading rates (ii) predict the durability of adhesive-dentin interface subjected to monotonically increasing load and (iii) calculated the permanent deformation in hot mix asphalt pavement under repeated tire pressure.

1.4 Organization of Dissertation

Chapter 1 -Introduction: This chapter describes the background, presents the motivation, objectives and scope of the current work.

Chapter 2 - Mechanical Properties of Methacrylate Based Model Dentin Adhesives Effect of Loading Rate and Moisture Exposure: This chapter presents the experimental protocol and results of mechanical testing on dentin adhesive beam samples. In particular, creep and monotonic tests are performed on dentin adhesives under three moisture conditions (a) dry, (b) wet and (c) dry to wet. Experimental results from this chapter will be used to cross validate the developed micromechanical model.

Chapter 3 - Viscoelastic Properties of Collagen-Adhesive Composites under Water Saturated and Dry Conditions: This chapter presents the results of creep and monotonic tests on the adhesive infiltrated demineralized bovine dentin (AIDBD) samples or simply termed as collagen-adhesive composite under dry and wet condition. This AIDBD is one of the major components of adhesive-dentin (a-d) interface in a composite tooth restoration. The durability of composite tooth restoration primarily depends upon the properties of a-d interface. Moreover the experimental results from this chapter will be combined with granular micromechanical model to predict the mechanical response of a-d interface.

Chapter 4: Rate-Dependent Granular Micromechanics Model. This chapter describes the development of nonlinear rate dependent constitutive model with damage using micro-scale force-displacement relationship. Further, the constitutive model is implemented into an accurate and computationally fast numerical scheme to study the response of model under multiaxial loads. In particular, 2d and 3d failure envelopes for monotonic loading and creep-time-failure envelope are presented.

Chapter 5: **Thermo-mechanics based constitutive model for nonlinear rate dependent materials with damage and plasticity:** The current chapter presents the development of thermo-mechanical framework for granular materials. The framework is then used to obtain the nonlinear rate dependent constitutive model. Further, constitutive equation is validated and verified using the experimental creep and creep-recovery data for hot mix asphalt.

Chapter 6: **Implementation of Constitutive Model into a Euler Beam Bending Framework:** The explicit form of constitutive material model is implemented into a Euler beam bending framework to predict the mechanical response of dentin-adhesive and collagen–adhesive beams in a 3 point bending configuration.

Chapter 7: **Finite Element implementation of Micromechanical Model**: This chapter describes the various steps required to implement the nonlinear rate dependent granular micromechanical model into a finite element framework.

Chapter 8-10: Chapters 8 9 and 10 presents the application of developed finite element frame work to predict, 3 point bending of dentin adhesive beams, durability of a-d interface and the permanent deformation of hot mix asphalt pavement respectively.

Chapter 2

Mechanical Properties of Methacrylate Based Model Dentin Adhesives Effect of Loading Rate and Moisture Exposure

2.1 Introduction

The bond formed at the dentin-adhesive (a-d) interface is arguably the key to successful composite dental restorations and remains its weakest link [20, 21]. In restorative dentistry using polymer composites, the tooth surface is generally pre-treated with acids to increase the porosity. Acid-etching extracts the mineral from the dentin to expose the collagen matrix[22]. The composition of the acid-etched dentin is 30% collagen and 70% water[23]. The adhesive is expected to infiltrate the wet, collagen matrix and photo-polymerize to form a solid seal. Acid-etching provides effective mechanical bonding between enamel and adhesive, but bonding to dentin has been fraught with problems. Clinicians frequently find very little enamel available for bonding at the gingival margin of class II composite restorations and thus, the bond at this margin depends on the integrity of the adhesive seal formed with dentin [24, 25].

In the mouth, dentin adhesives are exposed simultaneously to mechanical loads and an environment that experiences fluctuating temperatures and acidic to basic conditions. The synergistic action of the caustic oral environment and mechanical loading accelerates degradation or failure of dentin adhesives, which further causes premature failure of the

composite restoration. Regardless of the reason for failure, the role of the dentin adhesive is paramount as the bridging material that provides the mechanism of load transfer between the dentin and the composite [26, 27, 28]. The causes of dentin adhesive failure under the combined influence of chemical and mechanical stress can be broadly categorized into the following: (a) proliferation of surface and subsurface flaws due to the combined effects of mechanical-loads and exposure to chemical challenges and (b) change in the chemical nature of the polymer in the form of phase-separation, crystallization or plasticization.

Most dentin adhesive characterization studies are focused on bond strength investigations that by nature incorporate the effects of dentin and composite [29-32]. Dentin adhesives are viscoelastic materials having rate-dependent mechanical properties; hence the bond test result should depend upon the loading rate. Since, bond strength tests are typically preformed at a high loading rate, the dentin adhesive should have a stiffer response which would lead to characteristically higher bond strengths that may not be always representative of the loading conditions under function. Moreover, the bond strength test does not identify the modes of failure. Failure in bond strength testing usually means complete separation of two surfaces, but failure for dentin adhesives can also be described by the magnitude of permanent deformation accumulated. For example, under constant load, dentin adhesives can accumulate large permanent strain without fracturing or breaking. This phenomenon where the specimen does not fracture into two pieces, but has large permanent deformation under a constant load, is defined as creep. This phenomenon is clinically relevant, because in the composite restoration, the dentin adhesive might not completely fracture but can deform considerably and create spaces that will be infiltrated by enzymes, bacteria and oral fluids. The penetration of these agents into the

spaces between the tooth and composite will undermine the restoration and lead to recurrent caries, hypersensitivity, and pulpal inflammation.

Therefore, independent characterization of the rate-dependent dentin adhesive mechanical behavior in the presence of water is required to better understand their role in the clinical environment. At present these dentin adhesive properties have not been widely investigated. In our previous work [5], we have shown that water acts as a plasticizer and decreases the elastic modulus and fatigue life of model dentin adhesives. In the current study we have further explored the effect of water on the mechanical behavior of methacrylate-based dentin adhesives. We note that this study focuses upon the adhesive behavior and not the interaction of the adhesive and the dentin substrate. In particular, we have investigated the properties of two model dentin adhesives under creep and rate-dependent monotonic loading in different moisture conditions. The hypothesis of the investigation reported herein is that the mechanical properties of methacrylate based dentin adhesive are affected by loading rate and moisture content. We have found that these dentin adhesives exhibit various responses under different moisture conditions and loading rates, including an anomalous creep response.

2.2 Materials and Methods

2.2.1 Material

In this study we have used two formulations of dentin adhesives, (a) control dentin adhesive consisting of 2-Hydroxyethylmethacrylate (HEMA, Acros Organics, NJ) and 2,2-bis[4-(2-hydroxy-3-methacryloxypropoxy) phenyl]-propane (BisGMA, Polysciences, Warrington, PA) with a mass ratio of 45/55 (HEMA/BisGMA) and (b) experimental formulation consisting of

HEMA, BisGMA and 2-((1,3-bis(methacryloyloxy)propan-2-yloxy)carbonyl)benzoic acid (BMPB, synthesized by our group) [28] with a mass ratio of 45/30/25. The following photoinitiators (all from Aldrich, Milwaukee, WI) were used in the study: camphorquinone (CQ), ethyl-4-(dimethylamino) benzoate (EDMAB) and diphenyliodonium hexafluorophosphate (DPIHP). The amounts of photosensitizer, co-initiator amine and iodonium salt were fixed at 0.5 mass% with respect to the total amount of monomer. Continuous shaking and sonication for 48 hours were required to yield well-mixed resin solutions. All the materials in this study were used as received. Figure 2-1 shows the monomers used in the study

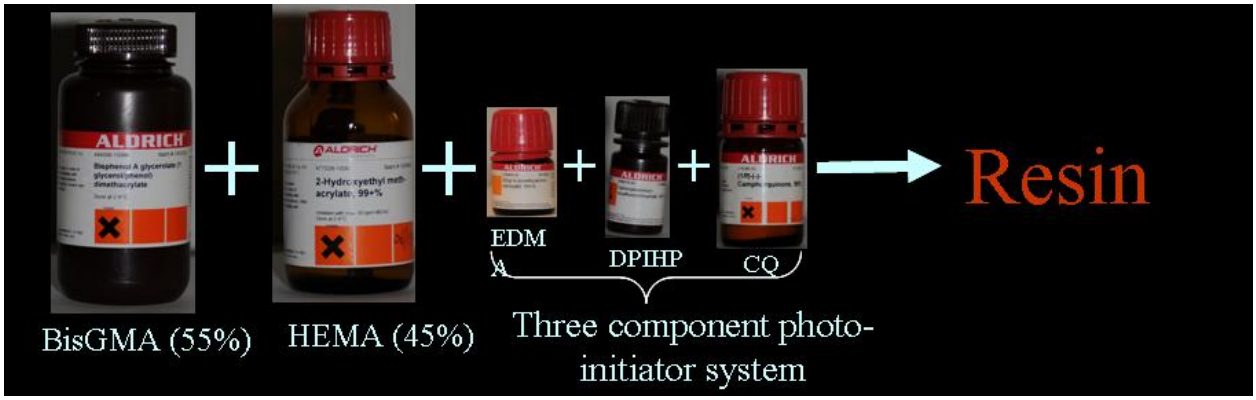

Figure 2-1 Monomers used to make resin

2.2.2 Sample Preparation

Rectangular beam samples of cross sections 1mmx1mm and length 15mm were made by curing the resin in a glass-tubing mold (Fiber Optic Center Inc, #CV1012, Vitrocom Rectangular Capillary Tubing of Borosilicate Glass). The model adhesives were injected into glass tubes using a micro-pipette, and subsequently, polymerized for 10 seconds in a light curing box which has both top and bottom LED plates of irradiance 250mW/cm^2 and area 6.25mm^2 (LED Curebox, Proto-tech, Portland, OR, USA). The polymerized samples were stored in the dark at

room temperature for 2 days to provide adequate time for post-cure polymerization. The samples were then extracted from the glass tubing mold and stored for 3 days in a vacuum oven in the presence of a drying agent at 37^{o}C to remove water that may have been absorbed during sample preparation.

2.2.3 Degree of Conversion

The degree of conversion (DC) of polymerized and stored samples as described above was determined using Raman spectroscopy. Spectra were collected using a LabRAM ARAMIS Raman spectrometer (LabRAM HORIBA Jobin Yvon, Edison, New Jersey) with a HeNe laser (λ=633 nm, a laser power of 17 mW) as an excitation source. To determine the DC, spectra of the uncured resins and beam samples were acquired over a spectral range of 700 – 1800 cm^{-1}. The change of the band height ratios of the aliphatic carbon-carbon double bond (C=C) peak at 1640 cm^{-1}and the aromatic C=C at 1610 cm^{-1} (phenyl) in both the cured and uncured states was monitored [33]. DC was calculated using the following formula based on the decrease in the intensity band ratios before and after light curing:

DC (%) = 100[1- ($R_{cured}/R_{uncured}$)], R = (band height at 1640 cm^{-1}/band height at 1610 cm^{-1})

2.3 Mechanical Tests

2.3.1 Instrument and Data Interpretation:

Bose Electroforce 3200 (Bose Corporation, Electroforce System Group, Eden Praire, Minnesota, USA) was used in a 10 mm 3-point bending configuration for all the mechanical testing. All the

tests were performed at room temperature of 25°C. For comparison of results, the applied load and measured displacement were converted to apparent stresses and strains using the equations of elastic beam theory for long slender beam undergoing small deformations. Figure 2-2 shows the instrument used along with the 3 point bend setup.

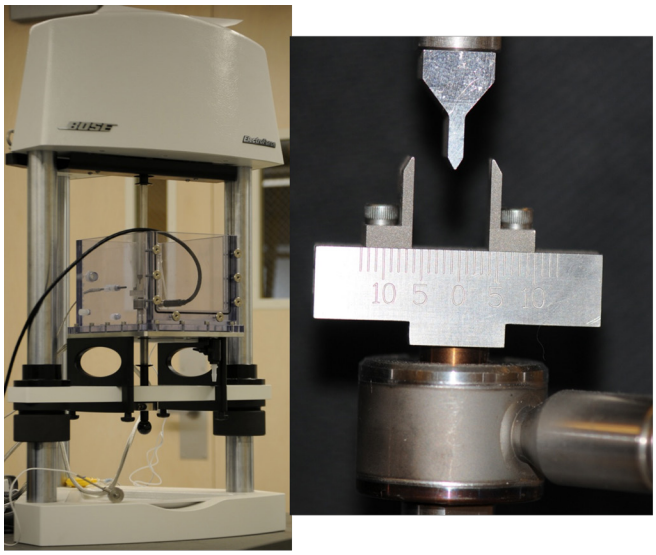

Figure 2-2 Mechanical test setup saline chamber and 3 point bending clamp

2.3.2 Moisture conditions

The monotonic and creep tests were performed under following moisture conditions:

Dry (D) Series: Beam samples were stored dry and tested dry.

Wet (W) Series: Beam samples were submerged in water for 5 days for complete saturation [34] and then tested submerged in water.

Dry to Wet (D+W) Series: Samples were stored dry and then tested submerged in water.

In addition, a D200+W *series* creep tests were performed in which the samples were stored dry and tested in the dry condition for the first 200 minutes and then water was added and the test continued with the samples submerged in water.

2.3.3 Monotonic tests

Static or monotonic tests were performed on dentin adhesives in different moisture conditions to obtain the stress-strain curves (n=3). These tests were performed at two different loading rates of 60 μm/min and 2 μm/min to investigate the effect of loading rate on the stress-strain behavior. D+W s*eries* tests were performed only at the rate of 2 μm/min.

2.3.4 Creep tests:

The creep tests for the two dentin adhesive formulations were performed under stress amplitude of 4.5MPa (n=3). This low stress amplitude was chosen such that the tested samples are primarily in the linear viscoelastic condition. D200+W s*eries* test was only performed for the control formulation.

2.3.5 Viscoelastic Model for Dentin Adhesive

To understand the viscoelastic behavior of the dentin adhesives in rheological terms we have used a Prony series [5] formed by five Kelvin-Voigt elements connected in series with different retardation times to fit the creep data from dry *(series D)* and wet *(series W)* experiments. The creep compliance function in this case is given by the following equation

$$J(t) = J_0 + J_1(1-e^{-\frac{t}{\tau_1}}) + J_2(1-e^{-\frac{t}{\tau_2}}) + J_3(1-e^{-\frac{t}{\tau_3}}) + J_4(1-e^{-\frac{t}{\tau_4}}) + J_5(1-e^{-\frac{t}{\tau_5}}) \qquad (2.1)$$

where J_0, J_1, J_2, J_3, J_4 and J_5 are creep constants, and τ_1, τ_2, τ_3, τ_4 and τ_5 are the retardation times associated with each rheological spring-dashpot system. In this study, the retardation time τ_1, τ_2,

τ_3, τ_4 and τ_5 to obtain the best fit were found to be 0.1,100,1000,10,000 and 100,000 seconds, respectively.

2.4 Results

2.4.1 Degree of Conversion

Three randomly selected samples from each batch (control adhesive and experimental adhesive) were tested for degree of conversion measurement. The average value of DC was obtained from spectra acquired from three different locations on the sample. The measured mean degree of conversion was found to be 90.0% (±1.5%) and 88.0% (±1.25%) for control and experimental formulations, respectively. Typically for these types of samples the initial degree of conversion which is measured immediately after the polymerization is 8-10% lower than the final degree of conversion after 5 days.

2.4.2 Monotonic tests

Results of the monotonic testing at different loading rates and three moisture environments are shown in Figure 2-3 We can observe that under dry conditions (*series D*) both the control and experimental dentin adhesives have similar apparent stress-strain behavior and show similar influence of loading rates. The effect of loading on the apparent elastic modulus, which is the slope of linear portion of the stress-strain curves, flexural strength and yield point (defined here as linear limit) are shown in Figure 2-3.

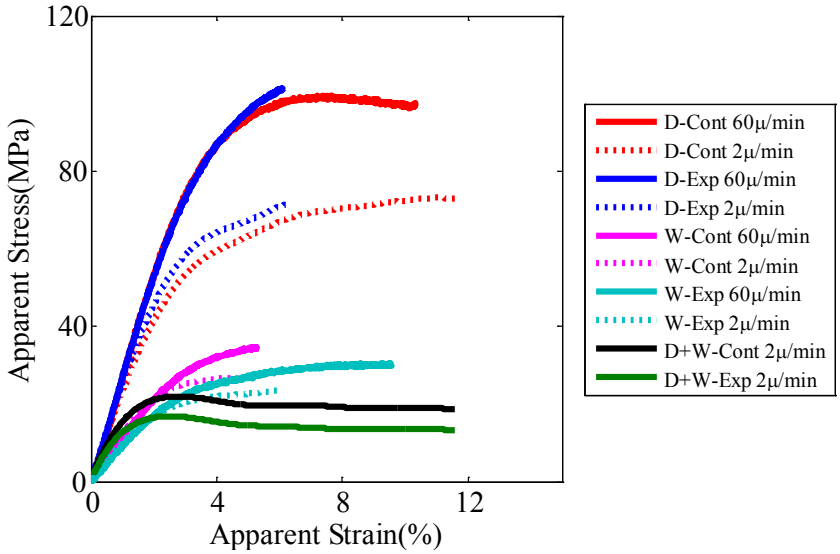

Figure 2-3 Apparent stress-strain curves for control and experimental dentin adhesives in different moisture conditions and different loading rates

Flexural strength at a loading rate of 60 μm/sec for both experimental and control adhesives in the dry state is approximately 100MPa, while at 2 μm/min flexural strengths are reduced to approximately 65MPa as shown in Table 2-1. The apparent elastic modulus is observed to have a small loading rate effect; however, we note that the yield point is achieved at a higher stress and strain under faster loading. When these dentin adhesives are stored and tested in water (*series W*), the behavior is significantly softer as compared to that in a dry environment. For the control adhesive, the apparent elastic modulus and flexural strength are reduced to 1.2GPa and 34.5MPa, respectively for the loading rate of 60 μm/min. Moreover for the experimental formulation apparent modulus and strength are reduced to 0.96GPa and 29.5MPa, respectively. Loading rate affects the behavior in wet conditions in a similar way as that in the dry conditions. In contrast, for the case of dry-to-wet moisture condition (*series D+W*), we observe that (1) the initial part of the apparent stress-strain curve is stiffer, (2) the flexural strengths and yield point are lower, and (3) the apparent stress-strain curve reach asymptote or peak stress at a smaller

strain when compared to the curves obtained for samples in completely wet conditions (*series W*).

Table 2-1 Apparent elastic modulus E, flexural strength σ_f and yield point σ_y for control and experimental dentin adhesive

Flexural Strength σ_f(MPa)	**98.5**	**67.5**	**34.5**	**21.9**	**NA**	**21.5**	**101.0**	**71.5**	**29.5**	**23.4**	**NA**	**16.8**
Yield Point σ_y(MPa)	**59.0**	**28.0**	**16.5**	**10.5**	**NA**	**7.0**	**59.0**	**30.5**	**15.5**	**9.0**	**NA**	**6.0**

2.4.3 Creep:

Results of the creep tests under different moisture conditions are shown in Figure 2-4. The following observations can be made for results from the different test series:

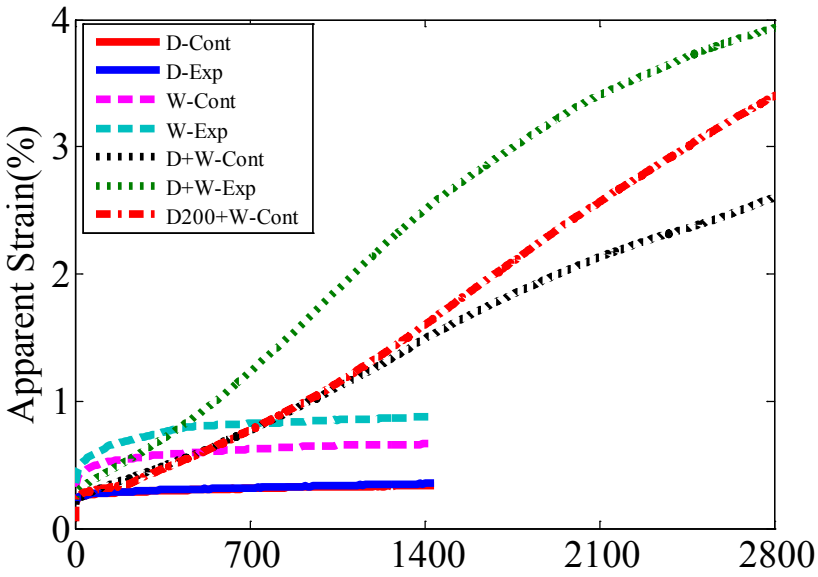

Figure 2-4: Creep curves for control and experimental dentin adhesives in different moisture conditions at apparent stress amplitude of 4.5MPa.

Series D: For the stored dry and tested dry samples, both of the adhesive formulations showed similar creep behavior. The average instantaneous strain at time, t=0, was approximately 0.23%, and these samples reached asymptotic value of creep strains 0.35% (in approximately 17 hours) indicating a linear viscoelastic response.

Series W: For the stored wet and tested wet samples, the experimental formulation showed larger creep deformation. The average instantaneous strain for the control adhesive was 0.39% and that for the experimental adhesive was 0.52% as compared to 0.23% in the dry condition. After 24 hours of testing, the samples for the control and experimental adhesive formulations had reached asymptotic strain of 0.66% and 0.88% strain, respectively, again indicating a viscoelastic linear response.

Series D+W: For the stored dry and tested wet samples, the instantaneous strain for both of the adhesives is 0.24% which is consistent with the dry condition results from *series D* test. However, as the test progressed, the samples from both the control and experimental adhesive formulations experienced considerable deformations that exceeded what the samples had in *series W* tests. During the 48 hour testing period, the control and experimental adhesive samples accumulated approximately 2.6% and 4.0% strain, respectively, and did not reach an asymptotic value.

Series D200+W: These series of tests are conducted on the control adhesive formulation only. As expected the instantaneous strain in this series was 0.23% consistent with the dry condition. Moreover, the behavior was similar to the *series D* result for the first 200 minutes when the dry conditions were maintained. However, once the water was introduced into the bath, samples experienced increasing creep deformation. During the 48 hour testing period, these samples accumulated approximately 3.5% strain, and did not reach an asymptotic value.

The creep response shown by the *series D* and *W* samples in Figure 2-4 was fitted using Prony series given in Eq (2.1). The predicted curves along with experimental curves are shown in Figure 2-5. A total of 6 unknown creep coefficients were required to be evaluated to fit the data. These creep coefficients were obtained using the non-linear least-square subroutine from Matlab

2007b. The calculated Prony series parameters are shown in Table 2-2 along with R^2 goodness of fit for both wet and dry conditions. The least-square fitting was performed under the constraint that the creep constants were non-negative [5].

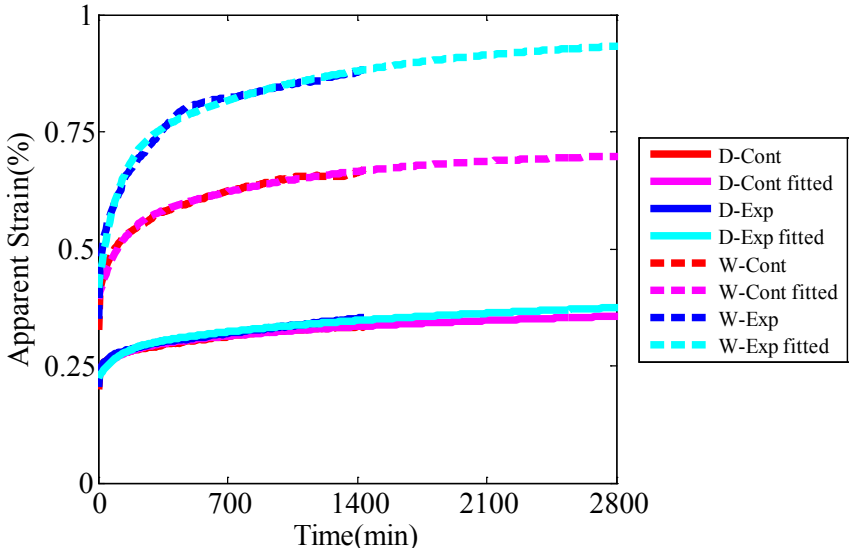

Figure 2-5 Predicted curves using Prony series for control and experimental formulation in dry and wet conditions.

Table 2-2 Prony series parameters for creep compliance function

	Control		Experimental	
	Dry x10^{-10}	Wet x10^{-10}	Dry x10^{-10}	Wet x10^{-10}
Unit-m^2/N	R2=0.9668	R2=0.9822	R2=0.9812	R2=0.9836
J0	2.44	4.30	2.30	4.60
J1	2.80	4.41	2.93	4.60
J2	0.94	3.15	1.13	6.20
J3	1.02	3.87	0.00	5.50
J4	3.78	0.00	0.00	0.00
J5	0.0	0.00	104.30	0.00

2.5 Discussion

In the current work we have evaluated the mechanical behavior of two different dentin adhesive formulations in different moisture conditions. To this end, we have performed (1) monotonic

tests at two different loading rates, and (2) creep tests at low loading levels where the behavior could be considered to linear viscoelastic. We have observed significant effect of loading rate on the failure strength and the linear limit (yield point) of the stress-strain curve, which is expected for rate-dependent material such as polymers. We have also found that the dentin adhesive formulations become softer and both the apparent elastic modulus and flexural strength decrease when the samples are stored in water (*series W*). It is important to note that when the dentin adhesives are tested dry to wet (*series D+W*) at the slow loading rate, the failure strength is the lowest and the failure occurs at a smaller deformation (~2% versus 3-4%). This is important from the clinical perspective where the composite restoration comes in contact with mechanical loading and the wet, oral environment simultaneously. If we compare the two adhesive formulations, when tested dry to wet (*series D+W*), the experimental adhesive has the lower failure strength of 16.75MPa as compared to 21.5MPa for the control adhesive. This is expected because of the more hydrophilic nature of the experimental formulation[28]. The behavior observed in this study suggests that these features are critical for the evaluation of dentin adhesives. The rate-dependent and the moisture sensitive behavior is ignored in many bond strength tests that are routinely used for evaluating dentin adhesives.

We have also observed significant differences in the creep response of the two dentin adhesives in the different moisture conditions. Creep curves for a material can be divided into three major regions: primary creep, secondary creep and tertiary creep as depicted in Figure 2-6. Primary creep is the initial region where the creep rate is high. Secondary creep is the region following primary creep where the creep rate becomes smaller and constant. Tertiary creep is marked by the region after secondary creep where creep rate becomes high again which leads to specimen

failure. Creep curves obtained from the experiments on dentin adhesives can be categorized into these creep regions.

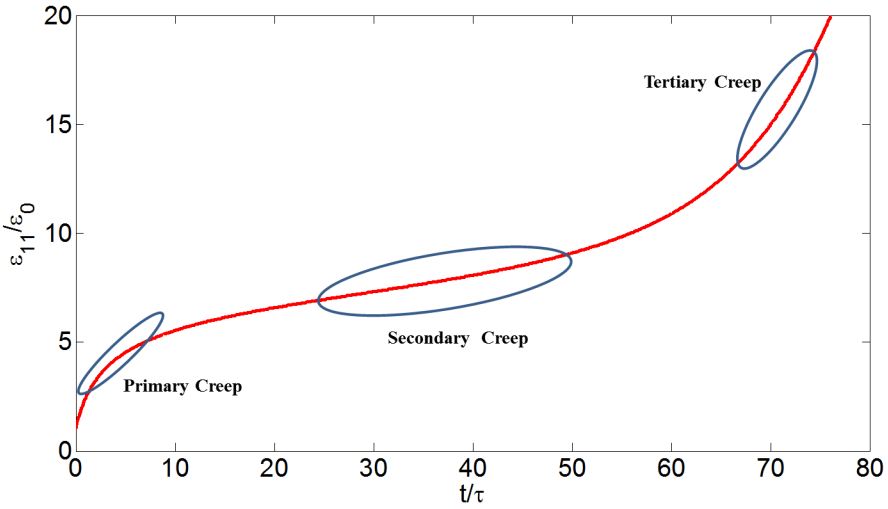

Figure 2-6 Schematic of creep response showing primary, secondary and tertiary regions

For the *series D* samples of both control and experimental adhesives, creep deformation started at 0.23% strain at time, t=0, and reached an asymptotic value of 0.32% strain after 17 hours of testing. These samples show only primary creep beyond which they reach an asymptote. *Series W* samples compared to *series D* accumulated larger strain in 1440 minutes (24 hours) of testing indicating softer behavior. The instantaneous strain in *series W* was roughly twice the instantaneous strain in *series D*, indicating plasticization of dentin adhesive due to storage in water. Similar to *series D*, *series W* samples only show primary creep.

The creep response of dry to wet tested samples (*series D+W*) shown in Figure 2-4 is very different from that of *series D* and *W* samples. Instantaneous deformation for this series is similar to *series D* indicating that the material is initially dry, but the behavior deviates from *series D* as the water diffuses into the sample. These samples undergo considerable secondary creep deformation with increasing creep rate suggestive of an imminent tertiary creep.

Remarkably, the secondary creep rate decreases after some time, and subsequently, the specimen deform under a new stable creep rate. In the results shown in Figure 2-4, the creep rate appears to slow down to a new stable rate after 1440 minutes (24 hours). It is also notable that after 2880 minutes (48 hours) the samples had accumulated 2.6% and 4% strain for the control and experimental adhesives, respectively. These strain-levels far exceed the values obtained in *series W* tests under completely wet conditions. In this work, we refer to this type of response as anomalous creep response of dentin adhesives. *Series D200+W* samples show a similar anomalous creep behavior as that of *series D+W* samples. In this case, for the first 200 minutes the response follows the dry samples consistent with results from *series D* test. Once the water is introduced into the bath, the behavior deviates as the creep rate increases and the samples accumulate strains similar to *series D+W* samples.

The anomalous creep behavior seen in the *series D+W* and *D200+W* samples are linked to the simultaneous effects of mechanical loading and water diffusion into the polymer network. When the model dentin adhesives samples are submerged, the water begins to diffuse and plasticize the polymer network by disrupting or further weakening the so called weak interactions (non-covalent bonds), such as Van de Waals, electrostatic and hydrogen bonds, in the polymer network. The plasticization process continues till the sample is completely saturated. During this period, the material can be expected to be in non-equilibrium state and susceptible to additional deformation under external loading. Therefore, we expect that the polymer behavior, such as anomalous creep or the loss of strength, will be affected by both the testing time, T_t, and the time for saturation, T_s. For further discussion, we define the ratio of saturation and testing time as $R = T_s/T_t$, which is similar to Deborah number defined as the ratio of relaxation time to interaction time [35]. When the saturation time is very large compared to

testing time, that is R>>1, the sample remains dry during the test. On the other hand, when the saturation time is small compared to testing time, that is R<<1, the sample behaves as completely saturated. In either of these cases, the sample is in an equilibrium state with respect to moisture intake during the mechanical loading. When the saturation and the testing time are of similar order, that is R≈1, the sample is in non-equilibrium state with respect to water intake and experiences anomalous creep or loss of strength. Saturation time depends upon the rate of water intake or diffusion properties of the polymer as well as the sample geometry. Furthermore, the diffusion properties are influenced by the polymer structure, stiffness of the crosslinked polymer network and its hydrophilicity[34]. The time required for complete saturation of the samples tested in this work is 24~48 hours based upon mass change with time measurements reported by our group[34]. The *series D+W* creep tests have a total testing time ~48 hours. The testing time required for *series D+W* under monotonic tests till peak stress is ~3 hours. Based upon our diffusion studies[34], the highly stressed outer ligaments should also experience substantial water invasion at ~3 hours. Consequently, the effects of the non-equilibrium material state are seen in both creep and monotonic *series D+W* tests

For *series D* tests, the sampled remain dry so no anomalous creep is observed. For the *series W* samples, once the sample is saturated and the diffusion process complete, the sample achieves an equilibrium state. Since no external energy is applied in form of mechanical loads during water diffusion or, the accompanying plasticization, anomalous deformations are not observed. Since the activation energy of saturated sample is lower as compared to dry sample because of plasticization, larger deformations compared to dry samples are produced. Thus, based upon the experimental results, it can be concluded that when the moisture content of dentin adhesive is at extreme level and constant, either completely saturated or completely dry during

mechanical testing, no anomalous creep or loss of strength is observed. When the moisture content of the dentin adhesive is changing during mechanical loading, anomalous creep and loss of strength are observed. Similar moisture-induced effects have been described for other materials like wood, wool, and Kevlar polyurethane. These effects have been attributed to molecular mobility, physical ageing, and sorption induced stress gradients [36-38].

We also note that the behavior of the *series D* and *W* samples is linear viscoelastic and can be modeled by the use of Prony series described in our previous work [5]. However, the creep behavior shown by *series D+W* and *D200+W* samples cannot be predicted using linear viscoelastic Prony series. More representative physics-based mathematical models are needed which take into account the moisture induced damage of non-covalent bonds in these types of polymers (see for example[39]).

Finally, we note that the composition of the adhesive formulations used in this study do not necessarily duplicate the current commercial dentin adhesives. Current dentin adhesives used in the clinic may be composed of different co-monomer systems. These clinical systems are likely to have similar behavior because of the hydrophilic component although the quantitative results may be different. Moreover the degree of conversion may have an effect on the quantitative results but the overall behavior is expected to be similar.

2.6 Summary

In the current chapter two type of model methacrylate-based dentin adhesives were studied for their mechanical properties under conditions that simulate the wet oral environment. Rate-dependent monotonic tests and creep tests were performed on rectangular beam samples of these dentin adhesives in 3 point bending configuration under different moisture conditions. The

monotonic test results showed that model dentin adhesives have significant rate dependent behavior. We found that the failure strength and yield point decreased with a decrease in loading rate. In addition, these tests showed that the failure strength is low and the failure occurs at a smaller deformation when the tests are performed under continuously changing moisture conditions. The creep test results showed that under constant moisture conditions, either completely dry or wet, the model adhesives exhibit only primary creep at low loading-levels. In these conditions the creep response can be characterized as linear viscoelastic. In contrast, the rate of creep and total creep strain increased substantially under the same low load-level when the moisture content of dentin adhesive was continuously changing while a constant load was applied. Creep behavior of dentin adhesives are important in many clinical situation, such as for patients with bruxing habits. In these cases, there is small relaxation time between high load conditions and the restoration will experience repeated stress cycles without complete relaxation leading to accumulation of the creep strains. Similarly in clinical situation where anomalous creep behavior is relevant, the dentin adhesive might not completely fracture but deform significantly. The resultant large creep strains will cause permanent deformation in restoration, which can create spaces that can be infiltrated by enzymes, bacteria and oral fluids that lead to recurrent caries, hypersensitivity, pulpal inflammation and the failure of the restoration. In addition, the conventional linear viscoelastic models like, Maxwell or Kelvin Voigt are not sufficient to explain the rate-dependent and anomalous creep behavior under varying moisture conditions. More rigorous physics-based mathematical models which take into account the water induced damage on polymer network are needed for characterizing and developing effective dentin adhesives.

Chapter 3

Viscoelastic Properties of Collagen-Adhesive Composites under Water Saturated and Dry Conditions

3.1 Introduction

The composites formed by infiltration of synthetic polymer resins into collagen matrices are common to many biomechanical applications, such as tissue adhesives [40, 41], collagen based scaffold materials [42-44] and restorative dentistry [20]. Particularly, in restorative dentistry, the dentin adhesive is expected to infiltrate the collagen matrix obtained by demineralizing dentin substrate using acid-etching and undergo in situ polymerization to form a solid collagen-adhesive composite. The composition of the bonding substrate following acid-etching is 30% collagen and 70% water[23]. This collagen-adhesive composite in restorative dentistry is characteristically identified as the hybrid layer and is a major component of adhesive-dentin (a-d) interface. Ideally, the hybrid layer serves as a durable connection between the bulk adhesive and subjacent mineralized dentin. In the mouth, the hybrid layer formed at the a-d interface is subjected to a combination of caustic environment and mechanical loading.

The a-d interface is arguably, the weakest link in composite restorations [20, 21, 24, 25]. The loss of integrity of this interface, even in the cases in which the restoration remains normally in-place is clinically relevant, because the micro-scale gaps will be infiltrated by enzymes,

bacteria and oral fluids. The penetration of these agents into the spaces between the dentin and the composite will lead to recurrent caries, hypersensitivity, pulpal inflammation, and will eventually undermine the restoration. Irrespective of the mechanism by which the restoration fails, the collagen-adhesive composite plays a vital role in load transfer and maintenance of the mechanical integrity of the a-d interface [26-28].

Traditionally, the mechanical behavior of the a-d interface has been investigated using bond strength tests. The bond strength tests treat the dentin-adhesive bond as an integrated entity. The bond strength investigations by nature incorporate the characteristics of dentin, the exposed demineralized dentin collagen, the collagen-adhesive composite, the adhesive in the form of tags or as an intermediate layer, the adhesive-dental composite interface and the dental composite [29-32]. However, the construct formed by these various components is quite complex especially, in the proximity of the a-d interface. Therefore, the bond strength tests seldom provide insight into the role played by each of the components that make up this important interface. Bond strength tests also ignore the rate and time dependent behavior of the dentin adhesive and the hybrid layer. Clearly, there are intrinsic merits to understanding how these components perform individually as these insights can be used to better engineer the a-d interface. In our previous work, we reported on the mechanical behavior of the dentin adhesive and the various phases it forms when polymerized in the presence of water under different loading conditions and moisture exposure [5, 34, 39, 45]. In this paper, we focus upon the viscoelastic behavior of the collagen-adhesive composites, under conditions that simulate the wet functional environment found in the oral cavity. These collagen-adhesive composites form a major component of the a-d interface and are critical for its long term durability. Currently, limited contradictory experimental results of a subset of mechanical properties have been

presented for dentin adhesive infiltrated demineralized dentin [46-50]. In particular creep and rate-dependent behavior have been rarely examined.

In this work, ideal collagen-adhesive composite are prepared under *in vitro* conditions by the infiltration of dentin adhesive into a collagen matrix obtained by the complete demineralization of bovine dentin. Two types of dentin adhesives with different hydrophilicity are used for the infiltration of demineralized bovine dentin. Further to obtain the time and rate dependent properties of these ideal collagen-adhesive composites creep and monotonic tests are performed in dry and wet conditions. The obtained time and rate dependent properties are compared with those of the neat dentin adhesives. Test results shows that the behavior of collagen-adhesive composite is much more significantly affected by water than the neat adhesive. A linear viscoelastic model for collagen-adhesive composite and dentin adhesives is developed. The applicability and significance of the linear viscoelastic model is demonstrated by predicting stress relaxation behavior, frequency dependent storage and loss moduli and rate dependent elastic modulus.

3.2 Materials and Methods

3.2.1 Adhesive-Infiltrated Demineralized Bovine Dentin (AIDBD)

3.2.1.1 Demineralized Bovine Dentin (DBD)

Bovine teeth were sectioned along buccal lingual plane into 15mm long, 1mm thick and 2mm wide slabs using low-speed water cooled diamond saw (Buehler Ltd, Lake Bluff, IL, USA). Prior to demineralization, the dentin slabs were stored in PBS with sodium azide to prevent any

bacterial contamination or growth. The dentin slabs were demineralized in 0.5M EDTA (pH 7.3) at 25^{o}C for 10 days. The solution was changed and samples were washed with distilled water every 24 hours to remove the dissolved mineral. Raman spectra were acquired before the start of the demineralization process. Schematic of various steps involved in obtaining and testing of AIDBD samples is shown in Figure 3-1. To determine if the demineralization was complete, Raman spectra were collected from the specimens after the 10 days of exposure to EDTA. These spectra were collected from various depths along an exposed section cut from a randomly selected sacrificial sample as shown in inset of Figure 3-4. The spectra collected prior to and following EDTA storage was compared. The absence of the mineral peak (P-O band at 960cm^{-1}) indicated complete demineralization. It was determined that after 10 days the mineral peak had completely disappeared which agrees with our previous demineralization experience [51]. Demineralized bovine dentin (DBD) slabs were kept in 70, 95 and 100% ethanol each for 12 hours to gradually replace the water with ethanol.

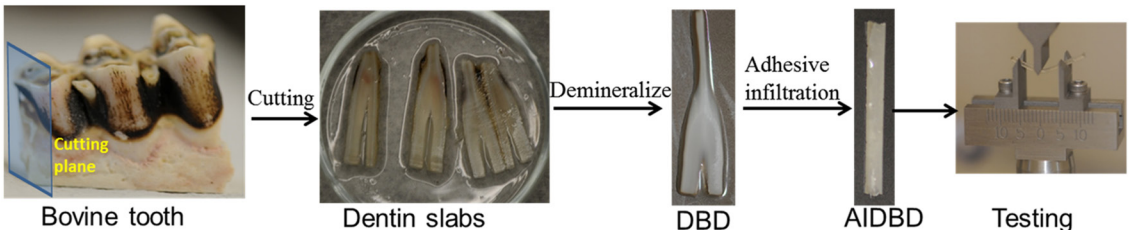

Figure 3-1: Steps involved in obtaining AIDBD samples

3.2.1.2 Adhesive Infiltration

For the adhesive infiltration, we used two adhesive formulations, (a) formulation-1:consisting of 2-Hydroxyethylmethacrylate (HEMA, Acros Organics, NJ) and 2,2-bis[4-(2-hydroxy-3-methacryloxypropoxy) phenyl]-propane (BisGMA, Polysciences, Warrington, PA) with a mass ratio of 45/55 (HEMA/BisGMA) and (b) formulation-2: consisting of HEMA, BisGMA and 2-

((1,3-bis(methacryloyloxy)propan-2-yloxy)carbonyl)benzoic acid (BMPB, synthesized by our group) [28] with a mass ratio of 45/30/25. The following photoinitiators (all from Aldrich, Milwaukee, WI) were added to both of the adhesives: camphorquinone (CQ), ethyl-4-(dimethylamino) benzoate (EDMAB) and diphenyliodonium hexafluorophosphate (DPIHP). The amounts of photosensitizer, co-initiator amine and iodonium salt were fixed at 0.5 mass% with respect to the total amount of monomer. All the materials in this study were used as received.

The adhesive formulations were diluted with ethanol in 60/40 weight ratio. The DBD samples were then immersed in the adhesive ethanol mixtures, and stored for 72 hours in a dark room. After 72 hours in the dark, the samples were desiccated in a vacuum oven for 24 hours to remove the solvent. After complete infiltration, adhesive-infiltrated demineralized bovine dentin (AIDBD) samples were polymerized using LED light curing unit of irradiance 250mW/cm^2 and area 6.25mm^2 for 40 seconds (LED Curebox, Proto-tech, and Portland, OR, USA). The polymerized samples were stored in the dark at room temperature for 48 hours to provide adequate time for post-cure polymerization. The AIDBD samples were stored for 72 hours in a vacuum oven in the presence of a drying agent at 37^o C to remove water that may have been absorbed during sample preparation

3.2.2 Neat Resin Samples

Rectangular beam samples of cross sections 1mm x 1mm and length 15mm of neat adhesive for both the formulations were made by curing the adhesive in a glass-tubing mold (Fiber Optic Center Inc, #CV1012, Vitrocom Rectangular Capillary Tubing of Borosilicate Glass)[28].

3.2.3 Degree of Conversion

The degree of conversion (DC) of the AIDBD and neat resin samples were determined using Raman spectroscopy. Spectra were collected using a LabRAM ARAMIS Raman spectrometer (LabRAM HORIBA Jobin Yvon, Edison, New Jersey) with a HeNe laser (λ=633 nm, a laser power of 17 mW) as an excitation source. To determine the DC, spectra of the uncured resins and polymerized samples were acquired over a spectral range of 700 – 1800 cm^{-1}. The change of the band height ratios of the aliphatic carbon-carbon double bond (C=C) peak at 1640 $cm^{-1}$and the aromatic C=C at 1610 cm^{-1} (phenyl) in both the cured and uncured states was monitored [33]. DC was calculated using the following formula based on the decrease in the intensity band ratios before and after light curing:

DC (%) = 100[1- ($R_{cured}/R_{uncured}$)], R = (band height at 1640 cm^{-1}/band height at 1610 cm^{-1})

3.2.4 Volumetric Composition

Two randomly selected DBD samples were measured for their wet weight M_{wet}. The samples were then dehydrated in vacuum chamber to remove the free water and their dry weight determined as M_{dry}. The water mass fraction of DBD was calculated as $\gamma_w = (M_{wet} - M_{dry})/ M_{wet}$.

The collagen and dentin adhesive mass and volume fractions in AIDBD were obtained as follows:

The DBD sample used for dentin adhesive infiltration was first weighed in its wet state to find the wet weight, S_{wet}. Thus the dry weight of DBD was then determined as, $S_{dry} = (1-\gamma_w)S_{wet}$, where w is the water mass fraction.

Subsequently, the DBD sample was infiltrated with dentin adhesive and polymerized to form the AIDBD sample, which was used to obtain the dry weight Pdry. The AIDBD sample was saturated with water to obtain wet weight Pwet. The mass fractions γ_a and γ_c of adhesive and collagen, respectively, in wet AIDBD were obtained as follows, $\gamma_a = \frac{P_{dry} - S_{dry}}{P_{wet}}$, $\gamma_c = \frac{S_{dry}}{P_{wet}}$

The volume fraction of collagen in wet AIDBD is then calculated using the following relation: $\phi_c = 1 - \phi_w - \phi_a$, where, ϕ_a and ϕ_w are the volume fractions of adhesive and water, respectively, in wet AIDBD. The volume fraction of adhesive and water are estimated using the following relations: $\phi_a = \frac{P_{dry} - S_{dry} / \rho_{dry}^a}{P_{wet} / \rho_{wet}^{AIDBD}}$, $\phi_{water} = \frac{P_{wet} - P_{dry}}{P_{wet} / \rho_{wet}^{AIDBD}}$, where ρ_{dry}^a and ρ_{wet}^{AIDBD} are the density of dry adhesive and wet AIDBD samples, respectively

3.2.5 Mechanical Tests

3.2.5.1 Mechanical Instrument and Data Interpretation

To obtain the mechanical properties of AIDBD and NR in dry and water-submerged conditions, creep and monotonic tests were performed using universal testing machine (Bose Electroforce 3200, Bose Corporation, Electroforce System Group, Eden Praire, Minnesota, USA) in a 3-point bending configuration with 10 mm span. Monotonic tests were carried out at the displacement rate of 60 μm/min[39]. The creep tests were performed on AIDBD and NR samples under the small stress amplitude of 4.5MPa in dry and wet conditions [5, 39]. During creep experiments, the loading is applied as a ramp with a rate of 9 N/min, such that the stress amplitude of 4.5MPa is achieved in ~2 seconds beyond which the stress is held constant. This loading rate is

approximately 100 times faster than the monotonic tests. Monotonic tests were also performed on the demineralized bovine dentin (DBD) sample using a tensile clamp but only in the wet environment. Before conducting mechanical tests under wet conditions both the AIDBD and NR samples were stored in water for at least 5 days for complete saturation. Further, to compute the stress and strain from the flexural load-displacement data elastic beam theory was used. The sample size for each test in this study was fixed at *n=3* and all the tests were performed at room temperature.

3.2.5.2 Linear Viscoelastic Model

The linear viscoelastic response of AIDBD and NR was modeled using a generalized Kelvin-Voigt representation with 4 elements [52, 53] as shown in Figure 3-2.

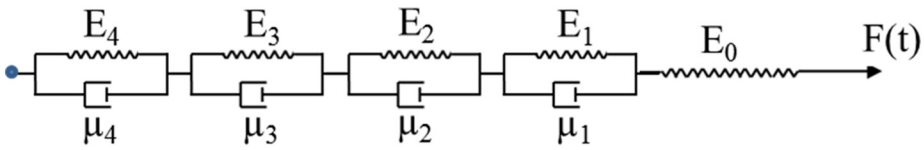

Figure 3-2: Generalized Kelvin-Voigt model with 4 elements

The governing equation for the model is given as follows:

$$\varepsilon(t) = \left(\frac{1}{E_0} + \frac{1}{E_1 + \mu_1 \frac{\partial}{\partial t}} + \frac{1}{E_2 + \mu_2 \frac{\partial}{\partial t}} + \frac{1}{E_3 + \mu_3 \frac{\partial}{\partial t}} + \frac{1}{E_2 + \mu_4 \frac{\partial}{\partial t}} \right) \sigma(t) \qquad (3.1)$$

Here, E_0, E_1 E_2, E_3, E_4, are the spring constants and μ_1 μ_2 μ_3 and μ_4 are the viscosities associated with each element of the model in Figure 3-2. To obtain the solution of the above differential equation either stress history or strain history is specified. For a constant stress history i.e. $\sigma = \sigma_0$, the following solution to Eq(3.1) is obtained using Laplace transformation

$$\varepsilon(t) = J(t)\sigma_0 \qquad (3.2)$$

In Eq(2), *J(t)* is the creep compliance function which takes the following form:

$J(t) = J_0 + J_1(1 - e^{-\frac{t}{\tau_1}}) + J_2(1 - e^{-\frac{t}{\tau_2}}) + J_3(1 - e^{-\frac{t}{\tau_3}}) + J_4(1 - e^{-\frac{t}{\tau_4}})$ where compliance coefficients, $J_0 = \frac{1}{E_0}; J_i = \frac{1}{E_i}$ and $\tau_i = \frac{\mu_i}{E_i}$ and *i=1…4*. For the numerical calculations, the retardation times $\tau_1, \tau_2, \tau_3, \tau_4$ were taken to be *1min, 10min, 100min* and *1000*min respectively. Equation 3.2 is often termed as Prony series. Similar to a constant stress history, for a constant strain loading i.e. $\varepsilon = \varepsilon_0$, the stress σ is related to strain ε through a relaxation function *G(t)* as:.

$$\sigma(t) = G(t)\varepsilon \tag{3.3}$$

here, $G(t) = G_0 + G_1(1 - e^{-\frac{t}{\tilde{\tau}_1}}) + G_2(1 - e^{-\frac{t}{\tilde{\tau}_2}}) + G_3(1 - e^{-\frac{t}{\tilde{\tau}_3}}) + G_4(1 - e^{-\frac{t}{\tilde{\tau}_4}})$ and relaxation constants G_0, G_1, G_2, G_3, G_4 and relaxation times $\tilde{\tau}_1, \tilde{\tau}_2, \tilde{\tau}_3, \tilde{\tau}_4$ are complex function of spring stiffness and damper viscosities. Therefore G_0, G_1, G_2, G_3, G_4 and $\tilde{\tau}_1, \tilde{\tau}_2, \tilde{\tau}_3, \tilde{\tau}_4$ are computed numerically in the current work.

Also the constitutive equation given in differential form in Eq(3.1) can be written in integral form using either creep compliance or stress relaxation function. If compliance function *J(t)* is known constitutive equation is represented as follows

$$\varepsilon(t) = J(t)\sigma(0) + \int_0^t J(t-s)\frac{d\sigma(t)}{dt}ds \tag{3.4}$$

On the other hand, if relaxation function *G(t)* is known constitutive equation takes the following form:

$$\sigma(t) = G(t)\varepsilon(0) + \int_0^t \mathrm{G}(t-s)\frac{d\varepsilon(t)}{dt}ds \tag{3.5}$$

During the creep test, constant stress is applied, therefore, $\frac{d\sigma(t)}{dt}=0$ in Eq(4) whereas, in a strain controlled monotonic test, strain is applied at a constant rate, that is $\frac{d\varepsilon(t)}{dt}=k$ in Eq(3.5), where *k* is the rate of loading. In addition, the creep compliance function *J(t),* can be used to compute the dynamic properties if sinusoidal stress history is applied such that

$$\sigma(t)=\sigma_0 \sin \omega s \tag{3.6}$$

Here, σ_0 is the stress amplitude and $\omega=2f\pi$, where *f* is the loading frequency. Substituting the dynamic stress given in Eq (3.6) into Eq(3.4) and simplifying, the real and imaginary part of creep compliance, *J'* and *J"*, are obtained as follows

$$J^{'}=J_{\infty}-\frac{J_1(\omega\tau_1)^2}{1+(\omega\tau_1)^2}-\frac{J_2(\omega\tau_2)^2}{1+(\omega\tau_2)^2}-\frac{J_3(\omega\tau_3)^2}{1+(\omega\tau_3)^2}-\frac{J_4(\omega\tau_4)^2}{1+(\omega\tau_4)^2} \tag{3.7}$$

where, $J_{\infty}=J_0+J_1+J_2+J_3+J_4$

$$J^{"}=-\frac{J_1(\omega\tau_1)}{1+(\omega\tau_1)^2}-\frac{J_2(\omega\tau_2)}{1+(\omega\tau_2)^2}-\frac{J_3(\omega\tau_3)}{1+(\omega\tau_3)^2}-\frac{J_4(\omega\tau_4)}{1+(\omega\tau_4)^2} \tag{3.8}$$

Now, the loss moduli G' and G" can be obtained as follows

$$G^{'}=\frac{J^{'}}{(J^{'})^2+(J^{"})^2} \tag{3.9}$$

$$G^{"}=-\frac{J^{"}}{(J^{'})^2+(J^{"})^2} \tag{3.10}$$

Finally, *tan(δ)* can be obtained from loss and storage modulus as $\tan\delta=\frac{G^{"}}{G^{'}}$

3.3 Results

3.3.1 Raman Spectroscopy and Degree of Conversion

Raman spectra were acquired on the randomly collected bovine dentin slabs before the start of demineralization process to identify the spectral features associated with mineral (P-O band at 960cm^{-1}) and collagen (amide I C=O 1653cm^{-1}). Figure 3-3 shows the Raman spectra with the normalized intensity acquired at different locations on the bovine dentin samples. Because of the concentration of mineral, the mineral peak dominates the amide I peak. After demineralization, the Raman spectra, given in Figure 3-4, show an absence of the P-O peak at 960 cm^{-1}and strong presence of amide I peak at 1653 cm^{-1}. This indicates complete demineralization of the bovine dentin slabs.

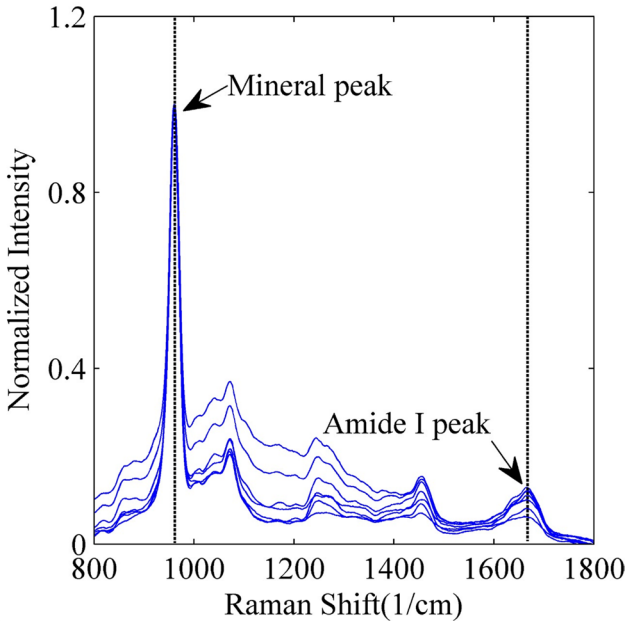

Figure 3-3: Raman spectra of bovine dentin acquired at different locations before demineralization process

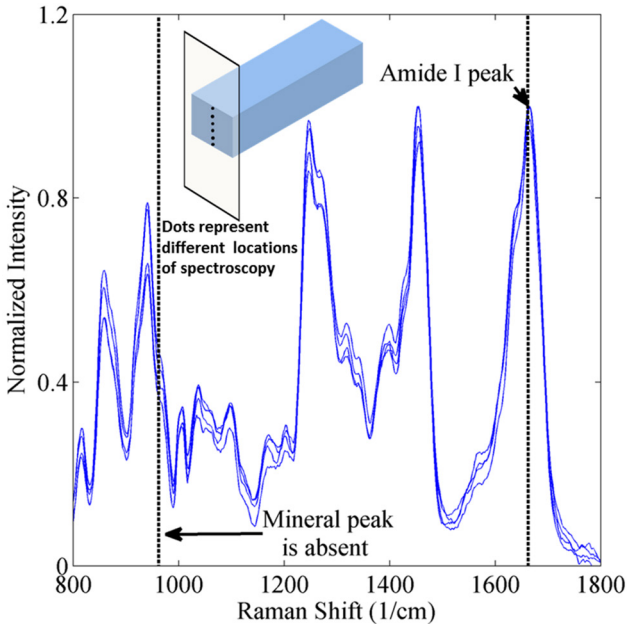

Figure 3-4: Raman spectra of bovine dentin after the demineralization process acquired along the thickness for one randomly selected sacrificial sample as shown in the inset

The adhesive infiltration in the AIDBD samples was determined by acquiring Raman spectra across the cross-section of randomly selected samples. Raman spectra for both the control and the experimental formulations are shown in Figure 3-5. The presence of spectral feature associated with the dentin adhesive (aliphatic C=C, peak at 1640 $cm^{-1}$and the aromatic C=C at 1610 cm^{-1}) across the cross-section indicated complete infiltration. The interference of amide I peak at 1653 cm^{-1} was removed while calculating the degree of conversion. The measured degree of conversion was found to be 87.0%(±0.5)% and 84.4%(±2.1)% for the AIDBD-1 and AIDBD-2 samples respectively. We note that the degree of conversion for the NR-1 and NR-2 samples was 90.0% (±1.5%) and 88.0% (±1.25%), respectively.

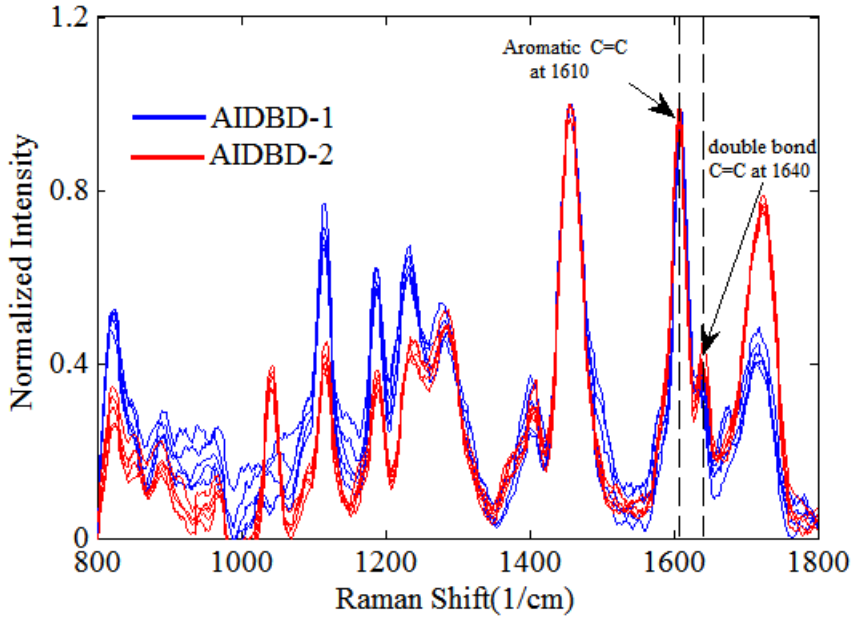

Figure 3-5 To check for complete infiltration of dentin adhesive into DBD, Raman spectra were acquired from points across the cross-section of one randomly selected sacrificial AIDBD samples as shown in the inset of Figure 3-4

3.3.2 Volumetric and Mass Composition

Calculated weight and volume fractions of DBD and dentin adhesive present in wet AIDBD are given in Table 3-1. Based upon the mass change study, the amount of water present in DBD samples was 50% (±0.3%). Further for the calculation of volume fractions, densities of dry adhesive and wet AIDBD are taken to be 1.2g/cm^3 and 1.1 g/cm^3 respectively. The volume fraction for adhesive and collagen in wet state was found to be 42.12 %(±1.10%) and 43.33 %(±1.14%) respectively.

Table 3-1 Weight fractions, volume fractions for AIDBD samples in saturated state

	Weight fraction (%)	Volume fraction (%)
Adhesive	**45.43(±1.15)**	**42.12(±1.10)**
DBD	**39.78(±1.62)**	**43.33(±1.14)**

3.3.3 Mechanical Tests

The results of the creep tests on AIDBD and NR samples in dry and wet condition are shown in Figure 3-6 a-d. From Figure 3-6a we observe that in the dry condition, the creep curves for both NR formulations was identical. The strain at the end-of-loading, considered at time t=0, was 0.2%, and the creep strain reached an asymptote of 0.35% in 1440 minutes (24hrs). The creep behavior of AIDBD in dry condition was similar to that of NR, strain at the end-of-loading was ~0.25% and the creep strain reached an asymptote of ~0.40% in 24 hours for both AIDBD samples. On the other hand, in the wet condition the NR samples have end-of-loading strain of 0.32% and 0.35%, and asymptotic creep strain of 0.67% and 0.88%, for formulations 1 and 2 respectively. Whereas, the AIDBD-1 and AIDBD-2 have end-of-loading strain of 0.60% and 0.81%, and asymptotic creep strain of 1.18% and 1.66%, respectively. Creep data is also plotted on a log-log plot in Figures 3-6c and 3-6d. The presence of inflection points in the log-log plot indicates that these materials are complex and have multiple retardation times.

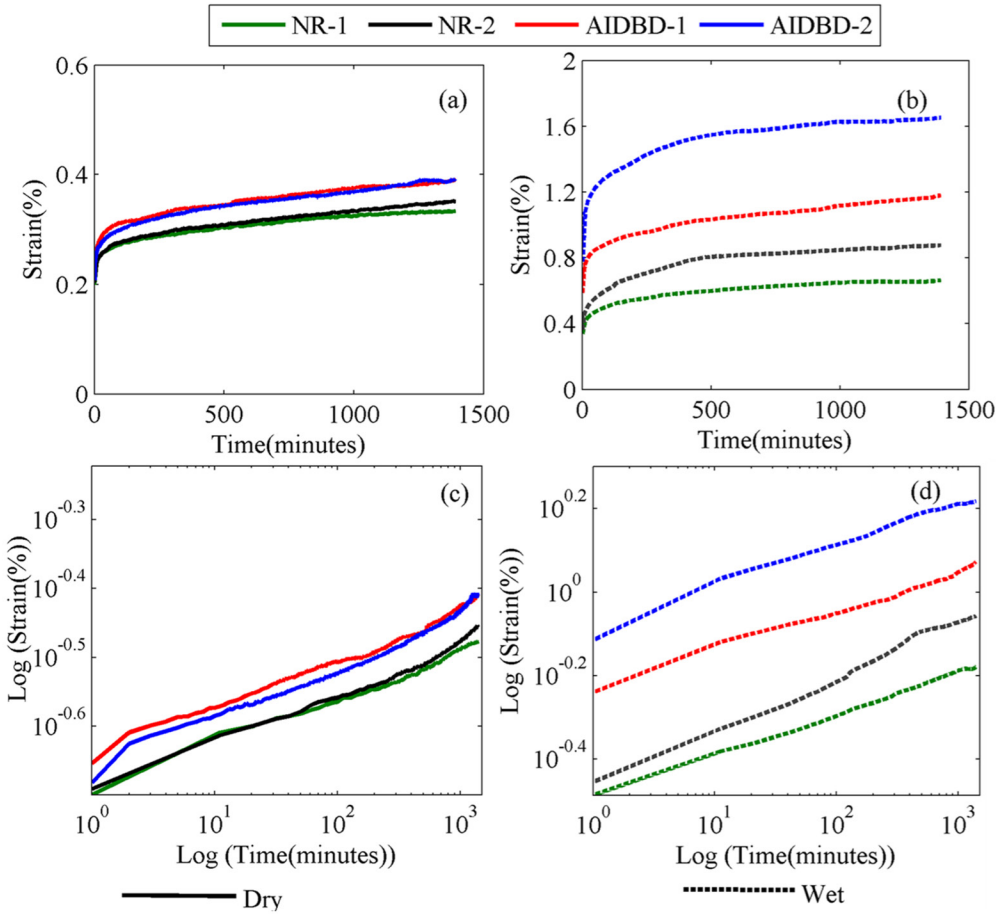

Figure 3-6: Apparent creep curves for AIDBD or hybrid layer mimics and the neat resins (NR) at stress amplitude of 4.5MPa, (a) dry condition, and (b) wet saturated environment. Plots (c) and (d) represent the creep data in log-log scales in dry and wet conditions respectively

Results of the monotonic test are given in Table 3-2 and Figure 3-7. The apparent elastic modulus, defined as the slope of the linear portion of apparent stress-strain curve, and flexural strength obtained from the monotonic tests on AIDBD and NR samples are presented in Table 2. Dry apparent elastic moduli were found to be 2.84(±0.47) GPa and 2.68(±0.20) GPa for AIDBD-1 and NR-1, respectively. For the formulation-2 in dry environment, AIDBD and NR samples have apparent elastic moduli of 2.50(±0.31) GPa and 2.67(±0.20) GPa, respectively. When AIDBD and NR samples were tested under wet saturated environment, apparent elastic moduli are reduced compared to that of dry conditions. For AIDBD-1, AIDBD-2, NR-1 and NR-2

apparent elastic moduli was found to be 0.90(±0.30), 0.50(±0.31), 1.27(±0.16) and 0.88(±0.2) GPa respectively in wet condition. Elastic modulus for demineralized bovine dentin (DBD) was found to be 41.56(±4.30)MPa in wet state.

Table 3-2: Apparent elastic modulus E(GPa) and flexural strength f(MPa)for AIDBD and neat resin

	AIDBD-1		AIDBD-2		NR-1		NR-2	
	Dry	Wet	Dry	Wet	Dry	Wet	Dry	Wet
E(GPa)	2.84 (±0.47)	0.90 (±0.30)	2.50 (±0.30)	0.50(±0.31)	2.68 (±0.20)	1.27 (±0.16)	2.67 (±0.020)	0.88 (±0.20)
f(MPa)	140(±13)	38(±2)	139(5)	17(±2)	100(±3)	42(±6)	104(±9)	26(±2)

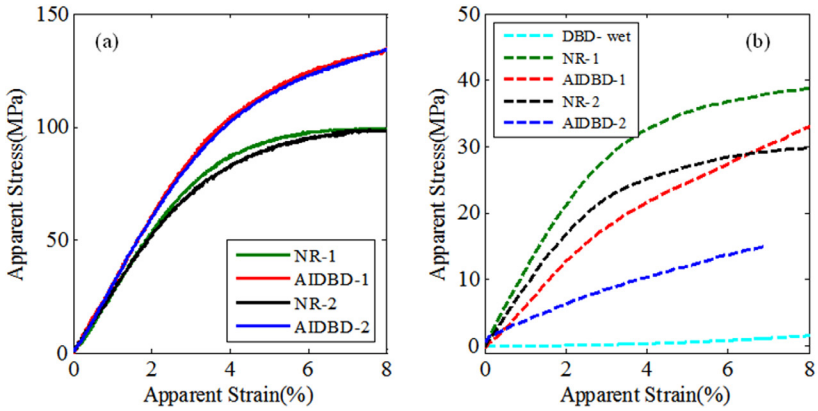

Figure 3-7: Apparent stress-strain curves for AIDBD or hybrid layer mimics and the neat resins (NR) under monotonic loading: (a) under dry condition and (b) under wet saturated condition

The flexural strength obtained from the monotonic tests is also given in Table 3-2. It was found to be 140(±13)MPa and 138(±5)MPa in dry, and 38(±2)MPa and 17(±2) MPa in wet conditions for the AIDBD-1 and AIDBD-2, respectively. The flexural strength for the NR-1 and NR-2 samples was 100(±3)MPa and 104(±9)MPa, respectively in dry conditions, and 42(±6)MPa and 26(±2)MPa, respectively in wet conditions.

3.3.4 Evaluation of Viscoelastic Model

To identify the creep compliance parameters J_0, J_1, J_2, J_3, J_4 for AIDBD and NR samples, creep data from the experiments was fitted with Eq(3.2) using a non-linear least-square subroutine from Matlab under the constraint that the creep constants are non-negative [54, 55]. The calculated model parameters along with the goodness of fit R^2 are given in Table 3-3.

Table 3-3: Creep compliance parameters for AIDBD and NR obtained using nonlinear least square fitting.

Parameters 1/GPa	AIDBD-1		AIDBD-2		NR-1		NR-2	
	Dry	Wet	Dry	Wet	Dry	Wet	Dry	Wet
J_0	0.493	1.278	0.462	1.706	0.445	0.726	0.452	1.045
J_1	0.024	0.136	0.046	0.340	0.005	0.027	0.004	0.070
J_2	0.121	0.360	0.100	0.320	0.113	0.176	0.105	0.115
J_3	0.040	0.195	0.047	0.723	0.040	0.243	0.038	0.564
J_4	0.243	0.820	0.272	0.803	0.188	0.410	0.228	0.566
Goodness of fit- R^2	0.995	0.994	0.990	0.987	0.985	0.990	0.979	0.984

The frequency dependent storage modulus, loss modulus and *tan(δ)* calculated from creep compliance data using Eq(3.4) are shown in Figure 3-8. The values of storage, loss and tan(δ) at the frequency of 0.1Hz, which is in the range of cited frequency during mastication [56-58], for AIDBD and NR are given in Table 3-4. Storage moduli for AIDBD-1 and AIDBD-2 in dry and wet conditions were found to be 1.94 and 2.0GPa and 0.7 and 0.5GPa, respectively. Relaxation function *G(t)* is also obtained from the creep compliance data. The calculated relaxation modulus parameters G_0, G_1, G_2, G_3, G_4 and relaxation times $\tilde{\tau}_1, \tilde{\tau}_2, \tilde{\tau}_3, \tilde{\tau}_4$ are given in Table 3-5 for AIDBD and NR. Stress relaxation response for AIDBD and NR at 1% applied strain is given in Figure 3-9. Under the wet environment, stress relaxes to a constant value for both AIDBD and NR in 1400 minute but, stress continues to decrease with time for both AIDBD and NR in the dry condition. Further we have also used the relaxation function *G(t)* with Eq(5) to predict rate dependent elastic modulus

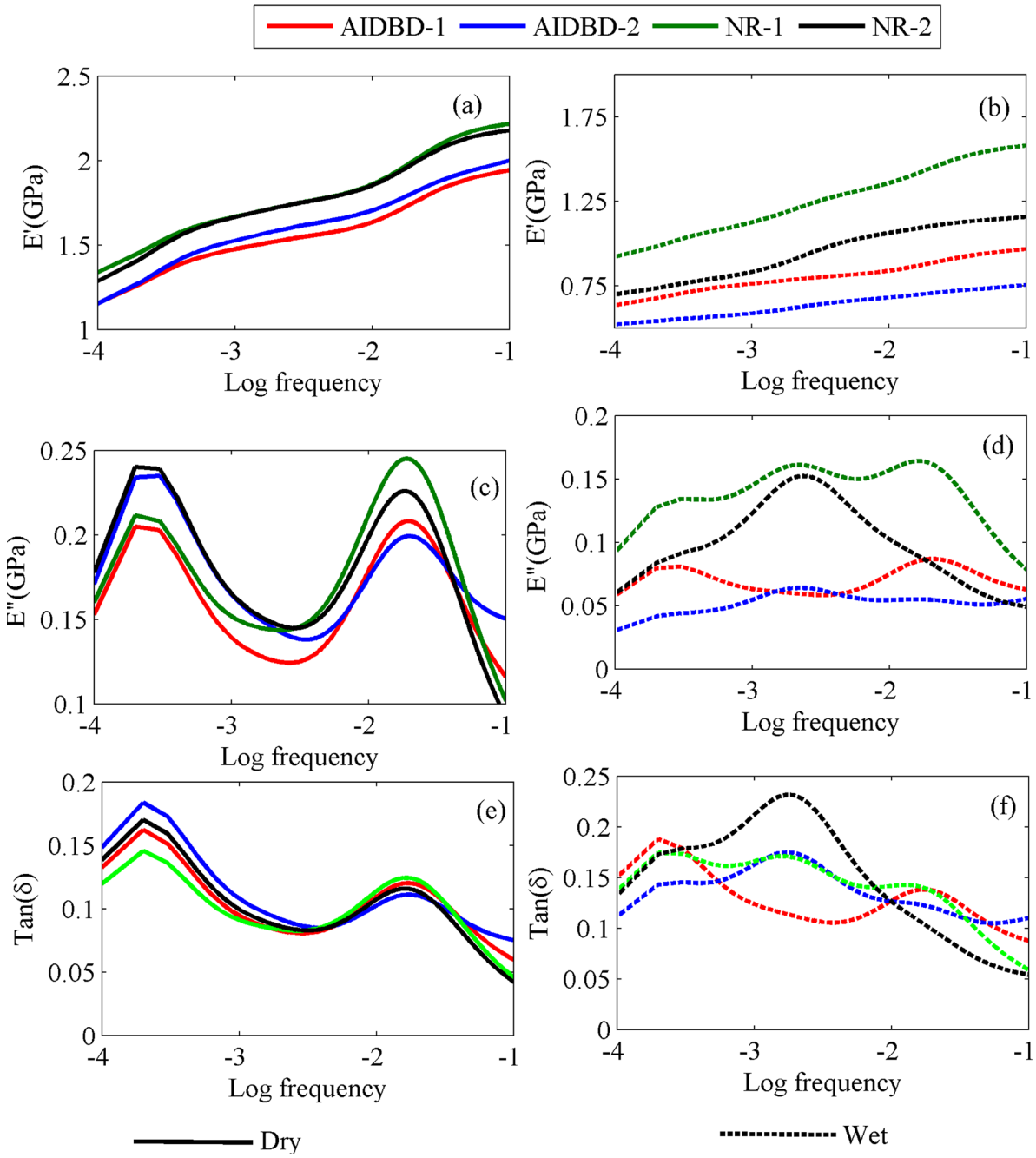

Figure 3-8: Predicted storage and loss moduli and tan(δ) at different frequencies (in Hz) for AIDBD and neat resins(NR) (a) dry storage modulus, (b) wet storage modulus, (c) dry loss modulus, (d) wet loss modulus, (e) dry *tanδ*, and (f) wet *tanδ*.

To be consistent with experimental data, strain was chosen to be 0.0036/min, which corresponds to 60 μm/min displacement rate in 3 point bending. The comparison of the predicted elastic modulus using the viscoelastic model and from monotonic experiments is given in Figure 3-10.

Table 3-4: Storage, Loss and Tan(delta) at 0.1Hz frequency obtained from viscoelastic model

Parameters	AIDBD-1		AIDBD-2		NR-1		NR-2	
	Dry	Wet	Dry	Wet	Dry	Wet	Dry	Wet
Storage(GPa)	1.94	0.7	2.00	0.50	2.21	1.33	2.21	0.90
Loss(MPa)	116	62.67	150.20	55.56.	101.85	78.36	91.75	49.15
Tan(δ)	0.06	0.087	0.075	0.11	0.046	0.06	0.042	0.055

Table 3-5: Stress relaxation modulus parameters and relaxation times for AIDBD and NR obtain from creep compliance data

Parameters GPa	AIDBD-1		AIDBD-2		NR-1		NR-2	
	Dry	Wet	Dry	Wet	Dry	Wet	Dry	Wet
G_0	1.086	0.360	1.080	0.257	1.266	0.632	1.207	0.473
G_1	0.100	0.080	0.204	0.101	0.027	0.053	0.023	0.009
G_2	0.370	0.142	0.322	0.067	0.456	0.263	0.415	0.010
G_3	0.095	0.058	0.124	0.099	0.118	0.224	0.116	0.290
G_4	0.381	0.144	0.435	0.062	0.386	0.206	0.448	0.175
Relaxation time (min)								
τ_1	0.950	0.900	0.900	0.830	0.990	0.960	0.990	0.990
τ_2	8.097	7.980	8.360	8.640	7.970	8.060	8.110	9.900
τ_3	94.03	89.88	92.64	76.46	93.38	79.06	93.56	70.10
τ_4	738.0	709.6	709.6	799.3	763.8	747.5	727.3	720.4

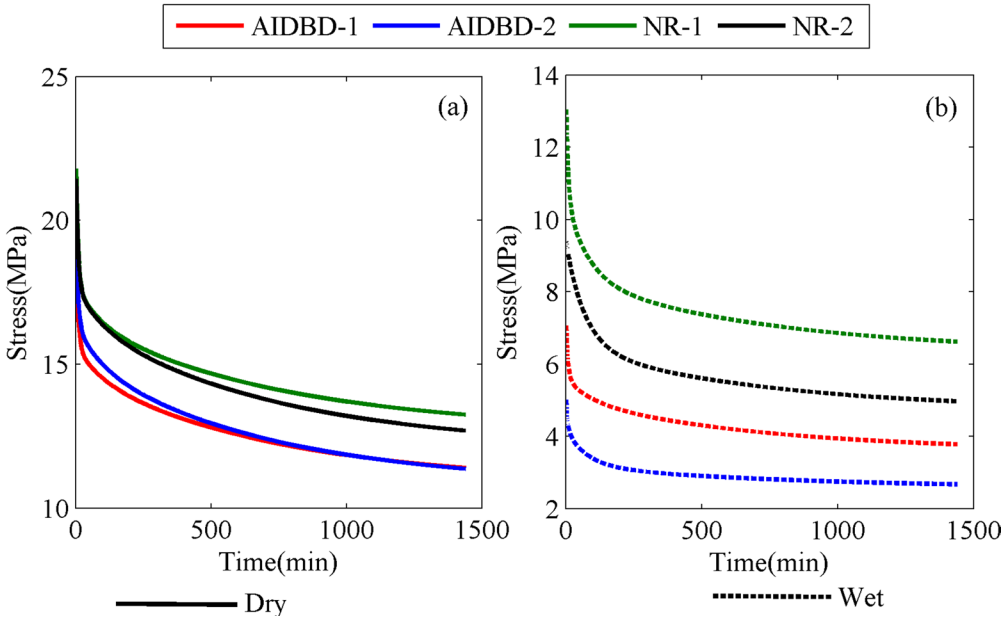

Figure 3-9: Predicted stress relaxation behavior at strain amplitude of ε_{11}=0.01, for AIDBD and neat resin (NR) sample (a) in dry and (b) wet environments.

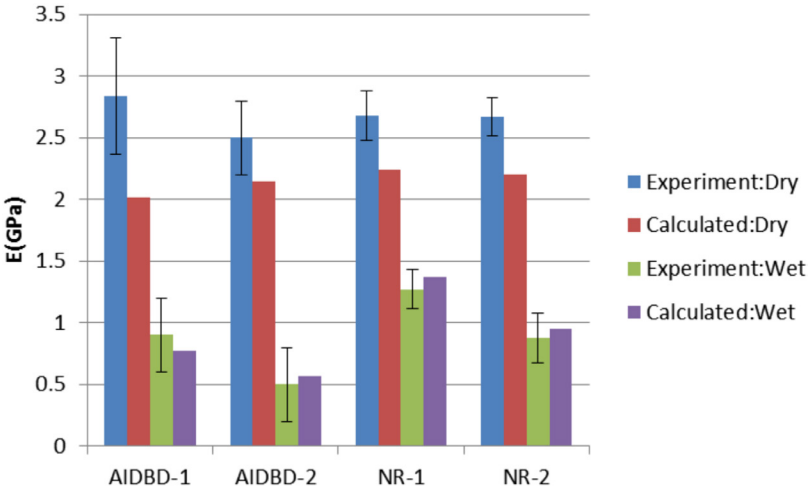

Figure 3-10: Comparison of predicted and calculated elastic moduli for AIDBD and neat resin (NR) sample in dry and wet environment

3.4 Discussion

Under dry conditions, the creep response for NR and AIDBD samples is similar for both formulations. In contrast, the creep curves for AIDBD samples stored and tested in water, show instantaneous strain almost ~3 and ~4 times of the dry case for formulations 1 and 2 respectively. This increase in instantaneous strain indicates plasticization of AIDBD due to storage in water. Similar results were also obtained for NR which are in the agreement with our previous work [39]. We also find that as compared to formulation-1, both the wet AIDBD and NR samples of formulation-2 have significantly larger deformation under creep loading. This difference is due to the relatively hydrophilic BMPB [28] in formulation-2, which increases the overall hydrophilicity resulting in a higher creep strain under applied stress. We note that in all the creep curves, the primary creep is dominant and the creep deformation appears to reach asymptotic value, indicating that the creep behavior under the low applied load can be treated as linear viscoelastic. This observation is confirmed by the excellent goodness-of-fit of the observed data with the linear 4-element generalized Kelvin-Voigt model. Further, it is interesting to observe that the 4-element model is necessary which suggests that both AIDBD and NR are complex materials with more than one characteristic retardation or relaxation times. The predicted storage moduli, based upon the fitted creep compliances, show an increase with frequency and appear to reach an asymptote at frequency of 0.1 Hz for AIDBD and NR in both dry and wet conditions. Compared to dry state, the storage moduli are significantly smaller under wet conditions. The predicted loss moduli in dry condition showed two peaks at 0.0003 and 0.02Hz. In contrast, the predicted loss moduli under wet conditions show a complex behavior with frequency including multiple peaks or saddles. The predicted tan(δ) was found to have a similar trend as that of loss modulus with well-defined peak for the dry case and a

complex trend for the wet case. We note that the fitted model appears to capture the behavior of the investigated materials both in dry and wet conditions as shown by the reasonable agreement of the predicted and the measured rate dependent elastic moduli shown in Figure 10. It should be noted however that, the predicted elastic moduli using the fitted linear viscoelastic model is sensitive to initial strain in creep data. A small variation can cause relatively significant change in the predicted elastic modulus. In this work, relatively small sample size $n=3$ was used, which for testing under dry condition results in larger standard deviation due to relatively smaller signal-to-noise ratio for small strain amplitudes. Therefore, the predictions for dry samples are not within the standard of deviation of measured values, although the trends are captured well by the model. Clearly, the advantage of viscoelastic modeling is that using a simple creep experiment we can obtain other properties such as storage and loss moduli as function of frequency, elastic moduli at different rates and stress relaxation behavior at different strain level. It is important to obtain all of these properties to understand the complete mechanical response of AIDBD (or collagen-adhesive composites) and the NR (or neat resin) samples. To obtain all of the above mentioned properties using lab experiments is both time consuming and expensive. Therefore prediction of viscoelastic properties using relatively simple creep experiment data is an attractive alternative to conventional mechanical tests.

From the results of the monotonic tests we found that apparent elastic moduli of NR and AIDBD in dry condition were not significantly different from each other. However, the flexural strengths of both AIDBD samples are significantly higher compared to their NR counterpart in the dry condition. This is due to the presence of demineralized bovine collagen in AIDBD samples which provides a fiber network that acts as reinforcement under the applied load. As a result, AIDBD samples fail at higher magnitudes of stress and strain. In NR beam samples this

type of fiber network is absent and the sample failure is not impeded by mechanisms such as fiber bridging. Consequently, we found that AIDBD samples have higher toughness when tested in dry environment. In contrast, when AIDBD sample is stored in water for 5 days and tested in water, the apparent elastic moduli decreases significantly. Similar softening is found for NR samples, however, in comparison, the AIDBD samples suffer a considerably greater softening. The softening of the NR polymers upon water exposure is attributable to plasticization, which leads to less constrained movement of the polymer chains and collagen fibers since part of the molecular scale interactions are disrupted by water. Furthermore, the wet AIDBD-2 samples suffer greater effect of plasticization due to the hydrophilicity of the polymer and generally have lower flexural strength. For both adhesive formulations, the presence of collagen seems to be a controlling factor for AIDBD samples. A simple volume averaging to estimate the elastic moduli for AIDBD in the wet environment gives ~0.6GPa and 0.4GPa for formulation 1 and 2, respectively, which is similar to that measured. However, the behavior at larger strain appears to deviate considerably from the simple volume average. We believe that not only the collagen softens considerably as seen from Figure 7(b), but the interactions of the dentin adhesive and collagen must experience significant disruption due to water.

Finally, it is worth commenting that relatively few previous studies have been conducted to obtain the mechanical properties of resin infiltrated dentin. Yasuda et al [49, 50] obtained the elastic moduli of adhesive infiltrated dentin samples using ultrasonic testing. They have reported the values of elastic moduli for their adhesive infiltrated dentin to be higher than that of the neat adhesive. These ultrasonic experiments were performed for saturated samples at high frequencies (5-10 MHz). Under these high frequencies a typically stiffer response is obtained for water saturated materials owing to the inability of unbound water to migrate under loading,

leading to un-drained conditions[39, 45]. Also a dimensional analysis of their expression for elastic modulus appears to indicate some inconsistency. Therefore the values reported by Yasuda et al cannot be directly compared to the elastic modulus obtain from our experiments. Recently Ryou et al [48] performed nanomechanical studies to characterize resin-infiltrated dentin. These nanomechanical tests were performed at very small indentation depth <10nm at frequency of 100Hz and reported a value of 3.5(±0.3) GPa for adhesive infiltrated dentin and 2.7(±0.3) GPa for neat adhesive under hydrated condition with uncharacteristically small standard deviations. The nanomechanical tests interrogates very small volumes, therefore the properties obtained from these nanomechanical tests cannot be considered as the true representation of bulk properties obtained from the conventional mechanical tests used in this study. In a study measuring bulk properties under quasi-static conditions, Chiaraputt et al [46] performed 3 point bending tests and reported that for saturated wet environment, the elastic moduli of resin infiltrated dentin is lower than its neat resin counterpart, which agrees with the our experimental findings. Similarly Gu et al [47] also reported lower elastic moduli for resin infiltrated dentin compared to neat resin using simple volume averaging. It is clear, that these few contradictory experimental efforts have only examined a subset of mechanical behavior and none appears to have investigated creep and rate-dependent behavior in the depth performed herein.

The results presented in the work show that the mechanical behavior of even ideal collagen adhesive composites, termed here as adhesive infiltrated demineralized bovine dentin, depends upon a number of factors, such as (a) the moisture conditions, (b) dentin adhesive characteristics, (c) the relative proportions of dentin adhesive and collagen, (d) the loading level, and (e) the loading rate. The collagen-adhesive composite formed in clinical conditions is much

more complex than the adhesive-collagen composite investigated here. In the clinical environment dentin adhesive only partially infiltrates demineralized dentin and undergoes phase separation [45, 51, 59]. The extent of adhesive penetration at the a-d interface was studied by Wang and Spencer [60]. The hydrophilic adhesive components (including HEMA) diffuse more readily into the demineralized dentin zone than the relatively hydrophobic BisGMA. The resulting adhesive phased polymerized in the presence of water can have complex mechanical behavior[45].

In contrast to the clinical setting, the AIDBD spcemines used in this study were produced under controlled laboratory conditions resulting in complete infiltration of demineralized dentin. Furthermore, the dentin demineralization is highly heterogeneous [22, 61] and the dentin composition at the scales at which a-d interface forms can be profoundly affected by caries [62, 63]. In addition, the dentin adhesives used under clinical conditions may also be composed of different co-monomer systems as well as various solvents.

It is noteworthy that the adhesive-collagen composite represents only one component of the complex material-structural construct formed at the a-d interface. In our previous work we have reported through finite element simulations how the load is transferred at the a-d interface and how its fatigue behavior and durability is affected by the material components and microstructure of this complex construct [26, 27, 64]. We have also shown that the mechanical properties of dentin adhesive are affected by the moisture conditions, loading rate and loading-level [5, 6]. The non-linear, moisture and rate-dependent behavior requires new physics-based mathematical model to describe the behavior of adhesive and adhesive-collagen composites in a comprehensive manner [39, 45]. To this end, the study reported here forms part of a larger effort

to understand a-d interface through a combination of mathematical modeling and experimental characterization.

3.5 Summary

Ideal collagen-adhesive composites formed by the infiltration of dentin adhesives into demineralized bovine dentin was investigated for their time and rate dependent behavior under conditions that simulate the wet functional environment found in the oral cavity. To study the effect of adhesive hydrophilicity on the properties of composites two types of dentin adhesives of different hydrophilicity were used. Creep and monotonic tests were performed on rectangular beam samples in 3 point bending configuration under dry and wet conditions. The monotonic test results showed that collagen-adhesive composites samples have similar elastic modulus, however higher modulus of toughness than neat adhesive in dry conditions. Whereas, under wet condition both the elastic modulus and the strength of collagen-adhesive composites decrease compared to that of neat adhesives. The results of the creep tests under small stress amplitude showed that for both the collagen-adhesive composites and the neat resins, the behavior is linear viscoelastic in dry and wet environment. Creep and rate-dependent behavior of such composites have been rarely examined and the current literature information on their mechanical properties contains contradictory results.

To capture the creep response, a linear 4-element generalized Kelvin-Voigt model was required, indicating that the adhesive-collagen composites are complex materials with several characteristics time-scales whose mechanical behavior will be significantly affected by loading rates and frequencies even under small amplitudes. The developed model was used to predict frequency-dependent and rate-dependent properties of collagen-adhesive composites and neat

resin samples. The model was shown to perform satisfactorily for linear behavior. However, at higher stress-levels and under transient moisture condition we expect the creep behavior to be highly nonlinear, which will require enhanced models for describing the behavior as well as further creep testing at higher stress-levels and monotonic testing at different loading rates.

Finally we note that these materials form a part of the adhesive-dentin interface, which is a thin complex construct of several material components extending over the cavity surface of a complicated geometrical shape. The overall behavior of the restoration is, therefore, not only affected by adhesive-collagen composites, but also by its interactions with the other material components, as well as the overall mastication loading. A systematic study is needed to determine how these materials impact the overall performance of the restoration. However, it is clear from the findings of this paper that these materials represent a weak link.

Chapter 4

Rate-Dependent Granular Micromechanics Model

4.1 Introduction

When we derive constitutive laws suitable for use in continuum mechanics, it is useful to model explicitly some significant underlying mechanisms that occur at scales smaller than the representative volume element (RVE). This view of constitutive modeling is applicable to a broad class of material systems in which we want to explicitly represent the effects of composition or structure on the overall (RVE-scale) behavior. Such an approach is widely applied for modeling matrix or reinforced composites, materials with microcracks and voids, and other materials with well-identified structure [65]. Models based upon this viewpoint are also sought when our interest is in discovering how the interactions between atoms, molecules or grains influence the RVE behavior. In this work, we concern ourselves with materials in which the interactions between molecules or grains have a significant role in determining the overall behavior. In such cases, our physical view at the sub-RVE scale is that of a particulate media. We begin from this particulate/discrete description and derive continuum constitutive relationships. Approaches that begin with a particulate description have a rich history that can be traced to the genesis of continuum mechanics in the work of Navier (presented in 1821 and printed later, see for example [66]) and later, also in the work of Cauchy[67]. In the derivations

for the equilibrium conditions for deformable solids, Navier considered the body composed of molecules. Continuum evolution equations and materials constant were then derived by considering the Taylor series expansions of the molecular displacement and integrating over all the inter-molecular forces. In recent years such approaches have been sought for molecular or atomic systems [68-70], granular systems [71, 72], truss-systems [73-75], or for modeling fracture assuming a pseudo-granular structure [76-78]. In many of these recent approaches, the concept of stress is also introduced when developing the passage from the discrete/particulate to the continuum descriptions. The continuum constitutive laws derived from this approach have the advantage of capturing the discrete nature of the materials. The current work develops the above approach further for obtaining constitutive laws for materials in which the interactions between molecules or grains have a rate-dependent characteristic, such as cross-linked polymers (dentin adhesives), asphalt concrete, portland cement paste, and frozen soils.

The work presented in this chapter is divided into following sections. Section (4.1) describes the micro-structural idealization that provides the discrete granular description of the materials. In section (4.2) grain-scale kinematics and rate-dependent inter-granular force relationships are used to develop constitutive relationship for an RVE containing large number of grains or polymer chain interactions. Section (4.3) presents the inter-granular force displacement with damage obtained from the rheological element. Further sections (4.3) and (4.4) present the numerical scheme and results obtained for the model. The examples presented amply demonstrate the ability of this approach to capture the effect of the granular nature of materials. The examples are also used to elaborate the thermodynamic potential and the dissipative energy for this type of material.

4.2 Micromechanical Model

4.2.1 Microstructure Idealization:

We idealize monolithic materials, in which the interactions between molecules or grains have a significant role, to have a granular meso-structure. In this idealization, the grains are viewed as atom aggregations in which the intra-granular atomic interactions have a qualitatively different nature than the inter-granular interactions. In some cases, such as in cemented granular materials, the grains can be easily identified as domains demarcated by natural grain boundaries. In these cases, the intra-granular and the inter-granular interactions can be clearly separated and, potentially, can be directly modeled. In other cases it may not be possible to clearly demarcate the domain forming the grains or identify the inter-granular interactions. For example in cross-linked polymers, the intra-granular interactions are the covalent bonds at the cross-links or those within the polymer chains. While the inter-granular interactions comprise of the non-covalent bonds, H-bonds, van der Waals forces and other physical interactions. In these cases, the overall inter-granular interaction may be viewed in a statistical sense. In principle, the inter-granular interaction may be treated in a manner analogous to that used for deriving molecular potential energy functions [79]. However such an approach is not attractive for granular materials and cross-linked polymeric systems with billions of atoms and ill-defined structure. From a practical viewpoint, we can formulate appropriate functions to describe the inter-granular interactions in which the essential sub-granular scale mechanisms are represented. The parameters of these functions can then be obtained by fitting with experimental data. In the spirit of this more

practical approach, we consider the granular meso-structure for these materials as depicted in Figure 4-1.

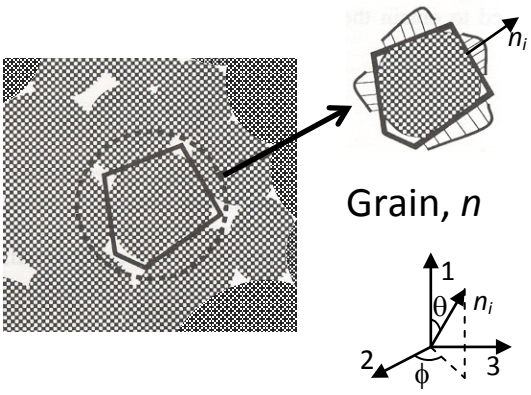

Figure 4-1 Idealized granular meso-structure and inter-granular forces on grain *n*

4.2.2 Inter-Granular Kinematics and Force-Displacement Relationship

Under external action, the grains of the meso-structure may translate or rotate resulting in a relative displacement between grains [80, 81]. For simplicity as a first approximation, we ignore the grain rotations. Thus, the relative displacement, δ_i, between two nearest neighbor (contacting) grains n and p is given by

$$\delta_i = u_i^p - u_i^n \tag{4.1}$$

here u_i = particle displacement; superscripts refer to the interacting particles. The subscripts follow the tensor summation convention unless noted otherwise. For passage to continuum description of this discrete model, we utilize the Taylor series expansion of the displacement such that the displacement of grain p may be written as:

$$u_i^p = u_i^n + u_{i,j}^n \left(x_j^p - x_j^n \right) \tag{4.2}$$

where the point of expansion is chosen as the centroid of grain n. Higher order terms of the Taylor series may also be considered that will lead to 2nd or higher gradient models [68, 72, 82-

88]. however, we postpone that treatment to a future work. Thus, the relative displacement, δ_i, between two nearest neighbor grains *n* and *p* is given by

$$\delta_i = u^n_{i,j}\left(x^p_j - x^n_j\right) \tag{4.3}$$

The relative displacement, δ_i, between two grains may be decomposed into two components, (1) δ_n, along unit vector, n_i, defined in the direction of vector $x^p_j - x^n_j$, termed as the normal direction, and (2) δ_w, orthogonal to vector, n_i, referred to as shear-direction. The relative displacement in the normal direction is given by, $\delta_n=\delta_i n_i$, and the relative displacement in the shear-direction is given by, $\delta_w = \sqrt{(\delta_i s_i)^2 + (\delta_i t_i)^2}$, where unit vectors n_i, s_i and t_i form a local Cartesian coordinate system. The vectors s_i and t_i are arbitrarily chosen and lie on the plane perpendicular to the vector n_i, such that

$$\begin{aligned}
\mathbf{n} &= \langle \cos\theta, \sin\theta\cos\varphi, \sin\theta\sin\varphi \rangle \\
\mathbf{s} &= \langle -\sin\theta, \cos\theta\cos\varphi, \cos\theta\sin\varphi \rangle \\
\mathbf{t} &= \langle 0, -\sin\varphi, \cos\varphi \rangle
\end{aligned} \tag{4.4}$$

where θ and ϕ are shown in Figure 4-1.

For a two-body nearest-neighbor interaction with rate-dependent character, the inter-granular force resultant from the relative displacement of grains may be expressed, in general, as

$$f_i(t) = f_i\left(\delta_j, \dot{\delta}_j, \dot{f}_j\right) \tag{4.5}$$

where the superimposed dot ($\dot{}$) denotes time derivative (see for example the contact of two spherical viscoelastic bodies[89]), which can be assumed to take a linear elastic form as $f_i = f_i\left(\delta_j\right)$. As in our previous work [39], we consider the inter-granular interaction in the normal and the shear directions and express the force functions by the following nonlinear evolution equations.

$$f_n + \zeta_n \dot{f}_n = K_n \delta_n + \eta_n \dot{\delta}_n$$
$$f_w + \zeta_w \dot{f}_w = K_w \delta_w + \eta_w \dot{\delta}_w \tag{4.6a}$$

where the inter-granular stiffness, viscosity, and relaxation parameters K, η and ζ respectively are functions of contact force f and displacement δ. We have considered, for simplicity of further development, the case where the shear terms are decoupled from the normal terms. It is noteworthy, however, that in this simple case as well, the normal stresses and shear stresses are generally coupled at the RVE scale as will be shown later through examples.. The inclusion of coupling terms for the inter-granular interactions can further enrich the RVE scale behavior. For future reference, Eq. 4.6 can also be written in an alternate form in terms of the retardation time, $\tau n\delta$, and the relaxation time, τnf, as follows:

$$f_n = K_n(t)\delta_n(t) + \tau_{n\delta}(t)K_n(t)\dot{\delta}_n(t) - \tau_{nf}(t)\dot{f}_n(t)$$
$$f_w = K_w(t)\delta_w(t) + \tau_{w\delta}(t)K_w(t)\dot{\delta}_w(t) - \tau_{wf}(t)\dot{f}_w(t) \tag{4.6b}$$

The retardation time, $\tau_{n\delta}$, and the relaxation time, τ_{nf}, are defined by considering solutions of Eqs. 6a subjected to step force f_n^o or displacement δ_n^o as follows

$$\delta_n = f_n^o \left[\left(\frac{\zeta_n}{\eta_n} - \frac{1}{K_n} \right) \exp\left(-\frac{t}{\tau_{n\delta}} \right) + \frac{1}{K_n} \right]$$
$$f_n = \delta_n^o \left[\left(\frac{\eta_n}{\zeta_n} - K_n \right) \exp\left(-\frac{t}{\tau_{nf}} \right) + K_n \right] \tag{4.7}$$

where $\tau_{n\delta} = \dfrac{\eta_n}{K_n}$ and $\tau_{nf} = \zeta_n$. Clearly, the retardation time is the characteristic time required to reach an asymptotic displacement under step force (creep), while relaxation time the characteristic time required to reach an asymptotic force under step displacement (relaxation). Since the Eq. 4.6a for normal and shear directions have the same form, similar set of solutions can be found for the shear directions. If the stiffness, viscosity and relaxation parameters are

taken as constants, the resultant model will describe a linear viscoelastic solid. On the other hand, if these parameters are assumed to degrade with deformation, a nonlinear viscoelastic damage model will be obtained. Many specific forms of these parameters and their evolution can be assumed to describe particular material behavior

4.2.3 Constitutive Relationship for a Representative Volume Element (RVE)

We now consider the mean stress within grain *n* written as follows using Gauss's divergence theorem [90]:

$$\sigma_{ij}^{n} = \frac{1}{V^{n}} \int_{V^{n}} s_{ij} dV = \frac{1}{V^{n}} \int_{V^{n}} \left(s_{kj} x_{i} \right)_{,k} dV = \frac{1}{V^{n}} \int_{\partial V^{n}} s_{kj} x_{i} n_{k} dS \tag{4.8}$$

where in the absence of body force, $s_{kj,k}=0$ has been used and the position vector x_i in the surface integral can be written as $x_i = x_i^n + r_i$, where x_i^n is the centroid of grain *n* and r_i is the radius vector from the centroid to the surface. In view of the discrete nature of the granular description, Eq. (4.8) is written as a summation as follows:

$$\sigma_{ij}^{n} = \frac{1}{V^{n}} \sum\nolimits_{\alpha} s_{kj}^{\alpha} r_{i}^{\alpha} n_{k}^{\alpha} \Delta S = \frac{1}{V^{n}} \sum\nolimits_{\alpha} f_{j}^{\alpha} r_{i}^{\alpha} \tag{4.9}$$

where f_j is the inter-granular force and the superscript refers to the α-th contacting surface. We now consider an RVE containing a large number of grains and obtain the overall stress, σ_{ij}, as the following volume average

$$\sigma_{ij} = \frac{1}{V} \sum\nolimits_{n} V^{n} \sigma_{ij}^{n} = \frac{1}{V} \sum\nolimits_{n} \sum\nolimits_{\alpha} f_{j}^{n\alpha} r_{i}^{n\alpha} = \frac{1}{V} \sum\nolimits_{\alpha} l_{i}^{\alpha} f_{j}^{\alpha} \tag{4.10}$$

where the summation is now over all the grain pair-interactions, and l_i^{α} is the sum of the radius vector of two grains contacting at α-th contact. For the case that the radius vectors at the α-th

contact are collinear, the vector l_i^α can be represented as the product ln_i^α where l is the inter-granular distance and n_i^α is the unit vector for pair interaction. It is noteworthy that this method of obtaining RVE-scale stress tensor from the grain-scale does not use a scaling technique; instead it provides a continuum description of a finite number of grains. We further note that in this work the RVE stress was obtained by averaging over the grain-scale stress. Alternatively, and perhaps more fundamentally, the RVE stress should be derived by utilizing the average of local grain-scale deformation energies.

We observe that (1) the tensor product ln_if_j can be expressed in terms of the direction cosines, and (2) in an RVE there exist a large numbers of variously oriented inter-granular vectors n_i. We now introduce a directional probability density function (see Appendix) for the vectors n_i, denoted by $\xi(\theta,\phi)$, such that the product $N\xi(\theta,\phi)\Delta(\cos\theta)\Delta\phi$ gives the number density of pair interactions in the solid angle $\Delta(\cos\theta)\Delta\phi$, where N is the number density of pair interactions. Eq. 4.10 can then be expressed as the following Riemann sum over spherical coordinates θ and ϕ

$$\sigma_{ij} = N\sum_{\phi}\sum_{\theta} l(\theta,\phi)n_i(\theta,\phi)f_j(\theta,\phi)\xi(\theta,\phi)\Delta(\cos\theta)\Delta\phi \tag{4.11}$$

where $l(\theta,\phi)$ and $f_j(\theta,\phi)$ are the average inter-granular distance and force, respectively, at a contact oriented in the (θ,ϕ) direction as defined in Figure 4-1. For a sufficiently large number of pair interactions, Riemann sum in the Eq. 4.11 can be approximated by the following Riemann integral

$$\sigma_{ij} = Nl\int_0^{2\pi}\int_0^{\pi} f_j(\theta,\phi)n_i(\theta,\phi)\xi(\theta,\phi)\sin\theta d\theta d\phi \tag{4.12}$$

assuming a uniform inter-granular distance, l. For convenience, we incorporate the factor Nl with the force, f_j, such that it is expressed as a traction and normalize the relative displacement, δ_i, with l. The units of the stiffness and viscosity in Eq. 4.6 and 4.7 are appropriately modified. Now combining Eqs. 4.3, 4.6 and 4.12, we get the RVE stress-strain relationship in the following form

$$\sigma_{ij} = \int_0^{2\pi}\int_0^{\pi}\left(K_{jk}n_l\varepsilon_{kl} + \eta_{jk}n_l\dot{\varepsilon}_{kl} + \zeta_{jk}\dot{f}_k\right)n_i\xi(\theta,\phi)\sin\theta d\theta d\phi \tag{4.13}$$

where we have applied the widely used mean field kinematical assumption relating the grain-scale displacement gradient and strain to the overall RVE displacement gradient and strain as follows:

$$u^n_{k,l} = u_{k,l};\ \text{ and } \varepsilon_{kl} = u_{(k,l)} \tag{4.14}$$

Although not necessary, we have used for simplicity the symmetric part of the displacement gradient and its rate in Eq. 4.13. We note here that the relationship of the grain strain with the overall RVE strain is generally quite complex, not easily determined and requires additional assumptions to construct tractable solutions [81]. The mean field assumption considerably simplifies the derivation of the RVE constitutive law. Although the resulting relationships are approximate, they are able to describe a number of phenomena exhibited by granular materials [71]. Further, we note that an alternative anstaz based upon a statical assumption may be followed wherein the inter-granular force is given in terms of the overall RVE stress and the RVE strain is obtained as a volume average. The kinematic and the static assumption of relating the local variables (such as inter-granular forces and grain displacements) and global variables (such as RVE stresses and strains) have been widely discussed in microstructural granular mechanics.

The RVE stress-strain relationship in Eq. 4.13 can be rearranged in a classical secant format as follows:

$$\sigma_{ij}(t) = C_{ijkl}(t)\varepsilon_{kl}(t) + P_{ijkl}(t)\dot{\varepsilon}_{kl}(t) + Q_{ij}(t) \tag{4.15}$$

where C_{ijkl}, P_{ijkl} and Q_{ij} are the overall modulus, viscosity and relaxation tensors, respectively, which can be expressed as follows.

$$\begin{aligned}
C_{ijkl}(t) &= \int_0^{2\pi}\int_0^{\pi}\Big(K_n(t)n_j n_k + K_w(t)\big(s_j s_k + t_j t_k\big)\Big)n_i n_l \xi(\theta,\phi)\sin\theta d\theta d\phi \\
P_{ijkl}(t) &= \int_0^{2\pi}\int_0^{\pi}\Big(\eta_n(t)n_j n_k + \eta_w(t)\big(s_j s_k + t_j t_k\big)\Big)n_i n_l \xi(\theta,\phi)\sin\theta d\theta d\phi \\
Q_{ij}(t) &= \int_0^{2\pi}\int_0^{\pi}\Big(\zeta_n(t)n_j n_k + \zeta_w(t)\big(s_j s_k + t_j t_k\big)\Big)n_i \dot{f}_k \xi(\theta,\phi)\sin\theta d\theta d\phi
\end{aligned} \tag{4.16}$$

We note that for the differential forms of rate constitutive relations given in Eq. 4.15, additional conditions must be specified at jump discontinuities.

In general, the inter-granular displacement has a nonlinear relationship with the displacement gradient. For example, the grain-scale displacement gradient may be related to the overall RVE displacement gradient using a fluctuation terms or shift vectors, which have to be determined though energy minimization or by enforcing grain-scale equilibrium as discussed in [81] or more recently in the context of atomistic modeling [91]. However, for disordered systems, such as those treated in this work, determination of fluctuation terms is tantamount to obtaining solution of the displacement field within a simulated RVE, which for materials with ill-defined structures, requires as a first step simulation of some "reasonable" microstructure that are often based upon far reaching assumptions. It is also notable that nonlinear local kinematic fields may also imply the need for including higher gradients at the macro-scale (as in [88]) and formulations that account for geometrical changes (as in [63]), but these approaches need further careful analyses. The

mean field assumption adopted in this paper considerably simplifies the derivation of the RVE constitutive law and is able to describe a number of phenomena exhibited by granular materials [39, 71] provided the inter-granular force laws are chosen judiciously. In Eq. 4.13, the inter-granular stiffness, viscosity, and relaxation tensors are given as

$$\begin{aligned} K_{ij}(t) &= K_n(t)n_i n_j + K_w(t)\left(s_i s_j + t_i t_j\right) \\ \eta_{ij}(t) &= \eta_n(t)n_i n_j + \eta_w(t)\left(s_i s_j + t_i t_j\right) \\ \zeta_{ij}(t) &= \zeta_n(t)n_i n_j + \zeta_w(t)\left(s_i s_j + t_i t_j\right) \end{aligned} \tag{4.17}$$

where the subscripts *n* and *w* refer to normal and shear grain interactions, respectively. We observe that the inter-granular force functions given in Eq. 4.6 can be schematically represented by 3-element rheological model depicted in Figure 4-2.

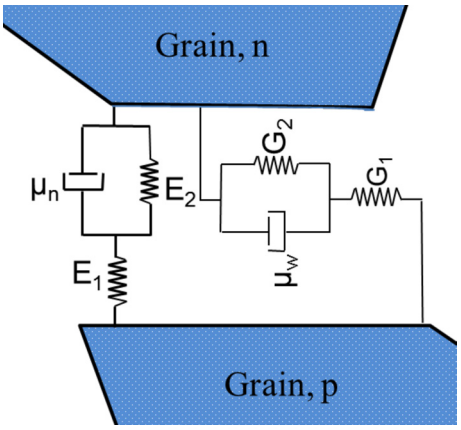

Figure 4-2: Rheological model assumed for the inter-granular interactions

Based upon the rheological element shown in Figure 4-2, the following expressions are obtained for the inter-granular stiffness, viscosity and relaxation behavior.

$$\begin{aligned} K_n(t) &= \frac{E_1 E_2(t)}{E_1 + E_2(t)}, \quad \eta_n(t) = \frac{E_1 \mu_n(t)}{E_1 + E_2(t)} = \tau_{n\delta}(t)K_n(t), \quad \text{and} \quad \zeta_n(t) = \frac{\mu_n(t)}{E_1 + E_2(t)} = \tau_{nf}(t) \\ K_w(t) &= \frac{G_1 G_2(t)}{G_1 + G_2(t)}, \quad \eta_w(t) = \frac{G_1 \mu_w(t)}{G_1 + G_2(t)} = \tau_{w\delta}(t)K_w(t), \quad \text{and} \quad \zeta_w(t) = \frac{\mu_w(t)}{G_1 + G_2(t)} = \tau_{wf}(t \end{aligned} \tag{4.18}$$

in terms of the element properties of the rheological model. Damage at the inter-granular scale is modeled by an exponential law [63, 71] such that the spring stiffness, E_2 and G_2, and the viscosity, μ_n and μ_w, are given by:

$$E_2(t) = E_n e^{-\left|\frac{\left(\delta_n(t)-\frac{f_n(t)}{E_1}\right)}{B_n}\right|}; \text{ and } \quad G_2(t) = G_w e^{-\left|\frac{\left(\delta_w(t)-\frac{f_w(t)}{G_1}\right)}{B_w}\right|}$$
$$\mu_n(t) = \mu_{n0} e^{-\left|\frac{\left(\delta_n(t)-\frac{f_n(t)}{E_1}\right)}{\beta B_n}\right|}; \text{ and } \quad \mu_w(t) = \mu_{w0} e^{-\left|\frac{\left(\delta_w(t)-\frac{f_w(t)}{G_1}\right)}{\beta B_w}\right|} \tag{4.19}$$

To model the asymmetric inter-granular behavior under tensile and compressive actions, we replace the parameters B_n and B_w in Eq. 4.19 by $\alpha_n B_n$ and $\alpha_w B_w$ for the tensile case, where $0 \le \alpha_n < 1$ and $0 \le \alpha_w < 1$. Parameters E_1, E_n, μ_{n0}, and B_n describe the elasticity, viscosity and damage behavior of the inter-granular interactions in the normal direction. Similarly, parameters G_1, G_w, μ_{w0}, and B_w describe the inter-granular interactions in the shear direction. We note here that the parameters B_n and B_w govern the displacement at which softening commences at the inter-granular scales. In addition, parameter β determines the displacement at which the viscous element begins to lose integrity. Consequently, these parameters also govern the peak inter-granular forces. Further, since no threshold is assumed at which the damage begins, the parameters B_n and B_w and their modifications $\alpha_n B_n$ and $\alpha_w B_w$ govern the complete force-displacement response. From Eqs. 4.6, 4.18 and 4.19 we observe that the inter-granular behavior for $B_n = B_w = \infty$ and $B_n = B_w = 0$ is bounded between a Zener solid and a Maxwell model.

The restrictions to the parameters for these rheological elements have been discussed previously (see for example [92]) based upon thermodynamic consistency. Other relevant and consistent

inter-granular force laws can be constructed by considering a contact-scale form of Clausius-Duhem inequality introduced here as:

$$\dot{\gamma} = f_i \dot{\delta}_i - \frac{\partial \varphi}{\partial t} \geq 0 \tag{4.20}$$

where $\dot{\gamma}$ is the rate of dissipation and φ is free energy at the inter-granular contact.

4.2.4 Thermodynamic Potential and Dissipative Energy

To assess the thermodynamic consistency of the above formulation, we consider the deformation and dissipation energies using the derived rate-dependent stress-strain relationship. For a material undergoing deformation to be in thermodynamic equilibrium, the rate of dissipative energy should be greater than or equal to zero [93]. Using the conservation of energy for an isothermal process in the absence of a heat vector, the rate of dissipative energy is defined per Clausius-Duhem inequality as:

$$\dot{\Gamma} = \sigma_{ij} \dot{\varepsilon}_{ij} - \rho \frac{\partial \psi}{\partial t} \geq 0 \tag{4.21}$$

where, $\dot{\Gamma}$ is the rate of dissipation, Ψ is Helmholtz free energy density and ρ is the material mass density. In Eq. 4.21, the first term is the rate of total work done in the system and the second term is the rate of maximum recoverable or elastic energy during a process. The total work is defined as follows[94-99]:

$$W(t) = \int_{-\infty}^{t} \sigma_{ij}(s) \dot{\varepsilon}_{ij}(s) ds \tag{4.22}$$

The maximum recoverable work or the elastic energy for a rate-dependent material may be obtained in terms of its modulus at $t \to \infty$ [97], thus we have the following

$$\Phi(t) = \frac{1}{2} C_{ijkl}(t)\varepsilon_{kl}(t)\varepsilon_{ij}(t) \tag{4.23}$$

where the modulus $C_{ijkl}(t)$ corresponds to the damaged state at time t. The total dissipated energy, Γ, is obtained as the difference $W(t)$- $\Psi(t)$, which is the integrated Clausius-Duhem inequality for an isothermal process [100]. For thermodynamic consistency, $\Gamma \geq 0$ and $\Psi(t) \geq 0$, which implies that $W(t) \geq 0$. The clear requirement is that the stiffness functions $K_n(t)$ and $K_w(t)$ must be non-negative. Further, for exploring the behavior when the stress rate is specified or when a jump strain is applied and held constant for material undergoing stress relaxation such that the strain rate is zero, Eq. 4.22 cannot be directly applied to calculate the total work. In this case, we perform integration by parts to get:

$$W(t) = \sigma_{ij}(t)\varepsilon_{ij}(t) - \frac{1}{2}\sigma_{ij}(0)\varepsilon_{ij}(0) - \int_{0^+}^{t} \varepsilon_{ij}(s)\frac{\partial \sigma_{ij}(s)}{\partial s} ds \tag{4.24}$$

where the jump condition is applied at t=0.

4.3 Numerical Implementation

The inter-granular force law given in Eq 4.6 is a nonlinear first order differential equation in force and displacement. In this work we present following three numerical schemes to solve the nonlinear first order differential equations: (a) backward Euler scheme, (b) backward Euler scheme with constant coefficients and (c) forward Euler scheme. Implementation of backward Euler scheme results in a nonlinear implicit equations. This nonlinear implicit equation can be solved iteratively and gives accurate results, but is computationally expensive. In contrast, the implementation of forward Euler scheme results in explicit expressions, which requires no iterations to obtain force or displacement for a given loading history. The Euler forward

difference method is computationally fast but is sensitive to step size and becomes unstable at a critical value of step size. The backward Euler scheme with constant coefficients results in explicit equations, which are both numerically stable and computationally fast.

4.3.1 Backward Euler Method: Implicit Iterative Scheme

For the backward Euler method we discretize the inter-granular force Eq 4.6 in time as follows:

$$f_n^t = K_n^t \delta_n^t + \eta_n^t \frac{\left(\delta_n^t - \delta_n^{t-\Delta t}\right)}{\Delta t} - \zeta_n^t \frac{\left(f_n^t - f_n^{t-\Delta t}\right)}{\Delta t} \tag{4.25}$$

The inter-granular normal force, f_n^t, at the current time, t, can then be written in the following form

$$f_n^t = C_n^t \delta_n^t + P_n^t \delta_n^{t-\Delta t} + Q_n^t f_n^{t-\Delta t} \tag{4.26a}$$

where

$$C_n^t = \frac{K_n^t \Delta t + \eta_n^t}{\Delta t + \zeta_n^t}; P_n^t = -\frac{\eta_n^t}{\Delta t + \zeta_n^t}; \text{ and } Q_n^t = \frac{\zeta_n^t}{\Delta t + \zeta_n^t} \tag{4.26b}$$

The second of Eq. 4.6 can be treated in the same manner such that

$$f_w^t = C_w^t \delta_w^t + P_w^t \delta_w^{t-\Delta t} + Q_w^t f_w^{t-\Delta t} \tag{4.27a}$$

where

$$C_w^t = \frac{K_w^t \Delta t + \eta_w^t}{\Delta t + \zeta_w^t}; P_w^t = -\frac{\eta_w^t}{\Delta t + \zeta_w^t}; \text{ and } Q_w^t = \frac{\zeta_w^t}{\Delta t + \zeta_w^t} \tag{4.27b}$$

We note that the coefficients, C, P and Q in Eq. 4.26 and 4.27 are functions of force, f, and displacement, δ, at time, t. Eqs. 4.26a and 4.26b are thus nonlinear implicit functions of f and δ,

and can be expressed in the following general form after dropping, for convenience, the subscripts *n* and *w*, superscript *t*, and replacing *t-Δt* with *0*

$$R(f,\delta) \equiv f - C(f,\delta)\delta - P(f,\delta)\delta^0 - Q(f,\delta)f^0 = 0 \tag{4.28}$$

where $R(f,\delta)$ denotes a residual force.

We now utilize Newton's method and expand the residual, $R(f,\delta)$, in Taylor series as follows

$$R(f,\delta) = R\left({}^{i-1}f, {}^{i-1}\delta\right) + {}^{i-1}\left[\frac{\partial R}{\partial \delta}\right]\Delta\delta + {}^{i-1}\left[\frac{\partial R}{\partial f}\right]\Delta f \tag{4.29}$$

where the right superscript, *i*-1, refers to the iteration step and the terms of order 2 or higher have been omitted. Combining Eqs. 4.28 and 4.29, we get

$$\left(1 - {}^{i-1}R_f\right)\Delta f = \left({}^{i-1}C + {}^{i-1}R_\delta\right)\Delta\delta + {}^{i-1}C\,{}^{i-1}\delta + {}^{i-1}P\delta^0 + {}^{i-1}Qf^0 - {}^{i-1}f \tag{4.30}$$

where

$${}^{i-1}R_\delta = {}^{i-1}\left(\frac{\partial C}{\partial \delta}\delta + \frac{\partial P}{\partial \delta}\delta^0 + \frac{\partial Q}{\partial \delta}f^0\right); \text{ and } {}^{i-1}R_f = {}^{i-1}\left(\frac{\partial C}{\partial f}\delta + \frac{\partial P}{\partial f}\delta^0 + \frac{\partial Q}{\partial f}f^0\right) \tag{4.31}$$

and the force and displacements at the *i*-th iteration are updated in the usual manner as

$${}^{i}f = {}^{i-1}f + \Delta f \text{ and } {}^{i}\delta = {}^{i-1}\delta + \Delta\delta \tag{4.32}$$

When purely strain-controlled loading is specified, the localization relationship given in Eq. 4.14 can be used to find the increment of inter-granular displacement *Δδ*. The iterative scheme in Eq. 4.30 is then utilized to find the inter-granular forces at time *t*, and subsequently, the RVE stress from Eq. 4.12. On the other hand, when purely stress-controlled or mixed stress-strain controlled loading is specified, a different approach is taken. In this case, an incremental stress for small deformation case is defined from Eq. 4.12 as follows:

$$\Delta\sigma_{ij} = Nl\int_0^{2\pi}\int_0^{\pi}\Delta f_j(\theta,\phi)n_i(\theta,\phi)\xi(\theta,\phi)\sin\theta\, d\theta\, d\phi \tag{4.33}$$

Combining Eqs. 4.30 and 4.33, the following relationship is obtained between incremental stress and strain for the *i*-th iteration:

$$\Delta\sigma_{ij}^{t} = {}^{i-1}\tilde{C}_{ijkl}^{t}\Delta\varepsilon_{kl}^{t} + {}^{i-1}\hat{C}_{ijkl}^{t}\,{}^{i-1}\varepsilon_{kl}^{t} + {}^{i-1}\hat{P}_{ijkl}^{t-\Delta t}\varepsilon_{kl}^{t-\Delta t} + {}^{i-1}\tilde{\sigma}_{ij}^{t-\Delta t} - {}^{i-1}\hat{\sigma}_{ij}^{t} \tag{4.34}$$

In Eq. 4.34, the coefficients are given as

$${}^{i-1}\tilde{C}_{ijkl}^{t} = \int_0^{2\pi}\int_0^{\pi}\left(\frac{{}^{i-1}C_n^t + {}^{i-1}R_{n\delta}}{\left(1-{}^{i-1}R_{nf}\right)}n_j n_k + \frac{{}^{i-1}C_w^t + {}^{i-1}R_{w\delta}}{\left(1-{}^{i-1}R_{wf}\right)}\left(t_j t_k + s_j s_k\right)\right)n_i n_l \xi(\theta,\phi)\sin(\theta)d\theta d\phi \tag{4.35a}$$

$${}^{i-1}\hat{C}_{ijkl}^{t} = \int_0^{2\pi}\int_0^{\pi}\left(\frac{{}^{i-1}C_n^t}{\left(1-{}^{i-1}R_{nf}\right)}n_j n_k + \frac{{}^{i-1}C_w^t}{\left(1-{}^{i-1}R_{wf}\right)}\left(t_j t_k + s_j s_k\right)\right)n_i n_l \xi(\theta,\phi)\sin(\theta)d\theta d\phi \tag{4.35b}$$

$${}^{i-1}\hat{P}_{ijkl}^{t} = \int_0^{2\pi}\int_0^{\pi}\left(\frac{{}^{i-1}P_n^t}{\left(1-{}^{i-1}R_{nf}\right)}n_j n_k + \frac{{}^{i-1}P_w^t}{\left(1-{}^{i-1}R_{wf}\right)}\left(t_j t_k + s_j s_k\right)\right)n_i n_l \xi(\theta,\phi)\sin(\theta)d\theta d\phi \tag{4.35c}$$

$${}^{i-1}\tilde{\sigma}_{ij}^{t} = \int_0^{2\pi}\int_0^{\pi}\left(\frac{{}^{i-1}Q_n^t f_n^{t-\Delta t}}{\left(1-{}^{i-1}R_{nf}\right)}n_j + \frac{{}^{i-1}Q_w^t f_{wt}^{t-\Delta t}}{\left(1-{}^{i-1}R_{wf}\right)}\left(t_j + s_j\right)\right)n_i \xi(\theta,\phi)\sin(\theta)d\theta d\phi \tag{4.35d}$$

$${}^{i-1}\hat{\sigma}_{ij}^{t} = \int_0^{2\pi}\int_0^{\pi}\left(\frac{{}^{i-1}f_n^t}{\left(1-{}^{i-1}R_{nf}\right)}n_j + \frac{{}^{i-1}f_w^t}{\left(1-{}^{i-1}R_{wf}\right)}\left(t_j + s_j\right)\right)n_i \xi(\theta,\phi)\sin(\theta)d\theta d\phi \tag{4.35e}$$

where

$${}^{i-1}R_{n\delta} = {}^{i-1}\left(\frac{\partial C_n}{\partial\delta_n}\delta_n + \frac{\partial P_n}{\partial\delta_n}\delta_n^0 + \frac{\partial Q_n}{\partial\delta_n}f_n^0\right);\ \text{and}\ \ {}^{i-1}R_{nf} = {}^{i-1}\left(\frac{\partial C_n}{\partial f_n}\delta_n + \frac{\partial P_n}{\partial f_n}\delta_n^0 + \frac{\partial Q_n}{\partial f_n}f_n^0\right) \tag{4.36}$$

The shear terms ${}^{i-1}R_{w\delta}$ and ${}^{i-1}R_{wf}$ are defined in a similar manner. Eq. 4.34 can be used to determine the unknown strain-increments, and subsequently, the increments of inter-granular displacements and the inter-granular forces.

4.3.2 Backward Euler Method with Constant Coefficient: Semi-Implicit Non-Iterative Scheme

The above iterative scheme can be computationally intense, especially from the point of view of implementation into numerical schemes for initial-boundary value problems (IBVP) and a non-iterative scheme is desirable. To this end, we observe from Eq. 4.30 that ${}^{i-1}R_f\Delta f$ and ${}^{i-1}R_\delta\Delta\delta$ contain product terms as well terms proportional to Δt^2, which, for sufficiently small loading increments and Δt, can be negligibly small compared to the remaining terms. In this case Eq. 4.30 is simplified and the coefficients C,P and Q are evaluated at previous time step $t=t-\Delta t$ after ignoring the subsequent iterations:

$$f^t = f^{t-\Delta t} + \Delta f = C^{t-\Delta t}\left(\delta^{t-\Delta t} + \Delta\delta\right) + P^{t-\Delta t}\delta^{t-\Delta t} + Q^{t-\Delta t}f^{t-\Delta t} \tag{4.37}$$

Substituting the inter-granular force from Eq. 4.37 into Eq.4.12 we get a non-iterative semi-implicit form of the stress-strain relationship at time t

$$\sigma_{ij}^t = C_{ijkl}^{t-\Delta t}\varepsilon_{kl}^t + P_{ijkl}^{t-\Delta t}\varepsilon_{kl}^{t-\Delta t} + \tilde{\sigma}_{ij}^{t-\Delta t} \tag{4.38}$$

In Eq. 4.38, the coefficients are given as

$$C_{ijkl}^{t-\Delta t} = \int_0^{2\pi}\int_0^{\pi}\left(C_n^{t-\Delta t}n_jn_k + C_w^{t-\Delta t}\left(t_jt_k + s_js_k\right)\right)n_in_l\xi(\theta,\phi)\sin(\theta)d\theta d\phi \tag{4.39a}$$

$$P_{ijkl}^{t-\Delta t} = \int_0^{2\pi}\int_0^{\pi}\left(P_n^{t-\Delta t}n_jn_k + P_w^{t-\Delta t}\left(t_jt_k + s_js_k\right)\right)n_in_l\xi(\theta,\phi)\sin(\theta)d\theta d\phi \tag{4.39b}$$

$$\tilde{\sigma}_{ij}^{t-\Delta t} = \int_0^{2\pi}\int_0^{\pi}\left(Q_n^{t-\Delta t}f_n^{t-\Delta t}n_j + Q_w^{t-\Delta t}f_w^{t-\Delta t}\left(t_j + s_j\right)\right)n_i\xi(\theta,\phi)\sin(\theta)d\theta d\phi \tag{4.39c}$$

4.3.3 Forward Euler Method: Explicit Scheme

For the forward Euler method we discretize the inter-granular force Eq 4.6 in time as follows:

$$f_n^t = K_n^t \delta_n^t + \eta_n^t \frac{\left(\delta_n^{t+\Delta t} - \delta_n^t\right)}{\Delta t} - \zeta_n^t \frac{\left(f_n^{t+\Delta t} - f_n^t\right)}{\Delta t} \tag{4.40}$$

Eq 4.40 is rearranged and the inter-granular normal force, $f_n^{t+\Delta t}$, at time, $t+\Delta t$, is written in the following form

$$f_n^{t+\Delta t} = C_n^t \delta_n^{t+\Delta t} + P_n^t \delta_n^t + Q_n^t f_n^t \tag{4.41a}$$

where

$$C_n^t = \frac{\eta_n^t}{\zeta_n^t}; P_n^t = \frac{K_n^t \Delta t - \eta_n^t}{\zeta_n^t} \text{ or } \frac{\Delta t - \tau_{n\delta}^t}{\zeta_n^t} K_n^t; \text{ and } Q_n^t = 1 - \frac{\Delta t}{\zeta_n^t} \text{ or } \frac{\tau_{nf}^t - \Delta t}{\tau_{nf}^t} K_n^t \tag{4.41b}$$

Similar expression is obtained for shear force, $f_w^{t+\Delta t}$, at time, $t+\Delta t$. Thus from Eq. 4.12, we obtain the stress-strain relationship as:

$$\sigma_{ij}^{t+\Delta t} = C_{ijkl}^t \varepsilon_{kl}^{t+\Delta t} + P_{ijkl}^t \varepsilon_{kl}^t + \tilde{\sigma}_{ij}^t \tag{4.42}$$

In Eq.4.42, the coefficients are given as

$$C_{ijkl}^t = \int_0^{2\pi} \int_0^{\pi} \left(C_n^t n_j n_k + C_w^t \left(t_j t_k + s_j s_k \right) \right) n_i n_l \xi(\theta, \phi) \sin(\theta) d\theta d\phi \tag{4.43a}$$

$$P_{ijkl}^{t-\Delta t} = \int_0^{2\pi} \int_0^{\pi} \left(P_n^t n_j n_k + P_w^t \left(t_j t_k + s_j s_k \right) \right) n_i n_l \xi(\theta, \phi) \sin(\theta) d\theta d\phi \tag{4.43b}$$

$$\tilde{\sigma}_{ij}^t = \int_0^{2\pi} \int_0^{\pi} \left(Q_n^t f_n^t n_j + Q_w^t f_w^t \left(t_j + s_j \right) \right) n_i \xi(\theta, \phi) \sin(\theta) d\theta d\phi \tag{4.43c}$$

The difference in the coefficients in Eq. 4.42 and Eq. 4.38 are quite notable. In the explicit scheme based upon forward Euler discretization, the coefficients P and Q represent the difference between the time increment Δt and the nonlinear retardation or relaxation times,

respectively. Therefore, this scheme is highly sensitive to the choice of the time increment, particularly for nonlinear problems with evolving retardation and relaxation times.

4.4 Result and Discussion

The above model and numerical schemes are evaluated for the particular nonlinear inter-granular force model that can describe rate-dependent damage and softening given in Eq. 4.18 and 4.19. In the subsequent sections we (1) compare three numerical schemes, (2) validate and verify the developed nonlinear visco-damage model using experimental data for hot mix asphalt at 20^{o}C (3) demonstrate model capability to predict material behavior under multi-axial loading through parametric studies and (4) perform parametric study to explore the capabilities of model under three types loading conditions, (a) stress-strain responses under monotonically increasing strain at different strain rates, (b) the stress relaxation response and (c), the creep response is computed

4.4.1 Comparison of Numerical Schemes

The accuracy of the three numerical schemes was evaluated for constant strain-rate confined uniaxial compressive loading condition (ε_{11}=0.0005/s, $\varepsilon_{22}=\varepsilon_{33}$=0) using the following model parameters: $G_1=0.8E_1$, $G_w=E_n$, $\mu_n=\mu_w$, and $B_n=B_w$=14.3x10^{-3}, where E_1 =2.4 GPa, E_n= 0.3 GPa, $\tau_{n\delta}(0)$=57s, $\tau_{nf}(0)$=6.33s, $\alpha_n=\alpha_w=0.175$ and β= 3.8. A number simulations were performed by varying $\Delta t/\tau_{n\delta}(0)$ from 0.02 to 0.5.

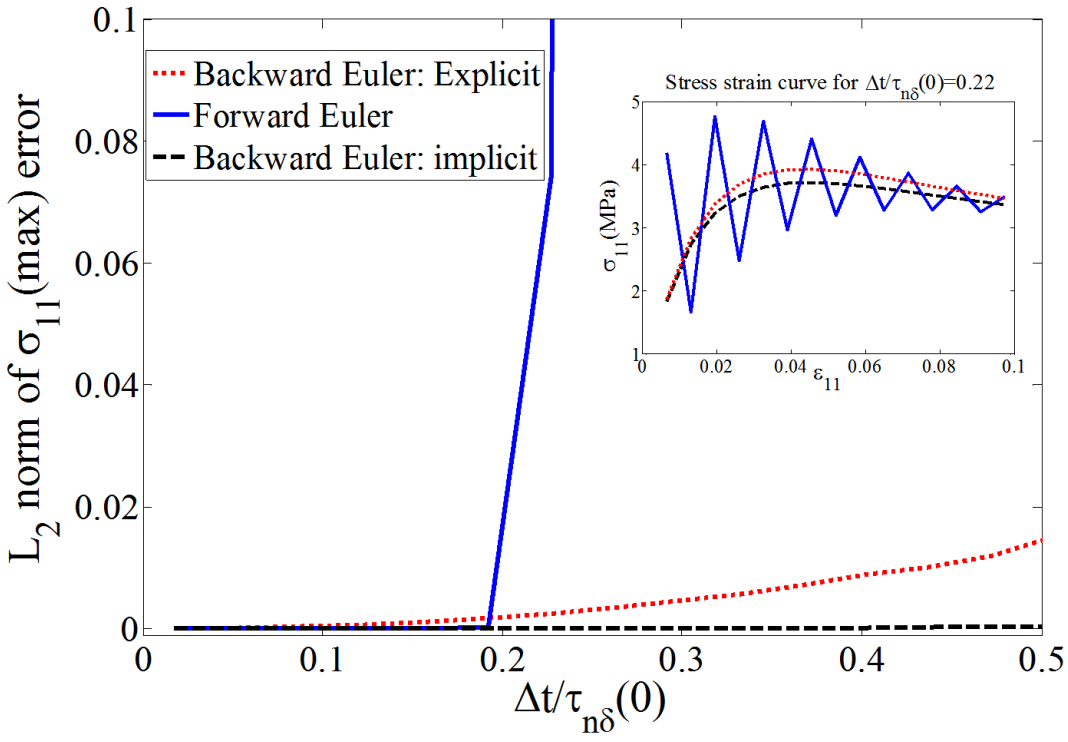

Figure 4-3: The L_2 norm of error in peak stress σ_{11}(max) plotted against normalized time increments (inset is the uniaxial stress-strain curves)

The insert in Figure 4-3 shows the stress-strain curve for the case $\Delta t/\tau_{n\delta}(0)=0.22$, while Figure 4-3 gives the error (L_2 norm) in peak stress (σ_{11}) at different value of time-step $\Delta t/\tau_{n\delta}(0)$. The L_2 norm of peak stress error is calculated using the following expression

$$L_2 = \frac{\left(\sigma_{11}^0 - \sigma_{11}\right)^2}{\left(\sigma_{11}^0\right)^2} \tag{4.44}$$

where σ^0_{11} is the true peak stress calculated using backward implicit scheme with very small $\Delta t/\tau_{n\delta}(0)=0.02$. If we compare the results of the three schemes in Figure 4-3, L_2 norm increases with the increase in time step $\Delta t/\tau_{n\delta}(0)$ for all numerical schemes, which indicates divergence from the true solution. Among three numerical methods, the forward Euler scheme diverges rapidly at certain $\Delta t/\tau_{n\delta}(0)$ and becomes unstable at $\Delta t/\tau_{n\delta}(0)=0.22$, at which solutions begins to

oscillate as shown by the stress-strain curves in Figure 4-3 insert. This instability is caused by the coefficients P_n and Q_n changing sign in Eq (4.39b) at the critical $\Delta t/\tau_{n\delta}(0)$. On the other hand, the explicit backward Euler scheme with constant coefficients is stable and reasonably accurate for up to large $\Delta t/\tau_{n\delta}(0)$. Although, the backward Euler scheme has the least error, it is computationally expensive since the solution requires a large number of iterations. In this case, the simulation of creep or stress relaxation behavior over long time span for structural components or other geometrically complex boundary value problems can become computationally prohibitive when each element is modeled with large number of integration points in the θ-ϕ spherical coordinates. For example in a finite element model with one thousand linear strain elements under plane strain or plane stress conditions there are 144000 nonlinear equations need to be solved at a given time step with 72 integration points in the θ-ϕ spherical coordinates. For constant strain-rate confined uniaxial compressive loading condition, the time taken by the implicit backward Euler scheme is 200 times that of the explicit backward Euler scheme on a desktop computer using Matlab programming environment. Therefore, for computational efficiency, all the calculations in this paper were performed using the explicit backward Euler scheme with constant coefficients.

4.4.2 Calibration and Identification of Model Parameters

The model applicability is evaluated by comparing the model prediction with the experimentally measured behavior for hot-mix asphalt (HMA) concrete under uniaxial unconfined creep and constant strain-rate loading in compression and tension, respectively, at a constant temperature of 20 ^{o}C [7]. The model parameters were first calibrated using the experimental creep data under

compressive axial stress σ_{11}=1.0 MPa ($\sigma_{22}=\sigma_{33}$=0.). First, the normal and shear stiffness and viscosity parameters E_1, G_1, G_w, E_n, μ_n and μ_w, were obtained by reducing constitutive equation to linear viscoelastic by assuming $B_n=B_w=\infty$ and fitting the reduced equation to the initial portion (first 100 sec) of the experimental creep curve. Thereafter, damage parameters B_n, B_w and β were introduced into the model and optimized to match the complete creep response curve. To account for the asymmetric inter-granular behavior under tension and compression, parameter α_n and α_w were included in the model and identified using the tensile creep data at 0.3MPa stress amplitude. The following model parameters were found from calibration process: $G_1=0.8E_1$, $G_w=E_n$, $\mu_n=\mu_w$, and $B_n=B_w=14.3\text{x}10^{-3}$, where E_1 =2.4 GPa, E_n= 0.3 GPa, $\tau_{n\delta}(0)$=57s, $\tau_{nf}(0)$=6.33s, $\alpha_n=\alpha_w=0.175$ and β= 3.8

4.4.3 Comparison of Model Predictions with Experiments

The calibrated parameters were used to obtain the model predictions for (1) creep behavior under uniaxial compressive stress σ_{11}=1.5MPa and tensile stresses σ_{11}=0.3, 0.5 and 0.7 MPa, respectively, and (2) stress-strain behavior under constant uniaxial strain rates of ε_{11}=0.005/s, 0.0005/s and 0.00005/s for compressive loading and ε_{11}=0.0167/s and 0.00167/s for tensile loading, respectively.

4.4.3.1 Creep Behavior

In our calculations for the uniaxial unconfined creep test, the axial stress was applied as $\sigma_{11}=\sigma_0$ and lateral stress were specified as zero, $\sigma_{22}=\sigma_{33}$=0. For the uniaxial unconfined constant strain-

rate test, the loading was applied as follows: $\varepsilon_{11}=\varepsilon_0 t$, and lateral stress were specified as zero, $\sigma_{22}=\sigma_{33}=0$.

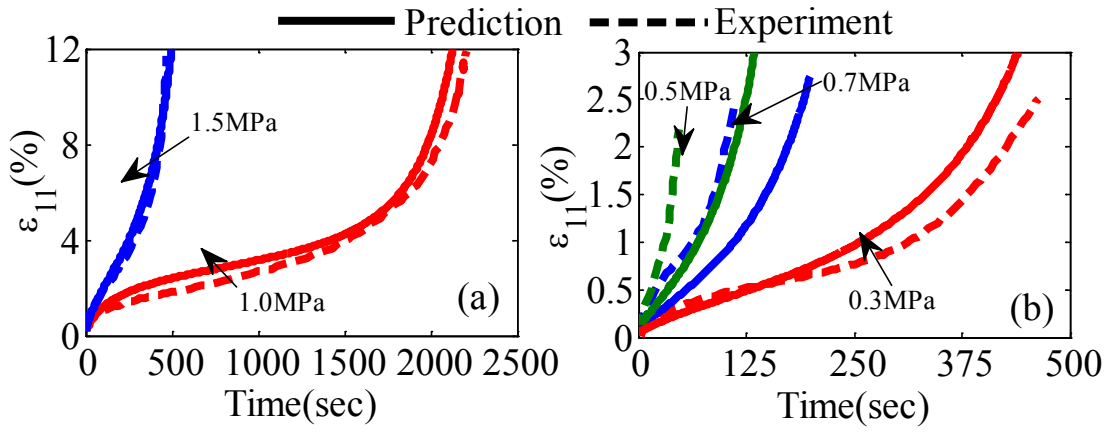

Figure 4-4: Comparison of measured and predicted creep curve for asphalt concrete under uniaxial (a) compressive and (b) tensile load.

The experimental, calibrated and predicted creep curves for compressive loading are shown in Fig 4-4(a), while the experimental and predicted creep curves for tensile loading are shown in Fig 4-4(b). The model not only replicates the primary, secondary and tertiary creep followed by creep failure shown by the calibration curve, but predicts well the creep behavior under the compressive and tensile loading. We note however that the discrepancy in the quantitative agreement with the measurements at stress-levels of 0.5 and 0.7 MPa under tensile loading. In addition to the usual uncertainty associated with testing of this type (such as heterogeneity between samples and non-uniform gripping conditions), we believe this discrepancy can be partly attributed to the initial loading conditions, that is the rate at which the load was ramped to the required test stress-levels, and partly to the varying characteristic time at different loading-levels.

Further we find it useful to examine how the inter-granular forces evolve during the creep process. As illustration, Figs 4-5(a) and 4-5(b) show the force in the normal and shear directions

in various selected inter-granular orientations as function of time corresponding to the creep curve under compressive axial stress σ_{11}=1.0 MPa given in Fig. 4-4(a). Since the loading is axi-symmetric, the inter-granular forces are independent of, ϕ. Thus, each curve in Fig 4-4 refers to θ measured with respect to the loading direction-1 (see Figure 1 for definition of θ, and ϕ). For clarity, polar diagrams in θ-coordinate of the normal and shear inter-granular forces are also included at selected times. Upon the onset of creep load, the inter-granular normal forces are the highest in the orientations closer to the loading direction, while the inter-granular shear forces are highest in the $\theta = \pi/4$ direction. However, as loading progresses the spring stiffness E_2 and G_2 in the directions receiving higher forces undergo damage and softening, resulting in a progressive crossover of directions that are required to sustain larger forces. Clearly, these normal and shear force distributions cannot be obtained by simple traction localization given as $\sigma_{ij}n_j$, and the results indicate that traction localization schemes need to incorporate fabric tensors and their evolution. Furthermore, these results indicate that the material will progressively develop damage or loading induced anisotropy. Such effects that manifest due to granular nature of materials are not easily represented by phenomenological constitutive relationships based upon the concepts of traditional Cauchy mechanics that seek correlations between stress and strain.

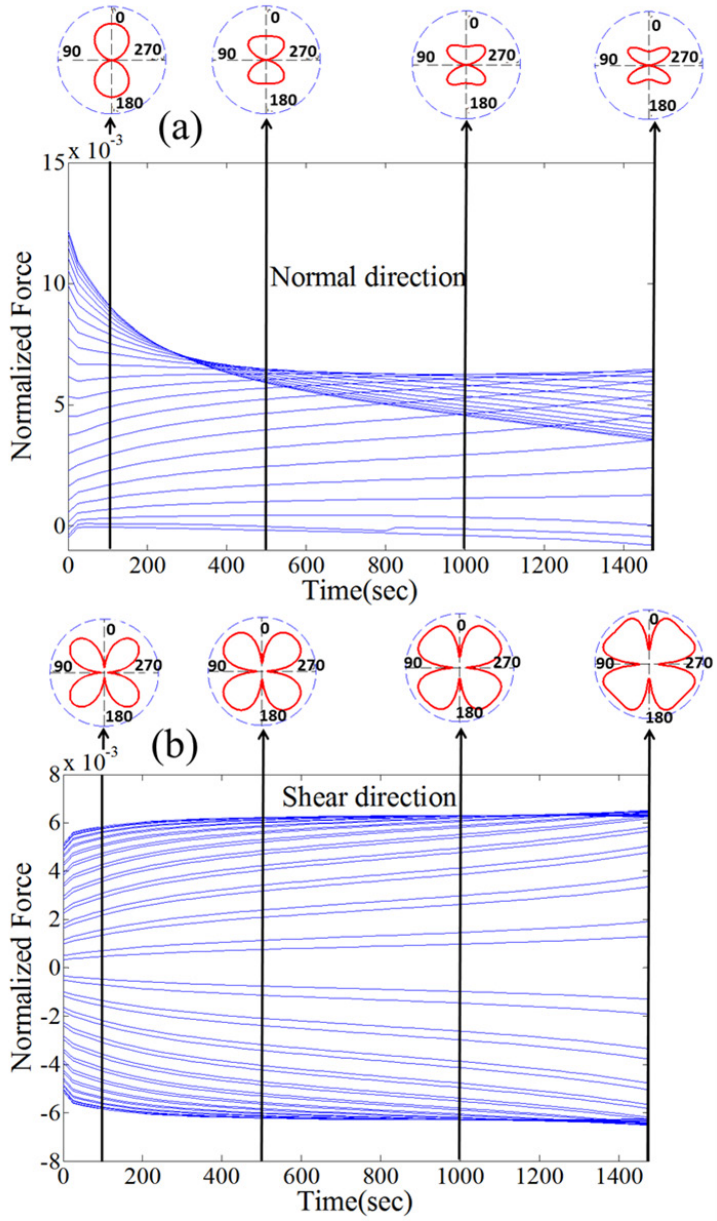

Figure 4-5: (a) Normal and (b) shear force distribution in the uniaxial compressive creep test corresponding to the creep curve under 1.0 MPa in Figure 4(a)

4.4.3.2 Monotonic Behavior

Measured and calculated normalized stress-strain curves and peak stresses for two strain rates under compressive and tensile loading are given in Figs 4-6(a) through (d). With the increase in the strain rate, the predicted stress-strain curves are found to shift towards the left for

compression, and right for tension test as seen in Figs 6(a) and 6(c) Also both the predicted and calculated peak stresses are observed to increase with strain rate.

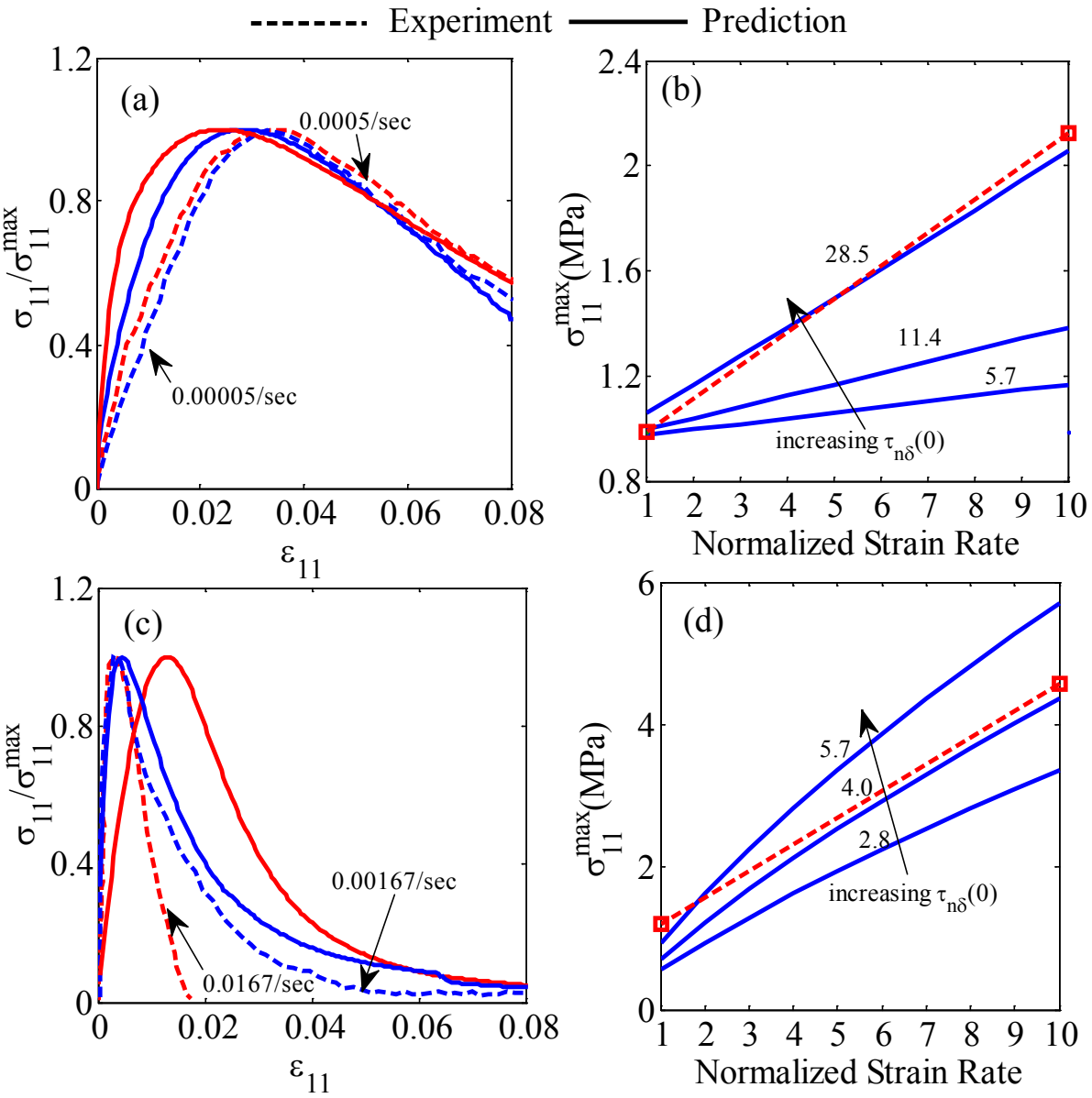

Figure 4-6: Measured and calculated stress-strain curves under uniaxial constant strain rate: (a) and (c) normalized σ_{11} versus ε_{11} in compression and tension respectively, (b) and (d) peak stress σ_{11} versus ε_{11}.in compression and tension, respectively

Such behavior is expected for rate-dependent material and indicates that at higher strain rates the material is stiff, brittle and fails at higher stress (see for example the experimental results on

Huanglong limestone presented in [101]). The peak stress is particularly found to be sensitive to the initial retardation and relaxation times $\tau_{n\delta}(0)$ and $\tau_{nf}(0)$, as shown by the model predictions in Figs 4-6(b) and 4-6(d) at $\tau_{n\delta}(0)$ varying from 2.85s to 28.5s (corresponding to the relaxation times τ_{nf} (0) =0.32s to 3.2s). The initial retardation (relaxation) times $\tau_{n\delta}(0)$=28.5s and 4.0s ($\tau_{nf}(0)$=3.2s to 0.44s) provide a good match for the peak stress measurements for the compression and tension tests, respectively. It is instructive to compare these retardation (relaxation) times to the time required for reaching the peak stress in the measurements, which are found to be 65s-650s for the two compression tests and 0.18s-1.8s for the two tension tests, respectively. From this comparison it appears that a smaller characteristic time is associated with the material response for tensile loading as opposed to compressive loading and that the characteristic time may be dependent upon loading-rate. Classically, the varying rate effects in hot mix asphalt (HMA) materials have been modeled using Prony series with terms spanning 4 to 5 decades in characteristic times [7]. The fundamental mechanisms that govern the predicted asymmetric tensile-compressive rate-dependent characteristic response time for these materials are unclear. However, these mechanisms are likely connected to the composition of HMA which consists of a highly compliant and viscous solid binder derived from complex hydro-carbons that binds together irregular shaped rock aggregates of a broad size distribution.

4.4.4 Evaluation of Multi-Axial Rate-Dependent Failure Behavior

In this study, the values of model parameters used were as follows: $E_1=G_1$, $G_w=0.5E_n$, $\mu_n=\mu_w$, and $B_n=B_w=0.005$, where $E_1=4$ GPa, $E_n=1.7$ GPa, $\tau_{n\delta}(0)$ = 52s, $\alpha_n=\alpha_w=0.2$ and β= 5. Model calculations were performed to study time-to-failure under biaxial creep, effect of loading rate on

failure envelopes under biaxial and triaxial loading, and evolution of failure envelope as a function of hydrostatic stress.

4.4.4.1 Biaxial Creep Behavior

Material can fail below its critical failure strength under creep load as shown in Figure 4-7. For obtaining the creep behavior under biaxial loading, the axial stress, σ_{11}, and the lateral stress, σ_{22}, were applied as follows: $\sigma_{11}=A\cos(\gamma)$, $\sigma_{22}=A\sin(\gamma)$ and $\sigma_{33}=0$, where A is the loading stress-level, and γ is constant between 0 and 2π. We note that different values of γ correspond to different proportional loading conditions in the biaxial stress plane σ_{11}-σ_{22} such that the norm of stress $\sqrt{\sigma_{11}^2+\sigma_{22}^2}=A$.

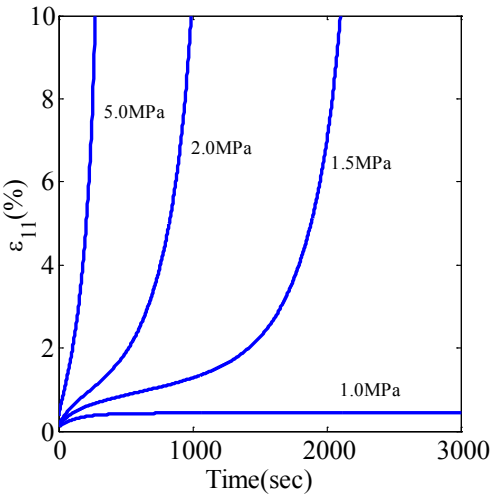

Figure 4-7: Creep curves at different stress level

The time-to-failure is identified as the time taken for the norm of strain to reach 10%. The time-to-failure is plotted as a point corresponding to each proportional loading condition. The resultant point cloud is fitted using a smooth surface as shown by the 'hat' shaped surface cutoff

at 3000s. Plots of 3d surface, top and side view of 3d surface are given in Figure 4-8(a) through (c). At larger stress amplitude, failure time is very small as expected. With decrease in stress time-to-failure increases, and below a critical value of stress the time-to-failure becomes very large and approaches infinity. In this study, we cease further computations beyond 3000s, thus the time-to-failure surface has a cutoff at that time.

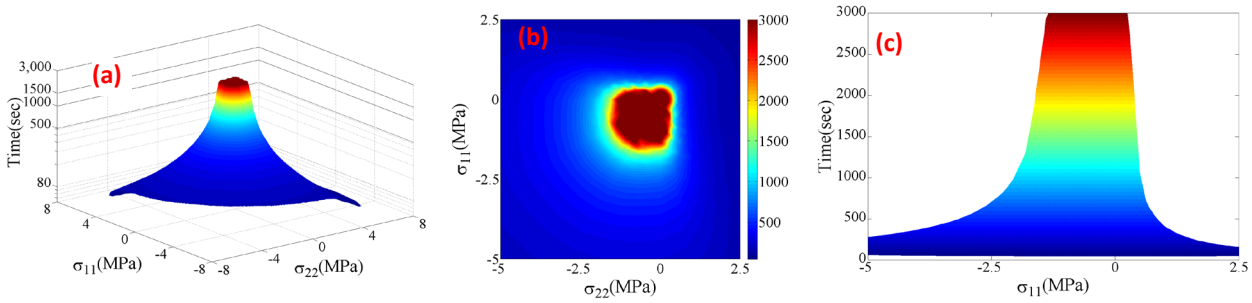

Figure 4-8: Creep time-to-failure plots: (a) 3d surface plot, (b) top view, and (c) side view

4.4.4.2 Biaxial and Triaxial Behavior under Constant Loading Rate

For computing the biaxial behavior, the axial stress, σ_{11}, and the lateral stress, σ_{22}, are varied at a constant rate such that, $\sigma_{11}=tA\cos(\gamma)$, $\sigma_{22}=tA\sin(\gamma)$ and $\sigma_{33}=0$, where A is the loading rate, γ is constant between 0 and 2π, and t is the time. We note that different values of γ correspond to different proportional loading paths in the biaxial stress plane σ_{11}-σ_{22} such that the norm of stress for all paths follows $\sqrt{\sigma_{11}^2+\sigma_{22}^2}=At$.

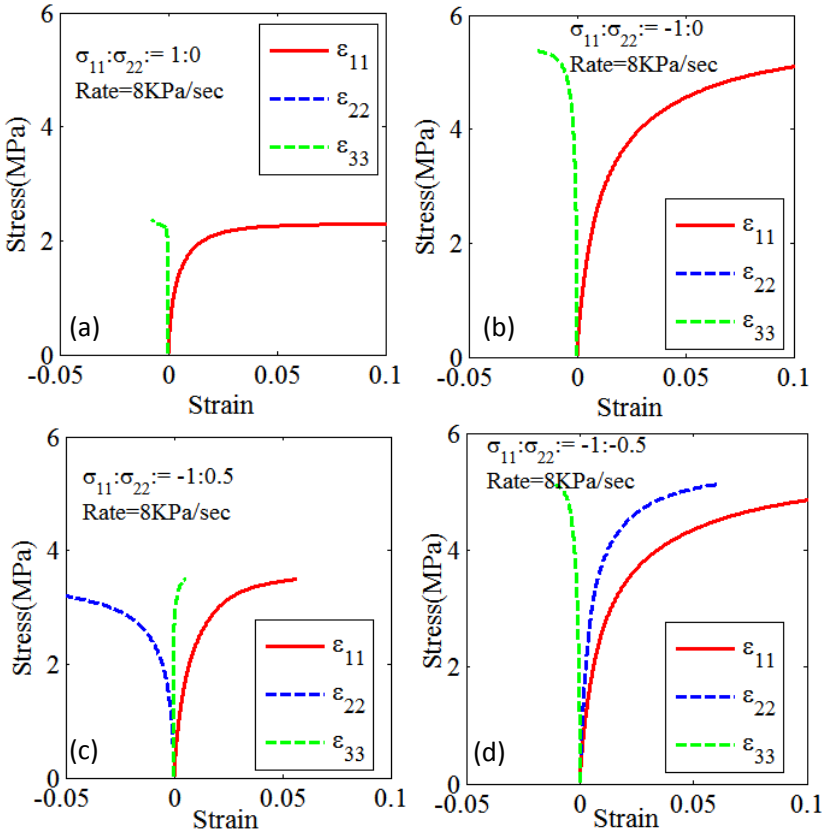

Figure 4-9: Example stress-strain curves under biaxial loading: (a) σ_{11}: σ_{22}=1.0:0.0, (b) σ_{11}: σ_{22}=-1.0:0.0, (c) σ_{11}: σ_{22}= -1.0:0.5, and (d) σ_{11}: σ_{22}=-1.0:-0.5

Figures 4-9(a) to (d) give illustrative examples of the stress-strain curves that are obtained for the cases of σ_{11}:σ_{22}=*1.0:0.0,-1.0:0.0, 1.0:0.5* and *-1.0:-0.5*, respectively. As expected, asymmetric stress-strain behavior is observed under purely tensile versus purely compressive loading. Further in this paper, the failure is identified as the stress state at which the norm of strain ≈10%, although other failure criterion based upon combinations of invariants can be also adopted [102] or detected using instability criterion [103]. The stress-state corresponding to failure is plotted on the stress plane σ_{11}-σ_{22} to obtain the failure envelopes shown in Figs 4-10(a) and 4-10(b). Fig 4-10(a) shows the failure envelops for varying parameter B_n at a constant loading rate of 2kPa/sec. The failure plots are not symmetric in tension and compression, because failure

strength in tension is much smaller when compared to compression. Furthermore if rate of loading is kept constant and damage is increased by decreasing the parameter B_n, failure envelope becomes smaller, indicating smaller strength with larger damage. Moreover for constant parameter B_n, a failure envelope shrinks with decrease in rate of loading as shown in Fig 4-10(b). Larger envelope with higher loading rate is expected, because of delayed damage.

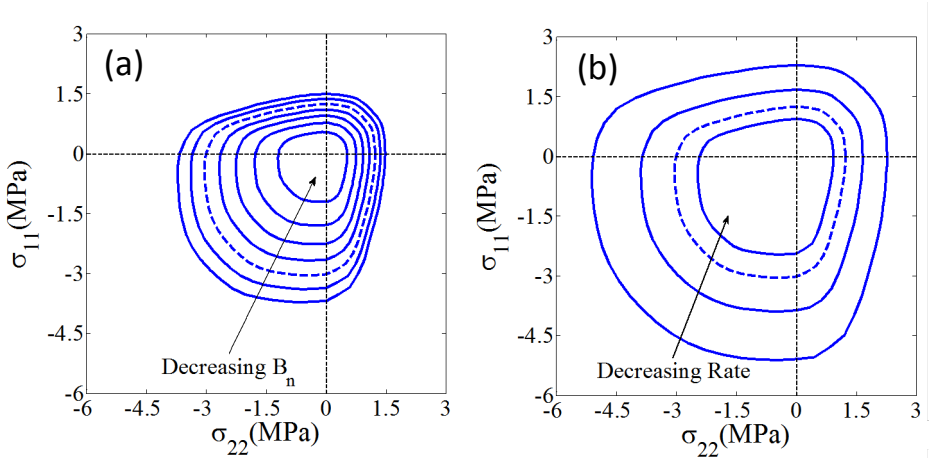

Figure 4-10: Predicted biaxial failure envelope: (a) effect of damage (b) effect of loading rate

Similarly for computing the triaxial behavior, the axial stress, σ_{11}, and the lateral stress, σ_{22}, are varied at a constant rate such that, $\sigma_{11}=tA\cos(\gamma)\sin(\varphi)$, $\sigma_{22}=tA\sin(\gamma)\sin(\varphi)$ and $\sigma_{33}=tA\cos(\varphi)$, where A is the loading rate, t is the time, γ and φ are constants between [0-2π] and [0-2π], respectively such that $\sqrt{\sigma_{11}^2+\sigma_{22}^2+\sigma_{33}^2}=At$. If $\varphi=\pi/2$, then the biaxial stress-path is recovered. Again the failure was identified as the stress state at which the norm of strain ≈10%. The stress-state corresponding to failure is plotted as a point cloud on the stress space σ_{11}-σ_{22}-σ_{33} and fitted using nearest-neighbor interpolation to obtain the failure envelopes shown in Figs 4-11(a). For ease of understanding, the triaxial failure envelopes can also be presented on the so-called "π plane" corresponding to the constant hydrostatic stress plane in the 3-dimenasional stress-space

at different value of hydrostatic stresses as shown in Figure 4-11(b). These failure envelopes at "π plane" are generated by the intersection of the fitted 3d failure envelope in Figure 4-11(a) with a plane parallel to hydrostatic axis at different levels of hydrostatic stress. These intersections are illustrated by different colored rings on triaxial failure envelope in Figure 4-11(a) and plotted on the π plane in Figure 4-11(b). We observe that the shape of the failure envelope on the π plane evolves with increasing hydrostatic stress from nearly circular to triangular with rounded corner. This evolution is in variance with the classical failure criteria that maintain their shapes on the π plane [102]. Further, as with the biaxial behavior, larger 3d failure surface is obtained for the faster loading rate as shown in Figure 4-12.

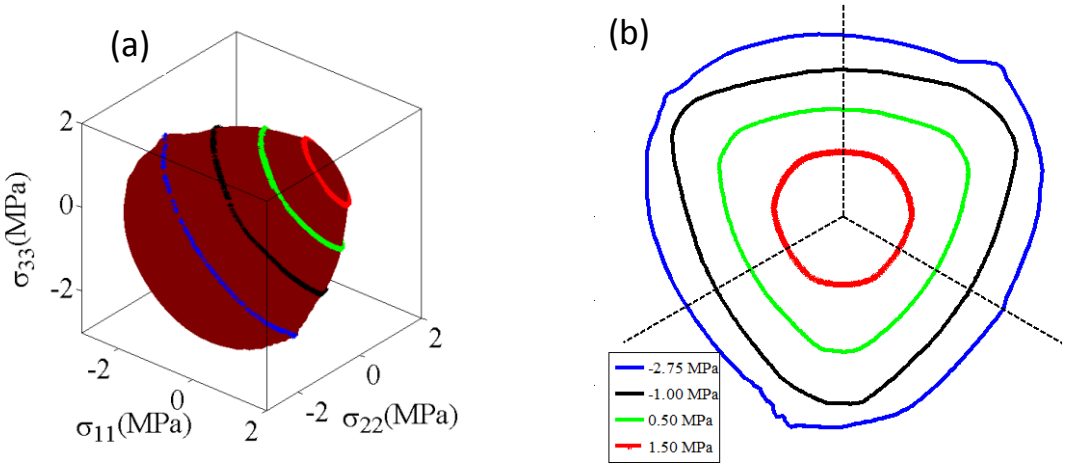

Figure 4-11: Predicted triaxial failure envelopes: (a) 3d failure surface, and (b) failure plot on π-plane at different hydrostatic stress

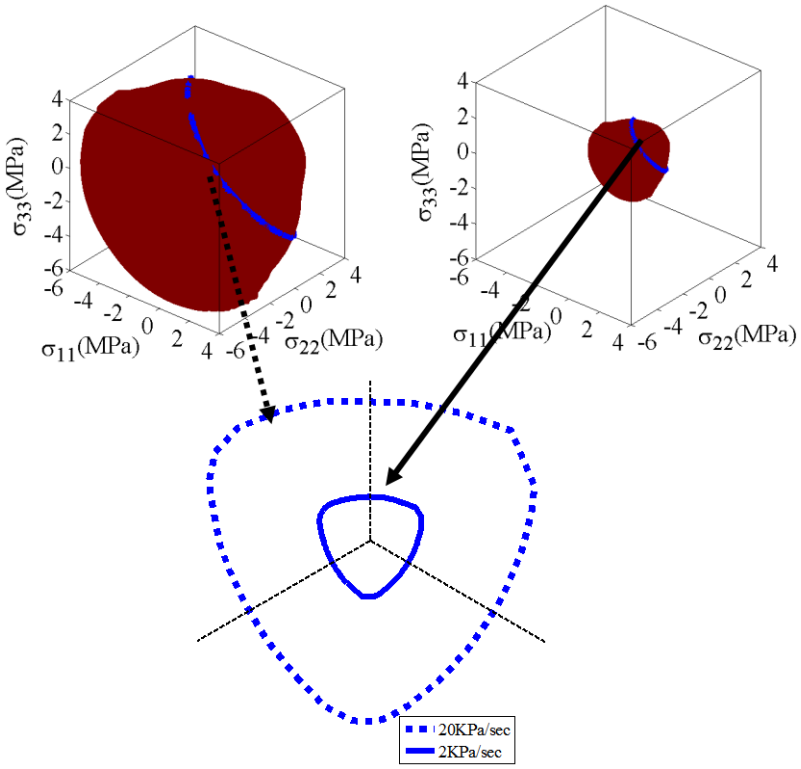

Figure 4-12: Effect of loading rate on 3d failure surface along with failure plots on π plant at zero hydrostatic stress

4.4.5 Parametric Study

In the following section we present three loading cases, (a) the stress-strain response under monotonically increasing strain under constant strain rate, (b) the stress relaxation response under a constant step strain history and (c), the creep response under a constant stress. Results for the three loading conditions and their associated dissipative and elastic energies are discussed below. Following set of parameters were used: $E_1=G_1$, $G_w=0.8E_n$, $\mu_n=\mu_w$, and $B_n=B_w=14.3\text{x}10^{-3}$, where E_1 =2.15 GPa/m, E_n= 0.3 GPa/m, μ_n/E_n = 59s, and β= 3.8.

4.4.5.1 Constant Strain-Rate Behavior

Figure 4-13 shows the predicted stress-strain curves at loading rates of $2x10^{-4}$ s^{-1} and $2x10^{-3}$ s^{-1}, where Figure 4-13a gives a plot of axial stress σ_{11} and strain ε_{11}, while Figure 4-13b gives a plot of lateral stress σ_{22} $(=\sigma_{33})$ with strain ε_{11}. For each loading rate, parameter B_n was varied from $3x10^{-3}$ to $8x10^{-3}$. Rate-dependent nonlinear stress-strain curves are obtained that exhibit damage related softening. As expected, (1) lower peak stress and corresponding strain are obtained with decreasing B_n, and (2) stiffer response with a higher peak stress is obtained at higher loading rate. In addition, the strain corresponding to the peak stress is found to be larger at higher strain rate as the commencement of damage is delayed due to the viscous response of the rheological model.

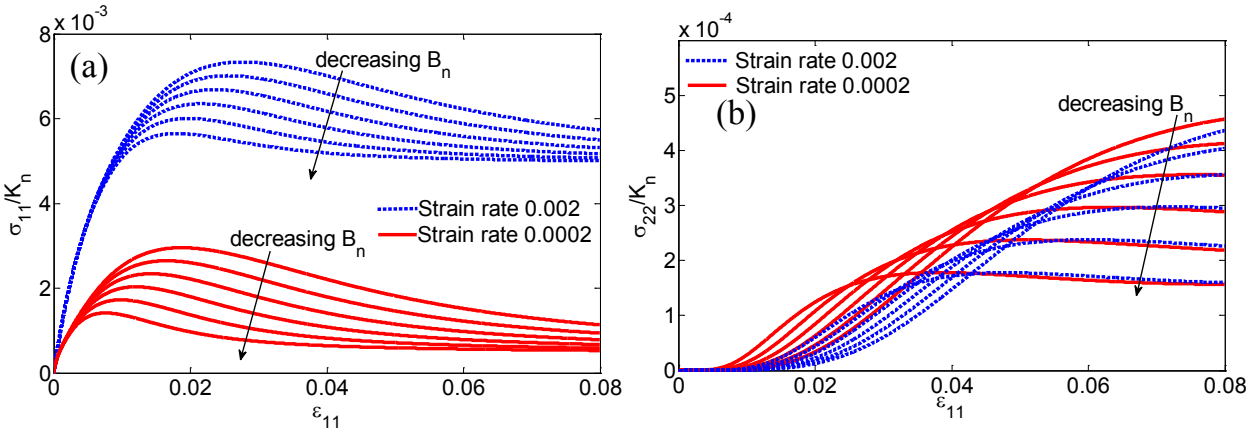

Figure 4-13: Stress versus strain curve under uniaxial constant strain rate loading for two different loading rates: (a) σ_{11} versus ε_{11}, and (b) σ_{22} versus ε_{11}

The effect of delay is also seen in the response of the lateral stress σ_{22}. Moreover, the lateral stress σ_{22} exhibits a response that captures the underlying discreteness of the material system. At very small strains, the lateral stress σ_{22} is close to zero, which is expected since the normal and shear parameters are taken to be equal such that the terms that couple σ_{22} and ε_{11} vanish at the

unloaded state. However, as ε_{11} increases, the normal and shear spring stiffness E_2 and G_2 diverge as they undergo different damage as governed by Eq. 4.19. As a consequence the coupling term becomes non-zero and evolves with loading. Furthermore, the damage evolution of the spring stiffness E_2 and G_2 depends upon the loading states which are a function of the inter-granular orientation n_i. Thus, the spring stiffness E_2 and G_2 become a function of direction cosines endowing a loading-induced anisotropy to the material.

The effect of damage evolution of the spring stiffness E_2 and G_2 on the inter-granular force is illustrated in Figure 4-14, which shows the force in the normal and shear directions in various inter-granular orientations. Since the loading is axi-symmetric, the inter-granular forces are independent of, ϕ. Thus, each curve in Figure 4-14 refers to θ measured with respect to the loading direction-1 (see Figure 4-1 for definition of θ, and ϕ). In the early part of the loading, the inter-granular normal forces are higher in the orientations closer to the loading direction, while the inter-granular shear forces are higher in the $\theta = \pi/4$ direction. However, as loading progresses the spring stiffness E_2 and G_2 in the directions receiving higher forces undergo damage and softening, resulting in a progressive crossover of directions that are required to sustain larger forces as seen by the highlighted (thicker) curves in Figure 4-14. Such effects of granular nature of materials are not easily represented by phenomenological constitutive relationships based upon the concepts of traditional Cauchy mechanics that seek correlations between stress and strain

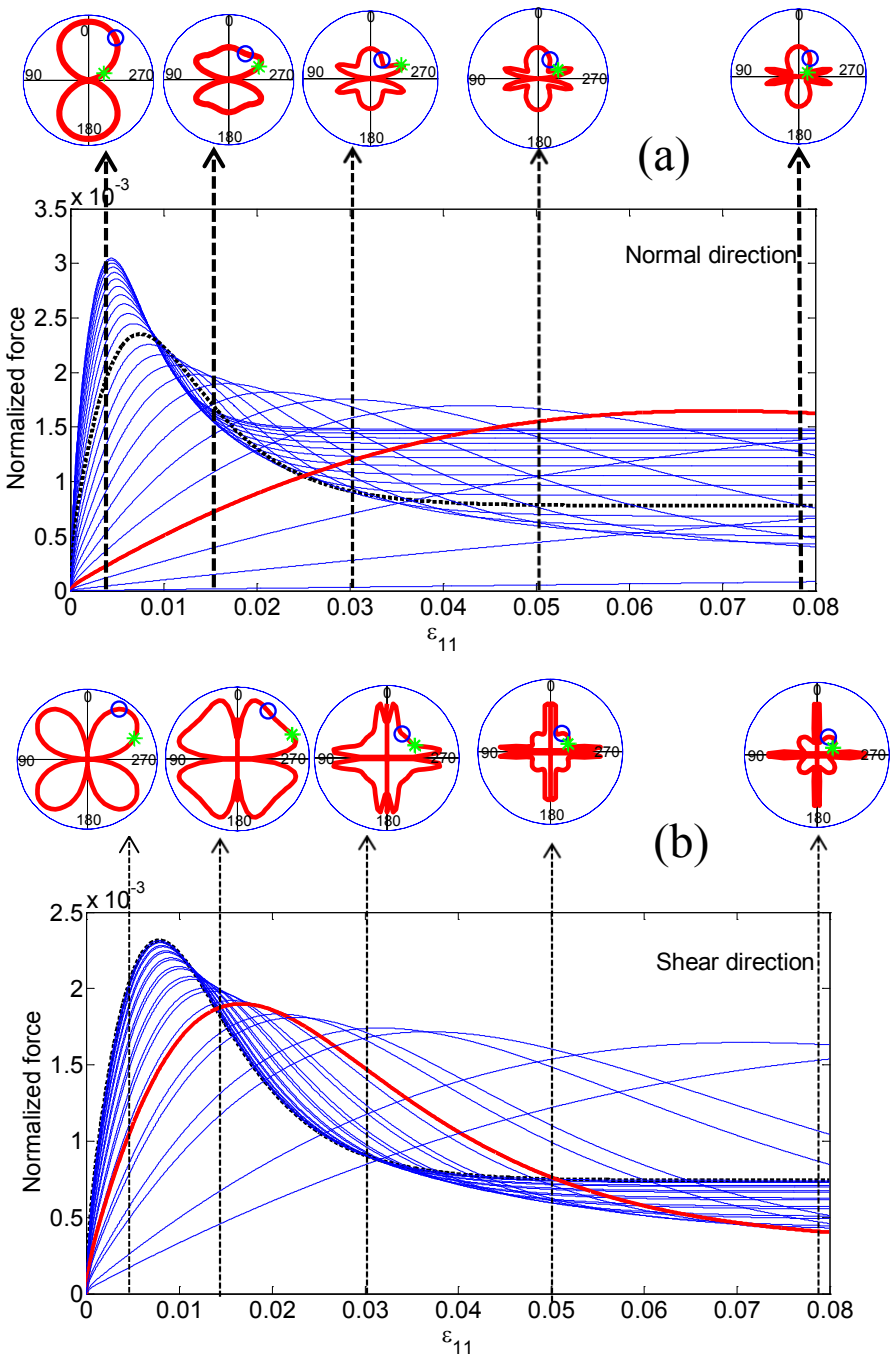

Figure 4-14: Evolution of inter-granular forces in various inter-granular orientations under uniaxial constant strain rate loading of 0.0002 s-1: (a) normal direction (b) shear direction

Finally, in Figure 4-15 we show how the elastic and dissipative energies, obtained using Eqs. 4.21 through 4.23, evolve with loading in this type of rate-dependent material with damage. The

elastic energy is normalized with respect to that of a linear viscoelastic Zener solid. As expected, the elastic energy (or maximum recoverable work) decreases and the dissipative energy increases with loading as the material undergoes damage and softening.

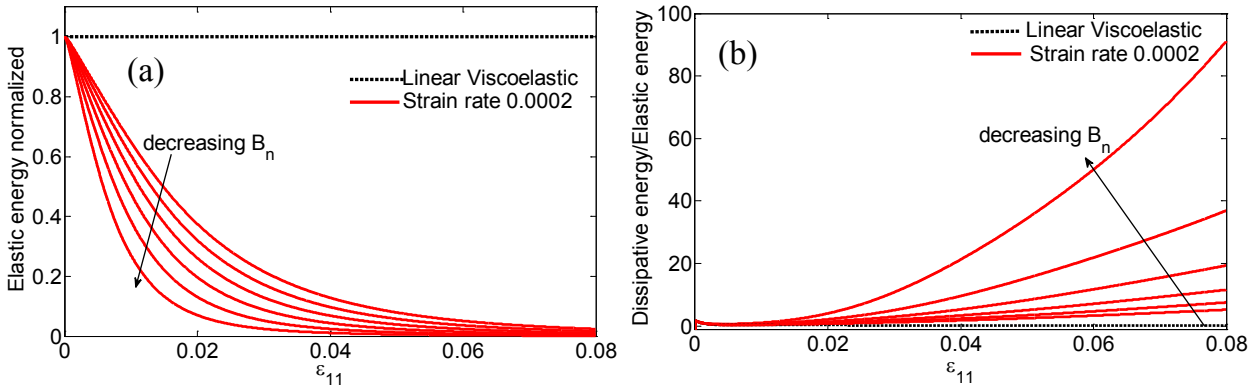

Figure 4-15: Evolution of (a) elastic energy and (b) dissipative energy under uniaxial constant strain rate loading of 0.0002 s-1

4.4.5.2 Constant Strain Behavior – Stress Relaxation

Figure 4-16 shows the stress relaxation behavior under a constant uniaxial strain ε_{11}=0.8%. The stress is normalized by the stress at time t=0, denoted by σ_0, and the time is normalized by the relaxation time $\tau=\mu_n/E_n$. We observe that both the axial stress σ_{11} and the lateral stress σ_{22} $(=\sigma_{33})$ relax to a steady state value. Again, due to the ability of the present model to represent the granular nature, the lateral stress σ_{22} shows a nonlinear evolution, although these stresses are comparatively small. Further, it is evident from the Figure 4-16 that the stress will relax at different rates and to different stress-levels depending upon the level of damage as governed by the parameter B_n. It is well known for linear viscoelastic Zener solids, the stress will relax to the value bounded by the relaxation modulus at time $t\rightarrow\infty$. Similarly, for the damage model described here, the stress relaxes to the value bounded by the damaged relaxation modulus evaluated at time $t\rightarrow\infty$, for the damage state corresponding to the applied strain and the

parameter B_n. The damaged relaxation modulus also determines the maximum recoverable work or elastic energy as noted in Eq. 4.23. Since for constant strain loading, the damage state evolves to a steady-state, both the elastic energy as well as the dissipative energy, obtained using Eqs. 4.21, 4.23 and 4.24, reach asymptotic values as shown in Figure 4-17.

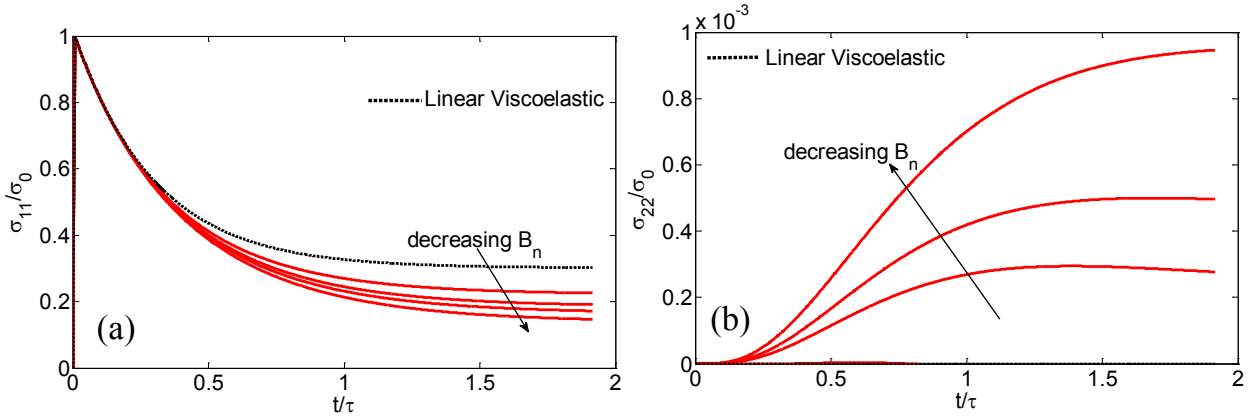

Figure 4-16: Stress relaxation under uniaxial loading of ε_{11} = 0.008: (a) σ_{11}, and (b) σ_{22}

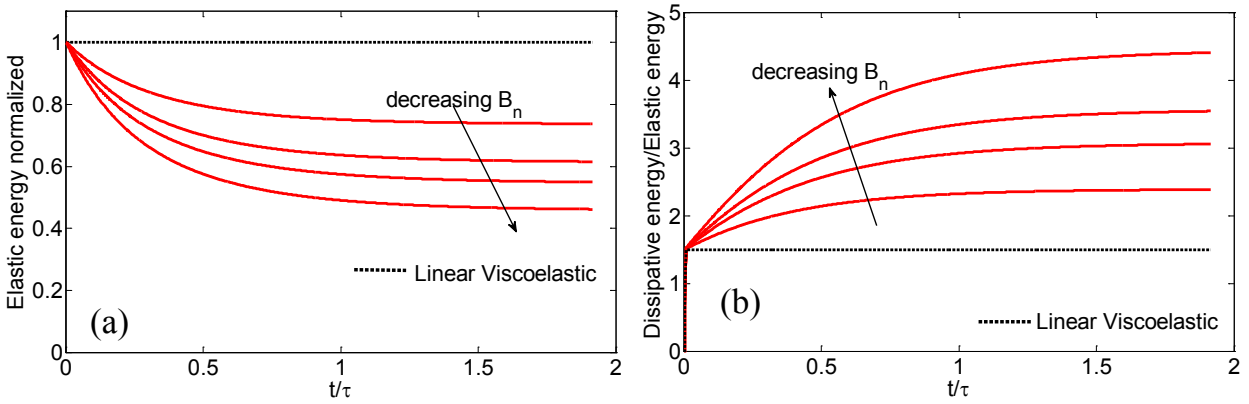

Figure 4-17: Evolution of (a) elastic energy and (b) dissipative energy under uniaxial stress relaxation

4.4.5.3 Constant Stress Behavior – Creep Deformation

Figure 4-18 shows the creep behavior under a constant uniaxial stress σ_{11}=5 MPa. The creep strain is normalized by the strain at time t=0, denoted by ε_0, and the time is normalized by the

relaxation time $\tau=\mu_n/E_n$. We observe that both the axial creep strain ε_{11} and the lateral strain ε_{22} $(=\varepsilon_{33})$ develop under the applied stress. However, depending upon the parameter B_n, the creep reaches either an asymptotic value or exhibits accelerated creep, sometimes termed as secondary creep. Clearly, in this model, the accelerated creep is a result of damage as certain inter-granular orientations creep to the deformation corresponding to the peak stress and, subsequently, undergo softening. Since smaller B_n implies damage development at smaller strains, we observe greater accelerated creep as B_n is decreased.

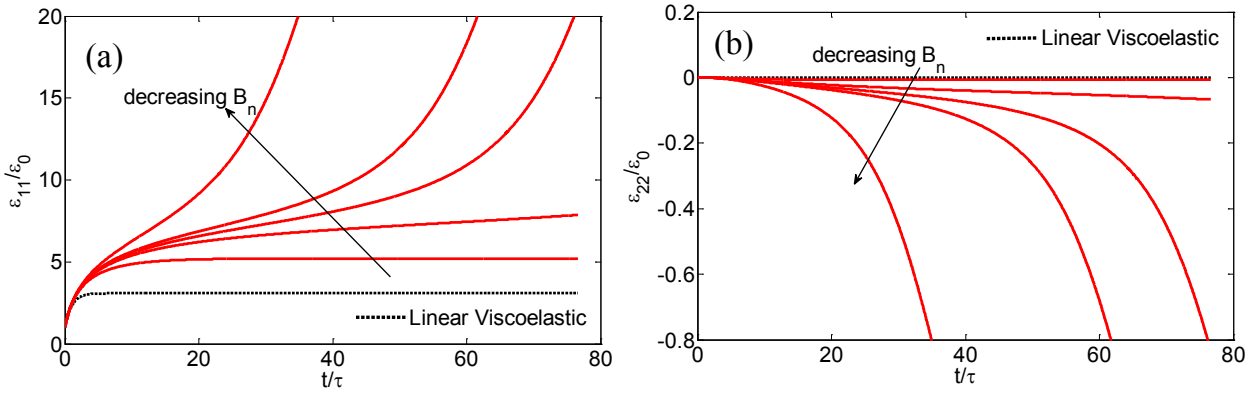

Figure 4-18: Creep deformation under uniaxial loading of σ_{11} = 5MPa: (a) ε_{11}, and (b) ε_{22}.

In Figure 4-19 we show how the dissipative energy, obtained from Eqs. 4.21 through 4.23, evolves under creep deformation. For a linear viscoelastic solid, the dissipative energy reaches an asymptote. However for material undergoing damage, the dissipative energy increases once certain inter-granular orientations begin softening. Finally, we note that the lateral strain ε_{22} show a nonlinear evolution as different inter-granular orientations undergo different loading history, indicating a non-linear material volume change during creep and reflecting the effects of material granularity.

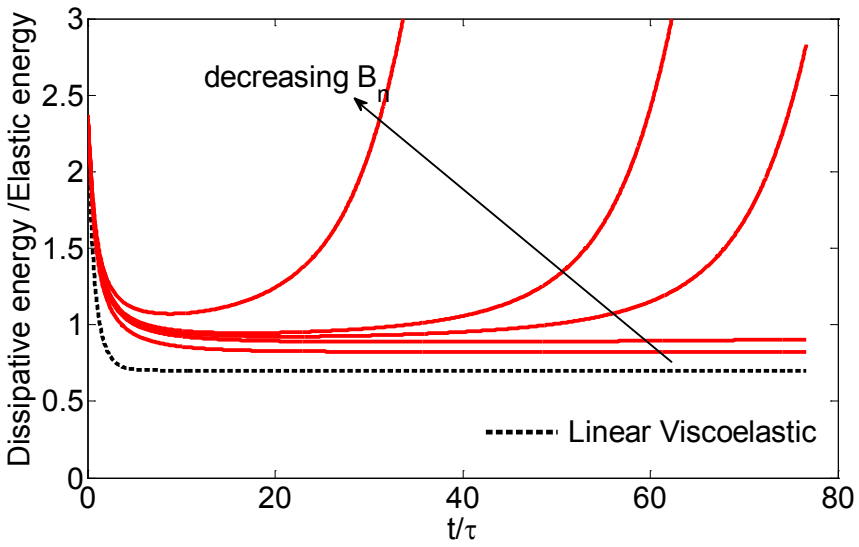

Figure 4-19: Evolution of dissipative to elastic energy under uniaxial creep

4.5 Summary

In this chapter we have presented a methodology for obtaining the constitutive relationships for non-linear rate dependent materials with damage using a granular micromechanics approach. In this approach, properties at macro or RVE scale is assumed to depend upon underlying grain scale or sub-RVE scale mechanisms, for example, influence of molecular effects on the nonlinear properties of cross-linked polymers, asphalt concrete etc. These sub-RVE scale mechanisms can be modeled by using appropriate force displacement relationships at sub-RVE scale. The overall constitutive law of the material is then obtained by averaging over the random network formed by these inter-granular interactions. Also the current work presents an explicit numerical scheme based upon Euler backward scheme to obtain fast and accurate solution of such constitutive equations.

For the validation and verification the model predictions are compared against experimental behavior for hot mix asphalt. In particular the model has been applied to investigate primary,

secondary and tertiary creep as well creep failure behavior under compressive loads. Also the model is able to capture effect of strain rate on the peak stress and corresponding strain for asphalt concrete for compressive loading regime. Further, the model capability to describe multi-axial behavior was demonstrated through parametric studies of time-to-failure under biaxial creep as well as the rate-dependent behavior of failure envelopes under biaxial as well as triaxial loading conditions. The advantage of the approach presented here is that we can predict the multi-axial effects without resorting to complex phenomenological modeling.

Chapter 5

Thermo-mechanics Based Constitutive Model for Nonlinear Rate Dependent Materials with Damage and Plasticity

5.1 Introduction

Materials with granular or pseudo-granular microstructure, such as asphalt concrete, soils, polymers, exhibit significant effect of grain-scale mechanisms on the macro-scale behavior. In these material systems, the relevant representative unit can be described as collection of grains formed by the aggregations of atoms or molecules such that the intra-granular interactions are qualitatively different from inter-granular interactions. In some materials, such grains are easily identifiable with distinct grain boundaries, such as in the cases of grain packings, sands and clays, asphalt concrete, sandstones or materials derived from sintering using grain precursors. However, there are a number of materials in which the grain identification is not straightforward although they exhibit a strongly granular texture, such as the case of hydraulic cements and certain polymers. In either case, the evidence of granular nature of materials and the ideas of coarse graining by combining atoms and molecules into larger grains have been prevalent (see for example [104-109]) and similar ideas have formed the basis of the early developments of continuum mechanics in the works of Navier [66], Cauchy [67], and Piola [110, 111]. The significance of micro-scale mechanisms has been further recognized in the context of continuum

mechanics in the pioneering works of Cosserat [112], Mindlin [113], Toupin [114], Eringen [115], Green and Rivlin [116] and Germain [117].

In the current work we develop continuum models of materials with granular micro-structure that exhibit rate-dependent mechanical behavior coupled with nonlinear material damage and plasticity. Numerous constitutive models have been proposed to model nonlinear viscoelastic behavior (see for example [8, 10, 11, 13, 14] including comprehensive reviews [9, 12]). Similarly continuum models for materials that show damage and plasticity abound in the literature (see review in [118, 119]. More recently models have been proposed using more refined description of elasticity [120], damage and plasticity including nonlocal effects[121-128], and rate-dependency [7, 18]. Some of these models have been specifically developed for granular materials such as asphalt [7, 129], rocks[130, 131], soils [123, 132] and concrete [133]. The above citations as well as the reference contained therein are by no means exhaustive. They provide only a subset of a vast literature base, however these could serve as an important starting point for readers interested in this topic. These models have successfully described a number of phenomena very well; however, these efforts characteristically focus upon the macro-scale without adequate direct considerations of the micro-scale mechanisms that are known to be significant for granular materials. In particular, the anisotropic evolution of material behavior, including damage and plasticity, under complex loading paths are expected to influence granular material behavior (this is well known for granular soils and has been often been treated using discrete approaches as in [134-136]). In the modeling approaches that proceed from purely continuum concepts, *a priori* assignment of a complex set of evolution laws are required that have to be phenomenologically motivated, which in the absence of adequate experimental set becomes rather difficult. An alternate to this conventional modeling is the granular

micromechanics approach utilized in this paper. The granular micromechanics approach traces its genesis to the continuum models of grain packings developed in the second-half of the last century (see for example [80, 90, 137-140]) and provides a feasible method for incorporating the influence of grain-scale mechanisms into a continuum model [71, 141-143]. In this approach, a granular meso-structure is considered and the inter-granular interactions modeled in a statistical sense since these materials at their grain-scale contain billions of atoms with ill-defined structure. Recently, the authors have used this approach to develop a rate-dependent damage model using mechanistic arguments [63]. With the motivation of developing continuum material models that are thermodynamically consistent, we focus here on the derivation of rate-dependent coupled damage-plasticity using granular micromechanics approach in a thermomechanical framework [12, 19, 144, 145].

In the subsequent discussion, we first present the general thermomechanical framework applicable to rate-dependent granular materials with coupled damage –plasticity. As a result, we obtain an expression for macro-scale Cauchy stress tensor along with conditions for defining the grain-scale constitutive relations. The grain-scale constitutive relations applicable for rate-dependent damage and plasticity modeling are then derived for loading and unloading conditions. These grain-scale constitutive relations are used along with the expression for Cauchy stress to find the macro-scale constitutive relationship. The developed model is then implemented into an efficient and accurate explicit time integration scheme to investigate the effect of load and unload time on the creep-recovery behavior of hot mix asphalt under uniaxial unconfined compressive and tensile loading. The model results are verified by comparison with experimental observations and the advantages of the current approach discussed.

5.2 Thermomechanical Framework for Granular Micromechanics

5.2.1 Thermomechanics of Rate Dependent Material With Damage and Plasticity

We consider a representative volume element (RVE) of mass density ρ. From first law of thermodynamics, the variation of internal energy density of the RVE is written as follows

$$\rho\dot{e} = p^i - q_{k,k} + \rho h \tag{5.1}$$

where, e is the internal energy per unit mass, p^i is the power density of internal forces, q_k is the heat flux vector, and h is the heat source per unit mass. Further, the second law of thermodynamics, which states that the change of entropy of the system is greater than equal to supply of entropy through heat, provides the following inequality

$$\rho\theta\dot{s} - \rho h + q_{k,k} - \frac{q_k\theta_{,k}}{\theta} \geq 0 \tag{5.2}$$

where, s is the entropy per unit mass, and θ is the thermodynamic temperature. Making use of Helmholtz free energy per unit mass, w, expressed as

$$w = e - s\theta \tag{5.3}$$

Eq. 1 can be written as

$$\rho\theta\dot{s} = p^i - q_{k,k} + \rho h - \rho\dot{\theta}s - \rho\dot{w} \tag{5.4}$$

Eqs. 2 and 4 are combined to find the well-known Clausius-Duhem inequality as

$$p^i - \rho\dot{w} - \rho\dot{\theta}s - \frac{q_k\theta_{,k}}{\theta} \geq 0 \tag{5.5}$$

For small deformation, Helmholtz free energy and entropy per unit volume may be defined as: $W = \rho w$ and $S = \rho s$. Ignoring the heat terms, we obtain the following usable form of Clausius-Duhem inequality

$$p^i - \dot{W} - S\dot{\theta} = d \geq 0 \tag{5.6}$$

where d denotes the dissipation per unit volume [146].

For further discussion, we assume that the power density of internal forces, p^i, is a function of the symmetric part of first gradient of displacement, that is $p^i = \sigma_{ij}\dot{u}_{(i,j)} = \sigma_{ij}\dot{\varepsilon}_{ij}$, where σ_{ij} is the Cauchy stress. In general, the power density of internal forces could be functions of higher gradients of displacements as well as rotations which would lead to higher gradient and micromorphic materials (see [117, 147, 148]). The Helmholtz free energy density of rate-dependent material with damage and plasticity is taken to be a function of the independent kinematic variable, ε_{ij}; the internal variable associated with rate-dependent phenomenon, ε_{ij}^v; a second internal variable associated with damage, D_{ij}; a third internal variable associated with plasticity, ε_{ij}^p; and the temperature, θ, expressed in the following general form: $W = W\left(\varepsilon_{ij}, \varepsilon_{ij}^v, D_{ij}, \varepsilon_{ij}^p, \theta\right)$. In addition, the dissipation density, d, is defined as

$$d = \frac{\partial \psi}{\partial \dot{\varepsilon}_{ij}^v}\dot{\varepsilon}_{ij}^v + \frac{\partial \psi}{\partial \dot{D}_{ij}}\dot{D}_{ij} + \frac{\partial \psi}{\partial \dot{\varepsilon}_{ij}^p}\dot{\varepsilon}_{ij}^p \geq 0 \tag{5.7}$$

where, $\psi = \psi\left(\varepsilon_{ij}, \theta, \varepsilon_{ij}^v, \dot{\varepsilon}_{ij}^v, D_{ij}, \dot{D}_{ij}, \varepsilon_{ij}^p, \dot{\varepsilon}_{ij}^p\right)$ is a dissipation potential. Differentiating the Helmholtz free energy, W, with time we obtain

$$\dot{W} = \frac{\partial W}{\partial \varepsilon_{ij}}\dot{\varepsilon}_{ij} + \frac{\partial W}{\partial \varepsilon_{ij}^v}\dot{\varepsilon}_{ij}^v + \frac{\partial W}{\partial D_{ij}}\dot{D}_{ij} + \frac{\partial W}{\partial \varepsilon_{ij}^p}\dot{\varepsilon}_{ij}^p + \frac{\partial W}{\partial \theta}\dot{\theta} \tag{5.8}$$

Combining Eqs 5.6, 5.7 and 5.8, we obtain following

$$\left(\sigma_{ij}-\frac{\partial W}{\partial \varepsilon_{ij}}\right)\dot{\varepsilon}_{ij}-\left(\frac{\partial W}{\partial \varepsilon_{ij}^{v}}+\frac{\partial \psi}{\partial \dot{\varepsilon}_{ij}^{v}}\right)\dot{\varepsilon}_{ij}^{v}-\left(\frac{\partial W}{\partial D_{ij}}+\frac{\partial \psi}{\partial \dot{D}_{ij}}\right)\dot{D}_{ij}-\left(\frac{\partial W}{\partial \varepsilon_{ij}^{p}}+\frac{\partial \psi}{\partial \dot{\varepsilon}_{ij}^{p}}\right)\dot{\varepsilon}_{ij}^{p}-\left(\frac{\partial W}{\partial \theta}+S\right)\dot{\theta}=0 \tag{5.9}$$

For Eq. 9 to hold under all conditions, the following must be satisfied

$$\sigma_{ij}-\frac{\partial W}{\partial \varepsilon_{ij}}=0 \tag{5.10a}$$

$$\frac{\partial W}{\partial \varepsilon_{ij}^{v}}+\frac{\partial \psi}{\partial \dot{\varepsilon}_{ij}^{v}}=0 \tag{5.10b}$$

$$\frac{\partial W}{\partial D_{ij}}+\frac{\partial \psi}{\partial \dot{D}_{ij}}=0 \tag{5.10c}$$

$$\frac{\partial W}{\partial \dot{\varepsilon}_{ij}^{p}}+\frac{\partial \psi}{\partial \dot{\varepsilon}_{ij}^{p}}=0 \tag{5.10d}$$

$$\frac{\partial W}{\partial \theta}+S=0 \tag{5.10e}$$

Clearly, Eq. 10a provides the definition of the Cauchy stress as $\sigma_{ij}=\frac{\partial W}{\partial \varepsilon_{ij}}$, Eqs. 5.10b, 5.10c and 5.10d represent Ziegler's orthogonality conditions associated with viscous, damage and plastic behavior and Eq. 5.10e provides the relationship between free energy and entropy, *S*. In a purely phenomenological continuum approach, appropriate forms of free energy and dissipation would be formulated and further derivation performed to determine the constitutive relationship, the yield function, and damage and plastic potentials. Here we depart from this conventional approach and consider the granular system from its micro-scale (grain-scale).

5.2.2 Thermomechanical Formulation For Granular System

5.2.2.1 Kinematics of Granular Meso-Structure

When the external load is applied, the grains translate and rotate resulting in a relative displacement between the grains [80, 81]. Relative displacement δ_i between two nearest neighbor grains *n* and *p* ignoring the grain rotations is written as

$$\delta_i = u_i^p - u_i^n \tag{5.11}$$

Where, u_i is the particle displacement; superscripts refer to the interacting particles. The subscripts follow the tensor summation convention unless noted otherwise. To obtain the continuum description of this discrete model, we utilize the Taylor series expansion of the displacement such that the displacement of grain *p* may be written as:

$$u_i^p = u_i^n + u_{i,j}^n \left(x_j^p - x_j^n \right) \tag{5.12}$$

where, the point of expansion is chosen as the centroid of grain n. In Eq. 5.12, $u_{i,j}$ is the displacement gradient, and x_j^n and x_j^p are the position vectors to the centroid of grains *n* and *p*, respectively. Thus, the relative displacement, δ_i, between two nearest neighbor grains *n* and *p* representing the α-*th* inter-granular interaction is given by

$$\delta_i^\alpha = u_{i,j}^n \left(x_j^p - x_j^n \right) = u_{i,j}^n l_j^\alpha \tag{5.13}$$

The relative displacement, δ_i, between two grains may be decomposed into two components, (1) δ_n, along unit vector, n_i, defined in the direction of vector $l_j^\alpha = x_j^p - x_j^n$, termed as the normal direction, and (2) δ_w, orthogonal to vector, n_i, referred to as shear-direction. The relative displacement in the normal direction is given by, $\delta_n = \delta_i n_i$, and the relative displacement in the

shear-direction is given by, $\delta_w = \sqrt{(\delta_i s_i)^2 + (\delta_i t_i)^2}$, where unit vectors n_i, s_i and t_i form a local Cartesian coordinate system. The vectors s_i and t_i are arbitrarily chosen and lie on the plane perpendicular to the vector n_i, such that

$$\begin{aligned} n_i &= \langle \cos\theta, \sin\theta\cos\phi, \sin\theta\sin\phi \rangle \\ s_i &= \langle -\sin\theta, \cos\theta\cos\phi, \cos\theta\sin\phi \rangle \\ t_i &= \langle 0, -\sin\phi, \cos\phi \rangle \end{aligned} \tag{5.14}$$

where θ and ϕ are shown in the inset in Figure 5.6. For the rate dependent inter-granular behavior for the type of materials considered in this work, we further decompose the inter-granular displacement δ_j^α into a part that is purely elastic and a part that incorporates a viscous element as follows (in an analogy to a Zener element)

$$\delta_j^\alpha = \delta_j^{e\alpha} + \delta_j^{v\alpha} \tag{5.15}$$

Thus the normal and the shear inter-granular displacement can be written as $\delta_n^\alpha = \delta_n^{e\alpha} + \delta_n^{v\alpha}$ and $\delta_w^\alpha = \delta_w^{e\alpha} + \delta_w^{v\alpha}$, respectively.

5.2.2.2 Thermomechanics Equations For Granular System

We observe that for a granular system, the RVE free energy, dissipation potential and temperature may be defined in terms of the micro-scale quantities arising from the inter-granular interactions. Thus, the Helmholtz free energy density, W, and the dissipation potential, Ψ, can be written as follows:

$$W = \frac{1}{V}\sum_{\alpha}^{N} W^\alpha \left(\delta_j^\alpha, \delta_j^{v\alpha}, D_j^\alpha, \delta_j^{p\alpha}, \theta^\alpha\right) \tag{5.16a}$$

$$\psi = \frac{1}{V}\sum_{\alpha=1}^{N}\psi^{\alpha}\left(\delta_j^{\alpha}, \delta_j^{v\alpha}, \dot{\delta}_j^{v\alpha}, D_j^{\alpha}, \dot{D}_j^{\alpha}, \delta_j^{p\alpha}, \dot{\delta}_j^{p\alpha}, \theta^{\alpha}\right) \tag{5.16b}$$

where each inter-granular interactions have been counted only once such that N is the total number of inter-granular interactions, W^{α} and Ψ^{α} denote the contributions to free energy and dissipation potential, respectively, from the α-th inter-granular interaction, and δ_j^{α} is the inter-granular displacement vector defined in Eq. 5.11, $\delta_j^{v\alpha}$, D_j^{α} and $\delta_j^{p\alpha}$ are the internal variables associated with rate dependence, damage and plasticity respectively, of the inter-granular interactions, and the superimposed dot ($\dot{}$) denotes the time derivative.

Now, from Eqs. 5.10a and 5.16a we obtain the following relationship between the macro-scale Cauchy stress, σ_{ij}, of the RVE and the micro-scale grain interaction forces, f_j^{α}, using the chain rule of differentiation

$$\sigma_{ij} = \frac{\partial W}{\partial \varepsilon_{ij}} = \frac{1}{V}\sum_{\alpha=1}^{N} f_k^{\alpha}\frac{\partial \delta_k^{\alpha}}{\partial \varepsilon_{ij}} \qquad \text{where,} f_k^{\alpha} = \frac{\partial W^{\alpha}}{\partial \delta_k^{\alpha}} \tag{5.17}$$

A somewhat simpler form of similar expression for Cauchy stress tensor has been derived previously using alternative approaches (see Chang and Misra 1989 and more recently Magoirec 2010 etc), where a particular mean field relationship between inter-granular displacement vector and strain tensor has to be assumed. Further, by substituting Eqs. 5.16a and 5.16b into the Ziegler's orthogonality conditions given in Eqs. 5.10b-d, we obtain the following relations, where also the chain rule has been used:

$$\sum_{\alpha=1}^{N}\frac{\partial W^{\alpha}}{\partial \delta_k^{v\alpha}}\frac{\partial \delta_k^{v\alpha}}{\partial \varepsilon_{ij}^{v}} + \sum_{\alpha=1}^{N}\frac{\partial \psi^{\alpha}}{\partial \dot{\delta}_k^{v\alpha}}\frac{\partial \dot{\delta}_k^{v\alpha}}{\partial \dot{\varepsilon}_{ij}^{v}} = 0 \tag{5.18a}$$

$$\sum_{\alpha=1}^{N}\frac{\partial W^{\alpha}}{\partial D_k^{\alpha}}\frac{\partial D_k^{\alpha}}{\partial D_{ij}} + \sum_{\alpha=1}^{N}\frac{\partial \psi^{\alpha}}{\partial \dot{D}_k^{\alpha}}\frac{\partial \dot{D}_k^{\alpha}}{\partial \dot{D}_{ij}} = 0 \tag{5.18b}$$

$$\sum_{\alpha=1}^{N}\frac{\partial W^{\alpha}}{\partial \delta_k^{p\alpha}}\frac{\partial \delta_k^{p\alpha}}{\partial \varepsilon_{ij}^{p}}+\sum_{\alpha=1}^{N}\frac{\partial \psi^{\alpha}}{\partial \dot{\delta}_k^{p\alpha}}\frac{\partial \dot{\delta}_k^{p\alpha}}{\partial \dot{\varepsilon}_{ij}^{p}}=0 \tag{5.18c}$$

Similalry, the use of Eqs. 16a and 10e provides

$$\sum_{\alpha=1}^{N}\frac{\partial W^{\alpha}}{\partial \theta^{\alpha}}+\sum_{\alpha=1}^{N}S^{\alpha}=0 \tag{5.18d}$$

Considering Eq. 18 term-by-term, we can deduce the following form of micro-scale Clausius-Duhem type inequality for the α-th inter-granular interaction:

$$f_j^{\alpha}\dot{\delta}_j^{\alpha}-\dot{W}^{\alpha}-S^{\alpha}\dot{\theta}^{\alpha}=d^{\alpha}\geq 0 \tag{5.19}$$

where, $f_j^{\alpha},\delta_j^{\alpha}$ are the inter-granular force and displacements, W^{α}, S^{α}, d^{α} are the free energy, entropy, total dissipation respectively, contributed by the α-th inter-granular interaction. The dissipation potential, d^{α}, is defined as follows:

$$d^{\alpha}=\frac{\partial \psi^{\alpha}}{\partial \dot{\delta}_j^{v\alpha}}\dot{\delta}_j^{v\alpha}+\frac{\partial \psi^{\alpha}}{\partial \dot{D}_j^{\alpha}}\dot{D}_j^{\alpha}+\frac{\partial \psi^{\alpha}}{\partial \dot{\delta}_j^{p\alpha}}\delta_j^{p\alpha}\geq 0 \tag{5.20}$$

where ψ^{α} is the micro-scale dissipation potential. Now, differentiating free energy in Eq (16a) with time to obtain:

$$\dot{W}^{\alpha}=\frac{\partial W^{\alpha}}{\partial \delta_j^{\alpha}}\dot{\delta}_j^{\alpha}+\frac{\partial W^{\alpha}}{\partial \delta_j^{v\alpha}}\dot{\delta}_j^{v\alpha}+\frac{\partial W^{\alpha}}{\partial D_j^{\alpha}}\dot{D}_j^{\alpha}+\frac{\partial W^{\alpha}}{\partial \delta_j^{p\alpha}}\delta_j^{p\alpha} \tag{5.21}$$

and combining with Eqs. 5.19, 5.20 and 5.21, we obtain the following expression:

$$\left(f_j^{\alpha}-\frac{\partial W^{\alpha}}{\partial \delta_j^{\alpha}}\right)\dot{\delta}_j^{\alpha}-\left(\frac{\partial W^{\alpha}}{\partial \delta_j^{v\alpha}}+\frac{\partial \psi^{\alpha}}{\partial \dot{\delta}_j^{v\alpha}}\right)\dot{\delta}_j^{v\alpha}-\left(\frac{\partial W^{\alpha}}{\partial D_j^{\alpha}}+\frac{\partial \psi^{\alpha}}{\partial \dot{D}_j^{\alpha}}\right)\dot{D}_j^{\alpha}-\left(\frac{\partial W^{\alpha}}{\partial \delta_j^{v\alpha}}+\frac{\partial \psi^{\alpha}}{\partial \dot{\delta}_j^{p\alpha}}\right)\dot{\delta}_j^{p\alpha}-\left(\frac{\partial W^{\alpha}}{\partial \theta_j^{\alpha}}+S^{\alpha}\right)\dot{\theta}^{\alpha}=0 \tag{5.22}$$

which yields a set of following relations that are similar to Eqs. 10a to 10e but apply to inter-granular interactions:

$$f_j^{\alpha}=\frac{\partial W^{\alpha}}{\partial \delta_j^{\alpha}} \tag{5.23a}$$

$$\frac{\partial W^{\alpha}}{\partial \delta_j^{p\alpha}} + \frac{\partial \psi^{\alpha}}{\partial \dot{\delta}_j^{p\alpha}} = 0 \tag{5.23b}$$

$$\frac{\partial W^{\alpha}}{\partial D_j^{\alpha}} + \frac{\partial \psi^{\alpha}}{\partial \dot{D}_j^{\alpha}} = 0 \tag{5.23c}$$

$$\frac{\partial W^{\alpha}}{\partial \delta_j^{v\alpha}} + \frac{\partial \psi^{\alpha}}{\partial \dot{\delta}_j^{v\alpha}} = 0 \tag{5.23d}$$

$$S^{\alpha} = -\frac{\partial W^{\alpha}}{\partial \theta_j^{\alpha}} \tag{5.23e}$$

Eq. 5.23a defines the micro-scale quasi-conservative inter-granular force, f_j^{α}, Eqs. 5.23b, 5.23c and 5.23d serve as the micro-scale orthogonality conditions, and Eq. 5.23e gives the expression for the micro-scale entropy production at the α-th contact. For further discussion, we focus upon Eqs. 5.17, 5.18, and 5.23a-5.23d, and discard the temperature effects. We note however that Eqs. 5.18d and 5.23e are relevant to analysis of thermodynamic temperature which will be pursued separately.

5.2.3 Rate Dependent Inter-Granular Coupled Damage-Plasticity Relationships

The free energy and dissipative potential at the micro-scale for a rate dependent material with damage and plasticity can be conveniently written as follows in terms of the normal and shear components following the kinematic decomposition described in section 5.2.2.1

$$\begin{aligned} W^{\alpha} &= W_n^{\alpha} + W_w^{\alpha} \\ \psi^{\alpha} &= \psi_n^{\alpha} + \psi_w^{\alpha} \end{aligned} \tag{5.24}$$

The inter-granular free energy are assumed to take the following quadratic form split additively into a part associated with the purely elastic deformation and a part associated with the rate-dependent process that undergoes damage and plasticity

$$\begin{aligned} W_n^\alpha &= \frac{1}{2}E_1^\alpha\left(\delta_n^{e\alpha}\right)^2 + \frac{1}{2}E_n^\alpha\left(1-D_n^\alpha\right)\left(\delta_n^{v\alpha}\right)^2\left(1-\beta_n^\alpha\right) \\ W_w^\alpha &= \frac{1}{2}G_1^\alpha\left(\delta_w^{e\alpha}\right)^2 + \frac{1}{2}G_w^\alpha\left(1-D_w^\alpha\right)\left(\delta_w^{v\alpha}\right)^2\left(1-\beta_w^\alpha\right) \end{aligned} \tag{5.25}$$

here, β_n^α and β_w^α are constant non-dimensional plastic parameters defined as a proportion of $\delta_n^{v\alpha}$ and $\delta_w^{v\alpha}$, the inter-granular displacement associated with the viscous element, as follows

$$\beta_n^\alpha = \frac{\delta_n^{p\alpha}}{\delta_n^{v\alpha}}; \quad \beta_w^\alpha = \frac{\delta_w^{p\alpha}}{\delta_w^{v\alpha}} \tag{5.26}$$

where $\delta_n^{p\alpha}$ and $\delta_w^{p\alpha}$ are the inter-granular plastic displacements in normal and shear directions, respectively. We note the plastic parameters β_n^α and β_w^α take a value between 0 and 1, where a value of zero implies an absence of plastic dissipation and the dissipation is purely due to damage. On the other hand, a value of 1 will lead to the second term in Eq. 5.25 or the rate dependent process making no contribution to the free energy. Using the above equation, inter-granular free energy takes the following form:

$$\begin{aligned} W_n^\alpha &= \frac{1}{2}E_1^\alpha\left(\delta_n^{e\alpha}\right)^2 + \frac{1}{2}E_n^\alpha\left(1-D_n^\alpha\right)\delta_n^{v\alpha}\left(\delta_n^{v\alpha}-\delta_n^{p\alpha}\right) \\ W_w^\alpha &= \frac{1}{2}G_1^\alpha\left(\delta_w^{e\alpha}\right)^2 + \frac{1}{2}G_w^\alpha\left(1-D_w^\alpha\right)\delta_w^{v\alpha}\left(\delta_w^{v\alpha}-\delta_w^{p\alpha}\right) \end{aligned} \tag{5.27}$$

The inter-granular dissipation potential are taken as the sum of the viscous, damage and plastic dissipation in the following classical form [149]

$$\psi_n^\alpha = \frac{1}{2}\mu_n^\alpha \left(\dot{\delta}_n^{v\alpha}\right)^2 + Y_n^\alpha \left|\dot{D}_n^\alpha\right| + Z_n^\alpha \left|\dot{\delta}_n^{v\alpha}\right|$$
$$\psi_w^\alpha = \frac{1}{2}\mu_w^\alpha \left(\dot{\delta}_w^{v\alpha}\right)^2 + Y_w^\alpha \left|\dot{D}_w^\alpha\right| + Z_w^\alpha \left|\dot{\delta}_w^{v\alpha}\right| \tag{5.28}$$

where terms Y and Z denote a generalized forces that are conjugates of the inter-granular damage and plastic dissipation, respectively. In light of Eq. 5.26, it is useful to rewrite Eq. 5.28 by splitting the plastic dissipation potential as follows:

$$\psi_n^\alpha = \frac{1}{2}\mu_n^\alpha \left(\dot{\delta}_n^{v\alpha}\right)^2 + Y_n^\alpha \left|\dot{D}_n^\alpha\right| + Z_{1n}^\alpha \left|\dot{\delta}_n^{v\alpha}\right| + Z_{2n}^\alpha \left|\dot{\delta}_n^{p\alpha}\right|$$
$$\psi_w^\alpha = \frac{1}{2}\mu_w^\alpha \left(\dot{\delta}_w^{v\alpha}\right)^2 + Y_w^\alpha \left|\dot{D}_w^\alpha\right| + Z_{1w}^\alpha \left|\dot{\delta}_w^{v\alpha}\right| + Z_{2w}^\alpha \left|\dot{\delta}_w^{p\alpha}\right| \tag{5.29}$$

The grain-scale free energy and dissipation defined in the manner of Eqs. 5.25-5.29 represent a coupled damage and plasticity wherein the dissipation due to damage is partly independent and partly coupled with plasticity. Similar coupling has been proposed in the context of purely continuum modeling (see among others [122, 125, 150, 151]). We now apply the grain-scale orthogonality condition given in Eq 5.23b along with Eqs. 5.27 and 5.29 to obtain the 'dissipative force' dual of inter-granular plastic displacements $\delta_n^{p\alpha}$ and $\delta_w^{p\alpha}$ denoted by $\chi_n^{p\alpha}$ and $\chi_w^{p\alpha}$ as follows

$$\chi_n^\alpha = -\frac{\partial W^\alpha}{\partial \delta_n^{p\alpha}} = Z_{2n}^\alpha \text{sign}\left(\dot{\delta}_n^{p\alpha}\right); \quad \chi_w^\alpha = -\frac{\partial W^\alpha}{\partial \delta_w^{p\alpha}} = Z_{2w}^\alpha \text{sign}\left(\dot{\delta}_w^{p\alpha}\right) \tag{5.30a}$$

where

$$\chi_{2n}^\alpha = \frac{1}{2}E_n^\alpha \left(1 - D_n\right)\delta_n^{v\alpha}; \quad \chi_{2w}^\alpha = \frac{1}{2}G_w^\alpha \left(1 - D_w\right)\delta_w^{v\alpha} \tag{5.30b}$$

It is clear from Eq. 5.30a that the 'dissipative force' $\chi_n^{p\alpha}$ and $\chi_w^{p\alpha}$ should take the same sign as the rate of inter-granular plastic displacements, which implies that plastic displacement should

vanish during unloading, and that during loading, $Z_{2n}^{p\alpha} = \chi_n^{p\alpha}$ and $Z_{2w}^{p\alpha} = \chi_w^{p\alpha}$. It is a matter of straightforward algebra to show that

$$Z_{1n}^{\alpha} = \frac{1}{2} E_n \left(1 - D_n\right) \delta_n^{p\alpha}; \;\; Z_{2n}^{\alpha} = \frac{1}{2} E_n \left(1 - D_n\right) \delta_n^{v\alpha} \tag{5.31}$$

such that the dissipation potential in Eq. 29 reduces to that of the classical form given in Eq. 5.28, where

$$Z_n^{\alpha} = \beta_n^{\alpha} E_n \left(1 - D_n\right) \delta_n^{v\alpha}; \quad Z_w^{\alpha} = \beta_w^{\alpha} G_w \left(1 - D_w\right) \delta_w^{v\alpha} \tag{5.32}$$

Further, the application of the micro-scale orthogonality condition given in Eq. 5.23c, in combination with Eqs. 5.27 and 5.29, yields the micro-scale generalized force, *Y*, the dual of inter-granular damage *D* as follows

$$Y_n^{\alpha} = \frac{1}{2} E_n^{\alpha} \left(\delta_n^{v\alpha}\right)^2 \left(1 - \beta_n^{\alpha}\right); \quad Y_w^{\alpha} = \frac{1}{2} G_w^{\alpha} \left(\delta_w^{v\alpha}\right)^2 \left(1 - \beta_w^{\alpha}\right) \tag{5.33}$$

These expressions show that the generalized force is the undamaged elastic energy associated with the rate-dependent inter-granular process. Note that for simplicity, the terms that cross-link normal and shear components have been neglected and the response on the shear plane (*s*-*t* plane) is taken to be isotropic. We also find it noteworthy to comment that in the granular systems composed of many components possibilities of sinks that trap the macroscopic energy in microscopic (grain-scale) motions may be present as shown by [152-154]. Further in lattice models, dissipation due to rupture of elastic links are used for describing material damage [155-157]. Such losses are modeled in the approach presented here in a phenomenological sense using contact dissipation mechanism given by Eq. 5.29.

Now combining Eq. 5.23a with Eqs. 5.27 and 5.29, the inter-granular forces are obtained as follows

$$\begin{aligned} f_n^\alpha &= \frac{\partial W^\alpha}{\partial \delta_n^\alpha} = E_1^\alpha \left(\delta_n^\alpha - \delta_n^{v\alpha}\right) \\ f_w^\alpha &= \frac{\partial W^\alpha}{\partial \delta_w^\alpha} = G_1^\alpha \left(\delta_w^\alpha - \delta_w^{v\alpha}\right) \end{aligned} \tag{5.34}$$

Finally, using the grain-scale orthogonality condition in Eq. 5.23d, we can find the grain-scale constitutive relationships during loading as follows:

$$\begin{aligned} &-E_1^\alpha \left(\delta_n^\alpha - \delta_n^{v\alpha}\right) + E_n^\alpha \delta_n^{v\alpha} \left(1 - D_n^\alpha\right) - \frac{1}{2} E_n^\alpha \delta_n^{p\alpha} \left(1 - D_n^\alpha\right) + \mu_n^\alpha \dot{\delta}_n^{v\alpha} + Z_{1n}^\alpha = 0 \\ &-G_1^\alpha \left(\delta_w^\alpha - \delta_w^{v\alpha}\right) + G_w^\alpha \delta_w^{v\alpha} \left(1 - D_w^\alpha\right) - \frac{1}{2} G_w^\alpha \delta_w^{p\alpha} \left(1 - D_w^\alpha\right) + \mu_w^\alpha \dot{\delta}_w^{v\alpha} + Z_{1w}^\alpha = 0 \end{aligned} \tag{5.35}$$

Combining Eqs. 31, 34 and 35 we arrive at the following inter-granular constitutive relationships

$$\begin{aligned} f_n^\alpha &= K_n^\alpha \delta_n^\alpha + \eta_n^\alpha \dot{\delta}_n^\alpha - \zeta_n^\alpha \dot{f}_n^\alpha \\ f_w^\alpha &= K_w^\alpha \delta_w^\alpha + \eta_w^\alpha \dot{\delta}_w^\alpha - \zeta_w^\alpha \dot{f}_w^\alpha \end{aligned} \tag{5.36}$$

where K, η and ζ can be interpreted as the inter-granular stiffness, viscosity, and relaxation parameters, respectively given as

$$\begin{aligned} K_n^\alpha &= \frac{E_1^\alpha E_n^\alpha \left(1 - D_n^\alpha\right)}{E_1^\alpha + E_n^\alpha \left(1 - D_n^\alpha\right)};\ \eta_n^\alpha = \frac{E_1^\alpha \mu_n^\alpha}{E_1^\alpha + E_n^\alpha \left(1 - D_n^\alpha\right)};\ \zeta_n^\alpha = \frac{\mu_n^\alpha}{E_1^\alpha + E_n^\alpha \left(1 - D_n^\alpha\right)}; \\ K_w^\alpha &= \frac{G_1^\alpha G_n^\alpha \left(1 - D_w^\alpha\right)}{G_1^\alpha + G_n^\alpha \left(1 - D_w^\alpha\right)};\ \eta_w^\alpha = \frac{G_1^\alpha \mu_w^\alpha}{G_1^\alpha + G_n^\alpha \left(1 - D_w^\alpha\right)};\ \zeta_w^\alpha = \frac{\mu_w^\alpha}{G_1^\alpha + G_n^\alpha \left(1 - D_w^\alpha\right)} \end{aligned} \tag{5.37}$$

Eq. 36 can also be written in an alternate form

$$\begin{aligned} f_n^\alpha &= K_n^\alpha \left(\delta_n^\alpha - \delta_n^{p\alpha}\right) + \tau_{n\delta}^\alpha K_n^\alpha \dot{\delta}_n^\alpha - \tau_{nf}^\alpha \dot{f}_n^\alpha \\ f_w^\alpha &= K_w^\alpha \left(\delta_w^\alpha - \delta_w^{p\alpha}\right) + \tau_{w\delta}^\alpha K_w^\alpha \dot{\delta}_w^\alpha - \tau_{wf}^\alpha \dot{f}_w^\alpha \end{aligned} \tag{5.38}$$

where $\tau_{n\delta}$ and $\tau_{w\delta}$ are the retardation times, and τ_{nf} and τ_{wf} is the relaxation times given as follows:

$$\tau_{n\delta}^{\alpha}=\frac{\mu_n^{\alpha}}{E_n^{\alpha}\left(1-D_n^{\alpha}\right)};\ \tau_{nf}^{\alpha}=\frac{\mu_n^{\alpha}}{E_1^{\alpha}+E_n^{\alpha}\left(1-D_n^{\alpha}\right)};$$
$$\tau_{w\delta}^{\alpha}=\frac{\mu_w^{\alpha}}{G_n^{\alpha}\left(1-D_w^{\alpha}\right)};\ \tau_{wf}^{\alpha}=\frac{\mu_w^{\alpha}}{G_1^{\alpha}+G_n^{\alpha}\left(1-D_w^{\alpha}\right)} \tag{5.39}$$

It is clear from Eqs. 5.36-5.39 that the assumed form of inter-granular free energy and dissipation potential lead to a three-parameter nonlinear inter-granular constitutive law of Zener solid-type. Other types of micro-scale laws can be introduced that are valid for materials such as granular soils [141] and polyurea [158]. Furthermore, the micro-scale laws derived here can serve for modeling rate-dependent damage and plasticity of octet-truss lattices discussed in [159].

5.2.4 Inter-Granular Loading-Unloading Criterion

To complete the inter-granular constitutive relationships for coupled damage-plasticity, we introduce the following criterion for unloading and reloading [160], utilizing inter-granular yield criterion F_n^{α} and F_w^{α}, defined independently for the normal and shear directions as:

$$F_n^{\alpha}=F_n^{\alpha}\left(\delta_n^{v\alpha},\delta_n^{p\alpha},D_n^{\alpha}\right)=0;\ \text{ and }\ F_w^{\alpha}=F_w^{\alpha}\left(\delta_w^{v\alpha},\delta_w^{p\alpha},D_w^{\alpha}\right)=0 \tag{5.40}$$

The loading, unloading and reloading conditions at the inter-granular scale can now be described as follows:

(1) Loading – $F_n^{\alpha}=0,$ and $\dot{\delta}_n^{v\alpha}>0,$ and $F_w^{\alpha}=0,$ and $\dot{\delta}_w^{v\alpha}>0$.

(2) Unloading – $F_n^{\alpha}<0,$ and $\dot{\delta}_n^{v\alpha}<0,$ and $F_w^{\alpha}<0,$ and $\dot{\delta}_w^{v\alpha}<0$.

(1) Reloading – $F_n^{\alpha}<0,$ and $\dot{\delta}_n^{v\alpha}>0,$ and $F_w^{\alpha}<0,$ and $\dot{\delta}_w^{v\alpha}>0$.

In this case the inter-granular flow rule can also be defined to obtain the inter-granular 'dissipative forces' $\chi_n^{p\alpha}$ and $\chi_w^{p\alpha}$ as follows

$$\chi_n^{p\alpha} = \lambda_n^{p\alpha} \frac{\partial F_n^{\alpha}}{\partial \delta_n^{p\alpha}}; \quad \chi_w^{p\alpha} = \lambda_w^{p\alpha} \frac{\partial F_w^{\alpha}}{\partial \delta_w^{p\alpha}} \tag{5.41}$$

where λ_n^{α} and λ_w^{α} are plastic the multipliers. The yield criteria can be obtained from the plastic dissipation defined previously which gives

$$\begin{aligned} F_n^{\alpha} &= \frac{1}{2} E_n^{\alpha} \beta_n^{\alpha} \left[\left(1 - D_n^{\alpha}\right) \left(\delta_n^{v\alpha}\right)^2 - \left(1 - {}^{\max}D_n^{\alpha}\right) \left({}^{\max}\delta_n^{v\alpha}\right)^2 \right] = 0; \\ F_w^{\alpha} &= \frac{1}{2} G_w^{\alpha} \beta_w^{\alpha} \left[\left(1 - D_w^{\alpha}\right) \left(\delta_w^{v\alpha}\right)^2 - \left(1 - {}^{\max}D_w^{\alpha}\right) \left({}^{\max}\delta_w^{v\alpha}\right)^2 \right] = 0 \end{aligned} \tag{5.42}$$

where the left superscript ‘max’ denoted the maximum accumulated values of the corresponding quantities. We can see that introducing Eqs. 5.42 and 5.26 into 5.41, we will find the ‘dissipative forces’ $\chi_n^{p\alpha}$ and $\chi_w^{p\alpha}$ to be same as obtained in Eq. 5.30. During unloading and reloading, the dissipation vanishes, therefore, the multipliers λ_n^{α} and λ_w^{α} takes a value of zero, while they take a value 1 during loading. As usual, the plastic potential F_n^{α} and F_w^{α} satisfy the Karush-Kuhn-Tucker (KKT) type conditions of complementarity and consistency stated as

$$\begin{aligned} F_n^{\alpha} \lambda_n^{\alpha} = 0 \text{ and } \dot{F}_n^{\alpha} \lambda_n^{\alpha} = 0 \\ F_w^{\alpha} \lambda_w^{\alpha} = 0 \text{ and } \dot{F}_w^{\alpha} \lambda_w^{\alpha} = 0 \end{aligned} \tag{5.43}$$

Further, the grain-scale constitutive relationships during unloading process can be derived as follows:

$$\begin{aligned} f_n^{\alpha} &= K_n^{u\alpha} \left(\delta_n^{\alpha} - \beta_n^{\alpha}\, {}^{\max}\delta_n^{v\alpha}\right) + \eta_n^{u\alpha} \dot{\delta}_n^{\alpha} - \zeta_n^{u\alpha} \dot{f}_n^{\alpha} \\ f_w^{\alpha} &= K_w^{u\alpha} \left(\delta_w^{\alpha} - \beta_w^{\alpha}\, {}^{\max}\delta_w^{v\alpha}\right) + \eta_w^{u\alpha} \dot{\delta}_w^{\alpha} - \zeta_w^{u\alpha} \dot{f}_w^{\alpha} \end{aligned} \tag{5.44}$$

where K^u, η^u and ζ^u are the unloading inter-granular stiffness, viscosity, and relaxation parameters, respectively given as

$$K_n^{u\alpha} = \frac{E_1^\alpha E_n^{u\alpha}}{E_1^\alpha + E_n^{u\alpha}};\ \eta_n^{u\alpha} = \frac{E_1^\alpha \mu_n^\alpha}{E_1^\alpha + E_n^{u\alpha}};\ \zeta_n^{u\alpha} = \frac{\mu_n^\alpha}{E_1^\alpha + E_n^{u\alpha}};$$
$$K_w^{u\alpha} = \frac{G_1^\alpha G_w^{u\alpha}}{G_1^\alpha + G_w^{u\alpha}};\ \eta_w^{u\alpha} = \frac{G_1^\alpha \mu_w^\alpha}{G_1^\alpha + G_w^{u\alpha}};\ \zeta_w^{u\alpha} = \frac{\mu_w^\alpha}{G_1^\alpha + G_w^{u\alpha}} \tag{5.45}$$

here, $E_n^{u\alpha} = \frac{E_n^\alpha \left(1 - {}^{\max} D_n^\alpha\right)}{\left(1 - \beta_n^\alpha\right)}$; and $G_w^{u\alpha} = \frac{G_w^\alpha \left(1 - {}^{\max} D_w^\alpha\right)}{\left(1 - \beta_w^\alpha\right)}$.

5.2.5 Constitutive Relationship For Granular Systems

The constitutive relationship for an RVE of a granular system can now be obtained by introducing Eq. 5.36 into Eq. 5.17 and using Eq. 5.13 as follows

$$\sigma_{ij} = \frac{1}{V}\sum_{\alpha=1}^{N} f_k^\alpha l_l^\alpha \frac{\partial \varepsilon_{kl}^n}{\partial \varepsilon_{ij}} \qquad \text{where } \varepsilon_{kl}^n = u_{(k,l)}^n \tag{5.46}$$

in which strain ε_{kl} is the symmetric part of the displacement gradient. It is clear a relationship between grain-scale strain and the overall RVE strain are necessary for further simplification. We note that the relationship of grain-scale kinematics in terms of the overall RVE scale strains is, in general, complex for random granular materials as discussed in [81, 161]. Moreover for materials with ill-defined random structure, wide-ranging, often unrealistic, assumptions have to be made to simulate some "reasonable" microstructure, which have to be analyzed to determine these micro-macro relationships. In light of this difficulty, the mean field assumption, albeit approximate, provides a feasible approach for the derivation of the RVE constitutive law and has been shown to describe a number of phenomena exhibited by granular materials [63, 71, 80]. In this case, the average stress tensor of an RVE given by Eq. 5.46 is simplified to:

$$\sigma_{ij} = \frac{1}{V}\sum_{\alpha=1}^{N} f_i^\alpha l_j^\alpha \tag{5.47}$$

which is a widely used expression for Cauchy stress tensor in granular mechanics (see for example [90, 162]). The stress defined in this way is also traced to the virial of Clausius [163, 164], has counterparts in the statistical mechanics of fluids [165, 166] and has been a subject of recent discussion in the context of molecular and atomistic modeling [167, 168]. For sufficiently large RVE containing variously oriented inter-granular interactions, the summation in Eq. 5.47 can be approximated by the following integral under certain simplifying assumptions [63, 90, 162]

$$\sigma_{ij} = Nl \int_0^{2\pi} \int_0^{\pi} f_j(\theta,\phi) n_i(\theta,\phi) \xi(\theta,\phi) \sin\theta d\theta d\phi \tag{5.48}$$

where N is the number density of pair interactions, l is the average grain size, n_i is a unit vector expressed in terms of the spherical coordinates (θ,ϕ), and $\xi(\theta,\phi)$ is a directional probability density function such that the product $N\xi(\theta,\phi)\sin\theta d\theta d\phi$ gives the number density of pair interactions in the solid angle $\sin\theta d\theta d\phi$. For convenience, we incorporate the factor Nl with the force, f_j, such that it is expressed as a traction and normalize the relative displacement, δ_i, with l. The units of the stiffness and viscosity in Eq. 5.37 and 5.45 are appropriately modified. Now, by combining Eqs. 5.36 and 5.48, the following differential form of rate constitutive relationship can be obtained

$$\sigma_{ij} = \int_0^{2\pi} \int_0^{\pi} \left(K_{jk} n_l \varepsilon_{kl} + \eta_{jk} n_l \dot{\varepsilon}_{kl} + \zeta_{jk} \dot{f}_k \right) n_i \xi(\theta,\phi) \sin\theta d\theta d\phi \tag{5.49}$$

where the inter-granular stiffness, viscosity, and relaxation tensors are given as

$$\begin{aligned} K_{ij}(t) &= K_n(t) n_i n_j + K_w(t)\left(s_i s_j + t_i t_j\right) \\ \eta_{ij}(t) &= \eta_n(t) n_i n_j + \eta_w(t)\left(s_i s_j + t_i t_j\right) \\ \zeta_{ij}(t) &= \zeta_n(t) n_i n_j + \zeta_w(t)\left(s_i s_j + t_i t_j\right) \end{aligned} \tag{5.50}$$

The specific form inter-granular damage functions are given in Eq 4.19 in chapter 4 and numerical implementation of the obtain constitutive model is described in sections 4.3 of chapter 4

5.3 Results and Discussion

The derived coupled damage-plasticity granular micromechanics model is numerically evaluated by comparison with experimental creep-recovery response to assess its applicability. In the subsequent discussion we present comparison with experimental results for creep-recovery behavior under compressive and tensile stress at different load and unload times. We then discuss the advantages that this type of model provides by investigating how the inter-granular elastic and dissipative energies as well as damage and plastic displacement evolve during the creep-recovery process.

5.3.1 Experimental Verification And Model Predictions

The developed material model is verified by comparing the model predictions with the experimental creep-recovery data at different load and unload times for hot-mix asphalt (HMA) concrete under uniaxial unconfined compressive and tensile stress at a constant temperature of 20 ^{o}C [7]. We then utilize the developed model to investigate the elastic and the dissipated energies as well as the anisotropic evolution of damage and plasticity in creep-recovery tests.

5.3.1.1 Calibration and Identification of Model Parameters

The model is calibrated using the experimental creep and creep-recovery data under compressive uniaxial stress σ_{11}=1.0 MPa ($\sigma_{22}=\sigma_{33}$=0) and tensile creep data at stress σ_{11}=0.3 MPa ($\sigma_{22}=\sigma_{33}$=0). First, the normal and shear stiffness and viscosity parameters E_1, G_1, G_w, E_n, μ_n and μ_w, were obtained by assuming $B_n=B_w=\beta=\infty$ and fitting the reduced equation to the initial portion of the experimental creep curve. Thereafter, damage parameters B_n, B_w and β were introduced into the model and optimized to match the complete creep response curve. Further, normal and shear plastic parameters β_n and β_w were identified to match the creep recovery curve at 1.0MPa in compression for a load time of 40 sec. To account for the asymmetric inter-granular behavior under tension and compression, parameter α_n and α_w were included in the model and identified using the tensile creep data at 0.3MPa stress amplitude. The following model parameters were found: $G_1=0.8E_1$, $G_w=E_n$, $\mu_n=\mu_w$, and $B_n=B_w=14.3\text{x}10^{-3}$, $\beta_n=\beta_w$ and $\alpha_n=\alpha_w$ where, E_1 =2.4 GPa, E_n= 0.3 GPa, $\tau_{n\delta}(0)$=57s, $\tau_{nf}(0)$=6.33s and β= 3.8, $\beta_n=\beta_w$=0.833, and $\alpha_n=\alpha_w$=0.175. The experimental and calibrated creep curves under uniaxial compressive and tensile loads for HMA are shown in Figure 5-1. Clearly, the model is able to replicate the primary, secondary and tertiary creep behavior as shown by the close agreement of the calibration and experimental curves at σ_{11}=1.0 MPa and σ_{11}=0.3 MPa for compressive and tensile loads respectively. Furthermore, after the identification of inter-granular plasticity parameter model is also able to accurately capture the creep-recovery response shown by HMA under 1.0MPa compressive stress.

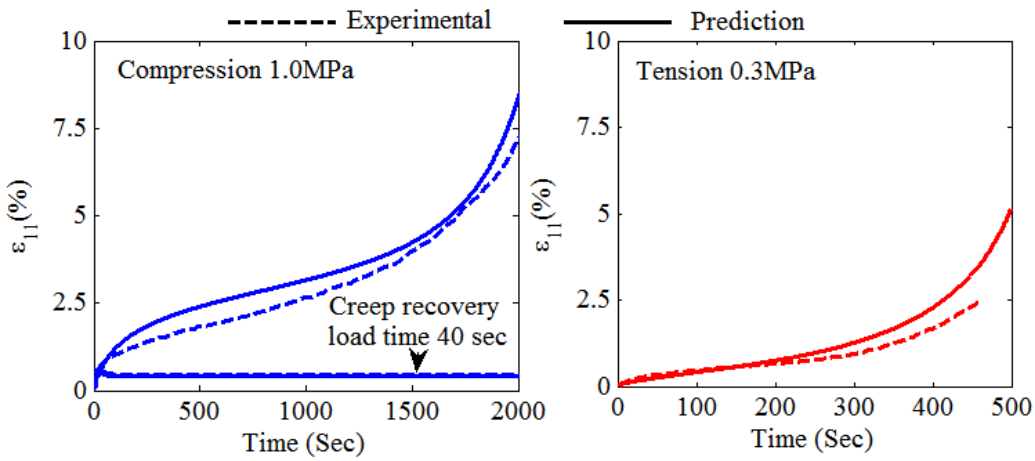

Figure 5-1: Experimental and model predicted creep curves under uniaxial compressive and tensile stress used for model parameter identification

5.3.1.2 Creep-recovery behavior

Under practical applications HMA experiences repeated cyclic load imposed by traffic on the roadway. Therefore it is useful to compare the model prediction with the experimental data under repeated loads. In this work model predictions are compared with creep-recovery response of HMA under uniaxial compressive and tensile stresses of 1.0MPa and 0.3MPa respectively under following three different load-unload sequences formed of different load-times (LT) and unload-times (UT), case 1: LT=120 sec, UT=100 sec, case 2: LT=60 sec, UT=100 sec, and case 3: LT=120 sec and UT=1500 sec.

The predicted and experimental creep curve under uniaxial compressive load of 1.0MPa at three load sequences is given in Figure 5-2. From Figure 5-2a we observe that in case 1 when LT is 120 sec and UT is 100 sec, model predictions are in close agreement with the experimental data. Not only model predicts both the failure-time and failure-strain correctly but also the amount of plastic or residual strain at the end of each creep-recovery cycle. When the load time is decreased to 60 sec in case 2, as expected, HMA samples suffer smaller strain at any given

time compared to LT of 120 sec as shown in Figure 5-2b. The model is able to closely match the creep-recovery response for the first 7 cycles. The model prediction and experimental data diverges beyond 7 cycles with the experimental response showing accelerated creep and sudden failure, whereas model indicates a more gradual increase in creep with a delayed failure. Since the LT is half of that in case 1, the sample undergoes smaller damage and accumulates smaller plastic strain, as the sample is well within its primary creep stage. For case 3 in which when LT is 60 sec but UT is increased to 1500 sec, results are presented in Figure 5-2c. In this case model predictions agree relatively well for the first 11 cycles. Beyond that, the predictions appear to be within the secondary creep regime, that is, the strains during every subsequent creep-recovery cycles increase gradually. The predictions do not show the accelerating trend exhibited by the experimental data. The predicted response is expected since the large UT provides sufficient time for the elastic recovery. We also note that the material response at such large length of time can be sensitive to small material variability.

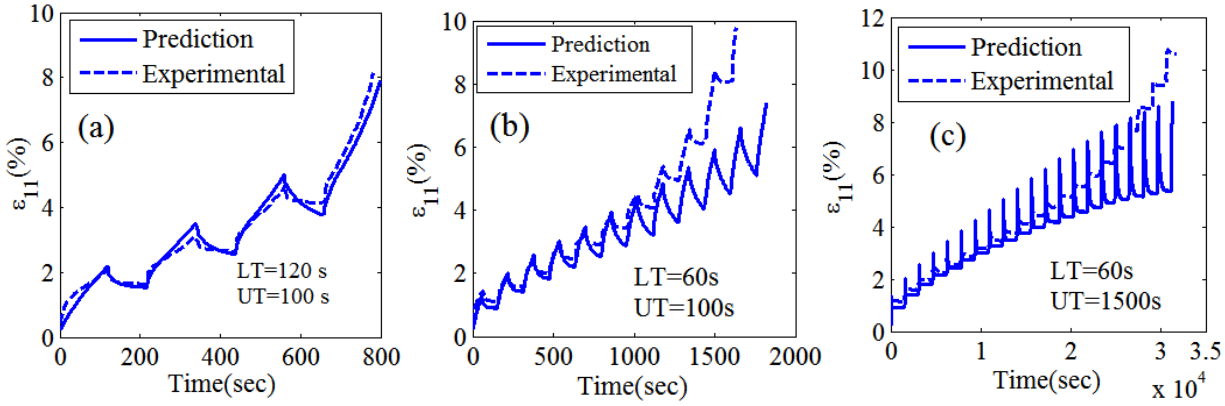

Figure 5-2: Comparison of predicted and experimental multi-cycle creep-recovery reponse under uniaxial unconfined compressive stress of 1.0 MPa: (a) load time =120s and unload time =100s , (b) load time =60s and unload time =100s and (c) load time =60s and unload time =1500s

The model capabilities to capture the asymmetric compression-tension behavior is shown in Figure 5-3, which gives the comparison of model prediction and experimental data for creep-recovery behavior under 0.30MPa tensile stress for the three different load-unload sequences. We observe from Figure 5-3a that the case 1 model predictions match very closely with the experimental data and predict both the failure-time and strain correctly. For case 2, in which the LT is decreased to 60 sec, the model prediction is close for the first 10 cycles. In the subsequent cycles, the model predicts accelerated creep strains reaching failure at a higher strain albeit similar time as that observed in the experiment. For case 3, we observe a much larger discrepancy between the model predictions and the experiments. Although the trends are captured well, the creep strains appear to be larger and recovery much smaller in the experiments than those in the predictions.

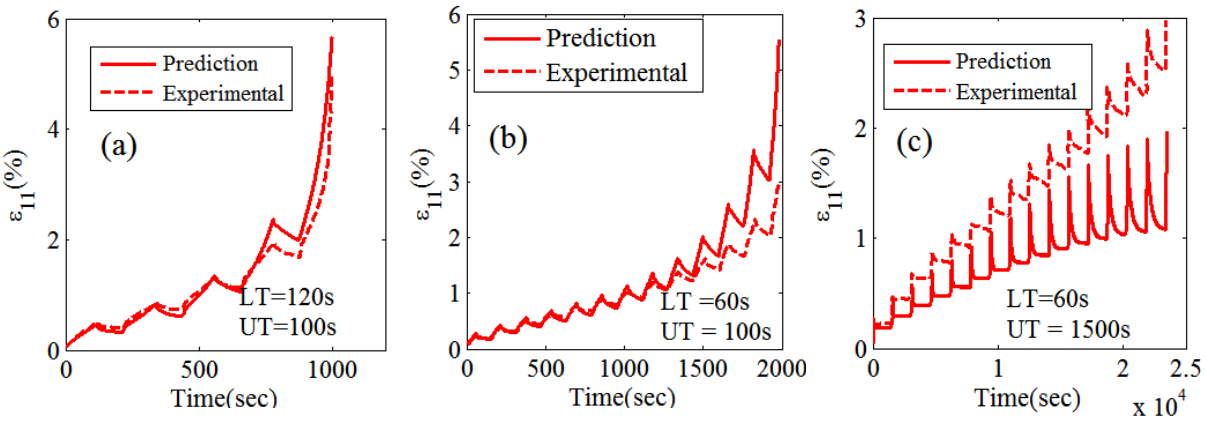

Figure 5-3: Predicted and experimental multi-cylce creep-recovery reponse under uniaxial unconfined compressive stress of 0.3 MPa: (a) load time =120s and unload time =100s , (b) load time =60s and unload time =100s and (c) load time =60s and unload time =1500s

5.3.1.3 Elastic and Dissipation Energies in Creep-Recovery

To understand the dissipation behavior during creep-recovery process, we have investigated the elastic energies, and the viscous, damage and plastic dissipation for case 1 loading sequence.

Figures 5-4a and 5-4b show the evolution of the elastic energy, and the viscous, damage and plastic dissipation for the multiple creep-recovery cycles. We observe from Figure 5-4 that the damage and plastic energies remain constant during recovery, which is expected since damage and plastic dissipation are assumed to vanish during unloading. During each subsequent creep cycles, the elastic energy becomes proportionally smaller compared do the dissipative energies. As the sample enters a tertiary creep regime accompanied by accelerating creep deformation, the viscous dissipation increases rapidly, although, both damage and plastic dissipation increase as well.

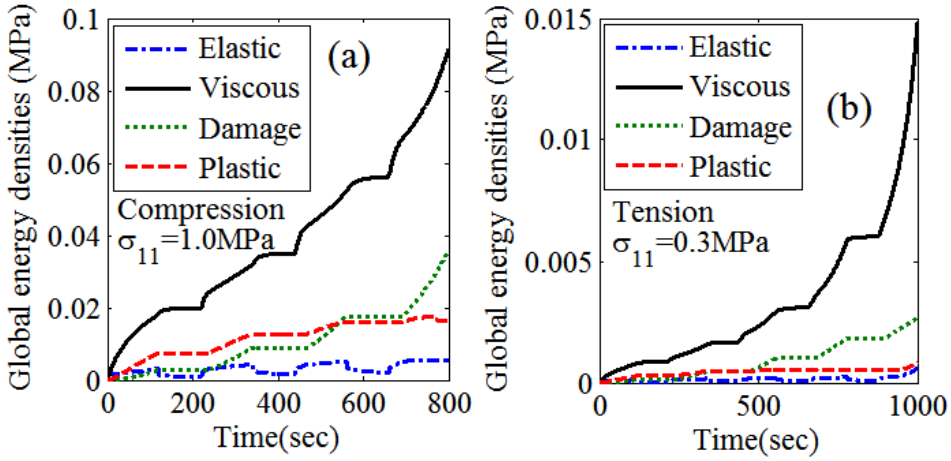

Figure 5-4: Predicted evolution of macro-scale energy densities for the creep-recovery responses showin Figures 2a and 3a

In Figures 5-5a and 5-5b, we show the creep-recovery curve as well as the evolution of energy densities for the first cycle of creep-recovery loading sequence for case 1. We particularly highlight the effect of plasticity on both the creep-recovery and the energy density evolution behavior by considering two scenarios (1) with only damage, and (2) with coupled damage and plasticity. We observed from Figure 5-5a that as expected when only damage is included material tends to recover to the un-deformed state, however when the plasticity is included the

material recovers to a significant residual strain. Figure 5-5b shows the corresponding evolution of energy densities with time. As the loading is applied, the elastic energy, which is the recoverable work at a given time if the applied stress is removed, shows a jump corresponding to the sudden application of creep load. As creep progresses, the viscous dissipation increases proportional to the creep rate while the dissipation due to damage and plasticity increase as a function of the creep deformation. In the model adopted in this work, the dissipation due to damage is independent from that due to plasticity and does not change in the absence of plasticity. However, in absence of plasticity, the elastic energy at any time is expectedly larger. Once the stress is removed at 120 sec and material is allowed to recover, the elastic energy decreases with time through viscous dissipation as seen from Figure 5-5b.

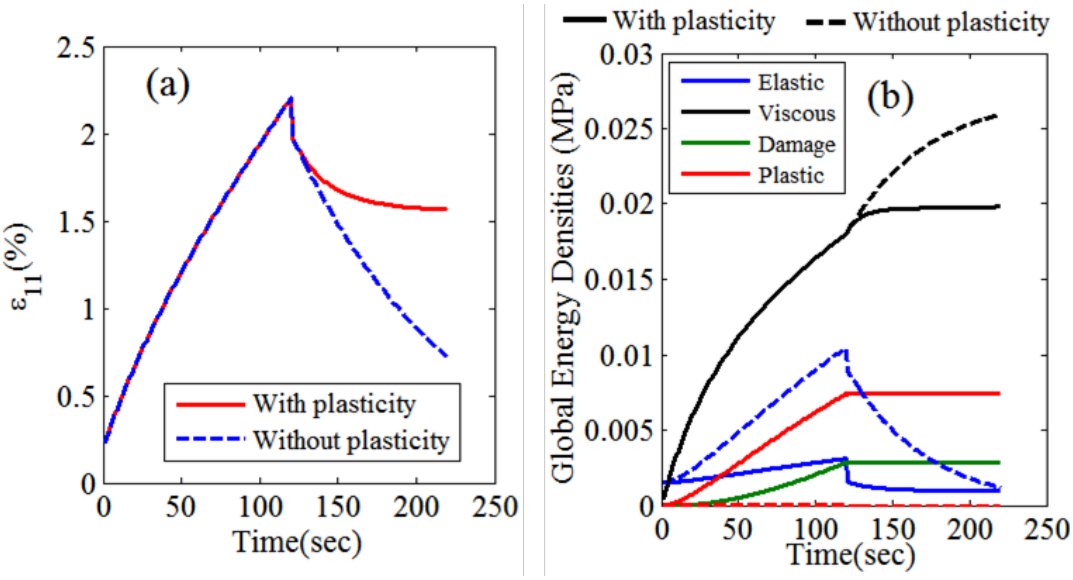

Figure 5-5: Predicted single-cycle creep-recovery response under uniaxial unconfined compressive stress of 1.0 MPa for materials with damage only (dashed curve) and materials with coupled damage and plasticity (solid curve). (b) Predicted evolution of macro-scale energy densities

During uniaxial creep-recovery, damage evolution in the materials is expected to be anisotropic depending upon the loading direction. To illustrate, how anisotropic damage develops, it is useful to examine the evolution of inter-granular energy densities and damage. Figure 5-6 shows

the inter-granular energy densities in selected orientations as function of time corresponding to the creep-recovery curves in Figure 5-5a. Since the loading is axisymmetric, the inter-granular energy densities are independent of azimuthal angle, ϕ. Thus, each curve in Figure 5-6 refers to θ measured with respect to the loading direction-1 (see inset Figure 5-6). From Figure 5-6 we can see that the inter-granular elastic energies, and viscous, damage and plastic dissipation evolve with time differently in the various directions.

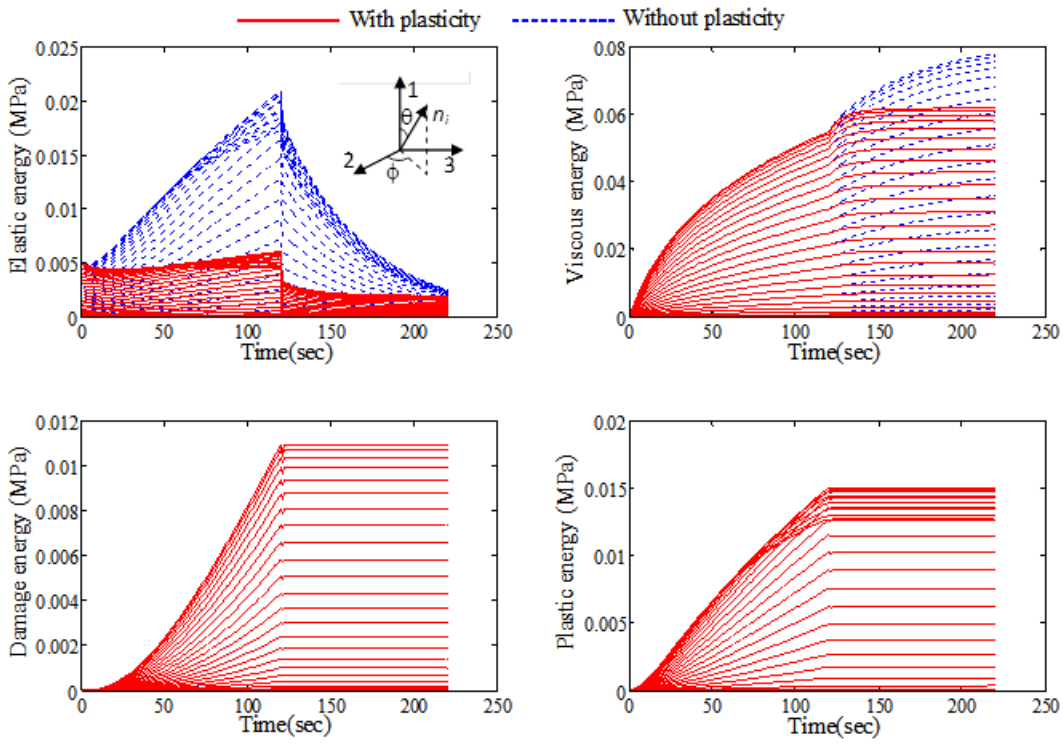

Figure 5-6: Predicted evolution of inter-granular (micro-scale) energy densities with time for the creep-recovery response shown in Figure 5

For further elucidating the relationship of this evolution with loading direction, polar diagrams are given in Figure 5-7 that show the normalized inter-granular energy densities in θ-coordinate at selected times. The normalization is done with respect to the total energy in a given orientation at any given time, such that the normalized elastic energy, the viscous, the damage

and the plastic dissipation densities, denoted by r_e, r_v, r_d and r_p respectively, sum to unity ($r_e + r_v + r_d + r_p = 1$). For the case when only damage is included, r_p is zero. Also, the evolution of inter-granular damage (D_n and D_w,) and normalized plastic displacement ($\delta_n^{p\alpha}$ and $\delta_w^{p\alpha}$ normalized with respect to the largest plastic displacement at the end of creep) in the normal and shear directions, respectively, are plotted as polar diagrams at selected times in Figure 5-8.

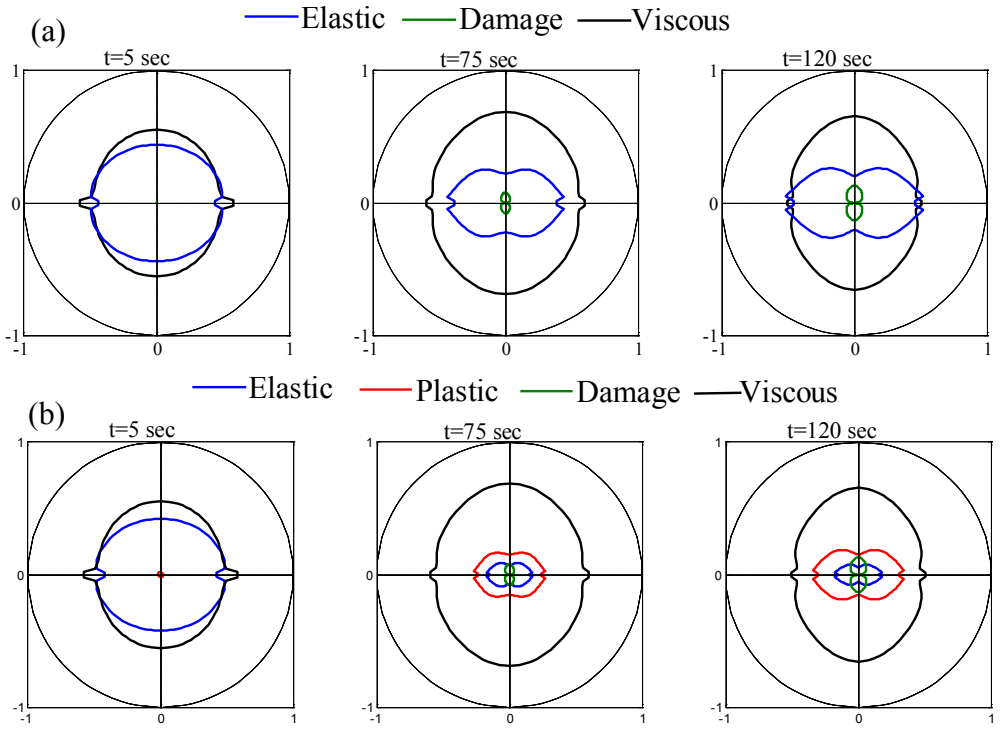

Figure 5-7: Polar plots of inter-granular (micro-scale) energy densities fractions at selected times corresponding to the creep response in Figure 5.

As the loading commences at time *t=0*, the elastic energy fraction r_e is unity due to sudden loading and viscous, damage and plastic energies fractions are zero as seen in Figures 5-6 and 5-7. As material undergoes creep deformation, the proportions of elastic energies decrease while that of the viscous, damage and plastic (when included) dissipation increases, however in different ratios in the different directions. Initially at *t=5s*, which is a small fraction of the initial

inter-granular retardation time of 57s, the elastic energy and viscous dissipation are in approximately same proportion in all orientations while both the damage and plastic dissipation is negligibly small. As creep deformation progresses, the proportion of damage and plastic dissipation increases with maximum being in the direction of loading. However, in the orientations orthogonal to loading direction, the proportion of elastic energy remains significantly larger. Beyond the characteristic time of 57sec, the proportion of available elastic energy begins to reduce while damage and plastic dissipation increases in all directions, however, in a characteristically orientation dependent manner. Moreover, a comparison of Figures 5-7a and 5-7b at t=75 sec shows that in the presence of plastic dissipation the elastic energy is smaller than the case when only damage is present. Clearly at the end of creep at t=12 sec, the plastic dissipation has a significant contribution especially in directions with larger inclination to the loading direction. The concomitant anisotropic development of damage and plastic displacement is seen clearly from the inter-granular damage and plasticity in normal and shear direction shown in Figure 5-8. These results indicate that the materials undergoing loading-unloading cycles with fixed stress amplitude will progressively develop induced anisotropy. Such effects that manifest due to granular nature of materials are not easily represented by phenomenological constitutive relationships based upon the concepts of traditional Cauchy mechanics or tensorial damage functions.

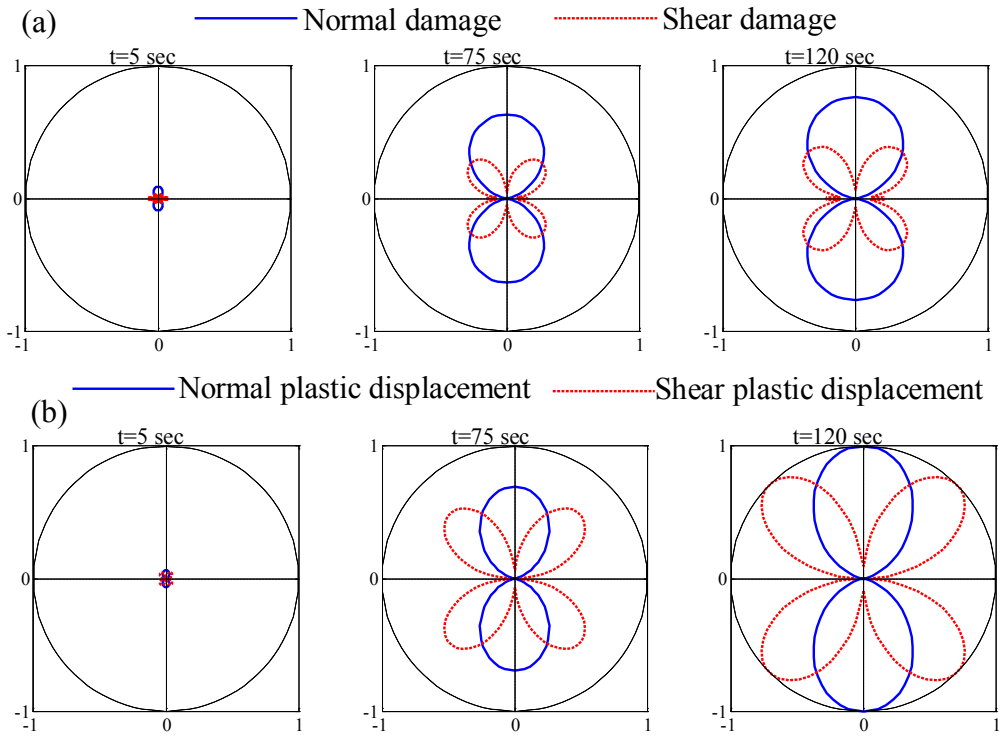

Figure 5-8: Polar plots of inter-granular normal and shear direction (a) damage and (b) normalized plastic displacement at selected times corresponding to the creep response in Figure 5

5.3.1.4 Monotonic Behavior

The monotonic behavior is investigated for uniaxial unconfined constant strain-rate loading applied as follows: $\varepsilon_{11}=\varepsilon_0 t$, and lateral stress, $\sigma_{22}=\sigma_{33}=0$. Here we demonstrate the effect of strain rates, ε_0, upon the evolution of energy densities and damage with loading. For our illustrative calculations we utilize an initial retardation time $\tau_{n\delta}(0)=5.7$s, and use all other model parameters same as that used for creep predictions. For the smaller initial retardation time, the effect of damage on the overall stress-strain behavior is significant at the strain rates for which

the simulation have been performed.. Predicted stress-strain curves for strain rates of ε_0=0.0025/sec and ε_0=0.0005/sec are given in Figure 5-9.

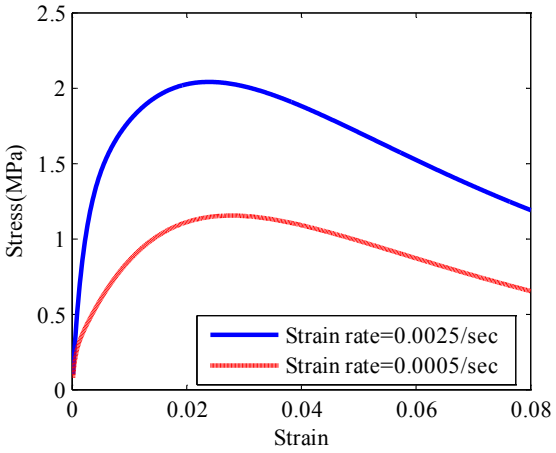

Figure 5-9: Predicted stress-strain curves for hot mix asphalt at two strain rates

With the increase in the strain rate, peak stress increases whereas the corresponding strains at peak stress decrease. Such behavior is expected for rate-dependent material and indicates that at higher strain rates the material is stiff, brittle and fails at higher stress. Elastic energy, and viscous and damage densities at two strain rates are shown in Figure 5-10. The elastic energy and damage dissipation show little effect of loading rate for the given set of model parameters, however, with an increase in the loading rate viscous dissipation appears to be considerably larger.

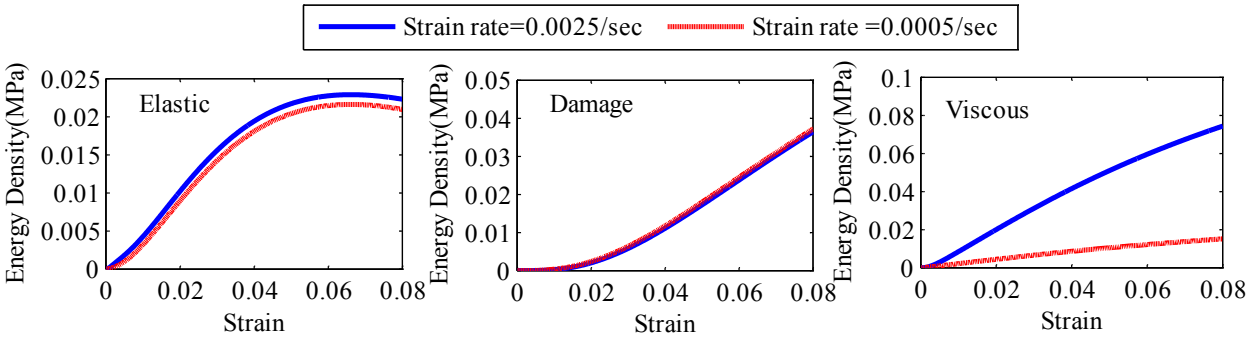

Figure 5-10: Predicted evolution of macro-scale energy densities with strain corresponding to the stress-strain curves given of Figure 5-9

We further illustrate the evolution of anisotropic dissipation and damage with loading by plotting inter-granular energy densities and damage. In Figure 5-11 we show the inter-granular energy densities in selected orientations as function of strain for the two strain rates. The normalized fractional inter-granular energy densities are also shown in polar plots in Figure 5-12 at selected strains for the two strain rates.

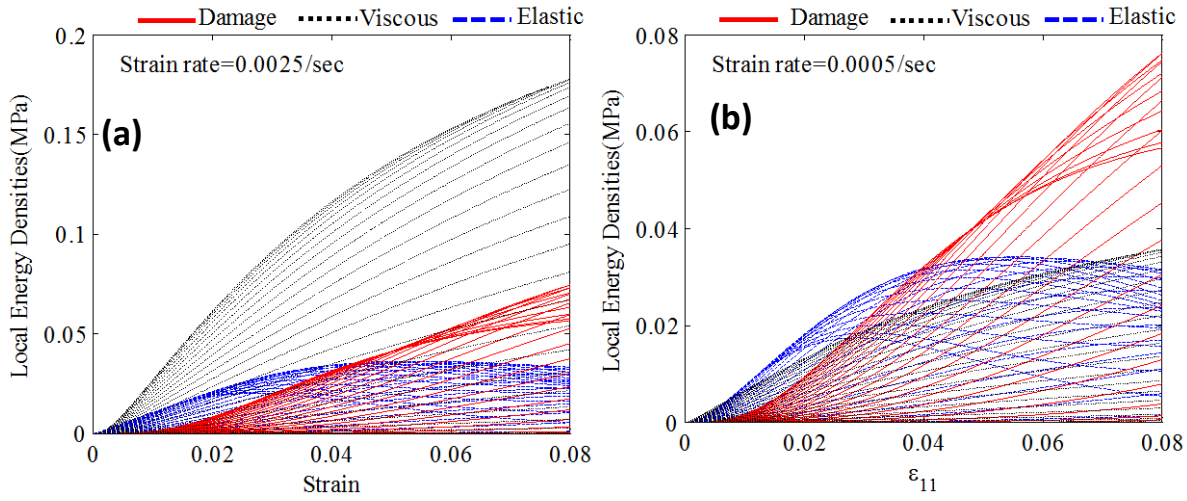

Figure 5-11 Predicted evolution of inter-granular (micro-scale) energy densities with strain under monotonic loading at (a) strain rate=0.0025/s, and (b) strain rate=0.0005/s

As in the case of creep, we can see that the inter-granular elastic energies, and viscous and damage dissipation evolve with strain differently in the various directions, however, we observe

that the viscous dissipation is dominant at the higher loading rate. From the polar plots it is evident that with the increase in strain, damage dissipation fraction, r_d of the inter-granular contacts oriented in direction of loading increases whereas the corresponding elastic energy fraction, r_e, decreases. This decrease in r_e is expected because contacts are undergoing softening process and their capacity to sustain load decreases.

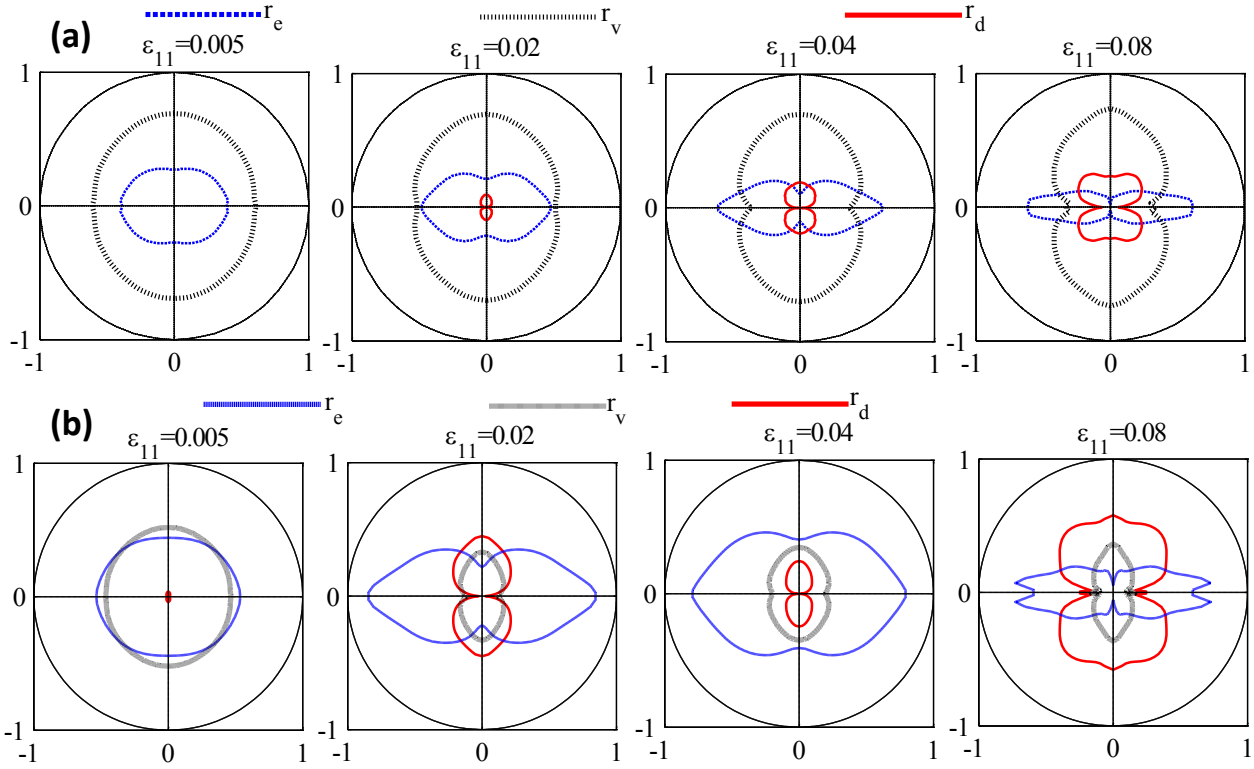

Figure 5-12: Polar plots of inter-granular (micro-scale) energy densities fractions at selected strain levels for the monotonic loading at (a) strain rate =0.0025/s, and (b) strain rate=0.0005/s

Finally, the polar plots of inter-granular damage in normal and shear directions are given in Figure 5-13 for the strain rate of 0.0025/sec. Similar results are obtained for slower loading rate since the damage dissipation is same for the two loading rates. As in the case of creep loading, these damage plots show the loading induced anisotropy in the medium, which will affect the

behavior under multi-axial loading, especially for cases in which the principal loading directions change during loading process.

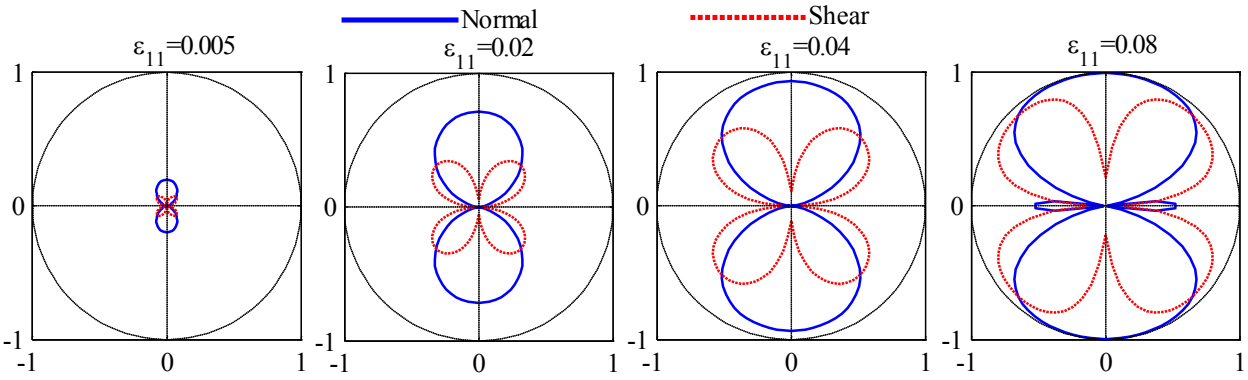

Figure 5-13: Polar plots of inter-granular normal and shear direction damage at selected strain levels for the monotonic loading at strain rate of 0.0025/s

5.3.1.5 Effect of Induced Anisotropy

To illustrate the effect of induced anisotropy, we compare the creep-recovery behavior for a two cycle loading sequence in which the loading direction is changed after the first cycle. The loading sequence is as follows. In case 1, the first cycle load is applied as σ_{11}=1.0 MPa (σ_{22}=σ_{33}=0) for LT=120 sec, UT=100 sec and the second cycle is kept identical. In case 2, the first cycle is same as that of case 1, however the second cycle load is applied as σ_{22}=1.0 MPa (σ_{11}=σ_{33}=0) for LT=120 sec, UT=100 sec. For the comparison purpose we plot in Figure 5-14 the nominal strain defined as γ_n=(ε_1+ε_2+ε_3)/3 and shear strain defined as $\tau_s = \frac{2}{3}\sqrt{(\varepsilon_1-\varepsilon_2)^2+(\varepsilon_2-\varepsilon_3)^2+(\varepsilon_3-\varepsilon_1)^2}$ for the two loading cases. The effect of induced anisotropy is clear from the response. Since the 2-diection has experienced smaller damage and plasticity in the first cycle, the response in the second cycle is stiffer for case 2. In many conventional

models that do not incorporate directional evolution of damage tensor and plastic potentials, the material would be treated as isotropic upon recovery. In this case, the second cycle response would have been identical for the two loading cases. While granular materials, in general, are known to exhibit such strong effects of induced anisotropy, experimental data on rate-dependent or creep-recovery response for these materials are scarce (unavailable to our knowledge) especially those that investigate effects of changing loading paths. To that extent, the illustrative calculations discussed here could serve as a basis for systematic investigation into the effect of path dependency of granular material behavior subjected to creep and rate-dependent loading under complex paths.

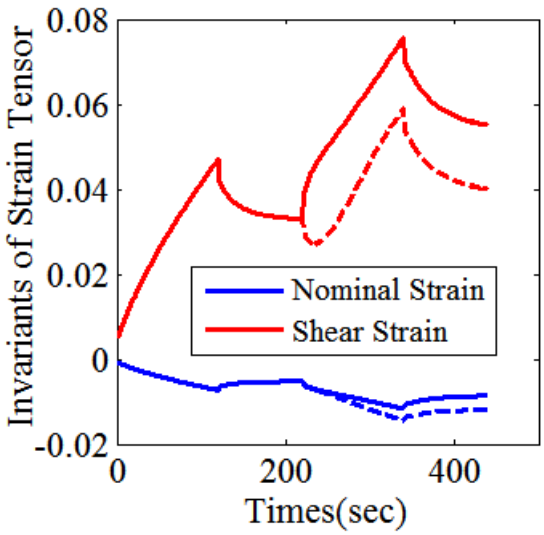

Figure 5-14: Predicted effect of induced anisotropy on a 2-cycle creep-recovery response. The 2nd cycle loading direction is same as the 1st cycle for the solid curve while it is orthogonal to the 1st cycle for the dashed curve

5.4 Summary

In this chapter we have used granular micromechanics approach in conjunction with the thermomechanics to develop a continuum material model for the rate-dependent behavior that

includes nonlinear material damage and plasticity. The main advantage of this approach is that the, resultant material model ensures that the deforming granular medium under investigation is thermodynamically consistent at each grain or interaction scale. The other advantage is that, the damage, plastic potential and flow rule are defined using simple 1d function at micro-scale, whereas in phenomenological approach one has to formulate complicated 3d plastic potentials, damage functions and flow rules for their evolution. The proposed thermo-mechanical framework in this work for the granular medium is general in that it only requires the specification of appropriate two inter-granular scalar potentials, (a) free energy function and (b) dissipation potential to obtain the macro-scale constitutive equation. Thus, the proposed approach can be applied to a range of physical or chemical phenomena [39] that effect inter-granular interactions in granular materials. The approach could be particularly useful for elucidating the effects of dissipation in porous media [123, 169-172], higher-gradient and micro-morphic continuum theories of granular systems. Using this approach we found a Clausius-Duhem type inequality applicable to inter-granular interactions which can be used to obtain the micro-scale constitutive relations for particular type of inter-granular interactions. Once identified these micro-scale constitutive relations can be used along with the expression of Cauchy stress to obtain the macro-scale constitutive relationship. In the current work to show the capability of the proposed approach we have compared the model prediction with the experimental data for the asymmetric creep-recovery response of hot mix asphalt under uniaxial compressive and tensile stress for different load and unload time.

It is noteworthy that the advantage of the resultant constitutive model is that it can describe loading induced material anisotropy particularly under evolving multi-axial loading, secondary and tertiary creep, creep rupture, accelerated stress relaxation, pressure sensitivity and

shear induced volume change. The mentioned rate-dependent characteristics are widely observed for materials such as Portland cement paste, asphalt concrete, frozen soils, cross-linked polymers, sands, glacial sediments, clays and rocks (see for example [101, 173, 174]) and are often a manifestation of the granular/discrete nature of materials. In addition, the developed approach can be extended to derive constitutive relations for enhanced continuum models, such as those for higher-gradient or micro-polar theories [73, 74, 76, 88, 175], that are necessary for describing phenomena requiring inherent length scales.

Chapter 6

Implementation of Constitutive Model into a Euler Beam Bending Framework

6.1 Introduction

The developed nonlinear rate dependent constitutive material model with coupled damage and plasticity is implemented into an Euler beam framework to predict the nonlinear bending of polymer beams in a 3 point bending configuration subjected to a constant moment and constant moment rate history. In the subsequent discussion, we first present the framework for the implementation of constitutive model into an Euler beam theory. Further, the developed framework is utilized to predict the bending response of dentin adhesives (NR1 as described in chapter 2) and collagen-adhesives composite rectangular beams (AIDBD-1 as described in chapter 3) under dry and wet conditions.

6.2 Euler Beam Bending Framework

In this work we have used the element beam theory with following assumptions, (a) plane sections before bending remains plane after bending and (b) the effect due to shear is negligible.

Now let's consider a rectangular beam of length L, width b and thickness h. Moreover, assumption that the plane section remains plane after bending implies that strain is linearly proportional to the distance from the neutral axis. Therefore,

$$\varepsilon_{11}^{t} = -\frac{y}{\rho^{t}} = -yK^{t} \tag{6.1}$$

where, ε_{11} is the axial strain, y is the distance measured from the neutral axis and K^{t} is the curvature of the beam.

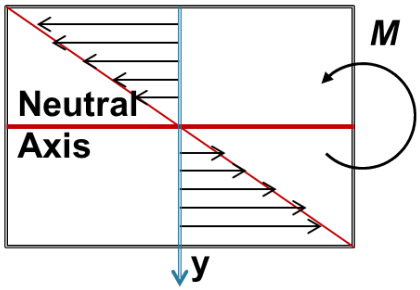

Figure 6-1: Cross-section of beam showing neutral axis and applied moment M

The balance of the internal moment (caused by the axial stress) and external applied moment M^{t} at the cross-section of the beam as shown in Figure 6-1 yields

$$M^{t} = -\int_{-\frac{h}{2}}^{\frac{h}{2}} b\sigma_{11}^{t} y dy \tag{6.2}$$

where, σ_{11}^{t} is axial stress on the cross-section of the beam and b is the width of the beam. The axial stress is derived using granular micromechanics approach and defined in Eq 4.42. Further the stress in the Eq 4.42 is rearranged for convenience and written as follows

$$\sigma_{11}^{t} = C_{11kl}^{t-\Delta t}\varepsilon_{kl}^{t} + \tilde{\sigma}_{11}^{t-\Delta t} \tag{6.3}$$

where $\tilde{\sigma}_{11}^{t-\Delta t} = P_{11kl}^{t-\Delta t}\varepsilon_{kl}^{t-\Delta t} + Q_{11}^{t-\Delta t}$

Now substituting the expression of axial stress σ_{11}^{t} from Eq 6.3 into the moment expression Eq 6.2 yields

$$M^{t} = b\int_{-\frac{h}{2}}^{\frac{h}{2}} \left(C_{11kl}^{t-\Delta t}\varepsilon_{kl}^{t} + \tilde{\sigma}_{11}^{t-\Delta t} \right) y dy \tag{6.4}$$

Now expanding the tensor C_{11kl}, in moment expression Eq 6.4 to obtain M^t

$$M^{t} = b\int_{-\frac{h}{2}}^{\frac{h}{2}} \left(C_{1111}^{t-\Delta t}\varepsilon_{11}^{t} + \left(C_{1122}^{t-\Delta t} + C_{1133}^{t-\Delta t} \right)\varepsilon_{22}^{t} + \tilde{\sigma}_{11}^{t-\Delta t} \right) y dy \tag{6.5}$$

Further, expressing strain ε_{22} in Eq 6.5 as function of axial strain ε_{11} and elastic constants as follows:

$$\varepsilon_{22}^{t} = \frac{\tilde{\sigma}_{22}^{t-\Delta t} - C_{1122}^{t-\Delta t}\varepsilon_{11}^{t}}{C_{2222}^{t-\Delta t} + C_{2233}^{t-\Delta t}} \tag{6.6}$$

Using equations Eq 6.1, 6.5 and 6.6, moment equation can be written as follows

$$M^{t} = K^{t}\tilde{M}^{t-\Delta t} + M^{t-\Delta t} \tag{6.7}$$

where, the quantities $\tilde{M}^{t-\Delta t}$ and $M^{t-\Delta t}$ are given below

$$\tilde{M}^{t-\Delta t} = 2b\int_{0}^{\frac{h}{2}} \left(C_{1111}^{t-\Delta t} + C_{1122}^{t-\Delta t}\frac{C_{1122}^{t-\Delta t} + C_{1133}^{t-\Delta t}}{C_{2222}^{t-\Delta t} + C_{2233}^{t-\Delta t}} \right) y^{2} dy = \frac{bh^{3}}{12}\left(C_{1111}^{t-\Delta t} + C_{1122}^{t-\Delta t}\frac{C_{1122}^{t-\Delta t} + C_{1133}^{t-\Delta t}}{C_{2222}^{t-\Delta t} + C_{2233}^{t-\Delta t}} \right)$$

$$M^{t-\Delta t} = 2b\int_{0}^{\frac{h}{2}} \left(\frac{C_{1122}^{t-\Delta t} + C_{1133}^{t-\Delta t}}{C_{2222}^{t-\Delta t} + C_{2233}^{t-\Delta t}}\tilde{\sigma}_{22}^{t-\Delta t} + \tilde{\sigma}_{11}^{t-\Delta t} \right) y dy = \frac{bh^{2}}{4}\left(\frac{C_{1122}^{t-\Delta t} + C_{1133}^{t-\Delta t}}{C_{2222}^{t-\Delta t} + C_{2233}^{t-\Delta t}}\tilde{\sigma}_{22}^{t-\Delta t} + \tilde{\sigma}_{11}^{t-\Delta t} \right)$$

The Equation 6.7 is an explicit expression, because quantities $\tilde{M}^{t-\Delta t}$ and $M^{t-\Delta t}$ at time $t=t-\Delta t$ are know from the previous time step and curvature K^t can be calculated for a given moment M^t.

After obtaining solution of Eq 6.7 for the curvature K^t , deflection y in bending for a small strain can be obtained as:

$$y(x) = \int_0^x \int_0^x K^t dx dx \tag{6.8}$$

In the case of pure bending Eq 6.8 can be integrated in a closed form to obtain the deflection *y*. Because curvature K^t is constant and do not change across the length of the beam. Whereas, for 3 point bending configuration, curvature varies across the length of the beam, therefore closed form solution is not feasible. Therefore, in the current work curvature K^t is calculated at three locations along the length of beam i.e. x at *L/6, L/3* and *L/2* using Eq 6.7. Thereafter Eq 6.8 is numerically integrated to obtain the deflection of beam.

6.3 Results and Discussion

The developed beam bending equations are used to predict the mechanical response of dentin adhesives (NR-1 described in chapter 2) and collagen adhesive composite beams (AIDBD-1 described in chapter 3) under monotonic and creep loading conditions. In particular, we first perform the calibration to identify the model parameters and then use same model parameter to predict other bending tests. Also model predictions are compared with the experimental data. Experimental procedure along with the materials used to obtain the monotonic and creep behavior of dentin-adhesives and collage-adhesive composites are presented in chapter 2 and 3 respectively.

6.3.1 Calibration to Identify Model Parameters.

The model parameters for dentin adhesive and collagen-adhesive composite in both dry and wet condition was identified using the using the experimental creep data. First, the normal and shear

stiffness and viscosity parameters E_1, G_1, G_w, E_n, μ_n and μ_w, were obtained by reducing constitutive equation to linear viscoelastic by assuming $B_n=B_w=\infty$ and fitting the reduced equation to the initial portion (100 min) of the experimental creep curve. Thereafter, damage parameters B_n, B_w and β were introduced into the model and optimized to match the complete creep response curve and monotonic curve at 60μm/min. In the current work shear parameter are related to normal parameter as follows $G_1=0.5E_1$, $G_w=E_n$, $\mu_n=\mu_w$, and $B_n=B_w$. Normal inter-granular model parameters are given in Table 6-1 for dentin adhesive and collagen-adhesive composite in dry and saturated wet condition.

Table 6-1:Model parameters for beam bending simulations

Parameters	Adhesive or NR-1		AIDBD-1	
	Dry	Wet	Dry	Wet
E_1(GPa)	6	3	5.4	1.8
E_2(GPa)	10.5	4.5	10.5	3
μ_n/E_2 (sec)	428	500	428	750
B_n	0.01	0.01	0.01	0.02
β	5	5	5	5

6.3.2 Creep Behavior

To simulate the creep behavior of polymer beams in 3 point bending configuration, a constant moment of 0.75Nmm is applied, which corresponds to a applied load of 0.3N. Further, to calculate the curvature, Eq 6.7 is used and thereafter Eq 6.8 is utilized to obtain the deflection. The experimental data and model prediction for both dentin adhesive (NR-1, see chapter 3) and collagen adhesive composite (AIDBD-1, see chapter 3) is given in Figure 6-2. From the Figure 6-2, we observe that predicted curves are able to capture the both the initial and overall response of the dentin adhesive and collagen-adhesive composites. Predicted curve shows that displacement quickly asymptotes to constant value, whereas experimental curve keeps increasing. This difference in the experiment and prediction is due to the fact that, material

under observation is complex and has multiple characteristic times spanning over several decades. But the constitutive model developed in this work has only one characteristic time.

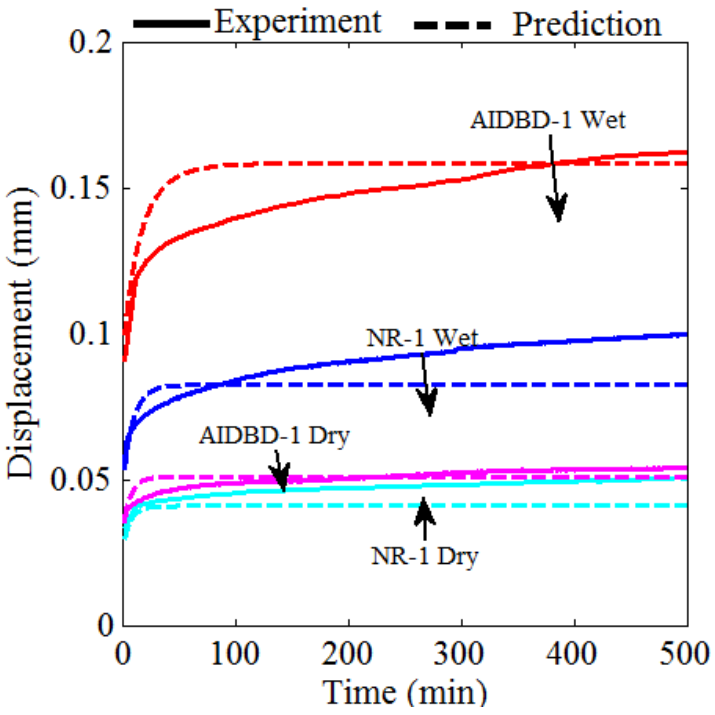

Figure 6-2: Creep behavior of dentin adhesive (NR-1) and AIDBD-1 under dry and wet environment

6.3.3 Monotonic Behavior

To predict the monotonic behavior of dentin adhesives and collagen-adhesive composite, load data obtain from the experiments was converted into moment data and fed into Eq 6.7 to predict the curvature K^t. After that Eq 6.8 was utilized to obtain the deflection data. In current work two loading rate of 60μm/min and 2μm/min were used for dentin adhesives (NR-1 see chapter 3), in both dry and wet condition, whereas due to the limited sample size only one loading rate of 60 μm/min was used for collagen adhesive composite (AIDBD-1 see chapter 3) testing.

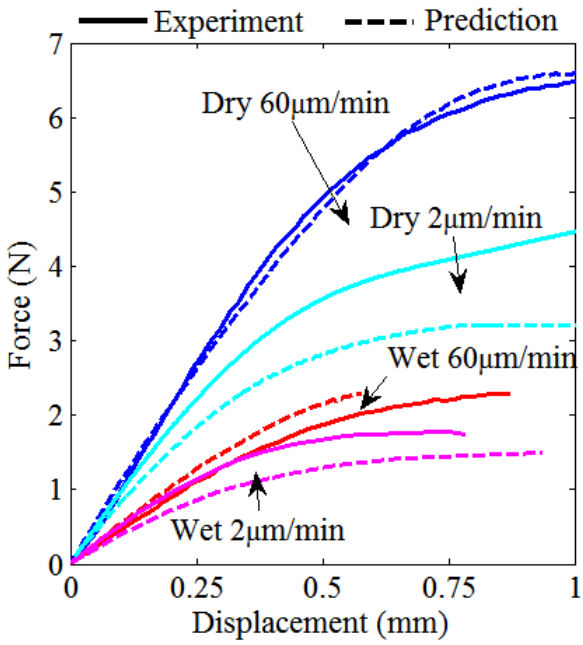

Figure 6-3:Experimental and predicted load displacement curves for dentin adhesives under different loading rate and moisture conditions.

Figure 6-3 and 6-4 shows the predicted and experimental load-displacement curves for dentin adhesive and collagen-adhesive composite respectively. From Figure 6-3 we observe that at the loading rate of 60um/min in dry condition model not only predicts the peak load value but also captures the overall load displacement behavior. Whereas, when the loading rate is decreased to 2um/min, model predicts the linear behavior accurately, but, under predicts the force at higher displacements. When the dentin adhesive samples were kept in water for complete saturation, sample becomes soft and weak which is evident from the experimental load displacement data. Model predicts the load displacement curves well at both the loading rate. In this study we have used the representative curve for each moisture and loading conditions, but average curve with standard deviation can also be used. In that case qualitatively results will be similar.

Similar to dentin-adhesive, predicted load displacement curves for collagen-adhesives composite in dry and wet environment are shown in Figure 6-4. In the case of dry sample, model

predictions do not agrees with experimental data, model predicts the softer behavior. For wet sample model prediction agree well with experimental data.

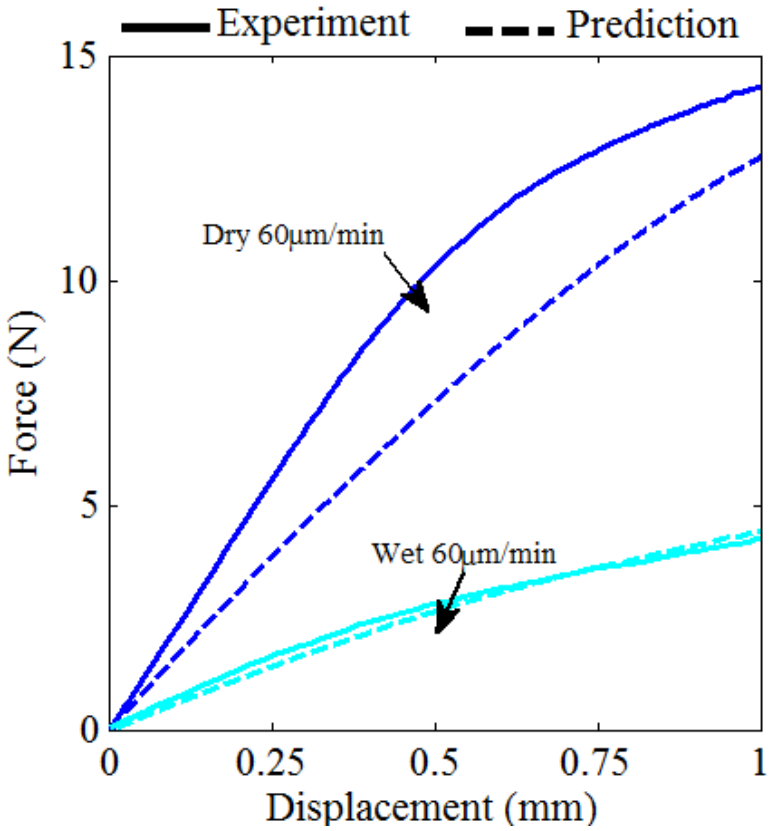

Figure 6-4:Experimental and predicted load displacement curves for collagen in dry and wet environment.

6.4 Summary

In this chapter we have implemented the developed constitutive equation for nonlinear rate dependent material with damage into the Euler beam bending framework. The obtained beam bending equations were used to predict (a) the creep behavior of dentin adhesive (NR-1) and collagen adhesive composite (AIDBD-1) at 0.3N load amplitude in dry and wet condition and (b) monotonic behavior for dentin adhesive and collagen adhesive composite at the displacement rate of 60μm/min and 2μm/min in dry and wet state. From the calculations we observe that,

model was able to capture both the time and rate dependent behavior shown by both the materials. Some discrepancies were observed between the experimental data and model prediction due to the multiple characteristic time of dentin adhesive and collagen-adhesive composite. In the current work only one characteristic time was used, in general inter-granular force displacement should be modeled using Prony series, which includes evenly spaced characteristic times over several decades. Also, relatively small sample size n=3 was used, which for testing under dry condition results in larger standard deviation due to relatively smaller signal-to-noise ratio for small strain amplitudes. But it is important to note that, the developed approach is general and can be used to interpret and analyze bending tests load-displacement data for nonlinear materials with damage and plasticity.

Chapter 7

Finite Element implementation of Constitutive Model

7.1 Introduction

Finite element technique is an attractive numerical platform to study the behavior of complex structural components under various loads and boundary conditions. In this chapter to study the behavior of structures whose components or material exhibits nonlinear viscoelastic behavior we implement the explicit form of developed nonlinear rate dependent micromechanical model with damage and plasticity into a finite element framework.

7.2 Weak Formulation

Using the principle of virtual work the equilibrium equation is obtained as follows

$$\sigma_{ij,j}^{t} - f_i^t = 0 \tag{7.1}$$

where, σ_{ij} is stress tensor and f_i is the force vector.

We now introduce the explicit stress tensor σ_{ij} from the constitutive equation given in Eq 4.42 and express stress equilibrium equation as

$$\frac{\partial}{\partial x_j}\left[C_{ijkl}^{t-\Delta t}\varepsilon_{kl}^{t} + P_{ijkl}^{t-\Delta t}\varepsilon_{kl}^{t-\Delta t} + \tilde{\sigma}_{ij}^{t-\Delta t} \right] - f_i^t = 0 \tag{7.2}$$

Further, we introduce the test function v_i and write the weighted residual integral of Eq 7.2 over the arbitrary body of volume Ω

$$\int_{\Omega}\left\{\frac{\partial}{\partial x_j}\left[C_{ijkl}^{t-\Delta t}\varepsilon_{kl}^{t}+P_{ijkl}^{t-\Delta t}\varepsilon_{kl}^{t-\Delta t}+\tilde{\sigma}_{ij}^{t-\Delta t}\right]\right\}v_i^t d\Omega-\int_{\Omega}f_i^t v_i^t d\Omega=0 \tag{7.3a}$$

Further using the definition of strain tensor as $\varepsilon_{kl}^{t}=\frac{1}{2}\left(u_{k,l}^{t}+u_{l,k}^{t}\right)$ we rewrite Eq 7.3a as

$$\int_{\Omega}\left\{\frac{\partial}{\partial x_j}\left[C_{ijkl}^{t-\Delta t}\frac{1}{2}\left(u_{k,l}^{t}+u_{l,k}^{t}\right)+P_{ijkl}^{t-\Delta t}\frac{1}{2}\left(u_{k,l}^{t-\Delta t}+u_{l,k}^{t-\Delta t}\right)+\tilde{\sigma}_{ij}^{t-\Delta t}\right]\right\}v_i^t d\Omega-\int_{\Omega}f_i^t v_i^t d\Omega=0 \tag{7.3b}$$

Now to reduce the differentiability condition on the independent variable u_i we use integration by parts (IBP) to transfer one order of differentiation from independent variable u_i to the test function v_i to obtain the weak form of functional in Eq 7.3b as follows:

$$\int_{\Omega}\left[\frac{1}{2}C_{ijkl}^{t-\Delta t}\left(u_{k,l}^{t}+u_{l,k}^{t}\right)\right]v_{i,j}^{t}d\Omega=\int_{\Gamma}\sigma_{ij}^{t}n_j v_i^t d\Gamma-\int_{\Omega}f_i^t v_i^t d\Omega-\int_{\Omega}\left[\frac{1}{2}P_{ijkl}^{t-\Delta t}\left(u_{k,l}^{t-\Delta t}+u_{l,k}^{t-\Delta t}\right)+\tilde{\sigma}_{ij}^{t-\Delta t}\right]v_{i,j}^{t}d\Omega \tag{7.4}$$

where, n denotes the outward unit normal to the boundary $\partial\Omega$.

Integration by parts helps to identify the essential and natural boundary conditions, specification of u_i is the EBC and specification of σ_{ij}^{t} at boundaries is NBC. From the representation viewpoint, the functional in the Eq 7.4 can be decomposed into bilinear and linear functional *B(u,v)* and *L(v)* respectively as follows:

$$\begin{aligned}B(u^t,v^t)&=\int_{\Omega}\left[\frac{1}{2}C_{ijkl}^{t-\Delta t}\left(u_{k,l}^{t}+u_{l,k}^{t}\right)\right]v_{i,j}^{t}d\Omega\\ l(v^t)&=-\int_{\Gamma}\sigma_{ij}^{t}n_j v_i^t d\Gamma+\int_{\Omega}f_i^t v_i^t d\Omega+\int_{\Omega}\left[\frac{1}{2}P_{ijkl}^{t-\Delta}\left(u_{k,l}^{t-\Delta}+u_{l,k}^{t-\Delta}\right)+\tilde{\sigma}_{ij}^{t-\Delta t}\right]v_{i,j}^{t}d\Omega\end{aligned} \tag{7.5}$$

It can be shown that the functional *B(u,v)* is both bilinear and symmetric.

Further a functional $I(u^t) = \frac{1}{2} B(u^t, u^t) - l(u^t)$ can be written so that its first variation $\delta I(u^t) = 0$ yields the integral given in Eq (7.5).

Now using the Galerkin method of approximation we define the independent variable u_i and test function v_i as follows

$$u_i^t = N_{ip} u_p^t ; v_i^t = N_{ip} v_p^t \tag{7.6}$$

where, N_{ip} are linear interpolation functions and u_p^t are the nodal displacements. Substituting Eq 7.6 into the weak formulations in Eq 7.4 the following discretized system of equation is obtained

$$K_{ij}^{t-\Delta t} u_j^t = F_i^t - \tilde{F}_i^{t-\Delta t} \tag{7.7}$$

where, $K_{ij}^{t-\Delta t}$ is the global stiffness matrix and F_i^t is the global forces vector and $\tilde{F}_i^{t-\Delta t}$ is global force due to rate dependent processes are defined as follows

$$K_{ij}^{t-\Delta t} = \int_\Omega \frac{\partial N_{pi}^T}{\partial x_q} C_{pqrs}^{t-\Delta t} \frac{\partial N_{rk}^T}{\partial x_s} d\Omega$$

$$F_i^t = \int_\Gamma N_{ji}^T T_j d\Gamma$$

$$\tilde{F}_i^{t-\Delta t} = \int_\Omega \frac{\partial N_{pi}^T}{\partial x_q} \left(P_{pqrs}^{t-\Delta t} \varepsilon_{rs}^{t-\Delta t} + \tilde{\sigma}_{pq}^{t-\Delta t} \right) d\Omega$$

To implement the displacement boundary condition procedure described by Wu et al [176] was implemented. In this method, known products are moved to the right hand column of the matrix equation. Thereafter, columns and rows of master stiffness matrix corresponding to the known displacement are replaced by zero and main diagonal coefficient remains unchanged. At last, the corresponding components of the right hand column are replaced by the product of specified displacement value and associated diagonal coefficient.

7.3 2d Triangular Element

The developed weak formulation for nonlinear rate dependent material is given in Eq (7.4) is implemented to study the 2d structural problem using linear strain element. 2d element having 3 nodes is represented by a triangle in the real coordinate system. Element matrices and equations obtained in real coordinates system becomes complex; therefore 2d linear strain elements are mapped to an iso-parametric element with fixed size in natural coordinate system as shown in Figure 7-1.

(a) (b)

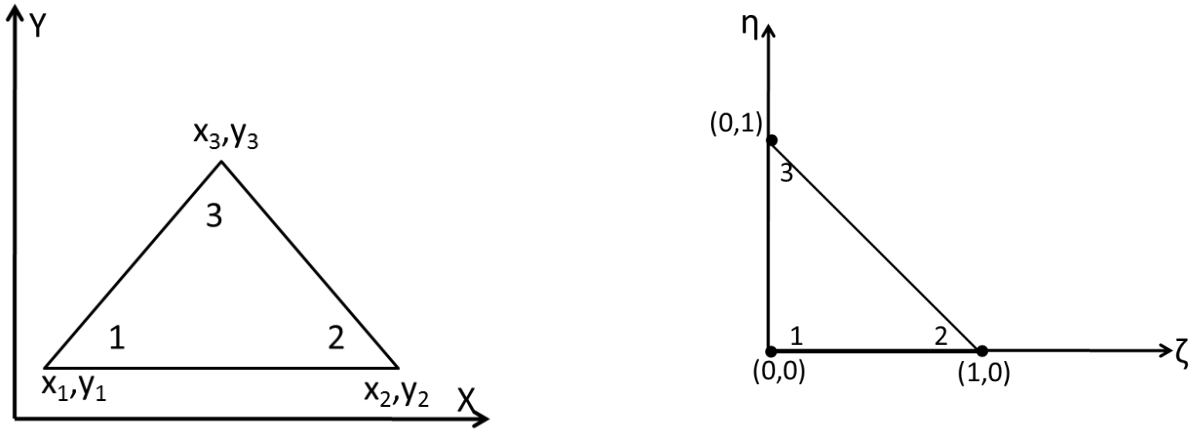

Figure 7-1:Linear triangle element in (a) real coordinate system and (b) isoparametric element

Displacement u_ζ in the interior of isoparametric element in ζ direction can be written as liner function of ζ and η as follows

$$u_\zeta = a_1 + a_2\zeta + a_3\eta \tag{7.8}$$

Now evaluating the above equation for u_ζ at 3 nodal points (0,0), (1,0) and (0,1) we get the following expression

$$
\begin{aligned}
{}^{1}u_{\zeta} &= a_1 \\
{}^{2}u_{\zeta} &= a_1 + a_2 \\
{}^{3}u_{\zeta} &= a_1 + a_3
\end{aligned}
\tag{7.9}
$$

Where, ${}^{1}u_{\zeta}$, ${}^{2}u_{\zeta}$ and ${}^{3}u_{\zeta}$ are the three nodal displacements in ζ direction.

Eq (7.9) can be written in matrix form to obtain the unknown coefficients a_1, a_2 and a_3

$$
\begin{Bmatrix} a_1 \\ a_2 \\ a_3 \end{Bmatrix} = A^{-1} \begin{pmatrix} {}^{1}u_{\zeta} \\ {}^{2}u_{\zeta} \\ {}^{3}u_{\zeta} \end{pmatrix}, \quad \text{where } A = \begin{pmatrix} 1 & 0 & 0 \\ 1 & 1 & 0 \\ 1 & 0 & 1 \end{pmatrix} \tag{7.10}
$$

Or

$$
\begin{Bmatrix} a_1 \\ a_2 \\ a_3 \end{Bmatrix} = \begin{pmatrix} {}^{1}u_{\zeta} \\ -{}^{1}u_{\zeta} + {}^{2}u_{\zeta} \\ -{}^{1}u_{\zeta} + {}^{3}u_{\zeta} \end{pmatrix}
$$

Substituting the value of coefficients a_1, a_2 and a_3 in Eq (7.8) to obtain the displacement u_{ζ} as function of nodal displacements

$$
u_{\zeta} = N_1 {}^{1}u_{\zeta} + N_2 {}^{2}u_{\zeta} + N_3 {}^{3}u_{\zeta} \tag{7.11}
$$

where, N_1, N_2, and N_3 are the shape function in the natural coordinates and defined as follows

$$
N_1 = 1 - \zeta - \eta;\ N_2 = \zeta;\ N_3 = \eta
$$

Similar to displacement u_{ζ} in ζ direction we can also obtain u_{η} in η direction as follows

$$
u_{\eta} = N_1 {}^{1}u_{\eta} + N_2 {}^{2}u_{\eta} + N_3 {}^{3}u_{\eta} \tag{7.12}
$$

Also any point in the *x,y* coordinate system can be mapped into the natural coordinate system using the same shape function as follows:

$$
\begin{aligned}
x(\zeta,\eta) &= N_1 x_1 + N_2 x_2 + N_3 x_3 \\
y(\zeta,\eta) &= N_1 y_1 + N_2 y_2 + N_3 y_3
\end{aligned}
\tag{7.13}
$$

After the identification of the shape function, element Stiffness matrix for the 2d constant strain element is written as.

$$\begin{aligned}[K]_{6\times6} &= \iint_A [B]^T_{3\times6}[C]_{3\times3}[B]_{3\times6}dxdy \\ &= \left|\det(J)\right|\iint_A [B]^T[C][B]d\zeta d\eta\end{aligned} \tag{7.14}$$

here, $$[B] = \begin{bmatrix} \frac{\partial N_1}{\partial x} & 0 & \frac{\partial N_2}{\partial x} & 0 & \frac{\partial N_3}{\partial x} & 0 \\ 0 & \frac{\partial N_1}{\partial y} & 0 & \frac{\partial N_2}{\partial y} & 0 & \frac{\partial N_3}{\partial y} \\ \frac{\partial N_1}{\partial y} & \frac{\partial N_1}{\partial x} & \frac{\partial N_2}{\partial y} & \frac{\partial N_2}{\partial x} & \frac{\partial N_3}{\partial y} & \frac{\partial N_3}{\partial x} \end{bmatrix}$$ and $$\begin{bmatrix} \frac{\partial N_i}{\partial x} \\ \frac{\partial N_i}{\partial y} \end{bmatrix} = J^{-1}\begin{bmatrix} \frac{\partial N_i}{\partial \zeta} \\ \frac{\partial N_i}{\partial \eta} \end{bmatrix}$$

and C is obtained from the micromechanical approach and defined in Eq 4.42

The Jacobian matrix J is defined as

$$J = \begin{bmatrix} \frac{\partial x}{\partial \zeta} & \frac{\partial x}{\partial n} \\ \frac{\partial y}{\partial \zeta} & \frac{\partial y}{\partial \zeta} \end{bmatrix}$$

After the formulation of stiffness matrix the FE equations are written in the classical form as:

$$[K]\{u\} = \{F\} \tag{7.15}$$

Here, u and F are the displacement and force vectors respectively and K is element stiffness matrix and force vector F is defined as follows.

$$F = \iint_s \left\{ \int_\Gamma \sigma^t_{ij} n_j v^t_i d\Gamma - \int_\Omega f^t_i v^t_i d\Omega - \int_\Omega \left[\frac{1}{2} P^{t-\Delta t}_{ijkl}(u^{t-\Delta t}_{k,l} + u^{t-\Delta t}_{l,k}) + \tilde{\sigma}^{t-\Delta t}_{ij} \right] v^t_{i,j} d\Omega \right\} [N]^T ds \tag{7.16}$$

Once the displacement vector u is obtain then the strain of element is calculated as

$$\begin{Bmatrix} \varepsilon_{xx} \\ \varepsilon_{yy} \\ \varepsilon_{xy} \end{Bmatrix} = [B]_{3\times 6} \{u\} \tag{7.17}$$

7.4 Summary

The current chapter presents the implementation of the developed nonlinear rate dependent constitutive material model into a finite element framework. It is important to note that, for the efficient (stable and computationally fast) implementation, constitutive model is expressed explicitly, i.e. no iterations are required to obtain the solution at each integration point. Thereafter, weighted residual integral are combined with integration by parts to obtain the weak formulation, which leads to the formulation of element stiffness matrices and force vectors. In this work 2d linear triangular elements are utilized, but the developed equations are general and can be easily extended to model 3d boundary value problems. The developed finite element framework can be used to predict the response of initial boundary value problems such as (a) nonlinear bending of polymer beams, (b) durability of adhesive-dentin interface and (c) permanent deformation in pavement under the repeated load.

Chapter 8

Finite Element Model of 3 Point Bending of Dentin-Adhesive Beams

8.1 Introduction

The developed finite element equations in chapter 7 are used to predict the rate dependent response of dentin adhesive (NR-1 see chapter 3) beams under different loading and moisture conditions:

(1) Monotonic: Constant displacement rate

   a. 60μm/min and 2μm/min:- stored dry and tested dry

   b. 60μm/min and 2μm/min:- stored wet and tested in submerged condition

(2) Creep: Constant load

   a. 0.3N stored dry and tested dry

   b. 0.3N stored wet and tested in submerged condition

   c. 0.3, 0.6 and 0.9N stored dry and tested dry-to-wet.

To model the mechanical response of the nonlinear viscoelastic beams when they are stored dry and tested dry to wet, the inter-granular stiffness and viscosity both in shear and normal direction are given moisture dependent properties. This dependence of inter-granular stiffness and viscosities on the moisture is attributed to the diffusion of water into the polymer sample. This

water diffusion weakens the non-covalent interactions within the polymer network. The rate of diffusion is influenced by the polymer structure, stiffness of the cross-linked polymer network and its hydrophilicity [34]. This diffusion process continues until the sample is completely saturated with water and all the weak intermolecular bonds have been disrupted

To account for the effects of moisture induced damage on the polymer network, inter-granular stiffness, viscosity and relaxation parameters were given moisture dependent properties such that micro-scale forces f_n and f_w in normal and shear directions takes the following form:

$$f_n = \frac{E_1\mu_n}{(E_1+E_2)}\dot{\delta}_n + \frac{E_2E_1}{(E_1+E_2)}\delta_n - \frac{\mu_n}{(E_1+E_2)}\dot{f}_n$$
$$f_w = \frac{G_1\mu_w}{(G_1+G_2)}\dot{\delta}_w + \frac{G_2G_1}{(G_1+G_2)}\delta_w - \frac{\mu_w}{(G_1+G_2)}\dot{f}_w \quad (8.1)$$

Where coefficients E_1, E_2, G_1, G_2 μ_n and μ_w are defined as fallows

$$E_2 = E_n\left(1-\frac{m}{2}\right)e^{-\frac{\left(\delta_n-\frac{f_n}{E_1}\right)}{B_n}}; \text{ and } \quad G_2 = G_w\left(1-\frac{m}{2}\right)e^{-\frac{\left(\delta_w-\frac{f_w}{G_1}\right)}{B_w}}$$

$$E_1 = E_{initial}\left(1-a_n m^2\right); \text{ and } \quad G_1 = G_{initial}\left(1-a_w m^2\right), \text{ here } a_n, a_w \text{ are constants and defined as } 0 \le a_n, a_w \le 1$$

$$\mu_n = \mu_{n0}\left(1-\frac{m}{2}\right)e^{-\frac{\left(\delta_n-\frac{f_n}{E_1}\right)}{\beta B_n}}; \text{ and } \quad \mu_w = \mu_{w0}\left(1-\frac{m}{2}\right)e^{-\frac{\left(\delta_w-\frac{f_w}{G_1}\right)}{\beta B_w}}$$

In the above equation *m* represents the normalized moisture content, *m=0* indicates perfectly dry material and *m=1* represents completely saturated. To obtain the moisture content, diffusion equation for the similar dimension beam was solved by Parthasarathy et al [34]using the finite difference scheme. Data from Parthasarathy et al [34] provides the amount of water content at any location across the beam. Variation of moisture content with time across the cross-section of beam is given in Figure 8-1. Model parameters a_n and a_w were taken to be 0.96.

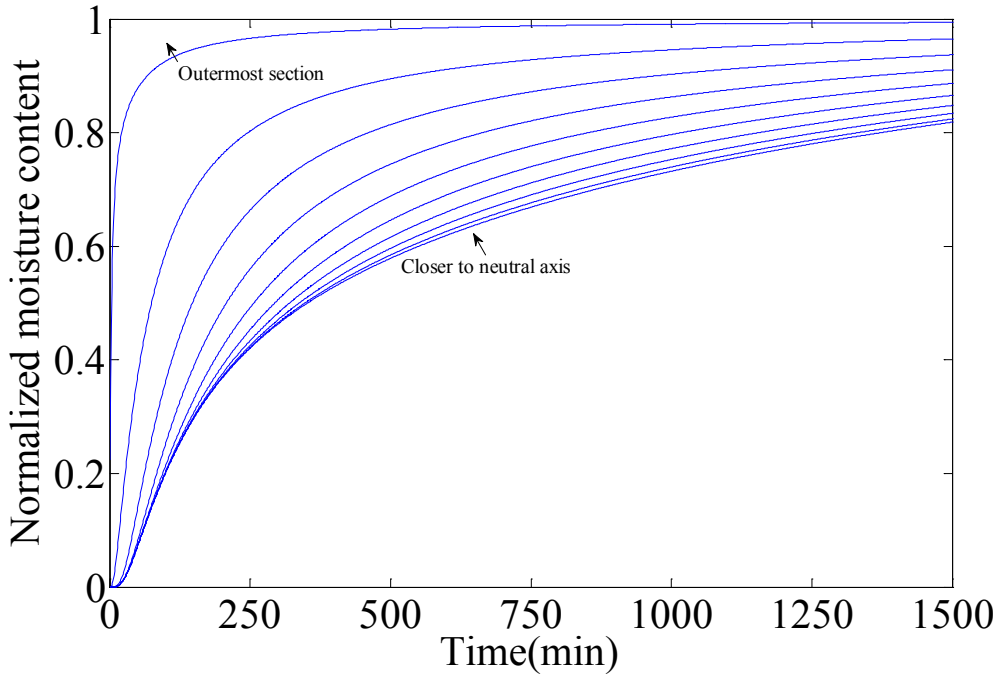

Figure 8-1:Variation of moisture content with time across the beam having a square cross-section of 1mm x 1mm.

8.2 FE Model.

We have constructed a 2d plane stress FE model of 3 point bending of beam of length 10mm and square cross-section of 1mm x 1mm. To save the computational time, symmetry of the problem is exploited and only half of the beam is modeled. The schematic of FE model of beam with boundary condition and loads is shown in Figure 8-2. On the left edge, nodal displacements in the *y* direction are fixed at zero and nodal displacements in x direction are free. A constant load or increasing displacement at constant rate depending upon the problem under investigation is applied on right edge i.e. at *x=5* simulating a creep or a monotonic test.

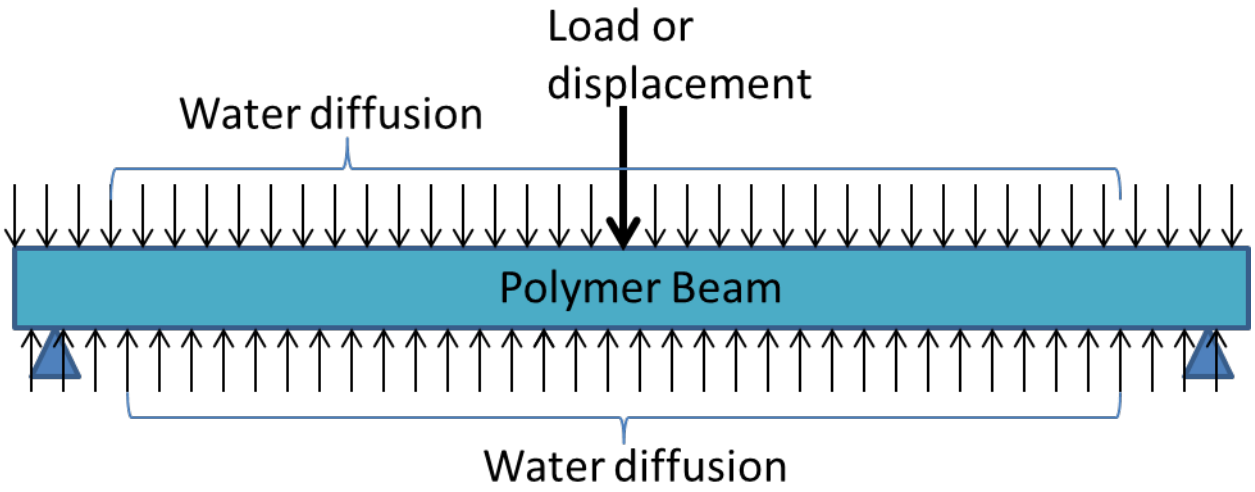

Figure 8-2: Schematic of polymer beam subjected to load and water diffusion in a 3 point bending experiment.

The FE model of 3point bending beam contains 2966 constant strain triangles with 1565 nodes as shown in Figure 8-3. It is important to note that, each element in FE model is modeled using the micromechanical stress-strain model as described in chapter 4 and 5. In this approach 144 equations are solved at each material/element level, when 72 integration points are used in the micromechanical model over θ-ϕ space. Therefore, to obtain the FE solution in a reasonable timeframe, explicit form of the constitutive model given in Eq 4.42 is utilized. Model parameters for dentin adhesive were obtained from the calibration process of Euler beam bending as described in chapter 6. Material properties of dentin adhesives for different moisture conditions are given in Table 8-1.

Table 8-1: Model parameters for finite element simulation of 3 point bending of dentin adhesive beams

Dentin Adhesive-Dry	Dentin Adhesive-Wet	Dentin Adhesive-Dry to Wet
E_1= 6GPa/m G_1=0.5E_1	E_1=3 GPa/m G_1=0.5E_1	$E_{initial}$= 3GPa/m $G_{initial}$=0.5E_1
E_n=10.5GPa/m G_w=E_n	E_n=4.5GPa/m G_w=E_n	E_n=10.5GPa/m G_w=E_n
μ_{n0}/ E_n=428 sec μ_{w0}=μ_{n0}	μ_{n0}/ E_n=500 sec μ_{w0}=μ_{n0}	μ_{n0}/ E_n=428 sec μ_{w0}=μ_{n0}
B_n=0.01 B_w=B_n	B_n=0.01 B_w=B_n	B_n=0.01 B_w=B_n
B=5	B=5	B=5
α_n=1 α_w=α_n	α_n=1 α_w=α_n	α_n=1 α_w=α_n

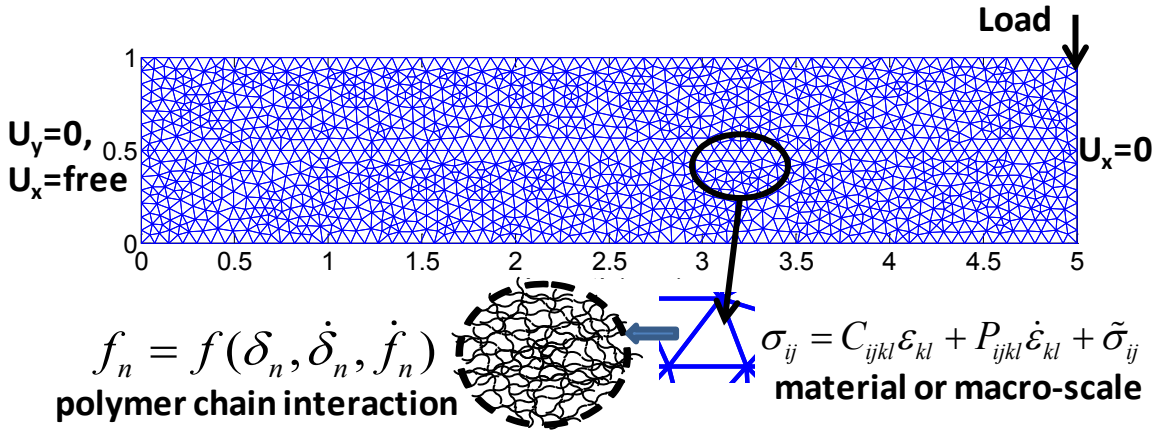

Figure 8-3:Schematic of FE model of 3 point bending showing only half of the beam

8.3 Results and Discussion.

8.3.1 Creep Behavior

The calculated and predicted creep curves at different load levels and moisture conditions are shown in Figure 8-4. Behavior under the extreme moisture conditions i.e. completely dry or saturated is linear viscoelastic and model is able to capture both the qualitative and quantitative

information. When the polymer beams (dentin adhesives) are subjected to moisture and load simultaneously, they accumulated large displacements and the behavior is nonlinear rate dependent as shows in Figure 8-4. Finite element model is able to capture the overall physics of the moisture induced deformation and predicts the asymptotic displacements and associated times very well. But we also observe that, at some time intervals model under predicts the displacements compared to experiments. The deviation in the prediction curves indicates that dentin adhesives are complicated materials having multiple characteristic times and experimental data for local moisture content along the cross-section of beam is absent. In the current work we have used one initial characteristic time, which is not sufficient to account for the completed creep response of dentin adhesives. In addition to this, the local diffusion information is obtained from the model calculations performed by Parthasarathy et al [34], to obtain better results experiments should be performed to obtain the moisture content across the beam.

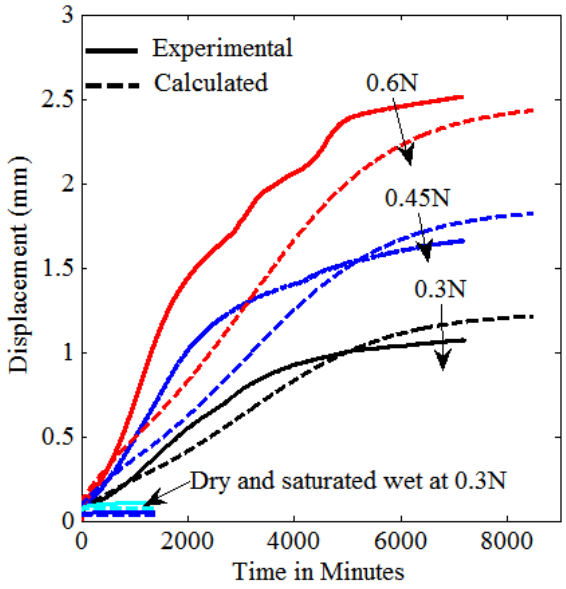

Figure 8-4: Predicted and experimental creep curves for dentin adhesive under different moisture conditions and load level.

Stress and strain contours for the polymer beam under (a) dry, (b) wet and (c) dry to wet at 0.3N load is shown in Figures 8-5 and 8-6. In the case of dry and wet polymer beams, the deformation is linear viscoelastic and stress distributions do not change with time, therefore Figure 8-5 only presents the stress and strain contours at the end of loading. As expected, higher stress and strains are observed on the outmost layer of the beam.

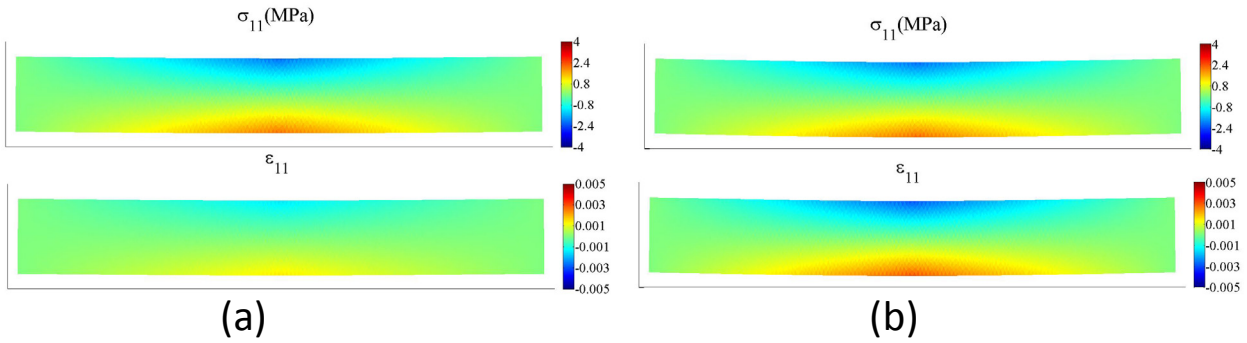

Figure 8-5: Stress-strain distribution under (a) dry and (b) wet saturated environment at 0.3N load amplitude.

But, for the case of dry-to-wet i.e. when the polymer beam is simultaneously subjected to moisture and load, behavior is nonlinear rate and time dependent, both the stress and strain distribution changes significantly with time. Figure 8-6a and 8-6b shows the stress and strain distribution at four different times, i.e. 1min, 1400 min, 5600 min and 8400 min. The variation of stress and strain across the beam as the polymer beam absorbs moisture is given in Figure 8-7. From Figure 8-7 we observe that, at the start of creep experiment, outer elements have the largest stress; this is expected, because outer layer of the beam experiences highest strain. But as the experiment progress, water gradually diffuses from the outmost layer to the center of the polymer beam (shown in Figure 8-1) and decreases the load carrying capacity of the polymer beam. This water diffusion causes reduction in stresses in the outermost layer of the beam (Figures 8-6a and 8-7a at 1400 minutes). The lower stresses on the outermost layer of the beam

indicate deformation induced damage. Since outer layer of beam experience largest strain (shown in Figures 8-6b and 8-7b at 1400 minutes), therefore have the highest amount of damage. In linear elastic models, there will be no strain induced softening, therefore no redistribution of stresses. Because the external moment has to be maintained, therefore, inner element carry larger stress compared to outside element as shown in Figure 8-7a. With the further increase in time, moisture content across the beam becomes uniform, causing redistribution of stress, and once again, the outer elements of the beam have higher stresses, as shown in Figures 8-6a and 8-7a at 8400 minutes.

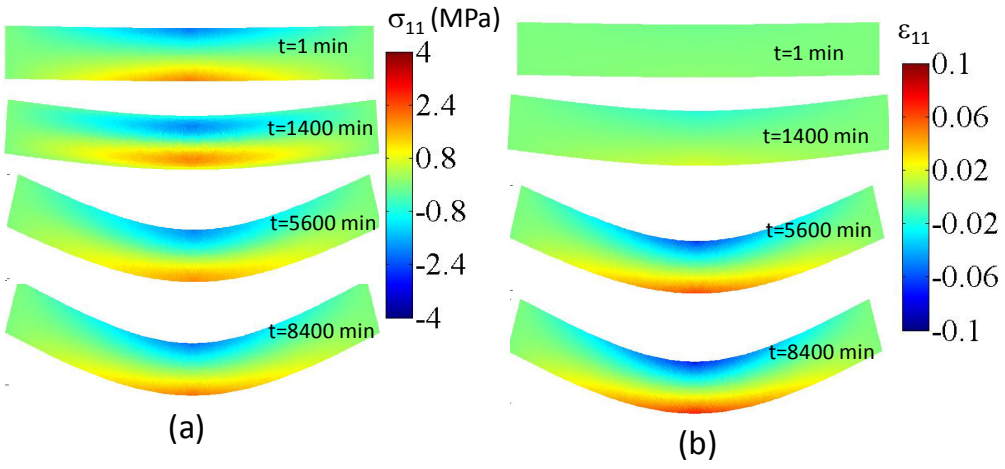

Figure 8-6: Stress-strain distribution under dry to wet saturated environment at 0.3N load Amplitude.

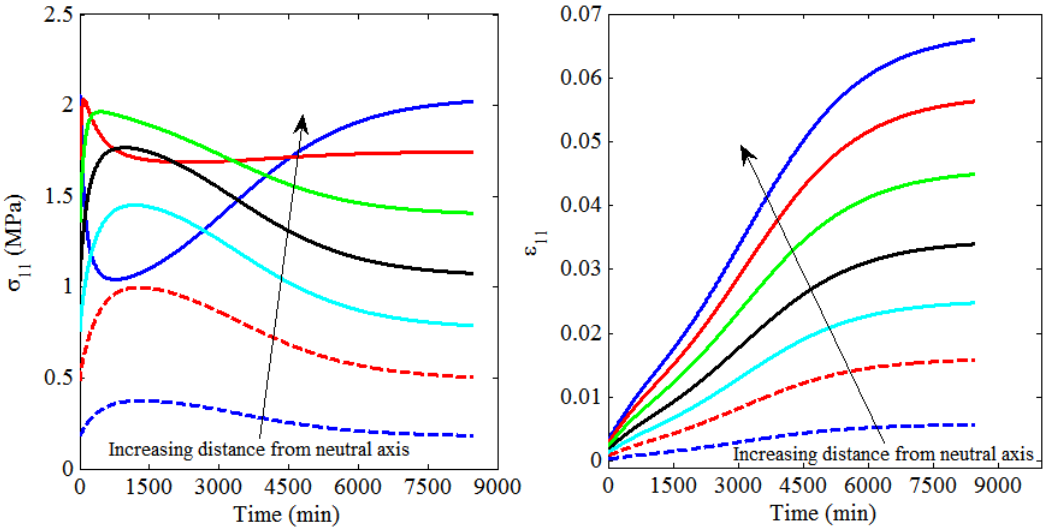

Figure 8-7: Variation of stress and strain across the beam cross-section under dry to wet environment at creep load of 0.3N.

8.3.2 Monotonic Behavior

The results of the monotonically increasing displacement at two loading rate under dry and wet condition on dentin adhesive is given in Figure 8-8. It is important to note that, for finite element simulations model parameter were obtained from the calibration process for the Euler beam bending simulation. FE simulation is able to predict the load displacement curve for dentin adhesives under both dry and wet conditions. Some discrepancies are observed in the results, especially at displacement rate of 60um/min in both dry and wet condition. This deviation in calculated results is due to model parameters which are obtained from Euler beam bending calibration and use of single characteristic time.

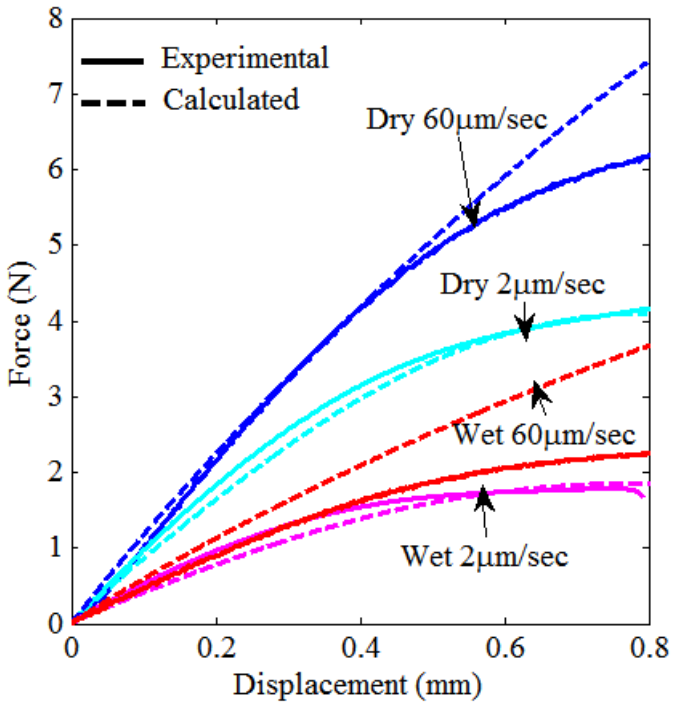

Figure 8-8:Predicted and experimental load displacement curve for dentin adhesives (NR-1) under different moisture content and loading rate.

Figure 8-9 and 8-10 presents the stress-strain distribution in the polymer beam at 60µm/min-dry and 2µm/min-wet environment respectively at selected displacements of δ=0.2mm, δ=0.6mm and δ=0.8mm. As expected dry polymer have larger stress compared to wet polymer at the same displacement level. In both the figures, as expected higher stresses and strains are observed on the outmost layer of the beam in start of the loading. But as the experiment progress elements on the outer layer of beam starts unloading, indicating failure (reduction in load carrying capacity) of corresponding element. Therefore to maintain the overall load, the stress is transferred to inside layers of the beam, as shown in Figure 8-9a δ=0.8mm.

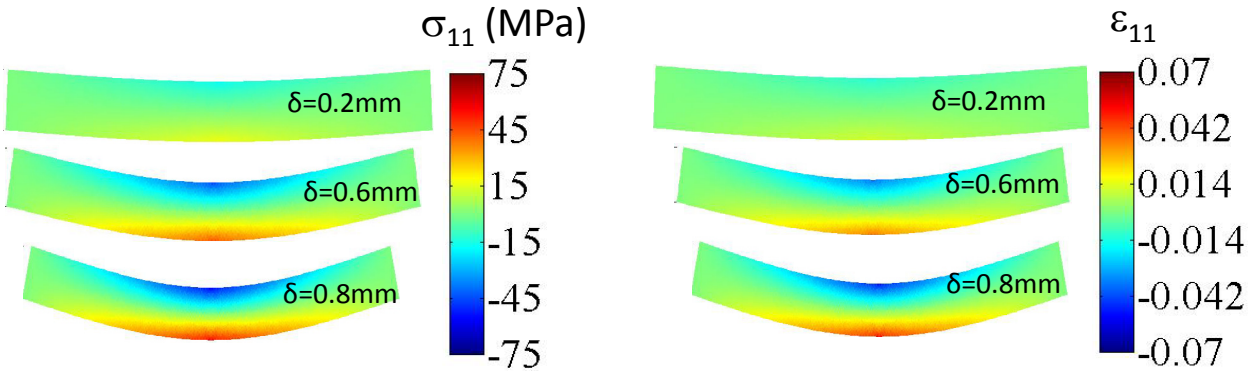

Figure 8-9:Stress distribution in dentin adhesive beam sample at 60μm/min under dry environment

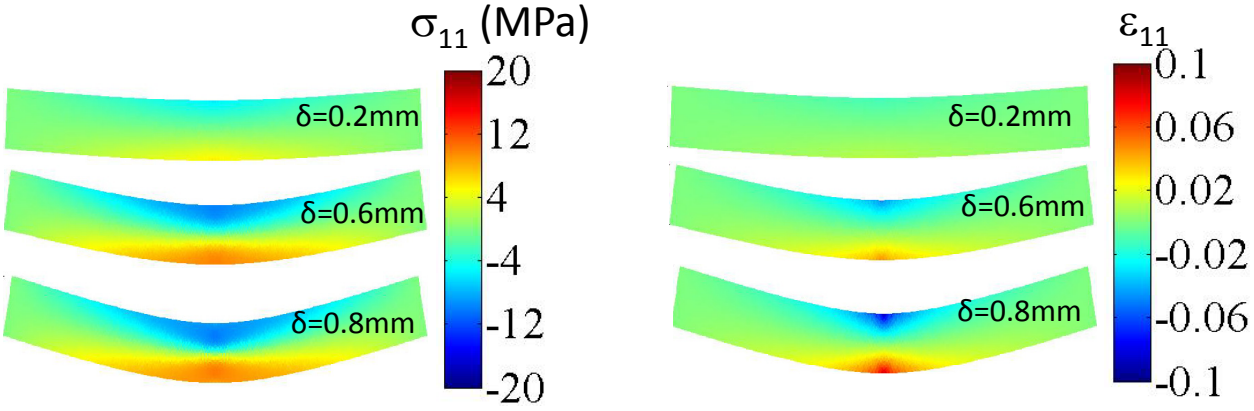

Figure 8-10: Stress distribution in dentin adhesive beam sample at 2μm/min under wet environment

8.4 Summary:

To predict the nonlinear bending of viscoelastic beam, finite element framework presented in chapter 7 is utilized. In particular FE model is utilized to predict the creep and monotonic behavior under different moisture and loading conditions. It is important to mention that, Euler beam bending is a 4^{th} order differential equation which requires at least 2^{nd} order approximation. But in the current work, Euler beam is approximated using a constant triangle element in a plane stress condition; therefore finite element solution depends upon the mesh size. To reduce mesh

dependence larger numbers of elements are used in FE simulation. The FE model is able to predict the overall rate dependent behavior of dentin adhesive under dry and wet environment along with the creep behavior in different moisture condition at load level of 0.3N. Some discrepancies are observed between the model predictions and the experimental observations, but the major advantage of FE is time saving. Creep experiments in laboratory setting took ~120 hours whereas FE simulations time is ~3 hours on a desktop computer.

The FE model results also shows that under simultaneous application of moisture and load, dentin adhesive beams accumulate larger displacements. This accumulation of displacement stops when the polymer beam is completely saturated with water.

Chapter 9

Finite Element model of Adhesive-Dentin (a-d) Interface

9.1 Introduction

The life of composite tooth restoration primarily depends upon the durability/strength of dentin-adhesive interface [20, 26, 27, 64]. Dentin-adhesive (d-a) interface is a transition zone between adhesive and dentin in a composite tooth restoration. Dentin is first etched using acidic agents and adhesive is applied to the etched surface and subsequently a relatively hydrophobic composite is attached to adhesive. This a-d interface is a complex system of different material components and their varying mechanical properties. As previously reported, the properties of these material components greatly affect the overall mechanical behavior of the d-a interface [26, 27, 64].

It has been reported that dentin adhesive and hybrid layer (collagen-adhesive composite) are viscoelastic material, whose properties depends upon loading rate and moisture content [5, 6]. But most of the finite element models of d-a interface previously reported [27, 64] have ignored rate dependent behavior and assumed dentin adhesive and hybrid layer to be linear elastic. In the current study we have developed a finite element model of adhesive-dentin interface, where the material components such as, dentin adhesive, hybrid layer and composite have nonlinear rate dependent behavior and includes deformation induced damage. The constitutive equation used

to describe mechanical response of dentin adhesive and hybrid layer is developed using micromechanical approach (described in detail in chapter 4 and 5 [177]).

9.2 Adhesive-Dentin Interface

Based upon micro-scale structure-property measurements, we have previously developed an idealized microstructural representation of the d-a interface [26, 27]. This idealized model of the d-a interface is utilized to perform micromechanical finite element (μFE) analyses.

Using the results of micro-Raman spectroscopy, scanning acoustic microscopy and optical microscopic imaging [60, 61, 178] tests, the d-a interface may be represented as shown in Figure 9-1. In this idealization the dentin-adhesive interface is considered to be composed of restorative dental composite, adhesive, the hybrid layer (AIDBD or adhesive-collagen composite), exposed collagen, the partially demineralized dentin, and dentin. As a result, a 2d rectangular volume element (RVE) is used to represent d-a interface.

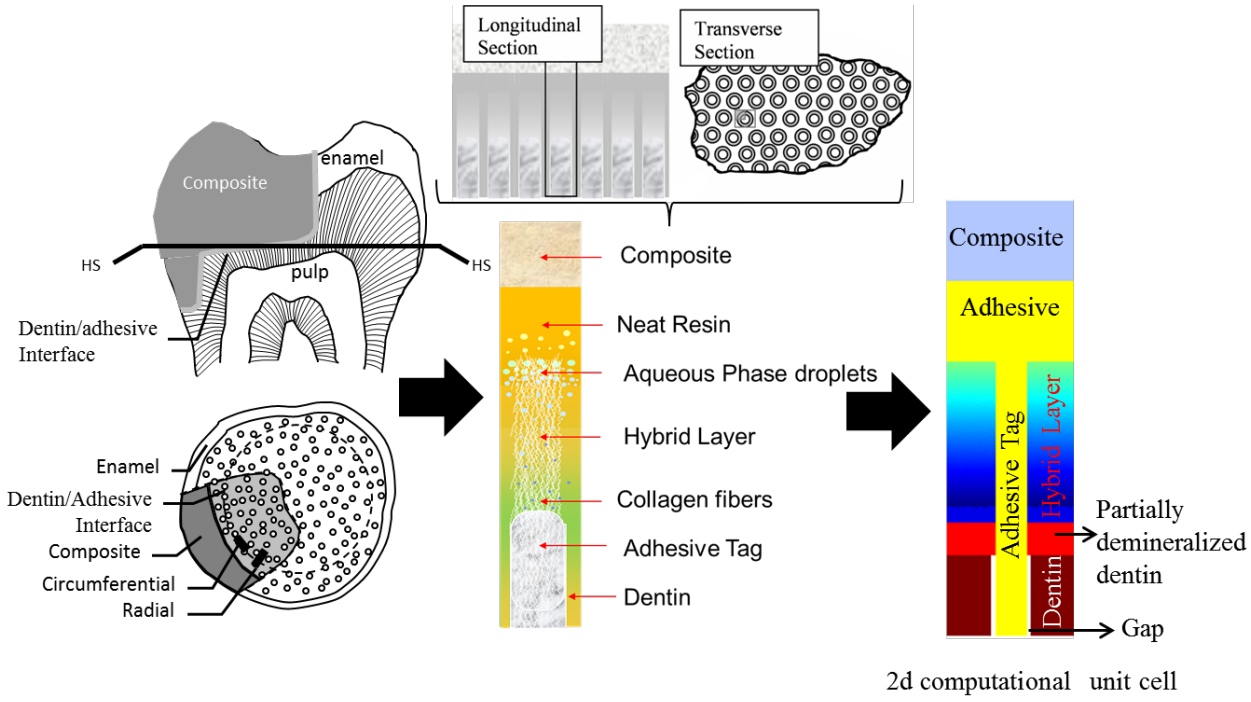

Figure 9-1: Schematic of the a-d interface and 2d rectangular idealized computational unit cell or representative volume element

To study the stress distribution in the d-a interface, the developed RVE of d-a interface was subjected to monotonic loading at different rates in an in-house developed finite element program. The geometrical properties of the interface components were taken from the literature [27]. The computational unit cell was 27.0µm and 8.0µm in longitudinal and transverse sections, respectively. The unit cell is further divided in different sections to represent individual material components in the d-a interface as shown in Figure 9-1. The different material components are: adhesive-collagen composite (hybrid layer), adhesive, restorative dental composite, partially demineralized dentin, peritubular-intertubular dentin and exposed collagen. In the current study peritubular and intertubular dentin is assumed to have similar mechanical properties and referred to as dentin, but under clinical condition peritubular and intertubular dentin will have different properties. The dentin adhesive in the composite tooth restoration appears predominantly in two

places (a) forms a layer under the dental composite and (b) as adhesive tags formed by the flow of adhesive into the dentinal tubules (tubules were opened as a result of acid-etching). The thicknesses of the restorative dental composite, the adhesive layer, and the partially demineralized dentin, dentin and exposed collagen are 5 µm, 5 µm, 2.0 µm, 5.0 µm and 3.0 µm, respectively. In the current study to show the effect of geometry on the overall response of dentin-adhesive interface following variants of the d-a interface are studied, (1) Uniform hybrid layer: mechanical properties of hybrid layer are assumed to be constant along depth of d-a interface, (2) Graded hybrid layer: properties decreases linear along the depth of a-d interface and (3) Graded hybrid layer with defect: case 2 with circular defect in the adhesive tag.

9.3 Boundary Conditions

To capture the mechanical response of a-d interface, we have applied quasi-periodic boundary conditions on the 2d computational cell. The computational unit cell along with the boundary conditions and applied load is given in Figure 9-2

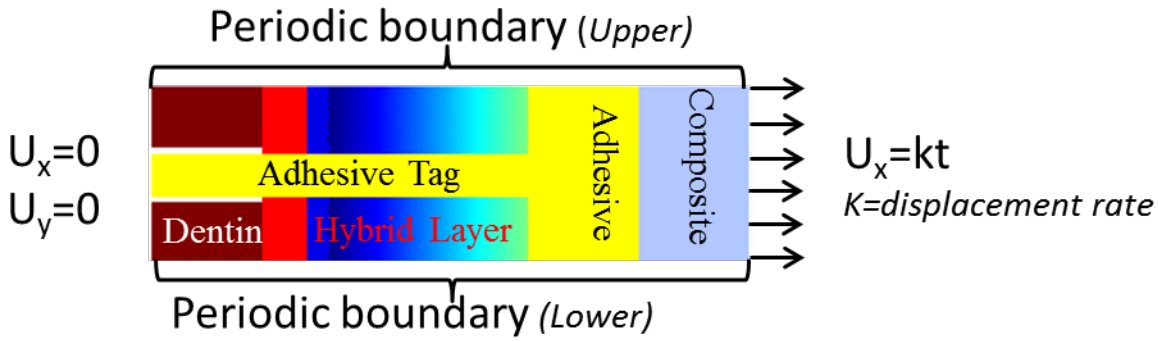

Figure 9-2:2d finite element model showing boundary conditions and load applied.

In the Figure 9-2, on the upper and lower edges of unit cell periodic boundary conditions are applied. Whereas, on the bottom edge of the d-a interface, all the nodes are fixed except those associated with the adhesive tag, because adhesive tag is freely suspended in the dentin tubules. The top surface of the idealized unit cell was subject to monotonically increases displacement at three different loading rates of 0.004um/sec, 0.002um/sec and 0.0002um/sec to show the effect of loading rate on the overall behavior of a-d interface. These simplified boundary conditions are chosen to study the behavior of d-a interface under ideal conditions which provides upper limit for the durability of a-d interface. But under clinical conditions boundary and loading conditions are complex as shown by Singh et al in 3-d FE analysis of a restored tooth [26, 64] In the current model there are 11735 3 node triangular elements and 12036 nodes.

The imposition of Quasi-Periodic Boundary conditions on Non-Periodic Meshes is not a trivial problem [179]. This becomes important with heterogeneous structures, example converting the micro X-ray chromatography data to images and modeling as a representative volume element (RVE) with periodic boundary conditions. Under these situations, the mesh generated is non-periodic which further makes imposition of periodic boundary condition difficult. The most common method of applying periodic boundary condition is slave-master approach. In this method, displacements of two opposite periodic edges are tied together. This approach is computationally expensive and does not include the proper boundary condition (force on the either side should be equal and opposite) and do not work for the non-periodic meshes.

The periodic boundary imply that shape and orientation of two opposite edges remains identical during the deformation and stress vectors acting on those side should be equal and opposite [180]. For the proper implementation of periodic following conditions should be satisfied.

Displacements of nodes on the lower edge in Figure 9-2 should be related to the displacement of nodes on upper edge as:

$$u_i^L = u_i^U - \overline{\varepsilon}_{ij} x_j \tag{9.1}$$

where, $\overline{\varepsilon}_{ij} x_j$ is any micro-strain present inside the RVE, in the absence of micro-strain above equation becomes $u_i^L = u_i^U$

In addition to the displacement condition described above, stress vectors should be equal and opposite on the lower and upper edges, which gives the following relation.

$$t_i^L = -t_i^U \tag{9.2}$$

To implement the periodic boundary condition in this study following procedure is followed:

After mesh generation and assembly of stiffness matrix, following finite element equations were obtain:

$$[K]\{u\} = \{F\} \tag{9.3}$$

where, K is the global stiffness matrix and u is the nodal displacements which are unknown and F is the force applied on the nodes.

The displacement vector u can be rearranged and written as combination of displacement at upper u_u, inner nodes u_i and lower nodes u_l as follows.

$$\{u\} = \begin{Bmatrix} u_u \\ u_i \\ u_l \end{Bmatrix} \tag{9.4}$$

Similarly stiffness matrix K and force vector F can be arranged to obtain the modified form of finite element equations given in Eq 9.3

$$\begin{pmatrix} K_{uu} & K_{ui} & K_{ul} \\ K_{iu} & K_{ii} & K_{il} \\ K_{lu} & K_{li} & K_{ll} \end{pmatrix} \begin{Bmatrix} u_u \\ u_i \\ u_l \end{Bmatrix} = \begin{Bmatrix} F_u \\ F_i \\ F_l \end{Bmatrix} \tag{9.5}$$

It is worth noting that the size of u_u and u_l are not equal for the non-periodic meshes.

Therefore the displacement vector u_u of upper edge is written in terms of u_l displacement vector of lower edge using the interpolation functions. In the current work only linear interpolation functions same as those used for finite element equation are utilized, but higher order interpolation functions can also be used.

$u_u = [z]u_l$ where, Z is the transformation matrix.

Now substituting the value of u_u into the modified FE equation Eq 9.5

$$\begin{pmatrix} K_{uu} & K_{ui} & K_{ul} \\ K_{iu} & K_{ii} & K_{il} \\ K_{lu} & K_{li} & K_{ll} \end{pmatrix} \begin{Bmatrix} [Z]u_l \\ u_i \\ u_l \end{Bmatrix} = \begin{Bmatrix} F_u \\ F_i \\ F_l \end{Bmatrix} \tag{9.6}$$

Further expanding these equations we obtain:

$$\begin{aligned} &[K_{uu}][Z]u_l + [K_{ui}]u_i + [K_{ul}]u_l = F_u \\ &[K_{iu}][Z]u_l + [K_{ii}]u_i + [K_{il}]u_l = F_i \\ &[K_{lu}][Z]u_l + [K_{li}]u_i + [K_{ll}]u_l = F_l \end{aligned} \tag{9.7}$$

In the Eq 9.7, force vector F_u and F_l cannot be added directly because they are of different sizes/dimension. Therefore, first equation in Eq 9.7 is pre-multiplied by [ZT] which is defined as $u_l = [ZT]u_u$ to obtain $[ZT]F_u$ which has same size as F_l.

$$[ZT][K_{uu}][Z]u_l + [ZT][K_{ui}]u_i + [ZT][K_{ul}]u_l = [ZT]F_u \tag{9.8a}$$

$$[K_{iu}][Z]u_l + [K_{ii}]u_i + [K_{il}]u_l = F_i \tag{9.8b}$$

$$[K_{lu}][Z]u_l + [K_{li}]u_i + [K_{ll}]u_l = F_l \tag{9.8c}$$

Now adding Eq 9.8a and 9.8c to obtain the modified form of Eq 9.8c

$$[ZT][K_{uu}][Z]u_l + [ZT][K_{ui}]u_i + [ZT][K_{ul}]u_l = [ZT]F_u \tag{9.9a}$$

$$[K_{iu}][Z]u_l + [K_{ii}]u_i + [K_{il}]u_l = F_i \tag{9.9b}$$

$$([ZT][K_{uu}][Z] + [K_{lu}][Z])u_l + ([ZT][K_{ui}] + [K_{li}])u_i + ([ZT][K_{ul}] + [K_{ll}])u_l = [ZT]F_u + F_l \tag{9.9c}$$

Now using Eq 9.9b and 9.9c and rearranging and collecting the terms associated with u_i and u_l we obtain the modified finite element equations

$$\begin{pmatrix} [K_{ii}] & [K_{iu}][Z] + [K_{il}] \\ [ZT][K_{ui}] + [K_{li}] & [ZT][K_{ul}] + [K_{ll}] + [ZT][K_{uu}][Z] + [K_{lu}][Z] \end{pmatrix} \begin{Bmatrix} u_i \\ u_l \end{Bmatrix} = \begin{Bmatrix} F_i \\ [ZT]F_u + F_l \end{Bmatrix} \tag{9.10}$$

In case of periodic meshes both Z and ZT are identity matrices. The Eq 9.10 is solved for u_i and u_l and thereafter u_u is obtained using the transformation matrix Z as $u_u = [z]u_l$.

9.4 Material Properties

In the current work all the components of adhesive-dentin interface i.e. dentin adhesive, hybrid layer, partially-demineralized-dentin, dentin and exposed collagen are modeled using the micromechanical approach presented in chapters 4 and 5. For dentin adhesive and collagen-adhesive composite (hybrid layer), model parameters obtained from the Euler beam bending calibration procedure were used. Dentin and partially demineralized were assumed to be stiff and less viscous compared to dentin adhesive. The complete list of parameters used is given in Table 9-1. To represents two different geometries of a-d interface, hybrid layer has constant or depth dependent material properties.

Table 9-1: Model parameters for different material components of a-d interface

Dentin Adhesive	Hybrid Layer	Partially Demineralized Dentin	Dentin	Exposed Collagen
E_1=3 GPa G_1=0.5E_1	E_1=1.8-0.3 GPa G_1=0.5E_1	E_1=30 GPa G_1=0.5E_1	E_1=45 GPa G_1=0.5E_1	E_1=0.3 GPa G_1=0.5E_1
E_2=4.5GPa G_w=0.5E_n	E_2=3-0.3GPa G_w=0.5E_n	E_2=45GPa G_w=0.5E_n	E_2=67.5GPa G_w=0.5E_n	E_2=0.3GPa G_w=0.5E_n
μ_n/ E_2=500sec μ_n=0.5μ_w	μ_n/ E_2=750-75sec μ_n=0.5μ_w	μ_n/ E_2=0.005sec μ_n=0.5μ_w	μ_n/ E_2=0.003sec μ_n=0.5μ_w	μ_n/ E_2=75sec μ_n=0.5μ_w
B_n=0.01 B_w=B_n	B_n=0.02-0.18 B_w=B_n	B_n=0.025 B_w=B_n	B_n=0.05 B_w=0.5B_n	B_n=0.18 B_w=0.5B_n
B=5	B=5	B=5	B=5	B=5
α_n=1, α_w=α_n	α_n=1, α_w=α_n	α_n=1, α_w=α_n	α_n=1, α_w=α_n	α_n=1, α_w=α_n

9.5 Finite Element Result

The results of finite element simulation of a-d interface under different loading and geometry are show in Figure 9-3 to 9-6. The Figure 9-3 shows the evolution of overall stress in a representative volume element of a-d interface as it is loaded under monotonically increasing displacement.

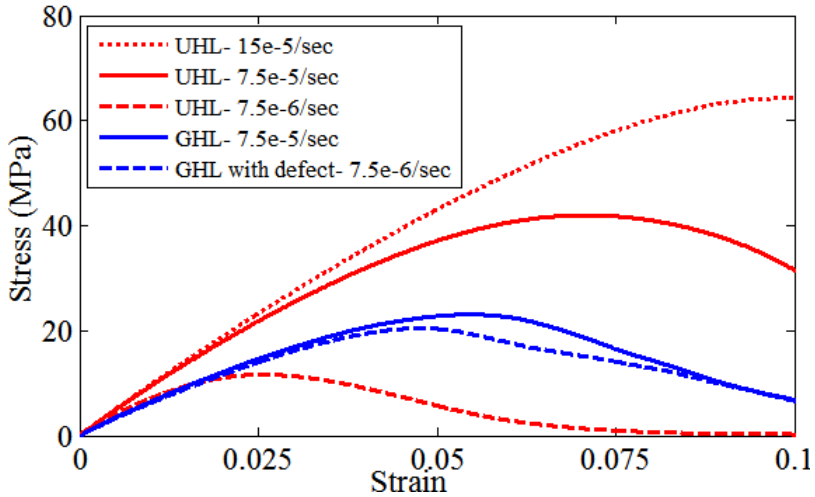

Figure 9-3: Overall stress-strain behavior of a-d interface at different loading rate and geometry

Figure 9-3 shows that, with the increase in loading rate, maximum stress obtain in a a-d interface increasing. This increasing in stress is expected, because of the rate dependent behavior of

material components such as adhesive, composite and hybrid layers. In particular the strength of a-d interface with uniform hybrid layer (UHL) decreased from ~64MPa at strain rate 15e-5/sec to ~11.5MPa at 7.5e-6/sec, which is 20 times lower. It is worthwhile to note that, not only the maximum stress increases with increase of loading rate, but also the strain corresponding to maximum stress increases; indicating stiffer and ductile behavior of a-d interface. On the other hand, if loading rate is kept constant and the geometry of a-d interface is changed, then also the strength/durability of d-a interface changes. As seen from the Figure 9-3 at strain rate of 7.5e-5/sec strength of a-d interface with UHL, GHL and GHL-with-defect is found to be ~42MPa, ~23MPa and ~20.5MPa respectively. It is important to note that, in this study defects smaller than 250nm are homogenized to get the materials properties. For example dentin adhesive will phase separate when formed in the presence of water. This phase separation will create nano-scale defects, these defects are homogenized in the current work. Defects larger than 250nm can be modeled as part of a-d interface. Not only the size of defect but also the location of the defect will affect the overall response of d-a interface. In this study a circular defect of size radius 500nm was introduced in the adhesive tag

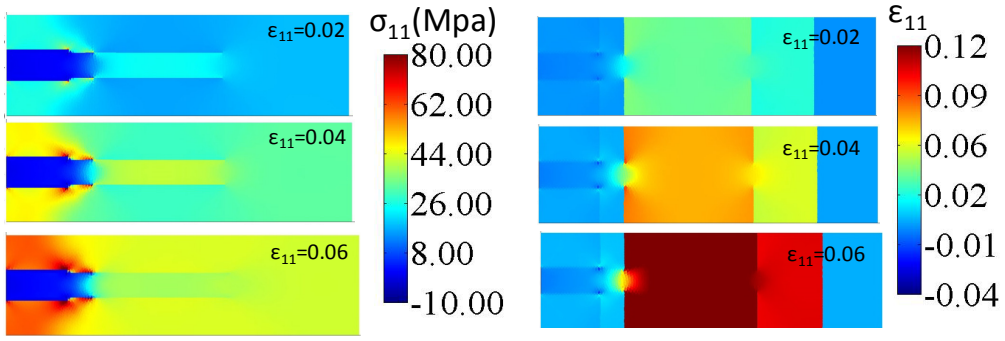

Figure 9-4:Stress-strain distribution in a-d interface with uniform hybrid layer at different strain levels

The developments of stress and strain contours in a-d interface with UHL, GHL and GHL-with-defect at strain rate of 7.5e-5 are shown in Figures 9-4, 9-5 and 9-6 respectively. The stress and strain contours are presented at the strain levels of 0.02, 0.04 and 0.06. In the case of a-d interface with UHL at 0.02 strain level, higher stress is observed in adhesive tags, these adhesive tags are formed when dentin adhesive flows into the hollow dentin tubules. Whereas, hybrid layer experiences small and uniform stress, due to the presence of constant material properties along the depth of hybrid layer. At the strain level of 0.04 adhesive tag experiences much larger stress, but when the strain level reaches 0.06, stress in the adhesive tag decreases as show in Figure 9-4. This decrease in the stress in adhesive tag with increase in strain indicates that, material component has reached its peak stress level and is exhibiting strain induced softening, which indicates failure. If the loading is continued further, stress in adhesive tag will continue to decrease and will ultimately lead to rupture of adhesive tag

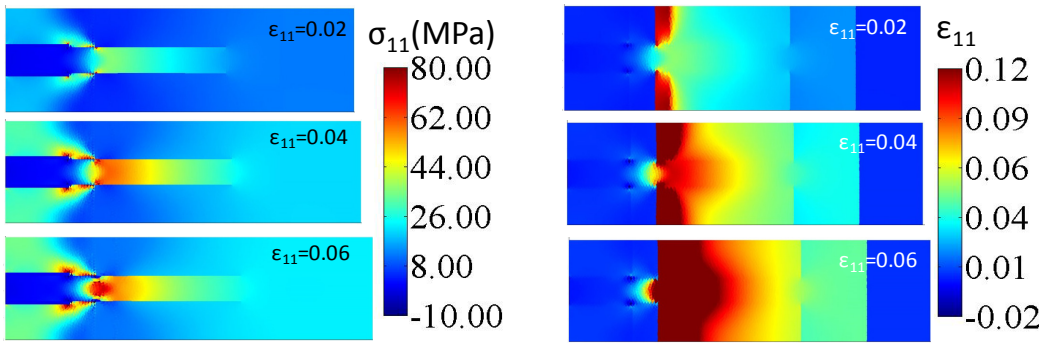

Figure 9-5: Stress-strain distribution in a-d interface with graded hybrid layer at different strain levels

Stress and strain distribution in a-d interface with GHL is presented in Figure 9-5. In a-d with GHL, adhesive flows into the demineralized dentin from top to bottom and forms a collagen-adhesive composite of gradually decreasing properties. This process results in a layer of un-infiltrated demineralized dentin sometimes termed as exposed collagen. This exposed collagen

is absent in the a-d interface with UHL. From Figure 9-5 we observe that, stress in adhesive tag increases gradually from top to bottom, whereas in UHL, stress is approximately uniform along the depth of adhesive tag at any given strain level. The increase in stress along the depth of adhesive tag is caused by the depth dependent material properties of hybrid layer. Material properties of hybrid layer decreases from top to bottom, which causes the transfer of stress from the hybrid layer to adhesive tag.

If we concentrate on the strain distribution in Figure 9-5, we observe that larger strains are observed in the exposed collagen, which is expected due to the soft nature of collagen, and can experience larger deformations without rupture. It is important to note that though exposed collagen region is the weakest and one would expect the failure to concentrate in this region. But from the stress distribution in d-a interface with GHL, we observe that comparatively small stresses are observed in exposed collagen, though the strains are very large. Also we observe that, similar to a-d interface with UHL, stress in adhesive tag in GHL decreases beyond a certain strain level, indicating failure, i.e. reduction in the capacity of a-d interface to sustain load. Other material components of a-d interface such as composite, adhesive, dentin experiences ~uniform stress distribution.

Stress and strain distributions in a-d interface with GHL along with a micro-scale defect in adhesive tag is presented in Figure 9-6

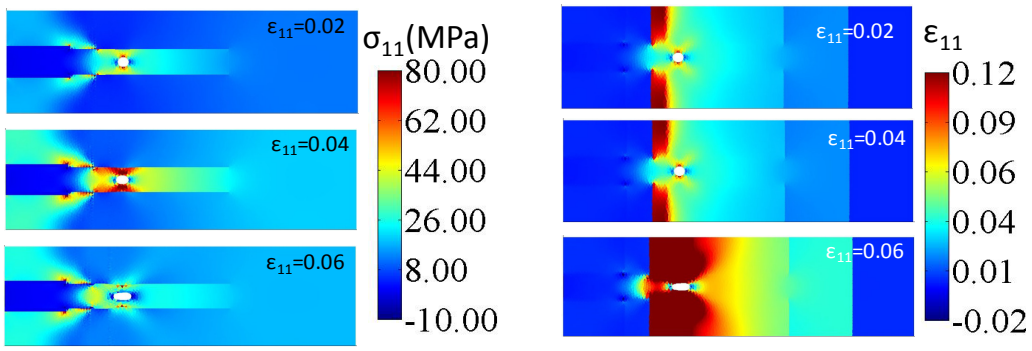

Figure 9-6: Stress-strain distribution in a-d interface with graded hybrid layer and micro-defect in adhesive at different strain levels

Presence of defect disrupts the stress and strain distribution as seen from the Figure 9-6. This micro-scale defect causes a localized failure in the adhesive tags, once the tag is failed stress is transferred to the neighboring hybrid layer. The transfer of stress can be seen in stress distribution at strain level of 0.06 in Figure 9-6. The presence of defects causes initial failure in tag and thereafter failure propagates through hybrid layer, ultimately causing the fracture of a-d interface.

9.6 Summary

This chapter presents the implementation of the developed finite element framework in chapter 7 to predict the durability of adhesive-dentin interface under monotonic loading condition. Two different geometries of a-d interface are considered, (a) material properties are constant along the depth of hybrid layer and (b) material properties gradually decrease along the depth. Further, to accurately predict the representative behavior of a-d interface, quasi-periodic boundary conditions are applied on the 2d computational unit cell of a-d interface. For the application of quasi-periodic boundary conditions, a robust scheme is proposed which can be applied to study asymmetric meshes under periodic boundary conditions. Finite element simulation shows that,

strength of a-d interface is affected by both the loading rate and geometry of a-d interface. For the constant loading rate, a-d interface with uniform hybrid layer have the highest strength, whereas a-d interface with graded hybrid layer with defect in adhesive tags have the lowest strength. Stress analysis showed that adhesive tag is the weakest components in a-d, i.e. it undergo strain induced softening earlier than other material components.

Chapter 10 Finite Element Model of Pavement

10.1 Introduction

Repeated application of tire loads on the asphalt pavement creates permanent deformation and surface cracks which causes discomfort to the driver. Therefore to predict the plastic deformation in the asphalt pavement we have developed a 2d finite element (FE) model of pavement. In the current work, the hot mix asphalt layer is modeled using a granular micromechanics approach to obtain the nonlinear rate-dependent material model with damage and plasticity. The FE model was subjected to different load levels to demonstrate the nonlinear response of pavement, further to estimate the plastic strain, load was removed and pavement was allowed to recover to a stress free condition.

10.2 Geometry, Load and Boundary Conditions

In the current work asphalt pavement is idealized using a two layers system, top layer constitutes of 50mm thick HMA and the second layer is 750mm base layer. Pavement width is taken to be 2800mm and load step to be 1/10 of the pavement width. Following boundary conditions were used, bottom edge of the base layer is fixed in both vertical and horizontal directions, and both the left and the right edges has displacement constrained in horizontal direction and free in vertical direction. The geometry and boundary conditions are show in Figure (10-1a). To simulate the repeated tire load, compressive pressure in the form of square wave is applied on the

280mm wide step, which corresponds to the MICHELIN radial 11R22.5 tire. Applied square load wave is shown in Figure (10-1b), one load-unload cycles constitutes of 0.5sec hold time at the peak load followed by a hold time of 0.5sec at zero load, this load-unload cycles is repeated 1000 times.

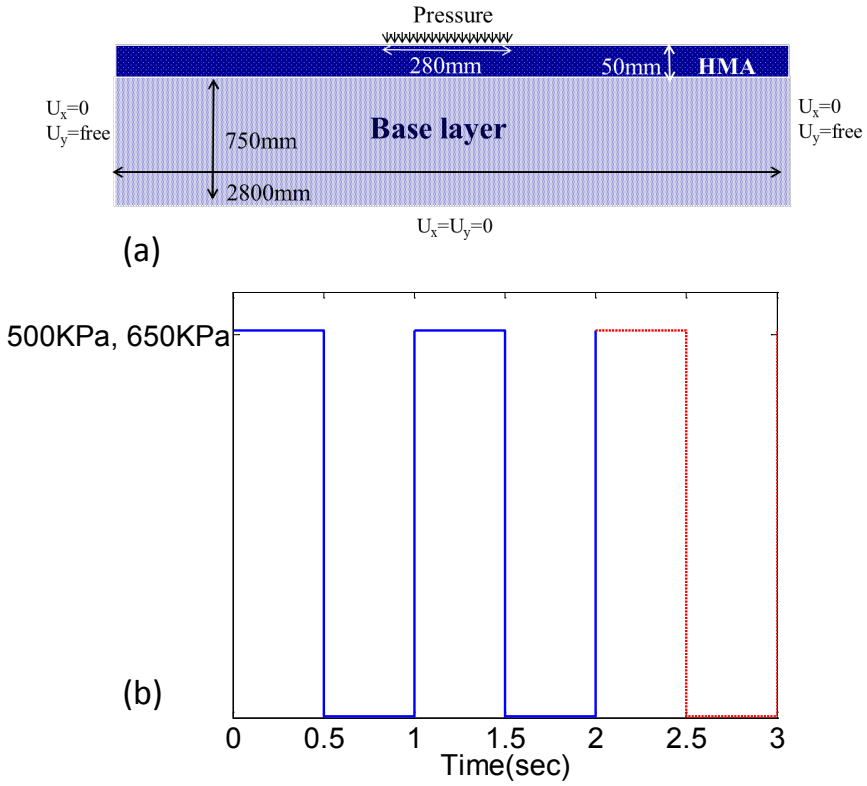

Figure 10-1: (a) FE model of asphalt pavement with applied loads and associated boundary conditions and (b) square wave used in the simulation

Also to save the computation time, symmetry of the boundary value problem is used and only half of the pavement is modeled. Further to show the effect of load levels on the rutting depth, we have considered two loading levels 500KPa and 650KPa for 1000 cycles. Thereafter load is removed and pavement is allowed to recover to estimate the permanent or plastic deformation. The pavement is meshed using constant strain triangle elements to generate 4702 elements and 2438 nodes.

10.3 Material Properties

Top layer of pavement i.e. HMA is modeled using the constitutive equation present in current work in chapter 4 & 5. The calibration process and model parameter for the asphalt layer is provided in chapter 5. The base layer is assumed to be stiffer and less viscous compared to that of HMA layer. It is important to note that, properties of base layer are chosen such that it has small damage and less permanent deformation, but other combination of parameter can be used. The parameter used for the two layers are given in Table 10-1

Table 10-1 Model parameters for HMA and baser layer in the pavement model

HMA	Base Layer
E_1=2.4 GPa, G_1=0.8E_1	E_1=24 GPa, G_1=0.8E_1
E_2=0.3Gpa, G_w=E_n	E_2=3GPa, G_w=E_n
μ_n/ E_2=57sec, μ_n=μ_w	μ_n/ E_2=0.057sec, μ_n=μ_w
B_n=0.0143, B_w=B_n	B_n=0.0715, B_w=B_n
B=3.8	B=3.8
β_n=0.833, β_w=β_n	β_n=0.333, β_w=β_n
α_n=0.175, α_w=α_n	α_n=0.175, α_w=α_n

10.4 Results and Discussion

Figure 10-2 to 10-5 presents the results of the FE simulations of pavement under 500KPa and 650Kpa stress. The stress distribution in vertical and horizontal directions in the pavement is given in Figure 10-2. As expected, in vertical direction larger compressive stresses are observed near the loading step, which gradually decreases with the depth. Stresses in the horizontal direction are small compared to that of vertical and tensile stresses are observed on the edge of loading step and at the interface of HMA and base layer.

Rutting depth at the center of loading step for the two load levels is shown in Figure 10-3a. Because the load and unload times were fixed at 0.5sec, the time for one complete cycle i.e. load-unload is 1sec, therefore Figure 10-36a also represents rutting depth as function of number

of cycles (N) or load passes. During the simulation, 1000 cycles were applied and thereafter load was removed and pavement was allowed to recover.

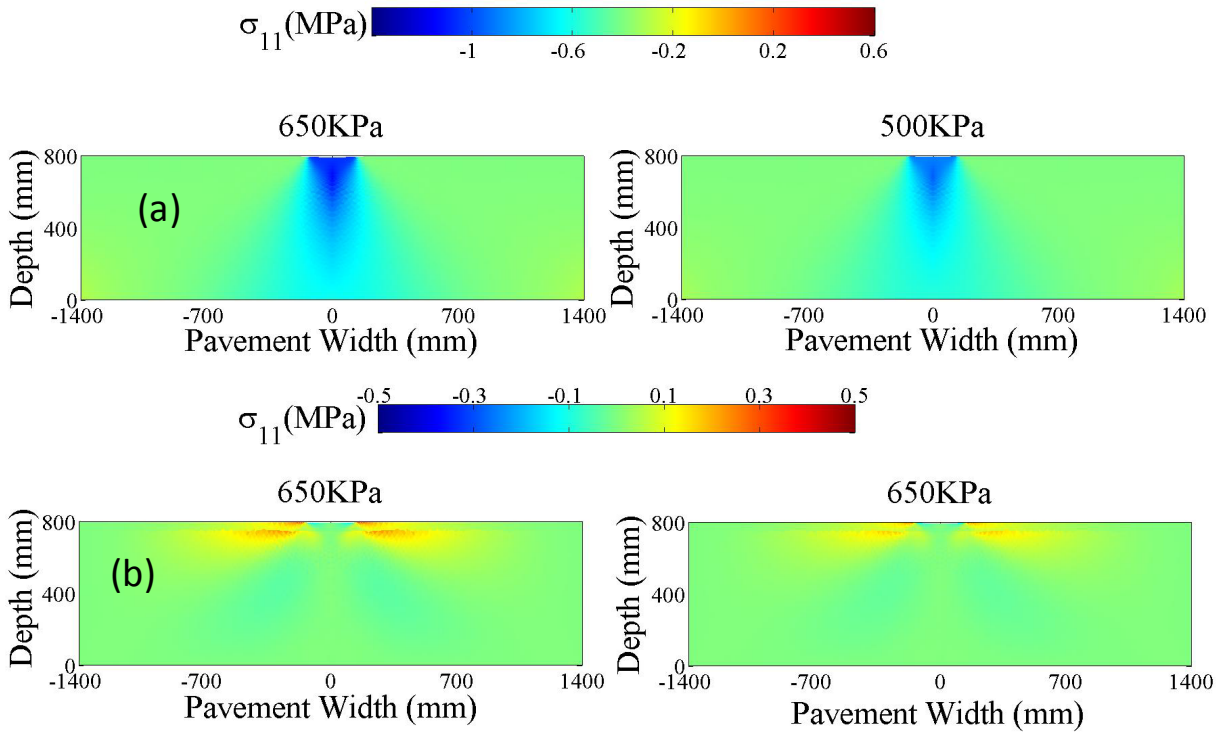

Figure 10-2: Stress distribution on asphalt pavement under 650KP and 500KPa (a) vertical stress distribution and (b) horizontal stress distribution

From Figure 10-3a we observe that at time t=0, instantaneously displacement is ~0.96mm and ~1.25mm for 500KPa and 65KPa respectively, this deformation at t=0 corresponds to the elastic nature of the pavement. We further observe that, for the small number of cycles, increase in the applied load causes a linear increase in the rutting depth. For example, at N=50 30% increase in load causes ~30% increase in rutting depth. But, as the tests progress, rutting depth increases at faster rate under 650KPa load level, after the completion of 1000 cycles, rutting depth was ~2.85mm and ~1.65mm for 650KPa and 500KPa. It is interesting to note that, though the applied load was only increased by 1.3 times from 500KPa to 650KPa, but final rutting depth

increases by a factor of 1.7 indicating nonlinear behavior. At last, after the completion of the load cycles, pavement was allowed to recover and amount of residual or plastic displacement was estimated, for the loads of 500KPa and 650KPa the plastic displacements were 0.575mm and 1.31mm respectively. Again the amount of plastic strain at 650KPa is 2.27 times of plastic strain at 500KPa.

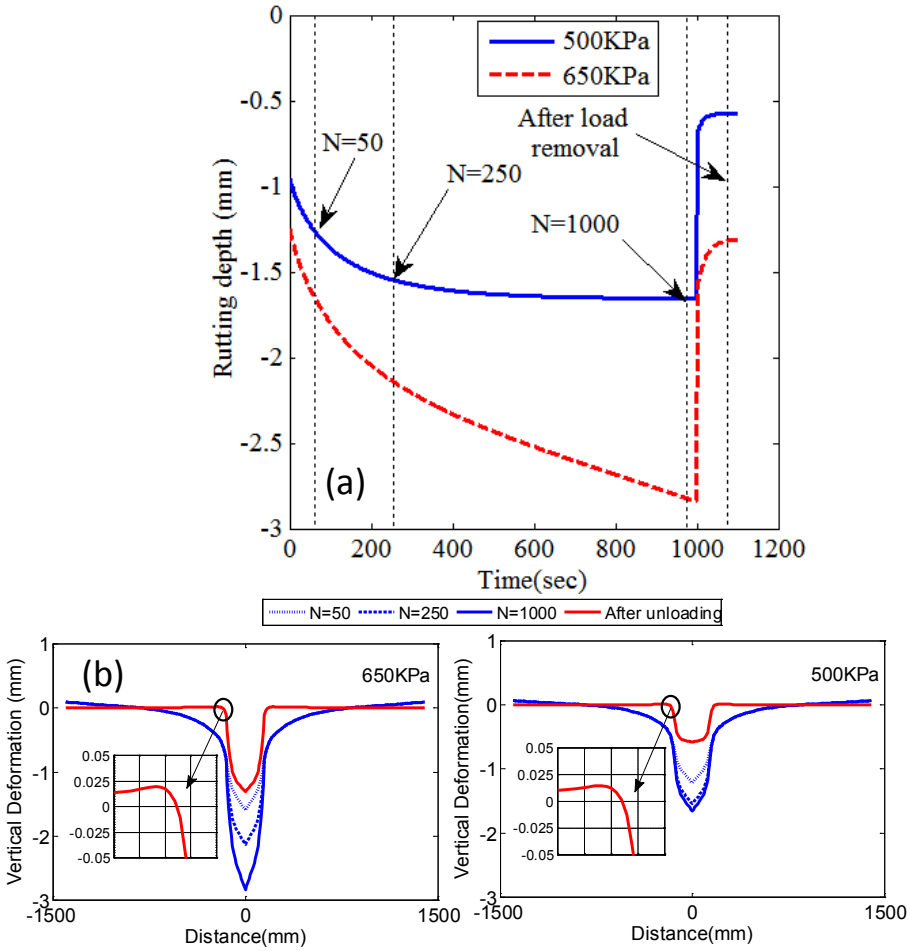

Figure 10-3: (a) Rutting depth at the center of loading step and (b) rutting depth with pavement width

For the illustration purpose we plot the rutting displacements across the pavement width at different number of cycle in Figure 10-3b. It worthwhile to note that, there is a small amount of

tensile displacement close to the edge of loading step, which is highlighted in the inset of Figure 10-3b.

Displacement contours in the vertical direction after 1000 cycles and after completion unloading process for the two stress amplitudes is plotted in Figure 10-4. From the results we observe that, after 1000 cycles, HMA layer accumulates larger vertical displacements and only part of the displacements are recovered after the removal of load resulting in plastic or permanent displacement. We also observe that, displacement of the base layer recovers almost to zero indicating little plastic deformation in the base layer. It is important to note that, properties of base layer were chosen such that there should be little plastic displacement.

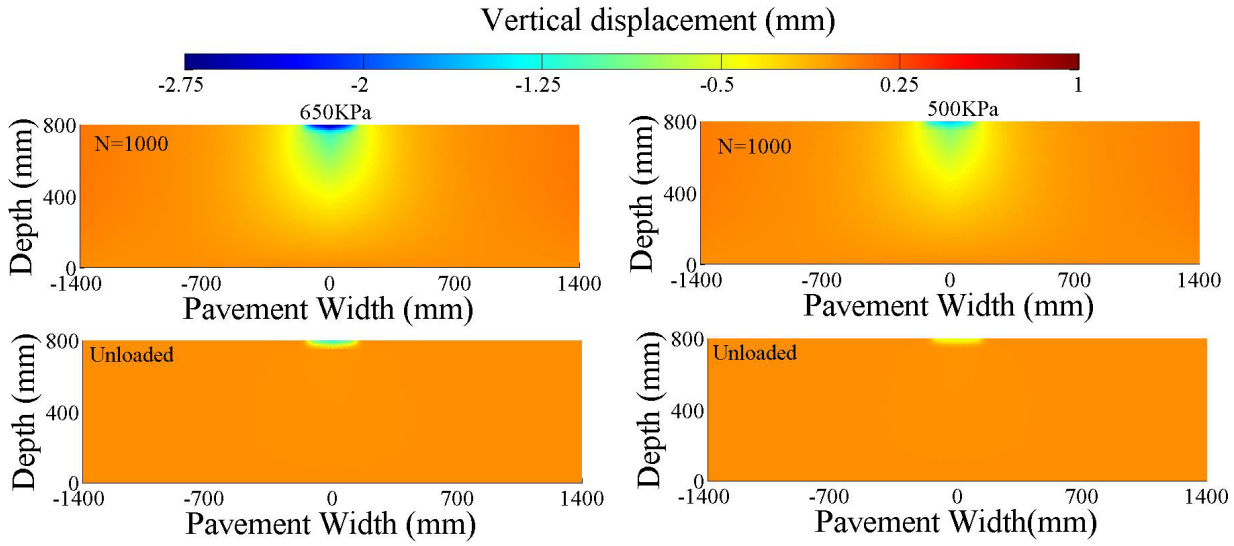

Figure 10-4: Vertical displacement in the pavement at the end of 1000 load pases and after removal of load

Strain distribution in vertical and horizontal in the 50mm HMA layer is plotted in Figure 10-5 at different number of load-unload cycles. For both the stress amplitudes, both the vertical and horizontal strains increases with the number of cycles, for the 500KPa stress amplitude strain distribution do not change significantly after 250 load passes, this shows that deformation in the

pavement has reached a asymptote. Further to estimate the amount of plastic strain, load was removed and pavement was allowed to recover for sufficiently long time, both load levels have significant plastic strain. Horizontal strain presented in Figure 10-5b show tensile stress on the edge of loading step, this indicates the initiation of crack on the surface of HMA.

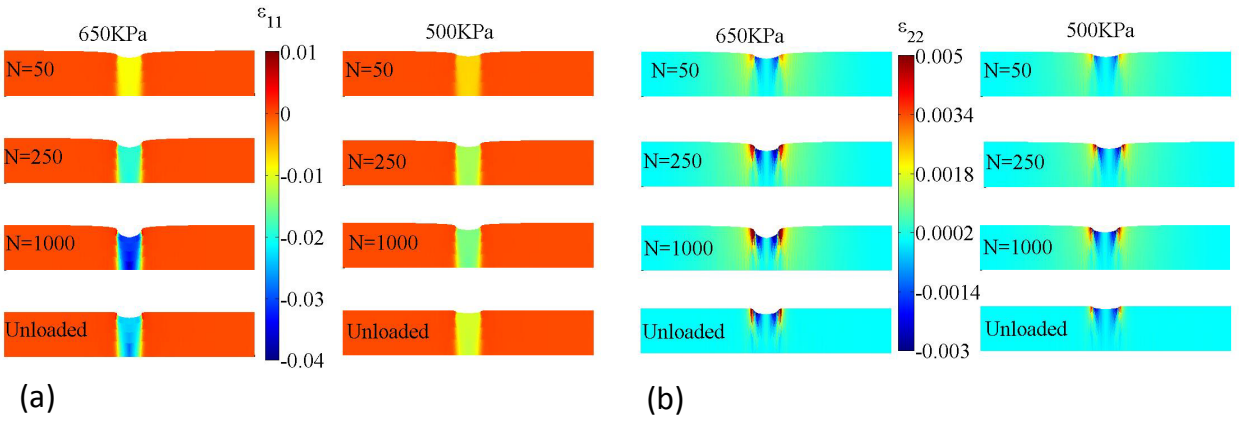

Figure 10-5: Strain distribution on the HMA layer (a) vertical direction and (b) horizontal direction

10.5 Summary

In the current work nonlinear rate-dependent material model with damage and plasticity is implemented into a finite element framework to predict the rutting and surface cracking of hot mix asphalt pavement under traffic conditions. The major advantage of the current methodology is that, complex yield criterion and plastic function are not required to model plastic deformation. To calculate plastic deformation of pavement, a 2d FE model was constructed and subjected to 1000 load-unload cycles, representing traffic load. For simplicity, the FE model has two layers, top layer constitutes of HMA and bottom layer represents the base material. The simulations results demonstrated that 30% increase in the applied load causes approximately 127% increase in the rutting depth at the center of loading step. Also horizontal tensile plastic strain is observed at the top of pavement, this indicates cracking of pavement under the applied load.

Chapter 11

Conclusion and Future Work

11.1 Conclusion

This work presents the granular micromechanics framework to obtain the constitutive equations, which includes the effect of micro-scale properties on the overall material response. The current methodology is utilized to obtain stress-strain relationships for nonlinear rate dependent Zener type solids, such as, dentin adhesive, hot mix asphalt and other polymeric materials. The framework presented is general and is not restrictive to a particular form of inter-granular or micro-scale interaction and can be applied to a range of physical or chemical phenomena that effect micro-scale interactions. The resultant constitutive model has the ability to predict loading induced material anisotropy, particularly under evolving multi-axial loading. This phenomenon is absent in most of the phenomenological models. In addition to this, plastic potential, damage function and flow rule are defined at the micro-scale using relatively simple 1d functions. Whereas, in classical plasticity and damage mechanics, complex yield criterion, plastic potentials, hardening functions, damage functions and their evolution laws with loading have to be formulated.

In addition to the theoretical development of the constitutive model, a robust explicit numerical scheme which is both stable and computationally fast is presented. Also the model is

implemented into an Euler beam bending and finite element framework to predict the responses of various structural components. Model capabilities are demonstrated by its ability to predict complex mechanical behaviors, such as, moisture induced nonlinear bending of dentin-adhesive beams, tertiary creep, creep-recovery and monotonic behavior of hot mix asphalt and prediction of the strength of adhesive-dentin interface and plastic deformation in pavement.

11.2 Future Work

Following recommendations are made for the future studies.

11.2.1 Experimental Work

(1) In the current work only bending experiments are performed, but to obtain the complete stress-strain response of polymer samples, shear experiments should be performed. Also it is assumed that dentin-adhesive have symmetric response in tension and compression. But in reality, polymers have asymmetric response; therefore tensile and compressive experiments should be performed.

(2) Collagen-adhesive (AIDBD) samples in this study were tested at the displacement rate of 60μm/min. But these are viscoelastic material and experiments should be performed at different displacement rates.

(3) Also, creep recovery and loading and unloading experiments should be performed to determine the amount of plastic deformation in the dentin-adhesive and collagen-adhesive composite samples.

11.2.2 Theoretical Work

(1) In the current work, while obtaining the constitutive equations, kinematic assumption was utilized to connect macro-scale deformation to micro-scale. But in general, this is not a strong assumption; therefore other possibilities should be explored.

(2) In the development of inter-granular kinematics, higher order terms in the Taylor series expansion of displacements were ignored. Higher order terms of the Taylor series should be considered. This will lead to second or higher gradient models, which are very useful in modeling crack propagation and facture problems.

(3) It is observed that many polymeric materials have multiple characteristic times, spanning over several decades. Therefore, inter-granular force displacement functions should be modeled using Prony series.

(4) Currently, trial-error approach is used to identify model parameters. In future, a more efficient and accurate optimization technique should be used

(5) Developed finite element framework should be extended to model 3d boundary value problems.

Appendix A

DIRECTIONAL PROBABILITY DENSITY FUNCTION

The probability density function of inter-granular orientation vector n_i, $\xi(\theta,\phi)$, is written in a discrete form as follows[181]:

$$\xi(\theta,\phi) = \frac{1}{M}\sum_{j=1}^{M}\delta\left(n_i - n_i^j\right) \tag{A.1}$$

where, M is the total number of inter-granular contacts, delta function $\delta(n_i - n_i^j) = \delta(\theta-\theta^j)\delta(\phi-\phi^j)/\sin(\theta^j)$, and the superscript j refers to the observed inter-granular vectors. Eq. A.1 can be estimated as smooth orientation distribution function by fitting with parametric forms discussed by Kanatani [182], among which the following polynomial form is simple to handle in 3-dimensions:

$$\xi(\theta,\phi) = \frac{1}{4\pi}\left[1 + \Phi_{ij}n_i n_j + \Phi_{ijkl}n_i n_j n_k n_l + \cdots\right] \tag{A.2}$$

where the n-th rank tensors Φ are coefficient tensors. The expansion is equivalent to the spherical harmonic expansion given as (see also [80]):

$$\xi(\theta,\phi) = \frac{1}{4\pi}\left\{1 + \sum_{k=2}^{\infty}{}'\left[a_{k0}P_k\left(\cos\theta\right) + \sum_{m=1}^{k}P_m^k\left(\cos\theta\right)\left(a_{km}\cos m\phi + b_{km}\sin m\phi\right)\right]\right\} \tag{A.3}$$

where Σ' = summation over even indices, P_k = k-th Legendre polynomial, P_k^m = the associated Legendre functions, and a_{k0}, a_{km} and b_{km} are the coefficients. Other forms of smooth directional distribution function, particularly exponential forms that appear as extensions of von Mises or

Fisher distributions may be used, especially when we need to represent highly directional data. For practical calculations, Eq. A.3may be truncated to model different material symmetry. For the calculations in this work, the materials is considered to be isotropic, thus

$$\xi(\theta,\phi)=\frac{1}{4\pi} \tag{A.4}$$

List of References

1. Stakston, A.D. and H.U. Bahia, *The effect of fine aggregate angularity, asphalt content and performance graded asphalts on hot mix asphalt performance*. WisDOT Highway research study. 2003, Madison, Wisconsin: Springfield, VA. vii, 148 leaves.
2. Stroup-Gardiner, M. and American Society for Testing and Materials., *Constructing smooth hot mix asphalt (HMA) pavements*. Stp. 2003, West Conshohocken, PA: ASTM. viii, 153.
3. White, T.D., et al., *Contributions of pavement structural layers to rutting of hot mix asphalt pavements*. NCHRP report,. 2002, Washington, D.C.: National Academy Press. 151, A-6.
4. Gunatillake, P.A. and R. Adhikari, *Biodegradable synthetic polymers for tissue engineering.* Eur Cell Mater, 2003. **5**: p. 1-16; discussion 16.
5. Singh, V., et al., *Viscoelastic and fatigue properties of model methacrylate-based dentin adhesives.* J Biomed Mater Res B Appl Biomater, 2010. **95**(2): p. 283-90.
6. Singh, V., et al., *Mechanical properties of methacrylate based model dentin adhesives: effect of loading rate and moisture exposure.* Journal of Biomedical Material Research: Part B-Applied Biomaterials, 2013.
7. Darabi, M.K., et al., *A thermo-viscoelastic-viscoplastic-viscodamage constitutive model for asphaltic materials.* International Journal of Solids and Structures, 2011. **48**(1): p. 191-207.
8. Pipkin, A.C. and T.G. Rogers, *A Non-Linear Integral Representation for Viscoelastic Behaviour.* Journal of the Mechanics and Physics of Solids, 1968. **16**(1): p. 59-&.
9. Wineman, A., *Nonlinear Viscoelastic Solids - A Review.* Mathematics and Mechanics of Solids, 2009. **14**(3): p. 300-366.
10. Lai, J. and A. Bakker, *3-D schapery representation for non-linear viscoelasticity and finite element implementation.* Computational Mechanics, 1996. **18**(3): p. 182-191.
11. Schapery, R.A., *On the characterization of nonlinear viscoelastic materials.* Polymer Engineering & Science, 1969. **9**(4): p. 295-310.
12. Schapery, R.A., *Nonlinear viscoelastic solids.* International Journal of Solids and Structures, 2000. **37**(1-2): p. 359-366.
13. Green, A.E. and R.S. Rivlin, *The Mechanics of Non-Linear Materials with Memory .1.* Archive for Rational Mechanics and Analysis, 1957. **1**(1): p. 1-21.
14. Drozdov, A.D., *A constitutive model for nonlinear viscoelastic media.* International Journal of Solids and Structures, 1997. **34**(21): p. 2685-2707.
15. Beijer, J.G.J. and J.L. Spoormaker, *Solution strategies for FEM analysis with nonlinear viscoelastic polymers.* Computers & Structures, 2002. **80**(14-15): p. 1213-1229.
16. Levesque, M., et al., *On the development and parameter identification of Schapery-type constitutive theories.* Mechanics of Time-Dependent Materials, 2008. **12**(2): p. 95-127.

17. Pipkin, A.C. and T.G. Roger, *A non-linear integral representation for viscoelastic behaviour.* Journal of the Mechanics and Physics of Solids, 1968. **16**(1): p. 59-72.
18. Abu Al-Rub, R.K. and M.K. Darabi, *A thermodynamic framework for constitutive modeling of time- and rate-dependent materials. Part I: Theory.* International Journal of Plasticity, 2012. **34**: p. 61-92.
19. Ziegler, H., *An Introduction to thermomechanics* Second ed. 1983: North-Holland.
20. Spencer, P., et al., *Adhesive/Dentin interface: the weak link in the composite restoration.* Annals of Biomedical Engineering, 2010. **38**(6): p. 1989-2003.
21. Spencer, P., et al., *Durable bonds at the adhesive/dentin interface: an impossible mission or simply a moving target?* Braz Dent Sci, 2012. **15**(1): p. 4-18.
22. Marangos, O., et al., *Scanning acoustic microscopy investigation of frequency-dependent reflectance of acid- etched human dentin using homotopic measurements.* IEEE Trans Ultrason Ferroelectr Freq Control, 2011. **58**(3): p. 585-95.
23. Pashley, D.H., et al., *Permeability of dentin to adhesive agents.* Quintessence Int, 1993. **24**(9): p. 618-31.
24. Kleverlaan, C.J. and A.J. Feilzer, *Polymerization shrinkage and contraction stress of dental resin composites.* Dent Mater, 2005. **21**(12): p. 1150-7.
25. Roulet, J.F., *Benefits and Disadvantages of Tooth-coloured Alternatives to Amalgam. J Dent.* J Dent, 1997. **25**: p. 459-473.
26. Misra, A., et al., *Micromechanical Analysis of Dentin/Adhesive Interface by the Finite Element Method.* J Biomed Mater Res Part B: Appl Biomater, 2004. **70B**: p. 56-65.
27. Misra, A., et al., *Parametric Study of the Effect of Phase Anisotropy on the Micromechanical Behavior of dentin-adhesive Interface.* Journal of Royal Society Interface, 2005. **2**: p. 145-157.
28. Park, J., et al., *Synthesis and evaluation of novel dental monomer with branched aromatic carboxylic acid group.* J Biomed Mater Res B Appl Biomater, 2011.
29. Armstrong, S., et al., *Adhesion to tooth structure: a critical review of "micro" bond strength test methods.* Dent Mater, 2010. **26**(2): p. e50-62.
30. Armstrong, S.R., D.B. Boyer, and J.C. Keller, *Microtensile bond strength testing and failure analysis of two dentin adhesives.* Dental Materials, 1998. **14**(1): p. 44-50.
31. Roeder, L., et al., *Spotlight on bond strength testing--unraveling the complexities.* Dent Mater, 2011. **27**(12): p. 1197-203.
32. Yiu, C.K.Y., et al., *Effect of resin hydrophilicity and water storage on resin strength.* Biomaterials, 2004. **25**(26): p. 5789-5796.
33. Park, J.G., et al., *Dynamic mechanical analysis and esterase degradation of dentin adhesives containing a branched methacrylate.* J Biomed Mater Res B Appl Biomater, 2009. **91**(1): p. 61-70.
34. Parthasarathy, R., et al., *Diffusion coefficients of water and leachables in methacrylate-based crosslinked polymers using absorption experiments.* J Mater Sci Mater Med., 2012. **23**(5): p. 1157-1172.
35. Israelachvili, J.N., *Intermolecular and surface forces*. 3rd ed. 2011, Burlington, MA: Academic Press. 674.
36. Habeger, C.C. and D.W. Coffin, *The role of stress concentrations in accelerated creep and sorption-induced physical aging.* Journal of Pulp and Paper Science, 2000. **26**(4): p. 145-157.

37. Habeger, C.C., D.W. Coffin, and B. Hojjatie, *Influence of humidity cycling parameters on the moisture-accelerated creep of polymeric fibers.* Journal of Polymer Science Part B-Polymer Physics, 2001. **39**(17): p. 2048-2062.
38. Wang, J.Z., D.A. Dillard, and F.A. Kamke, *Transient moisture effects in materials.* Journal of Material Science, 1991. **26**(19): p. 5113-5126.
39. Misra, A., et al., *Micro-poromechanics model of fluid-saturated chemically active fibrous media.* ZAMM-Journal of Applied Mathematics and Mechanics/Zeitschrift für Angewandte Mathematik und Mechanik, 2013.
40. Reece, T.B., T.S. Maxey, and I.L. Kron, *A prospectus on tissue adhesives.* The American journal of surgery, 2001. **182**(2): p. S40-S44.
41. Singer, A.J. and H.C. Thode Jr, *A review of the literature on octylcyanoacrylate tissue adhesive.* The American journal of surgery, 2004. **187**(2): p. 238-248.
42. Drury, J.L. and D.J. Mooney, *Hydrogels for tissue engineering: scaffold design variables and applications.* Biomaterials, 2003. **24**(24): p. 4337-4351.
43. Shanmugasundaram, N., et al., *Collagen-chitosan polymeric scaffolds for the in vitro culture of human epidermoid carcinoma cells.* Biomaterials, 2001. **22**(14): p. 1943-1951.
44. Tang, S.Q., W. Yang, and X. Mao, *Agarose/collagen composite scaffold as an anti-adhesive sheet.* Biomedical Materials, 2007. **2**(3): p. S129-S134.
45. Misra, A., et al., *Swelling equilibrium of dentin adhesive polymer formed on the water adhesive phase boundary: Experiments and micromechanical model.* Acta Biomaterialia, 2014. **10**: p. 330-342.
46. Chiaraputt, S., et al., *Changes in resin-infiltrated dentin stiffness after water storage.* J Dent Res, 2008. **87**(7): p. 655-60.
47. Gu, L.S., et al., *Changes in stiffness of resin-infiltrated demineralized dentin after remineralization by a bottom-up biomimetic approach.* Acta Biomater, 2010. **6**(4): p. 1453-61.
48. Ryou, H., et al., *A characterization of the mechanical behavior of resin-infiltrated dentin using nanoscopic Dynamic Mechanical Analysis.* Dent Mater, 2013. **29**(7): p. 719-28.
49. Yasuda, G., et al., *Changes in elastic modulus of adhesive and adhesive-infiltrated dentin during storage in water.* J Oral Sci, 2008. **50**(4): p. 481-6.
50. Yasuda, G., et al., *Determination of elastic modulus of demineralized resin-infiltrated dentin by self-etch adhesives.* Eur J Oral Sci, 2007. **115**(1): p. 87-91.
51. Wang, Y. and P. Spencer, *Hybridization efficiency of the adhesive/dentin interface with wet bonding.* J Dent Res, 2003. **82**(2): p. 141-5.
52. Lakes, R.S., *Viscoelastic solids*. CRC mechanical engineering series. 1999, Boca Raton: CRC Press. 476 p.
53. Wineman, A.S. and K.R. Rajagopal, *Mechanical response of polymers : an introduction*. 2000, Cambridge, England ; New York: Cambridge University Press. x, 317 p.
54. Chen, T., *Determining a Prony Series for a Viscoelastic Material from Time Varying Strain Data.* U.S Army Research Laboratory 2000.
55. Dooling, P.J., C.P. Buckley, and S. Hinduja, *An Intermediate Model Method for Obtaining a Discrete Relaxation Spectrum from Creep Data.* Rheological Acta, 1997. **36**: p. 472-482.
56. Walker, M.P., et al., *Effects of simulated functional loading conditions on dentin, composite and laminate structures.* j Biomed Mater Res B Appl Biomater, 2009. **88**(2): p. 492-501.

57. Po, J.M.C., et al., *Time-Frequency Analysis of Chewing Activity in the Natural Environment.* Journal of Dental Research, 2011. **90**(10): p. 1206-1210.
58. Nalla, R.K., et al., *In Vitro Fatigue Behavior of Human Dentin with Implications for Life Prediction.* Journal of Biomedical Material Research 2003. **66A**: p. 10-20.
59. Spencer, P. and Y. Wang, *Adhesive phase separation at the dentin interface under wet bonding conditions.* Journal of Biomedical Materials Research, 2002. **62**(3): p. 447-456.
60. Wang, Y. and P. Spencer, *Quantifying adhesive penetration in adhesive/dentin interface using confocal Raman microspectroscopy.* J Biomed Mater Res, 2002. **59**(1): p. 46-55.
61. Wieliczka, D.M., P. Spencer, and M.B. Kruger, *Raman mapping of the dentin/adhesive interface.* Appl. Spectrosc, 1996. **50**: p. 1500–1504.
62. Marangos, O., et al., *Physico-mechanical properties determination using microscale homotopic measurements: Application to sound and caries-affected primary tooth dentin.* Acta Biomaterialia, 2009. **5**(4): p. 1338-1348.
63. Misra, A. and V. singh, *Micromechanical model for viscoelastic materials undergoing damage.* Continuum Mechanics and Thermodynamics, 2013. **25**(2-4): p. 343-358.
64. Singh, V., et al., *Fatigue life prediction of dentin–adhesive interface using micromechanical stress analysis.* Dental Materials, 2011. **27**(9): p. e187-e195.
65. Nemat-Nasser, S. and M. Hori, *Micromechanics: Overall properties of heterogeneous materials*. 1993, New York: North-Holland.
66. Navier, C.L., *Sur les lois de l'equilibre et du mouvement des corps solides elastiques.* Memoire de l'Academie Royale de Sciences, 1827. **7**: p. 375-393.
67. Cauchy, A.-L., *Sur l'equilibre et le mouvement d'un systeme de points materiels sollicites par des forces d'attraction ou de repulsion mutuelle.* Excercises de Mathematiques, 1826-1830. **3**: p. 188-212.
68. Arndt, M. and M. Griebel, *Derivation of Higher Order Gradient Continuum Models From Atomistic Models For Crystalline Solids.* Multiscale Modeling & Simulation, 2005. **4**(2): p. 531-562.
69. Blanc, X., C. Le Bris, and P.L. Lions, *From molecular models to continuum mechanics.* Comptes Rendus De L Academie Des Sciences Serie I-Mathematique, 2001. **332**(10): p. 949-956.
70. E, W.N. and Z.Y. Huang, *A dynamic atomistic-continuum method for the simulation of crystalline materials.* Journal of Computational Physics, 2002. **182**(1): p. 234-261.
71. Misra, A. and Y. Yang, *Micromechanical model for cohesive materials based upon pseudo-granular structure.* International Journal of Solids and Structures, 2010. **47**(21): p. 2970-2981.
72. Suiker, A.S.J. and C.S. Chang, *Application of higher-order tensor theory for formulating enhanced continuum models.* Acta Mechanica, 2000. **142**(1-4): p. 223-234.
73. Alibert, J.J., P. Seppecher, and F. Dell'Isola, *Truss modular beams with deformation energy depending on higher displacement gradients.* Mathematics and Mechanics of Solids, 2003. **8**(1): p. 51-73.
74. Seppecher, P., J.-J. Alibert, and F. dell'Isola, *Linear elastic trusses leading to continua with exotic mechanical interactions* Journal of Physics: Conference Series, 2011. **319**(1): p. 012018.
75. dell'Isola, F. and S. Vidoli, *Continuum modelling of piezoelectromechanical truss beams: an application to vibration damping.* Archive of Applied Mechanics, 1998. **68**(1): p. 1-19.

76. Chang, C.S., H. Askes, and L.J. Sluys, *Higher-order strain/higher-order stress gradient models derived from a discrete microstructure, with application to fracture.* Engineering Fracture Mechanics, 2002. **69**(17): p. 1907-1924.
77. Askes, H. and A.V. Metrikine, *Higher-order continua derived from discrete media: continualisation aspects and boundary conditions.* International Journal of Solids and Structures, 2005. **42**(1): p. 187-202.
78. Yang, Y., W.-Y. Ching, and A. Misra, *Higher-order continuum theory applied to fracture simulation of nano-scale intergranular glassy film.* Journal of Nanomechanics and Micromechanics, 2011. **1**(2): p. 60-71.
79. Murrell, J.N., et al., *Molecular Potential Energy Functions*. 1984, New York: John Wiley.
80. Chang, C.S. and A. Misra, *Packing Structure and Mechanical-Properties of Granulates.* Journal of Engineering Mechanics-Asce, 1990. **116**(5): p. 1077-1093.
81. Misra, A. and C.S. Chang, *Effective elastic moduli of heterogeneous granular solids.* International Journal of Solids and Structures 1993. **30**(18): p. 2547-2566.
82. Triantafyllidis, N. and S. Bardenhagen, *On Higher-Order Gradient Continuum-Theories in 1-D Nonlinear Elasticity - Derivation from and Comparison to the Corresponding Discrete Models.* Journal of Elasticity, 1993. **33**(3): p. 259-293.
83. dell'Isola, F., G. Sciarra, and S. Vidoli, *Generalized Hooke's law for isotropic second gradient materials.* Proceedings of the Royal Society a-Mathematical Physical and Engineering Sciences, 2009. **465**(2107): p. 2177-2196.
84. dell'Isola, F. and P. Seppecher, *"Hypertractions and hyperstresses convey the same mechanical information Continuum Mech. Thermodyn. (2010) 22:163-176" by Prof. Podio Guidugli and Prof. Vianello and some related papers on higher gradient theories.* Continuum Mechanics and Thermodynamics, 2011. **23**(5): p. 473-478.
85. dell'Isola, F. and P. Seppecher, *The Relationship between Edge Contact Forces, Double Forces and Interstitial Working Allowed by the Principle of Virtual Power.* Comptes Rendus De L Academie Des Sciences Serie Ii Fascicule B-Mecanique Physique Chimie Astronomie, 1995. **321**(8): p. 303-308.
86. dell'Isola, F. and P. Seppecher, *Edge contact forces and quasi-balanced power.* Meccanica, 1997. **32**(1): p. 33-52.
87. dell'Isola, F., P. Seppecher, and A. Madeo, *How contact interactions may depend on the shape of Cauchy cuts in N-th gradient continua: approach "a la D'Alembert".* Zeitschrift für Angewandte Mathematik und Physik (ZAMP), 2012.
88. Yang, Y. and A. Misra, *Micromechanics based second gradient continuum theory for shear band modeling in cohesive granular materials following damage elasticity.* International Journal of Solids and Structures, 2012.
89. Johnson, K.L., *Contact mechanics*. 1985, Cambridge, U.K.: Cambridge University Press. 452 p.
90. Chang, C.S. and A. Misra, *Theoretical and Experimental-Study of Regular Packings of Granules.* Journal of Engineering Mechanics-Asce, 1989. **115**(4): p. 704-720.
91. Jiang, H., Y. Huang, and K.C. Hwang, *A finite-temperature continuum theory based on interatomic potentials.* Journal of Engineering Materials and Technology-Transactions of the Asme, 2005. **127**(4): p. 408-416.
92. Atanackovic, T.M., *A modified Zener model of a viscoelastic body.* Continuum Mechanics and Thermodynamics, 2002. **14**(2): p. 137-148.

93. Rajagopal, K.R., A.R. Srinivasa, and A.S. Wineman, *On the shear and bending of a degrading polymer beam.* International Journal of Plasticity, 2007. **23**(9): p. 1618-1636.
94. Breuer, S. and E.T. Onat, *On the determination of free energy in linear viscoelastic solids.* Zeitschrift für Angewandte Mathematik und Physik, 1964. **184-191**(2): p. 15.
95. Day, W.A., *Reversibility, Recoverable Work and Free Energy in Linear Viscoelasticity.* Quarterly Journal of Mechanics and Applied Mathematics, 1970. **23**: p. 1-&.
96. Deseri, L., G. Gentili, and M. Golden, *An Explicit Fourmula for the Mnimum Free Energy in Linear Viscoelasticity* Journal of Elasticity, 1999. **54**: p. 141-185.
97. Deseri, L. and J.M. Golden, *The minimum free energy for continuous spectrum materials.* Siam Journal on Applied Mathematics, 2007. **67**(3): p. 869-892.
98. Gentili, G., *Maximum recoverable work, minimum free energy and state space in linear viscoelasticity.* Quarterly of Applied Mathematics, 2002. **60**(1): p. 153-182.
99. Del Piero, G. and L. Deseri, *On the Concepts of State and Free Energy in Linear Viscoelasticity.* Archives of Rational Mechanics 1997. **138**: p. 1-35.
100. Christensen, R.M., *Theory of Viscoelasticity: An introduction*. 1982, New York: Academic Press.
101. Zhou, X.P., H.Q. Yang, and Y.X. Zhang, *Rate dependent critical strain energy density factor of Huanglong limestone.* Theoretical and Applied Fracture Mechanics, 2009. **51**(1): p. 57-61.
102. Yu, M.H., *Advances in Strength Theories for Materials Under Complex Stress State in The 20th Century.* Appl. Mech. Rev 2002. **55**(3): p. 169-218.
103. Misra, A. and P. Poorsolhjouy, *Micro-macro scale instability in 2D regular granular assemblies.* Continuum Mechanics and Thermodynamics, 2013: p. 1-20.
104. Benoit, H., et al., *Characterization of polystyrene networks by small-angle neutron scattering.* Journal of Polymer Science: Polymer Physics Edition, 1976. **14**(12): p. 2119-2128.
105. De Gennes, P.G., *Scaling concepts in polymer physics*. 1979: Cornell university press.
106. Hazony, D., et al., *Average acoustic pulse dispersion length in condensed matter channels.* Philosophical Magazine, 2006. **86**(20): p. 3043-3060.
107. Solar, M., et al., *Mechanical behavior of linear amorphous polymers: Comparison between molecular dynamics and finite-element simulations.* Physical Review E, 2012. **85**(2).
108. Greene, M.S., et al., *The archetype-genome exemplar in molecular dynamics and continuum mechanics.* Computational Mechanics, 2013: p. 1-51.
109. Steinhauser, M.O., et al., *Impact failure of granular materials - Non-equilibrium multiscale simulations and high-speed experiments.* International Journal of Plasticity, 2009. **25**(1): p. 161-182.
110. dell'Isola, F., U. Andreaus, and L. Placidi, *At the origins and in the vanguard of peri-dynamics, non-local and higher gradient continuum mechanics. An underestimated and still topical contribution of Gabrio Piola.* Mechanics and Mathematics of Solids 2013.
111. Auffray, N., et al., *Analytical continuum mechanics á la Hamilton-Piola: least action principle for second gradient continua and capillary fluids.* Mathematics and Mechanics of Solids, Accepted, 2013.
112. Cosserat, E. and F. Cosserat, *Theory of Deformable Bodies*, ed. T.b.D.H. Delphenich. 1909, Paris: SCIENTIFIC LIBRARY A. HERMANN AND SONS.

113. Mindlin, R.D., *Micro-Structure in Linear Elasticity.* Archive for Rational Mechanics and Analysis, 1964. **16**(1): p. 51-78.
114. Toupin, R.A., *Theories of Elasticity with Couple-Stress.* Archive for Rational Mechanics and Analysis, 1964. **17**(2): p. 85-112.
115. Eringen, A.C., *Microcontinuum field theories: foundations and solids*. Vol. 487. 1999: Springer New York.
116. Green, A.E. and R.S. Rivlin, *Multipolar Continuum Mechanics.* Archive for Rational Mechanics and Analysis, 1964. **17**(2): p. 113-147.
117. Germain, P., *Method of Virtual Power in Continuum Mechanics .2. Microstructure.* Siam Journal on Applied Mathematics, 1973. **25**(3): p. 556-575.
118. Chaboche, J.L., *A review of some plasticity and viscoplasticity constitutive theories.* International Journal of Plasticity, 2008. **24**(10): p. 1642-1693.
119. Horstemeyer, M.F. and D.J. Bammann, *Historical review of internal state variable theory for inelasticity.* International Journal of Plasticity, 2010. **26**(9): p. 1310-1334.
120. Kamrin, K., *Nonlinear elasto-plastic model for dense granular flow.* International Journal of Plasticity, 2010. **26**(2): p. 167-188.
121. Contrafatto, L. and M. Cuomo, *A new thermodynamically consistent continuum model for hardening plasticity coupled with damage.* International Journal of Solids and Structures, 2002. **39**(25): p. 6241-6271.
122. Marotti de Sciarra, F., *Hardening plasticity with nonlocal strain damage.* International Journal of Plasticity, 2012. **34**: p. 114-138.
123. Muraleetharan, K.K., et al., *An elastoplatic framework for coupling hydraulic and mechanical behavior of unsaturated soils.* International Journal of Plasticity, 2009. **25**(3): p. 473-490.
124. Vignjevic, R., N. Djordjevic, and V. Panov, *Modelling of dynamic behaviour of orthotropic metals including damage and failure.* International Journal of Plasticity, 2012. **38**: p. 47-85.
125. Voyiadjis, G.Z., R.K. Abu Al-Rub, and A.N. Palazotto, *Thermodynamic framework for coupling of non-local viscoplasticity and non-local anisotropic viscodamage for dynamic localization problems using gradient theory.* International Journal of Plasticity, 2004. **20**(6): p. 981-1038.
126. Collard, C., et al., *Role of discrete intra-granular slip bands on the strain-hardening of polycrystals.* International Journal of Plasticity, 2010. **26**(2): p. 310-328.
127. Naderi, M., S.H. Hoseini, and M.M. Khonsari, *Probabilistic simulation of fatigue damage and life scatter of metallic components.* International Journal of Plasticity, 2013. **43**: p. 101-115.
128. Brunig, M., et al., *A ductile damage criterion at various stress triaxialities.* International Journal of Plasticity, 2008. **24**(10): p. 1731-1755.
129. Darabi, M.K., et al., *A thermodynamic framework for constitutive modeling of time- and rate-dependent materials. Part II: Numerical aspects and application to asphalt concrete.* International Journal of Plasticity, 2012. **35**: p. 67-99.
130. Shen, W.Q., et al., *A micro-macro model for clayey rocks with a plastic compressible porous matrix.* International Journal of Plasticity, 2012. **36**: p. 64-85.
131. Chen, L., J.F. Shao, and H.W. Huang, *Coupled elastoplastic damage modeling of anisotropic rocks.* Computers and Geotechnics, 2010. **37**(1-2): p. 187-194.

132. Lai, Y.M., et al., *Strength criterion and elastoplastic constitutive model of frozen silt in generalized plastic mechanics.* International Journal of Plasticity, 2010. **26**(10): p. 1461-1484.
133. Contrafatto, L. and M. Cuomo, *A framework of elastic-plastic damaging model for concrete under multiaxial stress states.* International Journal of Plasticity, 2006. **22**(12): p. 2272-2300.
134. Nicot, F., L. Sibille, and F. Darve, *Failure in rate-independent granular materials as a bifurcation toward a dynamic regime.* International Journal of Plasticity, 2012. **29**: p. 136-154.
135. Tordesillas, A., et al., *Multiscale characterisation of diffuse granular failure.* Philosophical Magazine, 2012. **92**(36): p. 4547-4587.
136. Tsutsumi, S. and K. Kaneko, *Constitutive response of idealized granular media under the principal stress axes rotation.* International Journal of Plasticity, 2008. **24**(11): p. 1967-1989.
137. Digby, P.J., *The Effective Elastic Moduli of Porous Granular Rocks.* Journal Applied Mechanics, 1981. **48**: p. 803-808.
138. Walton, K., *The Effective Elastic Moduli of a Random Packing of Spheres.* J. Mech.Phys.Solids, 1987. **35**: p. 213-226.
139. Deresiewicz, H., *Stress-Strain Relations for a Simple Model of a Granular Medium.* Journal of Applied Mechanics, 1958. **25**: p. 402-406.
140. Duffy, J. and R.D. Mindlin, *Stress-Strain Relations of a Granular Medium.* Journal of Applied Mechanics, 1957. **24**(4): p. 585-893.
141. Chang, C.S. and P.Y. Hicher, *An elasto-plastic model for granular materials with microstructural consideration.* International Journal of Solids and Structures, 2005. **42**(14): p. 4258-4277.
142. Zhu, Q.Z., J.F. Shao, and M. Mainguy, *A micromechanics-based elastoplastic damage model for granular materials at low confining pressure.* International Journal of Plasticity, 2010. **26**(4): p. 586-602.
143. Yin, Z.Y., C.S. Chang, and P.Y. Hicher, *Micromechanical modelling for effect of inherent anisotropy on cyclic behaviour of sand.* International Journal of Solids and Structures, 2010. **47**(14-15): p. 1933-1951.
144. Coleman, B.D., *Thermodynamics of Materials with Memory.* Archive for Rational Mechanics and Analysis, 1964. **17**(1): p. 1-46.
145. Maugin, G.A., *The thermomechanics of plasticity and fracture*. Vol. 7. 1992: Cambridge University Press.
146. Puzrin, A.M. and C. Rabaiotti, *A thermomechanical framework for non-linear hyperviscoelastic materials.* Journal of Rheology, 2010. **54**(3): p. 619-642.
147. dell'Isola, F., P. Seppecher, and A. Madeo, *How contact interactions may depend on the shape of Cauchy cuts in Nth gradient continua: approach "à la D'Alembert".* Zeitschrift für angewandte Mathematik und Physik, 2012. **63**(6): p. 1119-1141.
148. Seppecher, P., *Second-gradient theory: application to Cahn-Hilliard fluids*, in *Continuum Thermomechanics*. 2002, Springer. p. 379-388.
149. Houlsby, G.T. and A.M. Puzrin, *Principles of hyperplasticity: an approach to plasticity theory based on thermodynamic principles*. 2006: Springer.

150. Abu Al-Rub, R.K. and G.Z. Voyiadjis, *On the coupling of anisotropic damage and plasticity models for ductile materials.* International Journal of Solids and Structures, 2003. **40**(11): p. 2611-2643.
151. Einav, I., G.T. Houlsby, and G.D. Nguyen, *Coupled damage and plasticity models derived from energy and dissipation potentials.* International Journal of Solids and Structures, 2007. **44**(7-8): p. 2487-2508.
152. Carcaterra, A., *Ensemble energy average and energy flow relationships for nonstationary vibrating systems.* Journal of Sound and Vibration, 2005. **288**(3): p. 751-790.
153. Carcaterra, A. and A. Akay, *Theoretical foundations of apparent-damping phenomena and nearly irreversible energy exchange in linear conservative systems.* Journal of the Acoustical Society of America, 2007. **121**(4): p. 1971-1982.
154. Culla, A., A. Sestieri, and A. Carcaterra, *Energy flow uncertainties in vibrating systems: Definition of a statistical confidence factor.* Mechanical Systems and Signal Processing, 2003. **17**(3): p. 635-663.
155. Rinaldi, A., et al., *Lattice models of polycrystalline micro structures: A quantitative approach.* Mechanics of Materials, 2008. **40**(1-2): p. 17-36.
156. Rinaldi, A. and Y.C. Lai, *Statistical damage theory of 2D lattices: Energetics and physical foundations of damage parameter.* International Journal of Plasticity, 2007. **23**(10-11): p. 1796-1825.
157. Rinaldi, A., *Bottom-up modeling of damage in heterogeneous quasi-brittle solids.* Continuum Mechanics and Thermodynamics, 2013. **25**(2-4): p. 359-373.
158. Shim, J. and D. Mohr, *Rate dependent finite strain constitutive model of polyurea.* International Journal of Plasticity, 2011. **27**(6): p. 868-886.
159. Mohr, D., *Mechanism-based multi-surface plasticity model for ideal truss lattice materials.* International Journal of Solids and Structures, 2005. **42**(11): p. 3235-3260.
160. Khan, A. and S. Huang, *Continuum theory of plasticity.*, 1995, New York: Wiley-Interscience.
161. Chang, C.S., A. Misra, and K. Acheampong, *Elastoplastic Deformation for Particulates with Frictional Contacts.* Journal of Engineering Mechanics-Asce, 1992. **118**(8): p. 1692-1707.
162. Magoariec, H., A. Danescu, and B. Cambou, *Nonlocal Orientational Distribution of Contact Forces in Granular Samples Containing Elongated Particles.* Acta Geotechnica, 2008. **3**: p. 49-60.
163. Clausius, R., *XVI. On a mechanical theorem applicable to heat.* The London, Edinburgh, and Dublin Philosophical Magazine and Journal of Science, 1870. **40**(265): p. 122-127.
164. Swenson, R.J., *Comments on Virial Theorems for Bounded Systems.* American Journal of Physics, 1983. **51**(10): p. 940-942.
165. Irving, J.H. and J.G. Kirkwood, *The Statistical Mechanical Theory of Transport Processes .4. The Equations of Hydrodynamics.* Journal of Chemical Physics, 1950. **18**(6): p. 817-829.
166. Tsai, D.H., *Virial Theorem and Stress Calculation in Molecular-Dynamics.* Journal of Chemical Physics, 1979. **70**(3): p. 1375-1382.
167. Subramaniyan, A.K. and C.T. Sun, *Continuum interpretation of virial stress in molecular simulations.* International Journal of Solids and Structures, 2008. **45**(14-15): p. 4340-4346.

168. Zhou, M., *A new look at the atomic level virial stress: on continuum-molecular system equivalence.* Proceedings of the Royal Society a-Mathematical Physical and Engineering Sciences, 2003. **459**(2037): p. 2347-2392.
169. Madeo, A., F. dell'Isola, and F. Darve, *A continuum model for deformable, second gradient porous media partially saturated with compressible fluids.* Journal of the Mechanics and Physics of Solids, 2013. **61**(11): p. 2196-2211.
170. Madeo, A., D. George, and Y. Remond, *Second-gradient models accounting for some effects of microstructure on remodelling of bones reconstructed with bioresorbable materials.* Computer Methods in Biomechanics and Biomedical Engineering, 2013. **16**: p. 260-261.
171. Dell'Isola, F. and K. Hutter, *What are the dominant thermomechanical processes in the basal sediment layer of large ice sheets?* Proceedings of the Royal Society of London Series a-Mathematical Physical and Engineering Sciences, 1998. **454**(1972): p. 1169-1195.
172. dell'Isola, F., L. Rosa, and C. Wozniak, *A micro-structured continuum modelling compacting fluid-saturated grounds: the effects of pore-size scale parameter.* Acta Mechanica, 1998. **127**(1-4): p. 165-182.
173. Kuhn, M.R. and J.K. Mitchell, *New Perspectives on Soil-Creep.* Journal of Geotechnical Engineering-Asce, 1993. **119**(3): p. 507-524.
174. Lade, P.V., C.D. Liggio, and J. Nam, *Strain Rate, Creep, and Stress Drop-Creep Experiments on Crushed Coral Sand.* Journal of Geotechnical and Geoenvironmental Engineering, 2009. **135**(7): p. 941-953.
175. Chang, C.S. and L. Ma, *Elastic-Material Constants for Isotropic Granular Solids with Particle Rotation.* International Journal of Solids and Structures, 1992. **29**(8): p. 1001-1018.
176. Wu, B.S., Z.H. Xu, and Z.G. Li, *A note on imposing displacement boundary conditions in finite element analysis.* Communications in Numerical Methods in Engineering, 2008. **24**(9): p. 777-784.
177. Misra, A., et al., *Micro-scale analysis of compositional and mechanical properties of dentin using homotopic measurements*, in *Biomedical Imaging and Computational Modeling in Biomechanics*, U. Andreaus and D. Iacoviello, Editors. 2013, Springer Netherlands. p. 131-141.
178. Wieliczka, D.M., M.B. Kruger, and P. Spencer, *Raman imaging of dental adhesive diffusion.* Appl. Spectrosc, 1997. **51**: p. 1593–1596.
179. Nguyen, V.D., et al., *Imposing periodic boundary condition on arbitrary meshes by polynomial interpolation.* Computational Materials Science, 2012. **55**: p. 390-406.
180. Kouznetsova, V., W.A.M. Brekelmans, and F.P.T. Baaijens, *An approach to micro-macro modeling of heterogeneous materials.* Computational Mechanics, 2001. **27**(1): p. 37-48.
181. Misra, A. and S.P. Huang, *Micromechanical stress-displacement model for rough interfaces: Effect of asperity contact orientation on closure and shear behavior.* International Journal of Solids and Structures, 2012. **49**(1): p. 111-120.
182. Kanatani, K.I., *Distribution of Directional-Data and Fabric Tensors.* International Journal of Engineering Science, 1984. **22**(2): p. 149-164.